EXPLORATION OF LEAD-FREE PEROVSKITE MATERIALS FOR PHOTOVOLTAIC APPLICATIONS

Ph.D. Thesis

By

PRAVEEN KUMAR

DEPARTMENT OF CHEMISTRY

INDIAN INSTITUTE OF TECHNOLOGY INDORE

JULY 2024

EXPLORATION OF LEAD-FREE PEROVSKITE MATERIALS FOR PHOTOVOLTAIC APPLICATIONS

A THESIS

Submitted in partial fulfillment of the requirements for the award of the degree
of
DOCTOR OF PHILOSOPHY

by
PRAVEEN KUMAR

DEPARTMENT OF CHEMISTRY
INDIAN INSTITUTE OF TECHNOLOGY INDORE
JULY 2024

INDIAN INSTITUTE OF TECHNOLOGY INDORE

CANDIDATE'S DECLARATION

I hereby certify that the work which is being presented in the thesis entitled **EXPLORATION OF LEAD-FREE PEROVSKITE MATERIALS FOR PHOTOVOLTAIC APPLICATIONS** in the partial fulfillment of the requirements for the award of the degree of **DOCTOR OF PHILOSOPHY** and submitted in the **DEPARTMENT OF CHEMISTRY, INDIAN INSTITUTE OF TECHNOLOGY INDORE**, is an authentic record of my own work carried out during the time period from **JULY 2019** to **JULY 2024** under the supervision of **Prof. SHAIKH M. MOBIN,** Professor, Department of Chemistry, Indian Institute of Technology Indore.

The matter presented in this thesis has not been submitted by me for the award of any other degree of this or any other institute.

Praveen Kumar 25/06/2025

Signature of the student with date

(PRAVEEN KUMAR)

This is to certify that the above statement made by the candidate is correct to the best of my/our knowledge.

M. Shaik June 25, 2025

Signature of Thesis Supervisor with date

(Prof. SHAIKH M. MOBIN)

Mr. PRAVEEN KUMAR has successfully given his Ph.D. Oral Examination held on **25/06/2025.**

M. Shaik June 25, 2025

Signature of Thesis Supervisor with date

(Prof. SHAIKH M. MOBIN)

ACKNOWLEDGEMENTS

Om Namah Shivaya

"Guru Brahma, Guru Vishnu, Guru Devo Maheshwara,
Guru Sakshat Param Brahma, Tasmai Sri Gurave Namaha"

It is my pleasure to express heartfelt gratitude to everyone who has contributed in various ways to the success of my thesis and made this experience memorable for me.

First and foremost, I would like to thank God for His blessings and allowing me to evolve.

Most importantly, I extend my sincere gratitude and warm regards to my supervisor, Prof. Shaikh M. Mobin, for recruiting me and providing the opportunity to conduct my research under his guidance. My research journey has been truly wonderful. I am deeply thankful to my supervisor for his constant support, motivation, encouragement, and valuable suggestions throughout my research. His efforts in providing the necessary facilities and striving to publish our work in high-quality journals have been invaluable. Finding a supervisor as supportive and dedicated as Prof. Mobin is rare, and I am grateful for his unwavering assistance. It has been a privilege to work under his supervision.

I also wish to convey my respect and sincere gratitude to Prof. Suhas S. Joshi, Director of IIT Indore, for providing excellent infrastructure and necessary facilities at the institute.

I also thank my PSPC members, Prof. Sampak Samanta and Prof. Sanjay Kumar Singh, for their constructive suggestions and comments that have greatly improved my work. I am grateful to Dr. Arun Lal and Mr. Sanjay Atri, Mr. Hari Singh, for motivating me to pursue Ph.D. and for their continuous support throughout my academic journey.

I extend my gratitude to all the faculty, staff members, and technicians in the Department of Chemistry at IIT Indore for their guidance and support during my coursework, departmental activities, and documentation. Special thanks to the SIC staff members Mr. Kinny Pandey, Mr. Ghanshyam, Mr. Nitin, Mr. Ravindra, and Mr. Atul for their assistance with various characterizations.

I also thank IIT Indore and DST-Inspire, New Delhi, India, for providing a research fellowship. My appreciation extends to SERB, CSIR, and BRNS for their financial support.

I convey my sincere respect and thanks to my seniors Dr. Archana Chaudhary, Dr. Sanjay Verma, Dr. Anoop Gupta, Dr. Anoop K. Saini, Dr. Akbar, Dr. Mohit, Dr. Prakash Chandra, Dr. Vinay, Dr. Ajeet, Dr. Pratibha, Dr. Kaushik, Dr. Pranav, Dr. Viresh, Dr. Navpreet, Dr. Diptanshu, Dr. Imtiaz, Dr. Kamal, Dr. Shagufi, Dr. Topi, Dr. Richa, Dr. Nabeela, and Dr. Neha for their needful suggestions. I also thank my colleagues and lab members Mr. Ravinder, Mr. Pawan Pratap Singh, Mr. Rakesh, Mr. Zahir, Ms. Nirmiti, Mr. Debashish, Ms. Vinita, Ms. Priya and Mr. Nisar.

I want to offer special thanks to my friends specially Dr. Atul Arya, Dr. Anil Garry, Dr. Ram, Dr. Rahul, Mr. Kapil Siwach, Mr. Amit Chahar, Mr. Deepak Jakhar, Mr. Ashish Rathee, Mr. Pradeep Siwach, Mr. Ajay, Mr. Keshav, Mr. Manan, Mr. Pankaj, Mr. Puneet, Mr. Yogesh, Mr. Shashank, Mr. Katewa and Ravechi Group for their encouragement and support during my Ph.D. journey. They were always behind to support me and gave valuable suggestions throughout.

A special thanks goes to Dr. Khursheed Ahmed for his unconditional support throughout my research, his valuable suggestions during experiments and manuscript writing, and his assistance from the start to the completion of my Ph.D.

Finally, last but not the least, I sincerely thank my parents wholeheartedly for their patience, constant support, blessings, and encouragement; my grandparents Late Mr. Surajmal Antil and Mrs. Ompati Devi, my parents Mr. Satbir Singh and Mrs. Sushila Devi, my brothers Mr. Rohit Antil and Mr. Mohit Antil, made me stronger. With God's grace, I am fortunate to have such a caring and loving family.

Special thank my wife from the bottom of my heart, Mrs. Kavita Antil, for her unwavering support, understanding, and motivation to complete my degree. Without her help and trust, I would not have been where I am today. Words cannot fully express my gratitude for my family's support in this journey.

Lastly, I extend my sincere gratitude to everyone who has directly or indirectly contributed to my educational journey.

"It always seems impossible, until it is done"

Praveen Kumar Antil

IIT Indore

DEDICATED TO MY BELOVED GRANDFATHER AND MY FAMILY

TABLE OF CONTENTS

ABSTRACT

The work demonstrated in the thesis entitled "**Exploration of Lead-Free Perovskite Materials for Photovoltaic Applications**" was initiated in July 2019 in the Department of Chemistry, Indian Institute of Technology Indore. The objectives of this thesis are to design and fabrication of lead-free perovskite materials and further explore them for photovoltaic applications.

Objectives and Scope

The thesis work focuses on the following key points-

1. Synthesis of Antimony and Bismuth based halide perovskite as a light absorber material for photovoltaic application.
2. Utilization of advanced characterization techniques to analyze the physiochemical and optoelectronic properties of the synthesized perovskite materials.
3. Controlling the rapid growth and the morphology of the light absorber.
4. Fabrication of electrodes for photovoltaic devices.

The thesis is divided into six chapters, the first of which introduces a few types of perovskite materials. A summary of energy consumption and the need for sustainable energy sources opens the literature review, which is then followed by information on the history, composition, and characteristics of perovskite materials. Discussions on various perovskite material synthesis techniques are then covered, along with the applications that halide perovskite have been explored. Lead-free perovskite materials and their utilization as light absorbers for photovoltaic applications are the main areas of focus. The synthesis process and its energy generation is covered in detail in later chapters.

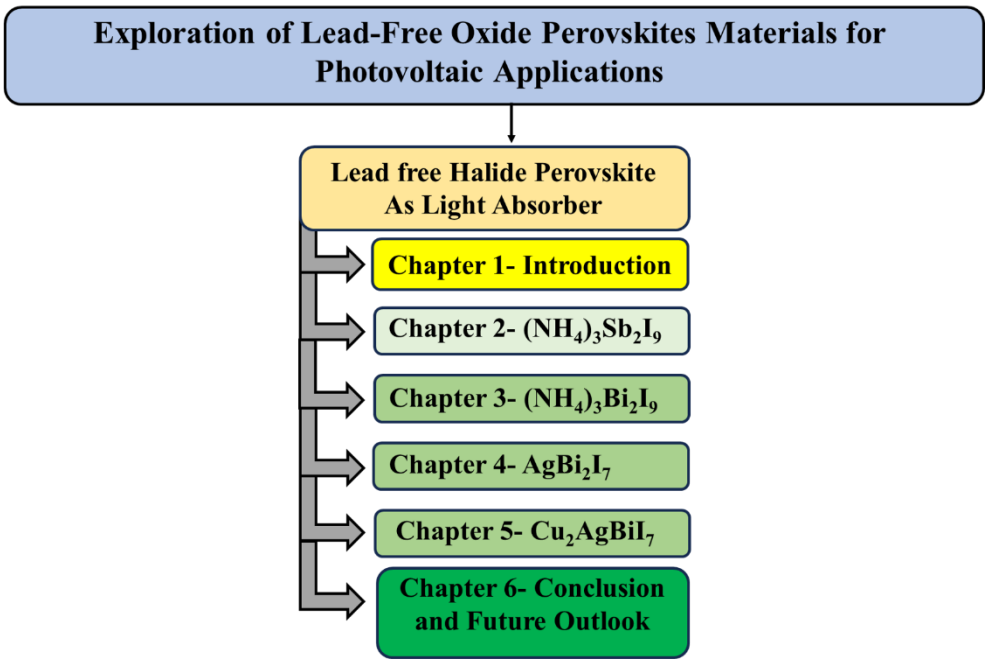

An extensive overview crucial to the thesis is presented in the introduction chapter, which also gives a summary of perovskite materials. Subsequent to diverse synthesis methodologies and employing perovskite materials for various types of sustainable energy applications, focusing on specific types of perovskite materials and the development of their halide, also every device used and its components is briefly covered **(Chapter 1).** This chapter provides a detailed explanation of the synthesis of novel ways for regulating the morphology of perovskite materials. The thesis focuses on using lead-free perovskite in photovoltaic applications.

Chapter 2 demonstrates antimony (Sb) based perovskite like-materials $(NH_4)_3Sb_2I_9$ thin films using one-step and two-step deposition approaches for photovoltaic applications. The fabricated $(NH_4)_3Sb_2I_9$ thin films showed good stability and optoelectronic properties, which suggested their potential for photovoltaic applications. We have utilized $(NH_4)_3Sb_2I_9$ as a light absorber for the construction of Pb free PSCs. Moreover, we have employed a modified two-step process for the preparation of $(NH_4)_3Sb_2I_9$. The developed Pb free PSCs device (FTO/CL-TiO_2/m-TiO_2/$(NH_4)_3Sb_2I_9$/HTM/Au) exhibited enhanced power conversion

efficiency (PCE) of 0.42%. The $(NH_4)_3Sb_2I_9$ based PSCs devices exhibited good open circuit voltage and decent photocurrent density.

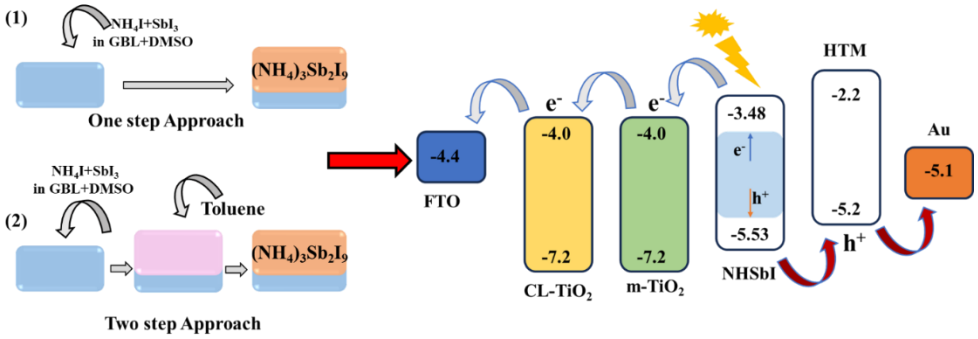

Figure 1. Representation of synthesis of $(NH_4)_3Sb_2I_9$ light absorber and device fabrication.

Chapter 3 Bismuth halide perovskite materials were prepared, which can be utilized as highly efficient perovskite light absorbers due to their good aerobic stability. We have investigated the optoelectronic properties of the $(NH_4)_3Bi_2I_9$ perovskite and employed it as a light absorber in the fabrication of Pb free PSCs. A solvent engineering approach was utilized to improve the photovoltaic performance of the $(NH_4)_3Bi_2I_9$ perovskite-based PSCs. The solvent engineering approach and the utilization of anti-solvent (chlorobenzene) influence the crystallization process. Furthermore, perovskite solar cells were developed by utilizing $(NH_4)_3Bi_2I_9$ perovskite light absorber. The probable HOMO and LUMO energy level values of the $(NH_4)_3Bi_2I_9$ perovskite were also investigated, and the band gap of the $(NH_4)_3Bi_2I_9$ perovskite was found to be 2.1 eV. The developed PSC device exhibited a power conversion efficiency (PCE) of ~0.6%. The developed perovskite solar cells exhibited better open circuit voltage and suggested the potential of $(NH_4)_3Bi_2I_9$ perovskite as energy material for photovoltaic applications.

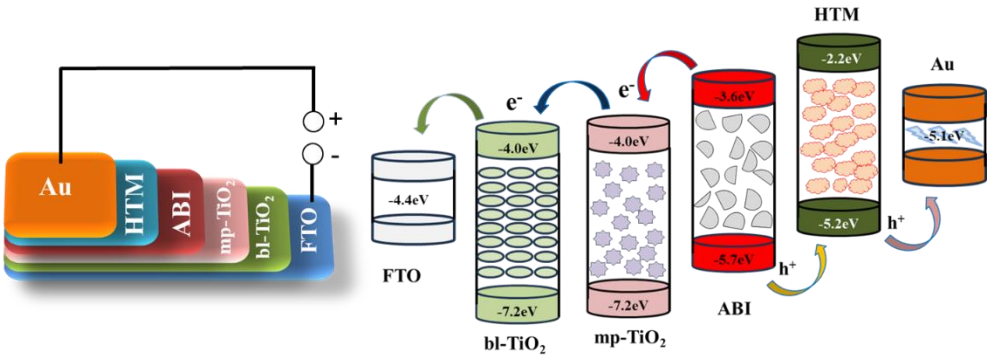

Figure 2. Representation of fabricated device by utilizing synthesis of $(NH_4)_3Bi_2I_9$ light absorber and device energy level.

Chapter 4 solvent engineering techniques were used to fabricate a silver-based bismuth perovskite ($AgBi_2I_7$) material as a light absorber for PSCs. Hybrid perovskites based on bismuth are good candidates for developing lead-free and air-stable photovoltaics, but poor surface morphologies and large bandgap energies have historically constrained them. Monovalent silver cations are incorporated into iodo-bismuthates as part of a novel materials processing method to fabricate improved bismuth-based thin-film photovoltaic absorbers. We examined bismuth iodide perovskite made of silver, which showed improvements in surface morphology and a narrow band gap and achieved high power conversion efficiency. The photovoltaic efficiency was improved by combining DMF and MeOH in an optimum ratio. The obtained device performance results demonstrate the efficiency of the solvent engineering method. We reduced the band gap to 1.89 eV and achieved a maximum power conversion efficiency of 0.96% and Voc (650 mV) using the solvent engineering approach. Additionally, simulation studies verified an efficiency of 13.26% by using $AgBi_2I_7$ as a light absorber perovskite material.

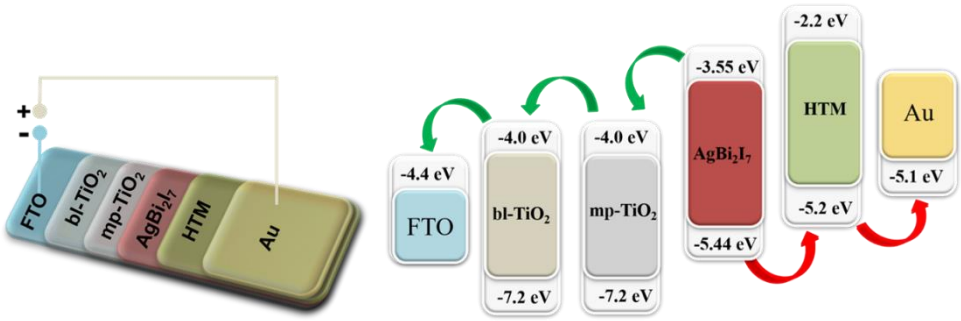

Figure 3. Representation of fabricated device by utilizing synthesis of $AgBi_2I_7$ light absorber and device energy level.

Chapter 5 demonstrates the use of the antisolvent technique to control the crystallization of the halide double perovskite (Cu_2AgBiI_6) as a light absorber for solar cell applications. Incorporating copper into silver and bismuth-based perovskite enhances its stability under moisture conditions. The Cu_2AgBiI_6 perovskite was immersed in water for several minutes, demonstrating its stability in wet conditions. The antisolvent method not only improves stability but also enhances the device's photovoltaic performance. The power conversion efficiency (PCE) of the Cu_2AgBiI_6-based device with various antisolvents was approximately 1%. Using the optimal antisolvent enables the fabrication of highly efficient and stable solar cells. Furthermore, theoretical and experimental research is significant and necessary. Theoretical studies allow us to predict the characteristics of novel perovskite compositions, identify potential issues, and develop materials with better performance. Additionally, SCAPS simulations were conducted for theoretical exploration. The simulation of the Cu_2AgBiI_6 perovskite showed a higher PCE of 8%, demonstrating its potential and paving the way for further utilization of Cu_2AgBiI_6 in photovoltaic cells.

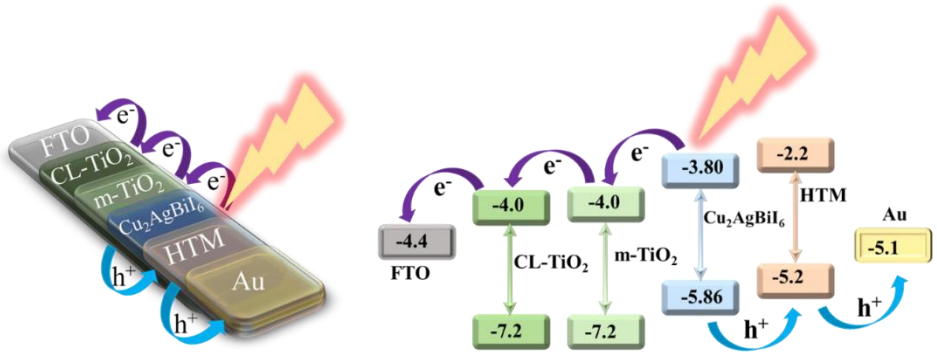

Figure 4. Representation of fabricated device by utilizing synthesis of Cu_2AgBiI_6 light absorber and energy level of the device.

Chapter 6 summarizes the conclusions and explores the future potential of advanced lead-free perovskite materials for sustainable and cost-effective photovoltaic applications. Perovskite materials have demonstrated significant potential across various applications, including solar cells, supercapacitors, and water splitting. However, achieving optimal performance in large-area modules remains challenging. Key areas for improvement include lowering the band gap, controlled morphology, and strategic doping. Employing suitable fabrication techniques is crucial for enhancing device performance. To further advance the efficiency of perovskite-based devices, it is essential to delve deeper into the carrier dynamics and crystallization mechanisms, reduce defect density, and identify suitable charge carrier materials for device fabrication. Additionally, perovskite materials hold promise to be used in tandem solar cells, presenting an exciting avenue for future research and development.

LIST OF PUBLICATIONS

1. **Kumar, P.;** Abbas, Z.; Kumar, P.; Das, D.; Mobin, S. M. Highlights in Interface of Wastewater Treatment by Utilizing Metal Organic Frameworks: Purification and Adsorption Kinetics. *Langmuir,* 2024, 40 (10), 5040–5059.
2. **Kumar, P.;** Ahmad, K.; M. Mobin, S. Improved Photovoltaic Performance of Pb-Free $AgBi_2I_7$ Based Photovoltaics. *Nanoscale Adv.,* 2023, 5 (6), 1624–1630.
3. Ahmad, K.; **Kumar, P.;** Kim, H.; Mobin, S. M. Optoelectronic and Photovoltaic Properties of $(NH_4)_3Bi_2I_9$: A Perovskite-like Energy Material for Pb-Free Perovskite Solar Cells. *ChemNanoMat,* 2022, 8 (6), e202200061.
4. **Kumar, P**.; Ahmad, K.; Dagar, J.; Unger, E.; Mobin, S. M. Two-Step Deposition Approach for Lead Free $(NH_4)_3Sb_2I_9$ Perovskite Solar Cells with Enhanced Open Circuit Voltage and Performance. *ChemElectroChem,* 2021, 8 (16), 3150–3154.
5. **Kumar, P.;** Mobin, S. M. Development of Moisture Stable Halide Double Perovskite (Cu_2AgBiI_6) with Improvement in Photovoltaic Performance. **(Communicated)**
6. Ahmad, K.; **Kumar, P.;** Shrivastava, P.; Mobin, S. M. Sn(IV) Inserted Lead-Free Perovskite Materials ($MA_3(Bi_{1-x}Sn_x)_2I_9$) as Light Absorbers: Bandgap Engineering and Enhanced Photovoltaic Performance. Energy Technol. 2022, 10 (3), 2100717.
7. Ahmad, K.; **Kumar, P.;** M. Mobin, S. A Highly Sensitive and Selective Hydroquinone Sensor Based on a Newly Designed N-rGO/$SrZrO_3$ Composite. Nanoscale Adv. 2020, 2 (1), 502–511.
8. Ahmad, K.; **Kumar, P.;** M. Mobin, S. Hydrothermally Grown Novel Pyramids of the $CaTiO_3$ Perovskite as an Efficient Electrode Modifier for Sensing Applications. Mater. Adv. 2020, 1 (6), 2003–2009.

9. Ahmad, K.; **Kumar, P.;** Mobin, S. M. Inorganic Pb-Free Perovskite Light Absorbers for Efficient Perovskite Solar Cells with Enhanced Performance. Chem. – Asian J. 2020, 15 (18), 2859–2863.

10. Ahmad, K.; **Kumar, P.;** Mobin, S. M. A Two-Step Modified Sequential Deposition Method-Based Pb-Free $(CH_3NH_3)_3Sb_2I_9$ Perovskite with Improved Open Circuit Voltage and Performance. ChemElectroChem 2020, 7 (4), 946–950.

11. Ahmad, K.; **Kumar, P.;** Mobin, S. M. Hydrothermally Grown SnO_2 Flowers as Efficient Electrode Modifier for Simultaneous Detection of Catechol and Hydroquinone. J. Electrochem. Soc. 2019, 166 (15), B1577.

12. Rajak, R.; Saraf, M.; **Kumar, P**.; Natarajan, K.; Mobin, S. M. Construction of a Cu-Based Metal–Organic Framework by Employing a Mixed-Ligand Strategy and Its Facile Conversion into Nanofibrous CuO for Electrochemical Energy Storage Applications. Inorg. Chem. 2021, 60 (22), 16986–16995.

13. Ghosh, T.; Natarajan, K.; **Kumar, P.;** Mobin, S. M. Nitrogen-Doped Mixed-Phase Cobalt Nanocatalyst Derived from a Trinuclear Mixed-Valence Cobalt(III)/Cobalt(II) Complex for High-Performance Oxygen Evolution Reaction. Inorg. Chem. 2021, 60 (4), 2333–2346.

14. Kumar, R.; Naz Ansari, S.; Deka, R.; **Kumar, P.;** Saraf, M.; Mobin, S. M. Progress and Perspectives on Covalent-Organic Frameworks (COFs) and Composites for Various Energy Applications. Chem. – Eur. J. 2021, 27 (55), 13669–13698.

15. Kumar, V.; **Kumar, P.;** Deka, R.; Abbas, Z.; Mobin, S. M. Recent Development of Morphology-Controlled Hybrid Nanomaterials for Triboelectric Nanogenerator: A Review. Chem. Rec. 2022, 22 (9), e202200067.

16. Nabeela, K.; Deka, R.; Abbas, Z.; **Kumar, P.;** Saraf, M.; Mobin, S. M. Covalent Organic Frameworks (COFs)/MXenes Heterostructures for Electrochemical Energy Storage. Cryst. Growth Des. 2023, 23 (5), 3057–3078
17. **Kumar, P.;** Kumar, V.; Ahmad, K.; Mobin S. M.; Perovskite $SrZrO_3$ cube behavior towards electrolyte-based supercapacitor application. **(Communicated)**

Book Chapter:

18. Khursheed Ahmad, **Praveen Kumar,** and Shaikh M. Mobin (2021), Recent Progress in All-Inorganic Hybrid Materials for Energy Conversion Applications. In: Kharissova O.V., Torres-Martínez L.M., Kharisov B.I. (eds) Handbook of Nanomaterials and Nanocomposites for Energy and Environmental Applications. Springer, Cham. (DOI: 10.1007/978-3-030-36268-3_204).

School/Conference/Workshop/Courses:

1. **"Perovskite Solar Cells" workshop** organized by National Centre for Photovoltaic Research and Education (NCPRE) and Indian Institute of Technology Bombay, Bombay, India, 15th-16th October, **2019**
2. **"Advanced Energy Science and Technology"** organized by Physics Department, TEQIP-3, IIT Indore, India, 7th-9th December, **2021**
3. **"Twitter-based poster competition, ChemSci2021: Leaders in the Field Symposium**" **(Poster Presentation)**" by RSC's flagship journal Chemical Science & JNCASR Bangalore, 10th-15th December, **2021 (Poster Presentation)**
4. "**7th International Conference on Advanced Nanomaterials and Nanotechnology (ICANN2021)"** organized by the Centre for

Nanotechnology, IIT Guwahati, Assam, India, during 14th-17th December **2021 (Flash Talk)**.

5. **"Use of Hydrogen as a future fuel" organized by Global Initiative of Academic Networks (GIAN) Course**, Indian Institute of Technology Indore, 20th -24th December, **2021**
6. **"3rd Commonwealth Chemistry Posters"** on 28th-29th September, **2022 (Poster Presentation)**
7. **"Symposium on Materials Sciences Towards New Horizon-2023**" organized by Royal Society of Chemistry and Department of Chemistry IIT Indore, 19th-20th Jan, 2023 **(Poster Presentation)**.
8. **"4th Commonwealth Chemistry Posters"** on 4th -5th October, **2023 (Poster Presentation)**.
9. **"International Conference on Energy and Environmental Materials (E_2M-2024)",** organized by MEMS, IIT Indore, 11th-13th July, 2024 **(Poster Presentation)**.

LIST OF ABBREVIATIONS

HCl	Hydrochloric acid
HNO_3	Nitric acid
HI	Hydroiodic acid
GBL	Gamma-butyrolactone
DMSO	Dimethyl sulphoxide
MeOH	Methanol
DMF	Dimethylformamide
MAI	Methyl ammonium iodide
MA	Methylammonium
NH_4I	Ammonium Iodide
AgI	Silver Iodide
CuI	Copper Iodide
PIF8-TAA	Poly-indenofluoren-8-triarylamine
TQ1	poly[[2,3-bis(3-octyloxyphenyl)-5,8-quinoxaline diyl]-2,5-thiophenediyl]
P3TI	poly[N,N'-bis(2-hexyldecyl)iso-indigo-6,6'-diyl-*alt*-3,3"-dioctyl-2,2',5',2"-terthiophene-5,5"-diyl]
PCPDTBT	poly[2,1,3-benzothiadiazole-4,7-diyl[4,4-bis(2-ethylhexyl)-4H-cyclopenta[2,1-*b:*3,4-*b'*]dithiophene-2,6-diyl]]
PEA	Phenylethyl-ammonium
tBP	4-tert-butyl pyridine
MMT	Mont morillonite
NMP	N-methyl-2-pyrrolidone
FPDI	Fluorinated perylene diimide
CL	Compact layer
DI	Deionized Water
T	Temperature
SCXRD	Single crystal X-ray diffractometer

RT	Room temperature
T	Temperature
C	Celsius
°	Degree
mV	MiliVolt
mA	MiliAmpere
h	Hour
nm	Nano-meter
cm	Centi-meter
mm	Milli-meter
µm	Micro-meter
g	Gram
mg	Milligram
mL	Milliliter
L	Liter
a.u.	Arbitrary unit
Eg	Bandgap
eV	Electron volt
PXRD	Powder X-ray diffraction
RT	Room Temperature
UV	Ultraviolet
Vis	Visible
SEM	Scanning Electron Microscope
FESEM	Field-Emission Scanning Electron Microscope
EDX	Energy Dispersive X-ray analysis
PSCs	Perovskite solar cells
FTO	Fluorine doped tin oxide
ITO	Indium doped tin oxide
HTM	Hole Transport Material
HTL	Hole Transport Layer
ETM	Electron Transport Material

ETL	Electron Transport Layer
GCE	Glassy Carbon Electrode
CV	Cyclic Voltammetry
EIS	Electrochemical Impedance Spectroscopy
V	Voltage
eV	Electron volt
HOMO	Highest occupied molecular orbital
LUMO	Lowest unoccupied molecular orbital
Spiro-OMeTAD	N2,N2,N2′,N2′,N7,N7,N7′,N7′-octakis(4-methoxyphenyl)-9,9′-spirobi[9H-fluorene]-2,2′,7,7′-tetramine
PEDOT:PSS	Poly(3,4-ethylenedioxythiophene)-poly(styrenesulfonate)
J_{SC}	Short circuit current density
FF	Fill factor
IPCE	Incident-photon-to-current-efficiency
EQE	External Quantum Efficiency
TRPL	Time resolved photo-luminescence
PL	Photoluminescence
PCE	Power conversion efficiency
Voc	Open circuit voltage
J-V	Current Voltage

LIST OF SCHEMES

LIST OF FIGURES

APPENDIX 1

CHAPTER 2

CHAPTER 3

CHAPTER 4

CHAPTER 5

ADDITIONAL TABLE

CHAPTER 1

1.1. Introduction

With technological advancements and the rapid depletion of fossil fuels, there is an increasing need for alternative clean and renewable energy sources to ensure sustainable development. Industrialization and population growth exert control of the energy supply. As per the International Energy Outlook 2023 report, energy consumption globally per primary energy source is projected to increase by over 50% between 2022 and 2050 [1]**.** The combustion of fossil fuels increases greenhouse gas concentrations, which contributes to global warming by trapping heat in the atmosphere [2]. The rise in global energy use will exert considerable pressure on primary energy supplies. Till now, utmost of the energy is produced by fossil fuels like natural gas, coal, and oil [3, 4]**.** Processing non-renewable resources like oil, natural gasses (methanol), and coal provides the main energy source in conventional energy systems. This phenomenon adversely impacts the Earth's ecosystems and exacerbates natural disasters such as rising sea levels and climate change [5]. The production and use of non-renewable energy sources have significant adverse environmental effects [6, 7]**.** Also, these sources are quickly depleted because of their massive usage, which has resulted in serious environmental challenges in addition to their emission of greenhouse gases. Moreover, the sustainable use of non-renewable resources is severely limited by reservoir depletion, geopolitical conflicts, and unstable fuel prices [2,7]. Given the aforementioned issues, new developments and enhancements to the energy landscape are required to maintain the current global energy profile. Several technologies have been developed in recent years to tackle the decline of fossil fuels and the release of greenhouse gases from non-renewable energy sources. These technologies aim to ensure a consistent energy supply for industries and individuals [9]**.** However, when it comes to addressing energy-related challenges, effectively storing and then utilizing the generated energy is the critical factor. These issues drive the search for alternative renewable energy sources to replace fossil fuels.

Solar, wind, geothermal, and hydrothermal energy are among the prominent alternatives that have garnered significant attention. Among all alternatives, solar energy demonstrates significant potential due to its environmental friendliness, renewability, universality, and high-power density. Consequently, solar cell (SC) devices are considered a promising solution to the energy crisis by directly converting solar radiation into electrical energy [10]. Sustainable renewable energy systems have remained acknowledged as innovative models to substitute traditional energy sources [11]**.** Beyond meeting the world's energy needs and supplies, the larger benefits of sustainable renewable energy lies in their ability to support governments in formulating policies aimed at combating and reducing greenhouse gas emissions as well as safeguarding a few remaining fossil fuel reserves. The nature of most of the aforementioned renewable energy supplies is discontinuous, which causes fluctuations in their energy generation [12, 13]**.** Non-renewable sources become more resilient and important when the energy is not generated. Due to the various obstacles and challenges accompanying renewable energy sources [14], as well as the ongoing dependence on non-renewable energy, material science, and nanotechnology offer a promising new approach to energy production and conversion. This approach focuses on improving efficiency and reducing costs [9, 12, 15]**.**

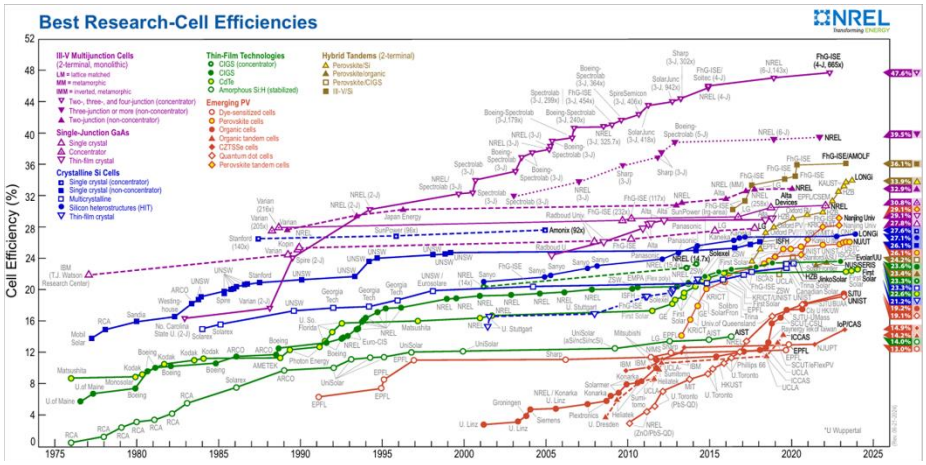

Figure 1.1. Diagram showing the efficiency of renewable energy cells. Figure reprinted with permission from ref. [16].

Non-precious metal-based materials, such as perovskites, metal-organic frameworks, low-energy band gap transitional metal oxides, and porous zeolites, have been reported as multi-functional electrocatalysts, photocatalysts and materials for energy conversion and storage during the past few years [17–19]**.** Utilizing novel materials as potential hosts or carriers for energy applications is quite advantageous. Being a magic box of many mysterious properties, perovskites have also triggered fundamental studies towards renewable energy sources such as solar energy which further emerged as the most promising of the aforementioned materials for usage in energy applications due to their low cost and high photo- and electrochemical activity [19]**.** This is because of its remarkable qualities, which include strong light absorption, excellent charge transport, ease of manufacture, and good crystalline purity. Perovskites also have superior catalytic capabilities, increased ion and electrical conductivity, and capacity for charge storage [17, 18].

One of the most promising innovations for meeting the increasing need for energy worldwide is solar energy, which also has the potential to lessen the ever-increasing energy issues caused by the widespread consumption of fossil fuels [20]. Solar cells (SCs), also known as photovoltaic (PV) cells, are a form of energy-harvesting technology that utilizes the photovoltaic effect to convert photon energy into electrical energy. SCs have evolved over numerous generations, including the 1st, 2nd, and 3rd generation SCs (Figure 1.1). SCs of the 1st generation (monocrystalline and polycrystalline), made of crystalline silicon, had great efficiencies but higher production costs. Thin film technology, utilized in 2nd-generation SCs, reduces the number of active components per cell. A few examples of the 2nd generation include cadmium telluride (CdTe), cadmium indium gallium selenide (CIGS), and amorphous silicon (a-Si), which used thin film technology to address the cost issue of the first generation. The production cost of electricity from second-generation solar cells has remained high. Additionally, their development may be limited due to their inherent toxicity, attributed to the presence of cadmium. The 3rd generation of PVs, which includes

organic, polymer, quantum dots, dye-synthesized solar cells (DSSC), and inorganic-organic perovskite solar cells (PSC), have therefore been the focus of extensive research and development (Scheme 1.1). By utilizing recently developed technology, solutions processed, and affordable precursors, 3rd generation PV has become more promising than 1st and 2nd generation PV [16].

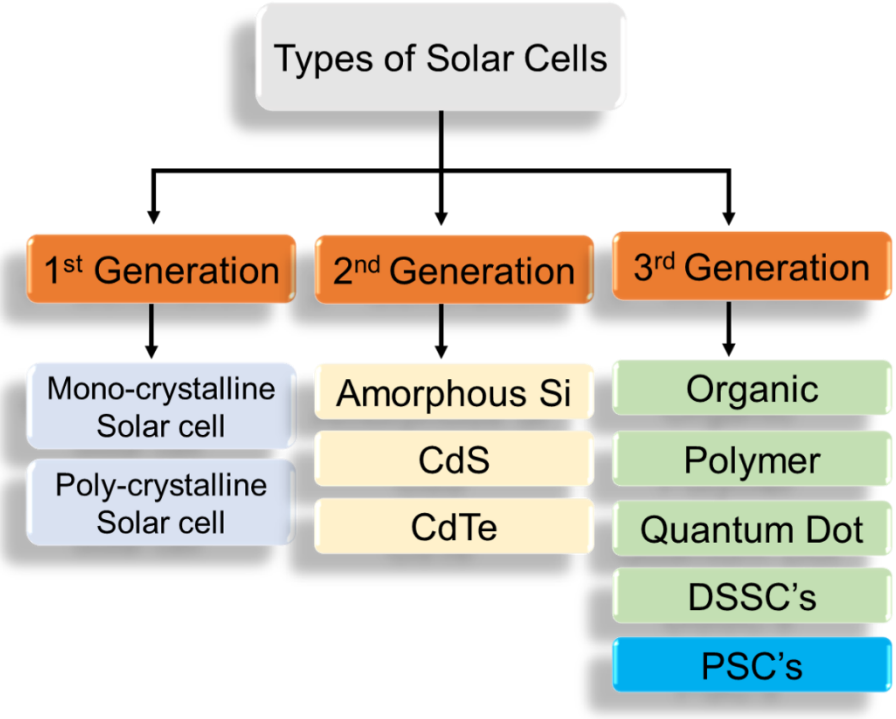

Scheme 1.1. Schematic representation of different types of solar cell development.

DSSCs, initially developed by Gratzel *et al.*, continue to attract a lot of interest because they are easy to make and have decent efficiency [21]. Widespread usage of DSSCs was hindered by their costly dye based on ruthenium, which was utilized as a light sensitizer, and their vulnerable power conversion efficiency (PCE). Therefore, there is significant interest in developing a novel light absorber for dye-sensitized solar cells (DSSCs) that is both cost-effective and energy-efficient. Subsequently, in 2009, Miyasaka *et al.* encountered perovskite, a novel light sensitizer for DSSCs [22]. Although these cells could be processed cheaply, their performance was limited to PCE of around 10%, limiting their chance of commercialization. PSCs are solar cells that include a perovskite-

structured material as the active layer. Hybrid halide perovskites has become a promising material in the solar field due to their advantages, including high optical absorption coefficient, carrier mobility, and tunable band structure. They have attracted much attention due to their great power conversion efficiency (PCE), which has increased from 3.9 to 26.1% in 10-15 years [16].

1.2. Fundamental properties and structural characteristics of halide perovskites

Perovskites have been investigated in various areas of material sciences due to their unusual and intrusive physical characteristics. The general formula of perovskite is ABC_3, and its crystalline arrangement is comparable to that of the perovskite mineral [23, 24]. The name "perovskite" was originally used to refer to metal oxide with a perovskite structure, a kind of crystal structure with the chemical formula ABO_3 (where A= Ca^{2+}, Sr^{2+}, Ba^{2+} and B= Ti^{2+}, Sn^{2+}) is represented by the word "perovskite". Perovskite was first discovered by Russian mineralogist Gustav Rose in 1839, and the mineral was subsequently named in honor of Lev Perovski (1792–1856). The word "perovskite" is widely used despite the fact that the precise mineral is composed of calcium, titanium, and oxygen, with the chemical formula $CaTiO_3$ [23, 24]. A perovskite structure can be modestly defined as a cubic unit cell with the general formula ABO_3, B atoms are located at the corner, oxygen atoms at the edge center, and A atoms at the body center [23, 24]. Rare-earth metal atoms are examples of positively charged A metals that have 12-fold coordinated with oxygen anion. Positively charged B metals, like transition metal atoms, are 6-fold coordinated with oxygen anion [23, 25]. At 25°C, the perovskite structure oxide is cubic and typically provides the A and B cations with a total charge of +6 [25, 26]. Unfortunately, most perovskites get deformed due to the creation of oxygen/cationic apertures due to steric limitations resulting from variations in ionic radii. In order to maintain the coordination of overall charge neutrality, an oxygen vacancy in the perovskite structure that produces mixed ionic and electronic conductivity is necessary [26, 27].

Double perovskite materials and Ruddlesden-Popper as substitute layered structures have been the focus of recent advances in perovskite structured materials research [28, 29]. The general representation of $A_2BB'O_6$ in these perovskite structure classes is accomplished by incorporating different substitutions at the A or B site. When double perovskite materials are used, the halide is coordinated to A-site cations while B and B′-site cations occupy substituting sites [29–31]. Generally, perovskite materials are commonly used in sensors, photocatalysis, electrocatalysis, and other applications due to their wide band gaps, high electrical conductivity, and robust thermal stability [32, 33].

On the other hand, Halide perovskite is a different kind of perovskite that is used in PV systems. Firstly, Miyasaka *et al.* explored these halide perovskite materials in solar cells. Its typical formula is ABX_3, where X is a halide anion (F^-, Cl^-, Br^- or I^-), B is a divalent metal cation (Pb^{2+}, Sn^{2+}), and A is a cation (Cs^+, MA=$CH_3NH_3^+$). A and B represent the 12-fold cuboctahedral and 6-fold coordination, respectively, by the X anion in an ideal cubic perovskite structure. A cation appears at the corner, B at the body center, and X at the face center position in a unit cell (Figure 1.2).

Goldschmidt tolerance factor (t), was used to determine the hybrid perovskite preparation using Equation 1.1.

$$(t) = \frac{rA+rX}{\sqrt{2(rB+rX)}} \quad \text{----------(Equation 1.1)}$$

Here, rA, rB, and rX are the effective ionic radii for A, B, and X ions, respectively.

Additionally, the perovskite stability was estimated using the computed octahedral factor (μ), given in equation 1.2.

$$(\mu) = \frac{rB}{rX} \quad \text{----------(Equation 1.2)}$$

When calculated t value within 0.813 and 1.107 and evaluated μ within 0.442 and 0.895, the perovskite has been determined to have stabilized. The perovskite with the above-mentioned values demonstrated a unique structure and exhibited a high absorption coefficient, good absorption

range, prolonged lifespan of the charge carrier, adjustable band gap, and low exciton binding energy. These perovskite materials are better for solar applications because of their very low band gap and greater absorption coefficient [34].

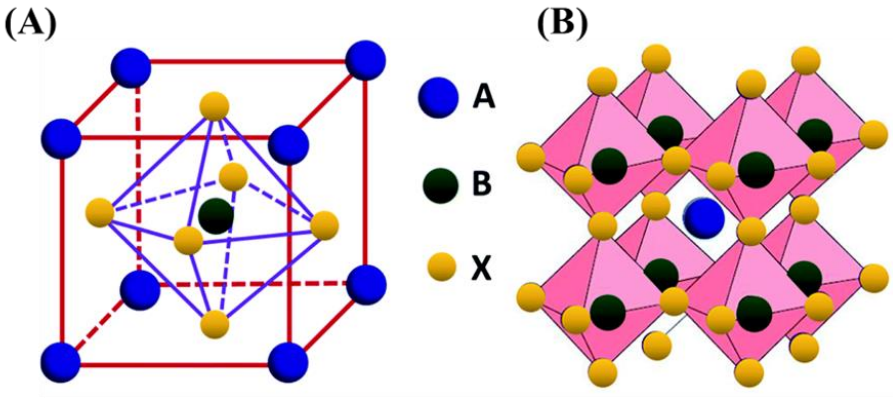

Figure 1.2. Structure of perovskites with ABX_3 formula. Figure reprinted with permission from Ref [35]. Copyright 2019, The Royal Society of Chemistry.

In 2019, Bartel *et al.* introduced a new formula for calculating the tolerance factor (τ) to predict the stability of perovskite equation 1.3 [36].

$$\tau = \frac{Rx}{RB} - nA\{nA - \frac{RA/RB}{ln\ (RA/RB)}\} \quad \text{----------(Equation 1.3)}$$

Here, nA is the oxidation state of A and $R_A > R_B$, R_A, R_B, and Rx represent the ionic radii of A, B and X ions respectively. Halide double perovskite (HDP) contains two different cations, and R_B refers to the average radii of +1 and +3 oxidation state cation ions. If the value of τ is less than 4.18, it may be concluded that the perovskite structure is stable.

In conclusion of tolerance and octahedral factor, the range for a stable structure is as follows: $0.813 < \mathbf{t} < 1.107$, $0.442 < \boldsymbol{\mu} < 0.895$, $\boldsymbol{\tau} < 4.18$

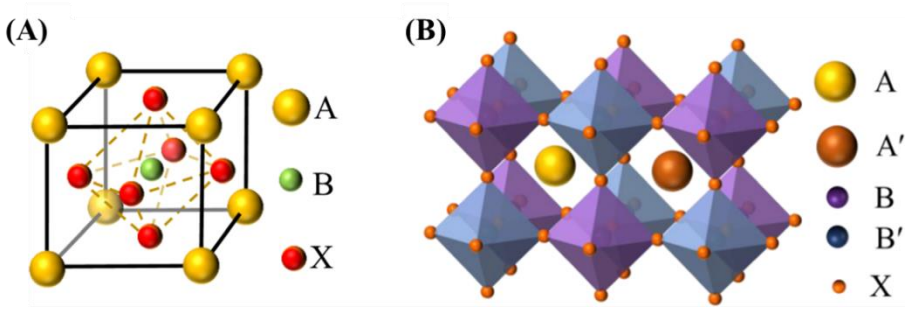

Figure 1.3. (A) Cubic crystal structure of perovskite (B) double perovskite crystal structure. Figure reprinted with permission from Ref (37) Copyright 2021, Springer Nature.

Consequently, lead-free perovskite materials with high structural dimensionality are more advantageous for higher solar efficiency. The development of stable, lead-free perovskites is the only way to address the toxicity and stability issues. HDPs with the general formula $A_2B^+B^{3+}X_6$ can be formed by one monovalent (B^+) and one trivalent (B^{3+}). These HDPs have an identical three-dimensional structure to lead perovskite, with A-site cations located in the cavities created by the octahedra of $[B^+X_6]^{5-}$ and $[B^{3+}X_6]^{3-}$ octahedra. A cation (Cs^+, $CH_3NH_3^+$) and X anion (Cl^-, Br^-, I^-) selection is somewhat limited, but B-site cation selection is more variable and can contain a variety of elements (monovalent or trivalent) (Figure 1.3). With a chemical formula of $A_2B^+B^{3+}X_6$, HDPs are becoming a more appealing choice [36]. Equations 1, 2, and 3 may be used to predict the stability of a perovskite structure. Moreover, HDPs have good optoelectronic qualities, outstanding stability, and a broad range of combinations. The crystal dimensionalities of other lead-free perovskite materials, except for HDPs, are 2-D or 0-D, as opposed to the 3D structure-linked BX_6 octahedra in Pb-based perovskites. Poor carrier transport and large carrier effective masses are caused by low structural dimensionality, which limits their use in PVs.

1.3. Working principle

Photovoltaic (PV) technologies, including solar cells, convert solar energy into electrical energy. The Sun, acting as a blackbody with a light spectrum, has a surface temperature of approximately 5800 K. The usual

condition for characterization of terrestrial solar cells is the AM 1.5 spectrum with a light intensity of 100 mW/cm²; however, the solar spectrum on the surface of the Earth varies based on the length of the light path through the atmosphere [38, 39]. When photons strike light-absorbing materials in semiconductor-based PVs, they provide enough energy to excite electrons from the valence band (HOMO) to the conduction band (LUMO) across the bandgap (Eg). This is followed by carrier extraction of both electrons and holes because of diffusion or built-in electric fields. Semiconductors with a lower Eg absorb more light and produce more current, but the difference in the quasi-Fermi levels of the electrons and holes limits the output voltage [38, 40]. Higher Eg, on the other hand, restricts current output and light absorption. Higher efficiency can be attained using a single-junction solar cell with an ideal Eg of between 1.1 and 1.4 eV [38]. Initially, it seemed that the PSC working principle was precisely the same, irrespective of the DSSC [41]. In this context, light-absorbing material (Perovskite) is coated on to the mesoporous TiO_2 surface, and by absorbing light with a wavelength that matches its band gap, this light-absorber material undergoes photoexcitation (Figure 1.4).

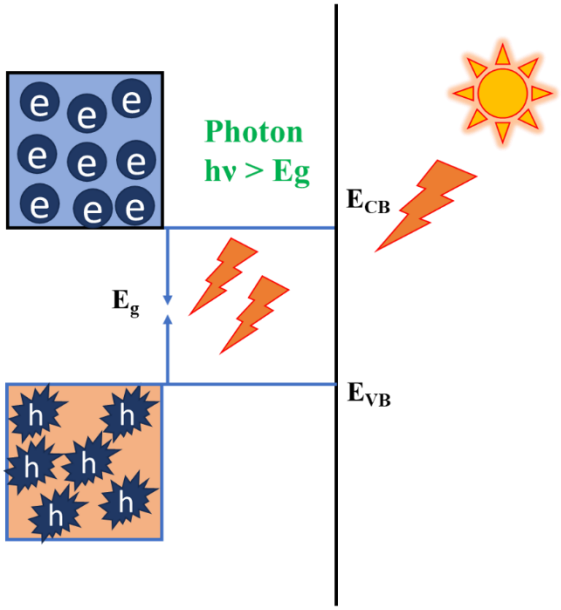

Figure 1.4. Electron and hole pair generation from light absorber material.

An electron is then injected into the TiO_2 conduction band (CB) from the LUMO level of the perovskite material and is carried by the layer to the FTO/ITO substrate. Through the use of an external circuit, it moves from the substrate to the counter electrode and combines to hole transport materials (HTM) to complete the circuit. The DSSC mechanism paved the way for the PSCs operating principle. However, as device designs advanced and became more diverse, it became evident that the PSCs operation closely resembled that of solid-state p-n junction solar cells. However, PSCs are composed of multiple layers for device fabrication. The structure includes a transport conductive glass (FTO/ITO) serving as the front electrode, perovskite materials acting as light absorbers, sandwiched between an n-type (ETL) and p-type (HTL) materials, with a back contact metal electrode. Currently, n-i-p and p-i-n solar cells are the most often used device architectures for PSCs; however, "i" prefers the intrinsic light absorber positioned between the n and p contacts. Perovskite materials function as intrinsic absorbers in an n-i-p structure, and n-type is an electron transport material (ETM).

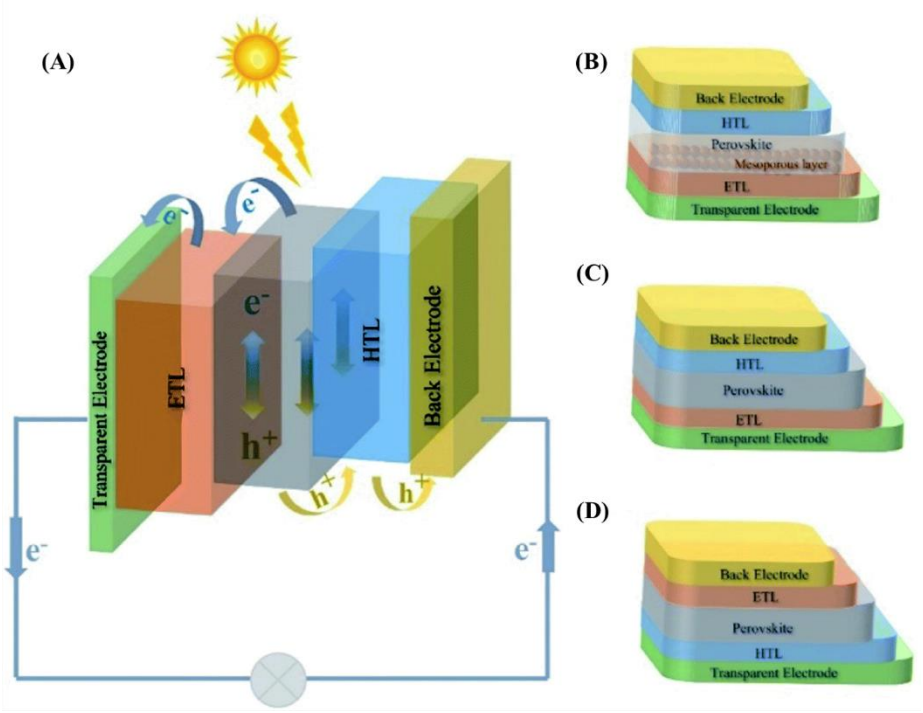

Figure 1.5. PSCs working principle (A) Device designs, (B) mesoporous n–i–p, (C) planar n–i–p, and (D) inverted p–i–n structured PSCs. Figure

reprinted with permission Ref. [43]. Copyright 2022, The Royal Society of Chemistry.

Meanwhile, HTM in the p-type completes the solar cell design (FTO or ITO/ETM/perovskite/HTM/metal contact). Instead, the perovskite material is sandwiched between p-type materials at the bottom and n-type materials at the top within the p-i-n structure, commonly referred to as an inverted architecture (FTO/HTM/perovskite/ETM/metal contact).The device can be fabricated in either p-i-n or n-i-p type architecture and is generally categorized into mesoporous and planar structures, with planar being more common [42]. Typically, ETLs such as TiO_2, ZnO, and SnO_2 are used, while HTLs including spiro-OMeTAD, PTAA, PEDOT: PSS, and NiOx are utilized. The selection of ETL and HTL is determined by energy band alignment and solvent processing.

When light is absorbed, the perovskite material generates electrons (e^-) and holes (h^+). The ETM and HTM selectively accumulate electrons and holes, respectively. The excited electron from the n-type material flows through the external circuit to the p-type material, which is combined with holes. Although this working concept is currently well acknowledged, it is not quite as easy to transport, generate, and separate as it is for Si p-i-n type solar cells. For p-i-n or n-i-p solar cells, the open circuit voltage (Voc) is limited by the disparity in the fermi levels or work function of the contact (n and p-type) (Figure 1.5). The hybrid perovskites of inorganic and organic materials determine an assortment of unique photophysical properties that ultimately lead to the device's superior PV performance [43]. The remarkable properties of perovskite materials, including their ultralong carrier diffusion length, high absorption coefficient, slow carrier recombination rate, long carrier lifetime, unusually high defect tolerance, and moderate carrier mobility, are responsible for the exceptionally higher PCE and high Voc of perovskite light absorber based solar cells.

1.4. Synthesis of perovskite materials

Various fabrication techniques, including spray, vacuum-assisted deposition, and anti-solvent dripping, have been employed thus far to produce dense, lead-based films devoid of pinholes [44–47]. Because of the unpredictable crystallization of Bi-based films and the broader solubility range of BiI_3 than Pb-based precursors, it is more difficult to generate dense Bi-based films than Pb-based films. Any commonly used antisolvent (alcohols, DMSO, DMF, etc.) may then adversely impact or degrade the produced Bi-based film. Morphology and film quality must be optimized to enhance device performance.

The conventional growth and nucleation crystallization mechanism typically occurs in three stages. The first one is when a solution approaches supersaturation and nucleation and then grows toward large crystals, which is a one-step deposition technique. A supersaturated solution is necessary for nucleation. When the precursor solution is applied to the substrate, the solvent promptly evaporates, the solute concentration rises, and the solution swiftly achieves saturation. The atoms, ions, or molecules in the solution then start the nucleation process, which results in the formation of embryos. A rise in the rate of supersaturation led to an increase in the nucleation rate, which formed more small crystals [48, 49]. Reducing the concentration of the solution brings the nucleation process to a halt. Following the nuclei formation, crystal growth begins instantaneously, using the solute that was used to produce the nuclei. The crystal growing process persisted until the growth species concentration was reduced. Higher nucleation density produces more nuclei for the given solution concentration, and the nucleation density and subsequent solute supplement determine the eventual grain size. In contrast, two-step deposition techniques include first depositing metal halide onto the substrate, and then interpolating organic halide (either in the vapor or solution phase) into the metal halide crystal to generate a particular perovskite layer. The conversion process is demonstrated by the heterogeneous reaction between the metal halide and organic halide (in solution or vapor phase) [48, 49].

Spin coating is a commonly employed film fabrication method that has been thoroughly examined. Bi-based materials have been effectively produced using spin-coating techniques [50–53]. However, because of the complex crystallization process, standard spin coating is unable to generate dense films of a high grade. Furthermore, a disadvantage of this technology for scalable applications is the considerable material waste that occurs during spin coating. A few attempts have been made to optimize the spin-coating technique parameters. Ahmad *et al.* used a spin-coating technique (two-step) for $MA_3Bi_2I_9$ perovskite film deposition [54]. Spin-coating of CH_3NH_3I in 2-propanol was done after spin-coating BiI_3 onto mesoporous TiO_2. To create thin films, a brief annealing procedure lasting 20 minutes at 120°C was carried out. The spin-coating (two-step) method produced $MA_3Bi_2I_9$ films with a more homogeneous surface and increased crystallinity. Deng *et al.* introduced 1,3-bis[3,5-bis-(trifluoro methyl)-phenyl]thiourea (FS) into the $CsBi_3I_{10}$ precursor solution and employed quenching-assisted antisolvent technology to promote grain development and crystal nucleation, as a result of dense film and high-efficiency devices (~1.03%) were formed.

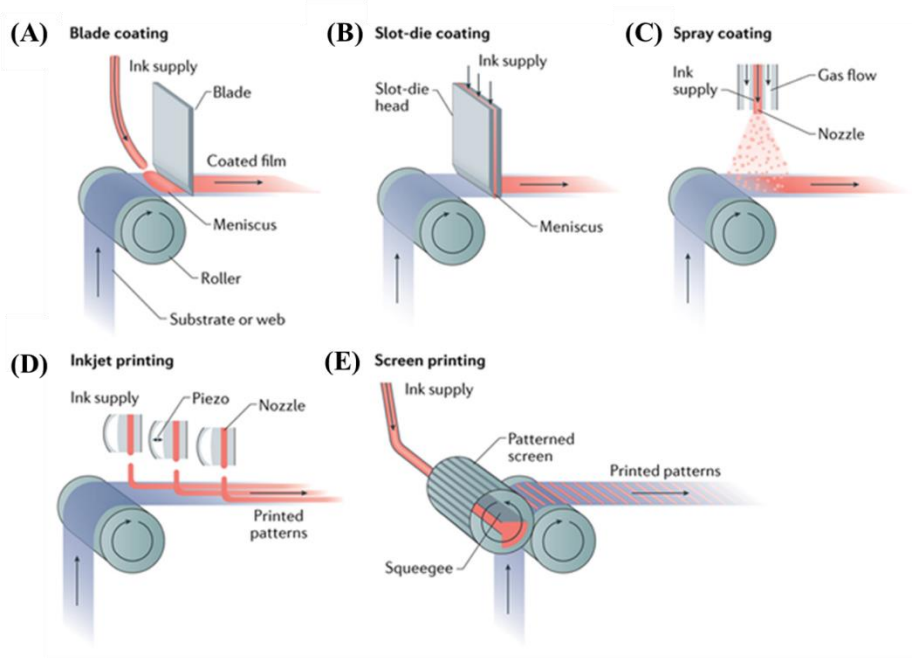

Figure 1.6. General scalable solution deposition techniques for fabrication of PSCs. Figure reprinted with permission Ref. [57]. Copyright 2018, Springer Nature.

Though, the film grain size is still rather tiny and has a lot of grain boundaries. This could lead to a significant leakage current in the device and prevent it from improving its PCE much more [55]. In order to regulate film formation, the vapor-assisted solution procedure was investigated. Jain *et al.* successfully tunned the surface morphology of $MA_3Bi_2I_9$ by reacting further with CH_3NH_3I (MAI) vapor using annealed BiI_3 sheets [56].

A few techniques for perovskite materials preparation are depicted (Figure 1.6), which provides an overview of solution deposition methods. A solvent-free technique for creating thin films, the vapor deposition approach can effectively prevent Bi-based material from dissolving in solvents [58]. The dense BiI_3 layer is first vaporized onto a TiO_2 substrate using a high vacuum vaporizer. Next, homogeneous conversion to $MA_3Bi_2I_9$ films was carried out in a ceramic vessel with a medium separation. The gas-solid reaction of MAI-BiI_3 was made easier by the container's homogenous MAI thermal atmosphere and sufficient reaction space. Following vacuum deposition, annealing in air increased the film crystallinity and gradually eliminated any remaining MAI. A significant steric hindrance is created to prevent rapid crystallization throughout the whole process by avoiding any crystallization in the solvent and contact. It was observed that the crystal growth time was essential to the development of defect-free and large grains. Consequently, the final dense $MA_3Bi_2I_9$ films would benefit substantially from the precise tuning of low vacuum deposition operations.

Wang *et al.* devised a progressive vapor deposition technique to produce superior Bi-based double perovskites. On the dense TiO_2-coated FTO substrate, AgBr was first applied, followed by $BiBr_3$ and CsBr to the film layer by layer [59]. The annealing process that followed induced a diffusion reaction that resulted in the formation of the double-perovskite phase. It is crucial to note that the sequence of deposition sources significantly influences crystal development. Thus, it might be possible to produce superior $Cs_2AgBiBr_6$ films with consistent surface characteristics, high crystalline phases, and superior photoelectronic

capabilities. $CsBi_3I_{10}$ thin films have also been produced via a single-source thermal evaporation technique [60]. The layered structure, high-purity hexagonal phase, and high homogeneity of the $CsBi_3I_{10}$ films made by evaporating its powder demonstrated a high degree of consistency with the crystal structure of the evaporated source material. As a result, following annealing, the film crystallinity was considerably enhanced the performance of materials. Thus, vapor deposition produces a more homogenous and compact surface because it is easier to manage the crystallization process than spin coating. The inability of the vapor deposition approach to precisely regulate the film composition is a drawback. Vapor deposition has limited large-scale applications because of its expensive equipment requirements and complicated operation procedures.

For the construction of Pb-based perovskite films, dip-coating has been thoroughly researched and used as a straightforward and effective fabrication technique [61–63]. Capillary-assisted Dip Coating (CDC), a general technique, has been effectively used to prepare dense, incessant $Cs_2AgBiBr_6$ films on a large scale [64]. A handmade CDC device is used to fabricate $Cs_2AgBiBr_6$ films. To ensure suitable capillary force viscosity and solvent evaporation rate, the precursor solution was heated and maintained at 60°C. The precursor solution was forced into a confined area constructed parallel to the substrate and glass plywood by capillary forces. A hot plate was used to heat the substrate. Double perovskite ($Cs_2AgBiBr_6$) film grows uniformly on the substrate when it is lifted at varied rates. The lifting speed and temperature of the hot plate can be changed to alter the structure of the film and morphology. This dip-coating technique produced dense, homogenous films. This approach has a lot of potential for making large-scale film fabrication.

1.5. Fabrication of solar cell

PSCs have garnered significant attention since their inception because of their remarkable rise in PCE growth, which has increased from 3.8% to over 25%. Nonetheless, researchers have developed a number of lab-scale device production techniques and are working to advance them to

the commercialization stage. Large-scale perovskite film quality and economical, scalable production are key factors influencing the PSC device performance and its commercialization. Perovskite thin films have been formed through a variety of methods, including one-step and two-step deposition approaches. Reasonable control over the formation procedure and extensive analysis are crucial for achieving high PCE and future-oriented fabrication of solar cells [16].

However, lead free perovskite light absorber is surrounded by an ETL and an HTL in a conventional PV device. The devices are divided into two categories based on where the charge transport layers are located: inverted and conventional architectures. After light stimulation, the charge transporters are essential in transporting the charge carriers. In addition to promising procedures, charge losses also happen through non-recombination, which is most likely taken on by crystal defects and energy disorders. The energy levels of a few samples of Bi-based materials, conductive electrodes, and charge conductors are summarized below (Figure 1.7). Based on this diagram, we will go into more detail about how HTL, back contact, light absorber, and ETL materials affect PV device performance.

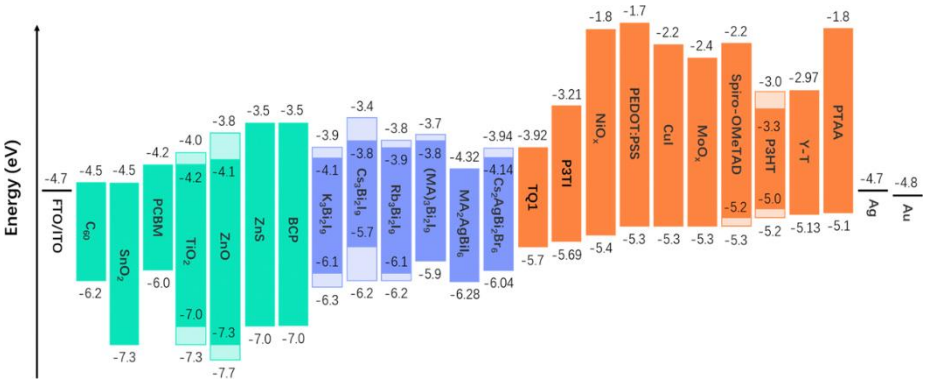

Figure 1.7. HOMO-LUMO level of a few perovskites, ETL, HTL, and back contact metal electrodes used in PV devices. Figure reprinted with permission Ref. [65]. Copyright 2022, The Royal Society of Chemistry.

1.5.1. Electron transport layer (ETL)

The electron transport layer (ETL) is a critical component in photovoltaic (PV) cells, especially in advanced and emerging solar cell technologies. Its primary role is to facilitate the effective transport of

electrons from the active layer to the electrode, improving the overall efficiency and performance of the PV cell. The ETL helps in minimizing losses and improving the collection of generated electrical charges. The ETL provides a pathway for the efficient movement of electrons generated in the active layer (such as the perovskite layer) [66]. It helps transport these electrons to the cathode or external circuit. By ensuring that electrons can travel with minimal resistance, the ETL reduces energy losses and improves the overall PCE of the SCs. The ETL aids in the separation of generated electron-hole pairs in the absorber layer and also helps to prevent the recombination of these charges by providing a conducive environment for electrons to move toward the electrode [67]. The ETL acts as an interface between the light-absorbing layer and the electrode. Figure 1.8 Summaries a few of ETLs with the HOMO and LUMO energy levels, which are essential for charge transportation and helps to reduce charge recombination.

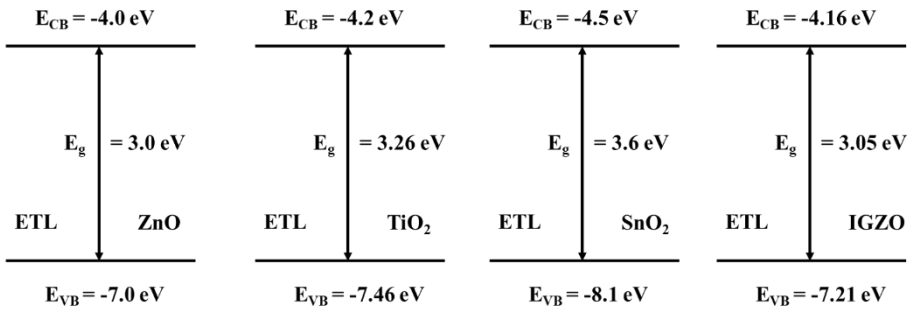

Figure 1.8. Energy level diagram of different layers of ETLs.

TiO_2 is a widely used ETL material in DSSCs and PSCs because of its high stability and electron mobility. ZnO is another common ETL material known for its high electron mobility and wide Eg. It is used in various PV technologies, including thin-film and perovskite cells. SnO_2, IGZO (Indium–gallium–zinc oxide), and WO_3 are used in some high-efficiency cells as an ETL material due to their good electronic properties and stability (Figure 1.8). The energy levels of the ETL must be well-aligned with those of the absorber layer and the electrode to ensure effective charge transfer and minimize energy losses. The ETL material must be chemically stable and compatible with other layers in the PV cell to ensure long-term performance and reliability. The ETL

should minimize recombination losses by providing a pathway for electron transport without allowing significant recombination of electron-hole pairs [67].

Since good surface roughness allows for effective electron injection and reduces electron transport pathways, nanostructured charge conductors like nanorods and nanowires are theoretically excellent for charge carriers. Bi-based materials crystallization behavior on compact and mesoporous TiO_2 surfaces was investigated by Zhang *et al.* [68]. They propose that the centrifugal force of the spinning deposition caused $MA_3Bi_2I_9$ crystals to fill the mesoporous TiO_2 layer from the bottom upward. The full porous structure was covered with $MA_3Bi_2I_9$ crystals when the 0.45 M precursor solution was applied, causing the pores to gradually fill. In contrast, coating the compact TiO_2 layer with $MA_3Bi_2I_9$ resulted in the formation of a low-density film with crystals and gaps aligned vertically. By encasing MgO on the surface of typical mesoporous TiO_2, Guo *et al.* further modified the structure [69]. The stability of device under moisture and UV conditions is considerably increased by this structure formation, and it effectively limits adsorption of water on TiO_2 surface and prevents direct contact with TiO_2 and the light absorber. The Fill factor (FF) and short-circuit current density (Jsc) of the devices were improved by this layered metal oxide construction, which also considerably inhibited interfacial recombination and raised the shunt resistance.

Three different mineral forms of TiO_2 (mesoporous brookite TiO_2, mesoporous anatase TiO_2, and compact planar TiO_2) (Figure 1.9 A-F) effect on thin film were studied by Singh *et al.* [70]. The authors discovered that mesoporous and the dense layers on the FTO had a significant influence on the shape of $MA_3Bi_2I_9$ films. Non-uniform growth is further caused by the fact that the crystals are not growing continuously on the TiO_2 flat substrate. Interparticle necking acts as a barrier, preventing $MA_3Bi_2I_9$ from entering the holes in the mesoporous brookite TiO_2 layer and inhibiting its uniform nucleation and growth. The insufficient physical connection between the brookite and planar scaffolds contributes to the relatively poor performance of $MA_3Bi_2I_9$

devices constructed on planar and brookite TiO_2. This suggests that these cells have significant carrier recombination and high internal resistance. However, the mesoporous anatase TiO_2 provides favorable conditions for the growth and nucleation of $MA_3Bi_2I_9$, resulting in excellent surface coverage and enhanced performance of the device [70].

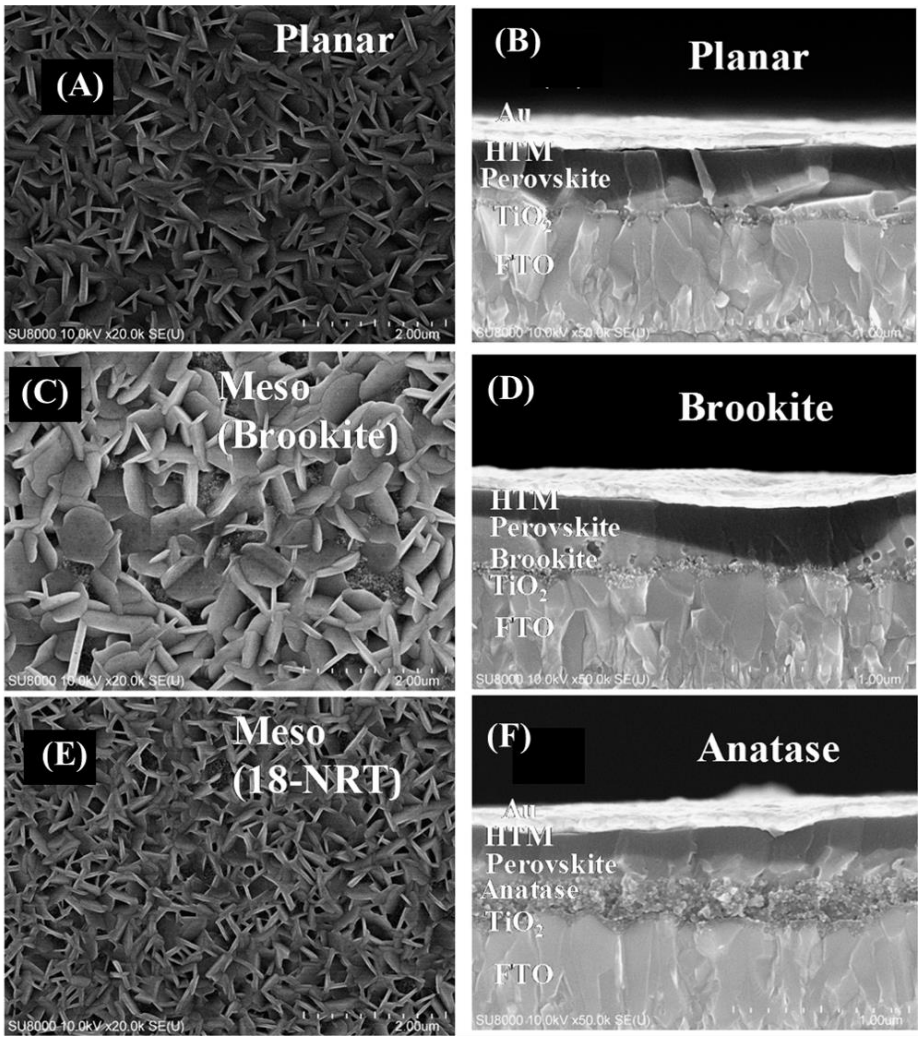

Figure 1.9. SEM and cross-section image of $(CH_3NH_3)_3Bi_2I_9$ perovskite layer deposited on compact layer TiO_2 (A, B), brookite mesoporous (C, D), anatase mesoporous (E, F). Figure reprinted with permission Ref. [70]. Copyright 2016, The American Chemical Society.

Comparably, interparticle necking stops $MA_3Bi_2I_9$ from penetrating the holes in the mesoporous brookite TiO_2 layer as well as from nucleating and growing uniformly. Due to the inadequate physical connection between the brookite and planar scaffolds, the comparatively low performance of $MA_3Bi_2I_9$ devices built on planar and brookite TiO_2

further implies that those cells have a high internal resistance and substantial carrier recombination. On the mesoporous anatase TiO_2, on the other hand, $MA_3Bi_2I_9$ grows and nucleates favorably, leading to good surface coverage and superior device performance.

Moreover, rutile-TiO_2 nanorod array films were used as the ETL in the preparation of $MA_3Bi_2I_9$-based solar cells by Chen *et al.* A PCE of 0.14% was attained by the rutile-TiO_2 nanorod array-based cell [71]**.** Despite having a low PCE, the cell demonstrated exceptionally excellent stability, with no deterioration over 67 days in a dark, humid environment with 450% relative humidity without encapsulation. In addition, reducing the thickness of ETLs is one method to improve FF and lower the transport resistance. For Bi-based solar cells, new transport materials with great mobility and suitable energy levels are therefore needed.

SnO_2 has also been employed as the ETL for Bi-based double chalcogenide, which exhibits good energy level matching in devices, in addition to the reports concerning TiO_2 [72, 73]**.** Meanwhile, utilizing PCBM or C_{60} as the ETL, other researchers have attempted to fabricate devices with an inverted topology. The detrimental effect of tBP in spiro-OMeTAD on Bi-based chalcogenides can be avoided in inverted devices by avoiding the application of spiro-OMeTAD as the HTL [74, 75]**.** Unfortunately, the majority of ETLs that are now in use rely on conventional materials that are frequently found in lead-based electronics. Further work is needed to create substitute contact materials that are tailored to the needs of Bi-based products, taking into account factors like energy levels.

1.5.2. Light absorber

In thin-film SCs, the light absorber layer is often considered the most crucial component, responsible for capturing sunlight and converting it into electrical energy. The effectiveness of a light absorber directly influences the overall efficiency of a PV cell. It is typically composed of semiconductor materials that have specific optical and electronic properties designed to maximize the conversion of sunlight into usable

electricity. The primary role of the light absorber is to absorb photons from sunlight. When photons interact with the absorber material, they transfer their energy to electrons within the cell, promoting them from the valence band to the conduction band and creating electron-hole pairs. The required energy for this process is known as the bandgap energy. Only photons having equal or greater energy than the Eg can be effectively absorbed and contribute to electricity generation. Upon absorbing photons, the semiconductor material generates electron-hole pairs. These free-charge carriers are essential for creating an electric current. The efficiency of this process depends on the absorption characteristics and the quality of the absorber material. After generation, the charge carriers are separated by the internal electric field of the PV cell. The separated electrons and holes are then collected by the electrodes to form an electrical current, which can be harnessed for power [66].

The Eg of the absorber material determines which part of the solar spectrum can be absorbed. An optimal Eg ensures maximum absorption of the available sunlight. The absorption coefficient indicates how well the material absorbs light at different wavelengths. Materials with high absorption coefficients can absorb more light within a shorter distance from the surface, reducing the need for thicker layers. The thickness of the light absorber affects its ability to capture photons. While thicker layers can absorb more light, they may also increase recombination losses. Thin-film technologies utilize high absorption coefficients to achieve effective light absorption with thinner layers. Surface texturing can enhance light trapping within the cell, leading to improved absorption by causing multiple reflections of light. Anti-reflective coatings reduce the reflection of incoming light, allowing more photons to enter the absorber and improve overall absorption efficiency.

1.5.3. Hole transport layer (HTL)

HTL or anode interfacial layers are a vital component in PV cells, particularly in advanced and emerging solar technologies. Its primary role is to facilitate the efficient transport of holes (positive charge carriers) from the light-absorbing layer to the electrode, improving the

overall efficiency and performance of the solar cell. The HTL ensures that the generated charge carriers are effectively collected and transported, contributing to the cell's electrical output. The device performance is enhanced by the deposition of HTM between the anode and the photoactive layer. The usage of HTLs in conventional polymer solar cells starts back to the late 1990s, after reports of comparable experiments with organic light-emitting diodes (OLEDs) [76].

The HTL provides a pathway for the efficient movement of holes generated in the light-absorbing layer (such as a perovskite layer) toward the anode or external circuit. By facilitating this transport, the HTL reduces energy losses and enhances the overall PCE of the PV cell. The HTL aids in the parting of electron-hole pairs created in absorber layer. By allowing holes to move toward the electrode while preventing the recombination of these charges, the HTL helps maintain the efficiency of charge collection. The HTL acts as an interface between the light-absorbing layer and the anode. So, there should be good electronic contact with both layers to ensure efficient charge extraction and minimize losses due to poor contact or interface resistance. High hole mobility is beneficial for HTL to facilitate the efficient transportation of holes from the active layer to the electrode. The band level of the HTL should align well with those of the absorber layer and the electrode to ensure effective charge transfer and minimize energy losses. The HTL material must be chemically stable and compatible with other layers in the PV cell to ensure long-term performance and reliability. It should minimize recombination losses by providing a pathway for hole transport without allowing significant recombination of charge carriers [77]. High transparency, high conductivity, favourable stability and solution processability, high work function, and primarily good hole mobility are some of the crucial requirements for HTM [78].

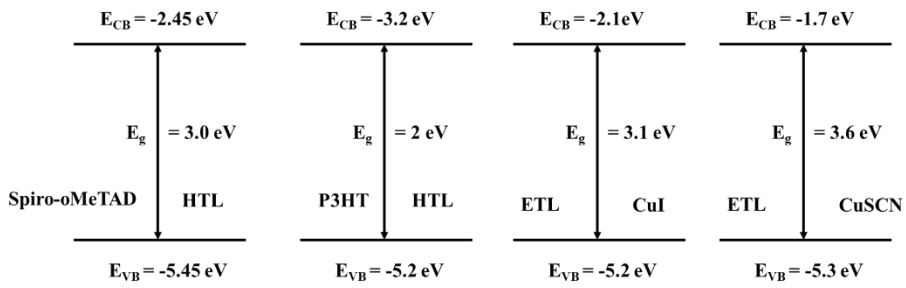

Figure 1.10. Energy level diagram of various HTLs.

The HTL is situated above the perovskite layer in conventional architecture. Higher roughness film necessitates a abundant HTL covering layer to segregate Bi-based layer and top metal electrode because of vertically directed crystallization for Bi-based materials. Consequently, choosing hole conveyance material with a higher conductivity is crucial. Efficient charge transfer requires a Bi-based light absorber and well-matched energy levels (Figure 1.10). In order to reduce the energy alteration at the interface, Shin *et al.* explored PIF8-TAA, a novel HTM for $MA_3Bi_2I_9$-based SCs. PIF8-TAA had lower HOMO level (5.51 eV) compared to spiro OMeTAD (5.13 eV). Improved charge transfer proficiency at the interfaces resulted in a rise in Voc [79]. Furthermore, PIF8-TAA's suppression of dark currents implied that it was more effective than spiro-OMeTAD at blocking electron's ability, raised FF.

Zhu *et al.* investigated three polymer materials (undoped) by using this HTM method of synthesis for utilization in $CsBi_3I_{10}$ based SCs (TQ1), (P3TI), and P3HT [80]. According to the study, the device Voc increased in the following order: P3HT (0.34 V) < P3TI (0.47 V) < TQ1 (0.48 V) This is consistent with the movement of the projected energy levels of HOMO, which are P3HT = 5.10 eV < P3TI = 5.69 eV < TQ1 = 5.70 eV. HOMO levels of the three polymers were higher than the valence band of $CsBi_3I_{10}$, despite fact that it is difficult to identify. Additionally, TQ1 has a superior hole extraction capacity, and the unique interaction between the TQ1 polymers and $CsBi_3I_{10}$ can enhance the device absorbance.

Bai *et al.* associated 3 extra common HTLs, spiro OMeTAD, CuI, and PTAA, with $Cs_3Bi_2I_9$-based perovskite light absorber [81]. The

observations indicate that CuI has high conductivity and is primarily responsible for the greater Jsc, FF, and Voc in devices. Additionally, when compared to other organic materials, devices using CuI and CuSCN showed improved environmental stability [82]. Pantaler *et al.* synthesized a novel HTM (PCPDTBT) to study the effects of photoinduced processes and interfacial quality on the efficiency of $Cs_2AgBiBr_6$ based double-perovskite devices [83]. The lower LUMO and shorter energy band of PCPDTBT contributed to the cell's comparatively poor performance.

Notably, the hole transport layer (HTL) extensively utilizes additives such as tBP, cobalt complexes, and lithium salts to enhance the rate of hole transport and significantly improve device efficiency [84]. On the other hand hygroscopic lithium salts, readily absorb water, hastening the breakdown of peroxide. Furthermore, it has been demonstrated that adding tBP readily forms compounds with Bi-based materials, promoting perovskite degradation and jeopardizing long-term stability. MMT with an implanted structure may be utilized as a buffer coating in the light absorber to reduce the tBP corrosion to the material by incorporating the tBP into the MMT's interlayer [85]. A novel pyridine additive (2-Py) that is non-corrosive to perovskite, chemically stable, and appropriate for replacement of tBP was described by Yue *et al*., at the o-position a long alkyl chain substituted presents [86]. Regarding the moisture-induced decomposition situation, more sophisticated sealing technologies should be able to resolve this problem.

1.5.4. Back contact

The back contact, or back electrode, is an essential component of photovoltaic (PV) cells, facilitating the electrical connection between the solar cell and the external circuit. It is crucial for the overall performance and efficiency of the PV cell to ensure effective charge collection and minimize electrical losses. The primary function of the back contact is to establish a conductive path for the flow of electrical current from the PV cell to the external circuit. Back contact in solar cells eliminates shading losses by placing both contacts on the back. It collects the

electrons that are transported through the cell and facilitates their movement to the external load.

The back contact must effectively collect and transport the charge carriers (electrons or holes) generated in the cell's active layer. This is critical for maintaining high efficiency and reducing losses associated with charge extraction. The back contact also provides structural support for the PV cell, helping to maintain its integrity and stability during operation and handling [66]. In PSCs, various metals or conductive polymers may be used as the back contact, depending on the specific design and requirements of the cell (Figure 1.11).

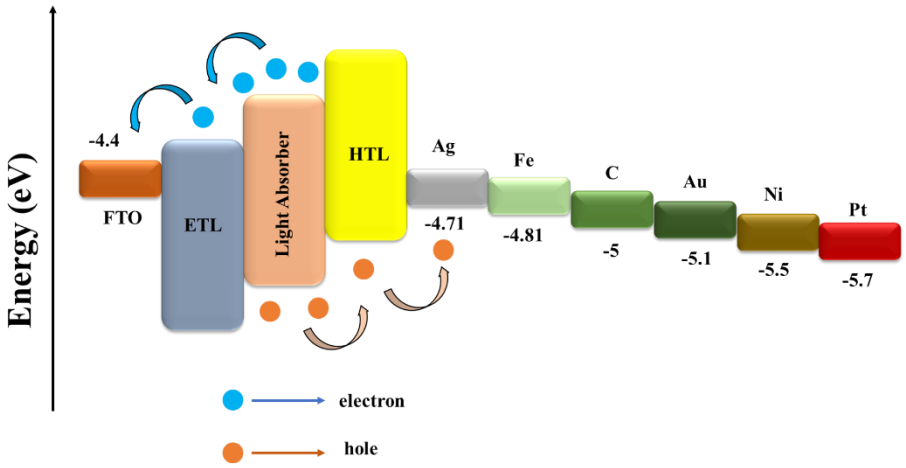

Figure 1.11 Various back contact metals with values work functions.

The back contact must have high electrical conductivity to minimize resistive losses, ensure efficient charge extraction, and adhere well to the underlying layers of the PV cell to maintain mechanical stability and electrical connectivity. It should be chemically compatible with the other layers of the PV cell to prevent degradation or adverse reactions that could affect performance. Back contact should minimize recombination losses by providing a good interface for charge collection and reducing the chances of charge carrier recombination. In these cells, electron-hole pairs created by light absorbed at the front surface are still collected at the back, even when the cell is made from high-quality, thin materials [87].

1.6. Photovoltaic parameters

1.6.1. Power conversion efficiency

Power conversion efficiency is a critical parameter for evaluating the performance of photovoltaic (PV) cells, representing the ratio of electrical power output to solar power input. Understanding and optimizing PCE is essential for advancing solar technology and making it a more viable alternative to traditional energy sources. Various factors affect the PCE of specific solar cell devices. The Eg energy of the light absorber material affects how efficiently it can convert sunlight into electricity. An optimal Eg (around 1.1-1.4 eV for single-junction cells) maximizes absorption of the solar spectrum. High carrier mobility allows for efficient transport of charge carriers, reducing recombination losses. An Anti-Reflective Coatings that reduce the reflection of sunlight, allowing more photons to enter the cell, texturing the surface of the cell can increase light absorption by creating multiple reflections within the cell. High temperatures can reduce PCE by increasing the charge carriers recombination and decreasing open-circuit voltage. The PCE can vary with spectrum of the incident light and the intensity. Standard test conditions (STC) are typically used to compare efficiencies.

1.6.2. Open-circuit voltage (voc)

Voc is a crucial parameter in the efficiency evaluation of PV cells. It is defined as the maximum voltage available from a solar cell when no external load is connected, meaning no current flows through the cell. Voc provides significant insights into the potential of a PV cell to convert sunlight into valuable electrical energy, and it is directly related to the efficiency of a solar cell; higher Voc values generally indicate better potential for PCE. The Eg of the light absorber material influences Voc, whereas wider Eg generally results in a higher Voc because the energy required to generate electron-hole pairs is greater. However, lower intrinsic carrier concentration in the perovskite material leads to higher Voc by reducing recombination losses. Surface passivation reduces recombination at the surface of the cell, leading to higher Voc.

Meanwhile, proper doping levels in the p-n junction can optimize Voc by balancing carrier concentration and recombination rates. High-quality materials with fewer defects and impurities enhance Voc by minimizing recombination centers. It decreases with increasing temperature, which may be due to increasing the intrinsic carrier concentration with higher temperature, resulting in a higher rate of recombination. While Voc slightly increases with higher illumination due to increased photocurrent, the relationship is not linear and is influenced by the cell's material and design.

1.6.3. Short-circuit current density

Jsc is a vital parameter in the efficiency assessment of PV cells. It represents the current generated per unit area of the cell when its output terminals are shorted, meaning the voltage across the cell is zero. Jsc provides insights into the cell ability to generate charge carriers (electrons and holes) under illumination and is directly related to the efficiency of the PV cell. Jsc is defined as the current flowing through a PV cell under short-circuit conditions normalized to the cell's area. It is typically measured under standard test conditions, including an irradiance of 1000 W/m², a 25°C cell temperature, and a 1.5 of air mass (AM). The ability of the cell material to absorb light at different wavelengths. Materials with higher absorption coefficients generate more electron-hole pairs, leading to higher J_sc. Materials with optimal bandgaps can maximize Jsc by effectively utilizing the available sunlight. Thicker absorber layers can capture more photons, increasing Jsc. However, there is a trade-off with increased recombination losses. Texturing the surface of the cell can increase light trapping, leading to higher photon absorption and, consequently, higher Jsc. Higher temperature generally decreases Jsc due to increased recombination rates, though it increases with higher illumination intensity as more photons are available to generate electron-hole pairs. Jsc reflects the cell's efficiency in converting incident photons into charge carriers. Higher Jsc values indicate better photogeneration and charge collection.

1.6.4. Fill factor (FF)

Fill Factor (FF) is a critical performance metric for PV cells that measures the quality of the SCs I-V curve and its overall efficiency. It represents the ratio of the maximum achievable power from a solar cell to the product of its open-circuit voltage (Voc) and short-circuit current (Isc). FF is a key indicator of how effectively a PV cell converts sunlight into usable electrical power, and a higher FF indicates that the cell is more efficient at converting sunlight into electrical power. High series resistance, often due to poor electrical contacts or thin metallic layers, can lower FF by reducing the current at the maximum power point. Low shunt resistance, often due to manufacturing defects or material impurities, can lead to leakage currents and lower FF. Both series and shunt resistances are temperature-dependent. High temperatures can increase series resistance and reduce shunt resistance, thereby decreasing FF.

1.6.5. External quantum efficiency (EQE)

The performance of optoelectronic devices is evaluated using EQE. The impacts of both optical and electrical processes within an optoelectronic device are combined into one comprehensive statistic called EQE. The ratio of the number of charge carriers (electrons or holes) that the device collects to the number of incident photons indicates how well photons are converted to electrons, or vice versa. A high EQE is a crucial factor in the development and optimization of these technologies since it shows how well the device converts light to electrical signals (or vice versa). EQE is measured as a function of the wavelength of incident light. This yields a spectrum response curve that illustrates the device's efficiency at varying wavelengths. When it comes to solar cells, EQE is useful in determining how well the device can convert solar radiation into electrical energy across the solar spectrum.

1.6.6. Photoluminescence

The emission of light from a material after photons have been absorbed is known as photoluminescence (PL). Due to the fact that it offers important insights into the optical and electrical characteristics of materials, this phenomenon is extensively researched. Photons excite the

material electrons, moving them from a lower energy state (VB) to a higher energy one (CB). The energy of the incident photons, which must be more than or equal to the energy difference between the two states, determines how much energy is absorbed. The electrons in the higher energy state may go through radiative or non-radiative processes following excitation. Heat is transferred to the lattice during non-radiative relaxation, whereas photon emission the primary source of photoluminescence occurs during radiative relaxation. Researchers can make cutting-edge technologies for a variety of uses and gain understanding of the basic characteristics of materials by researching PL.

1.6.7. Time-resolved photoluminescence (TRPL)

By tracking the photoluminescence's intensity over time following excitation, a sophisticated method called time-resolved photoluminescence (TRPL) is utilized to investigate the dynamics of excited states in materials. The creation and optimization of innovative materials and optoelectronic devices greatly depend on this technique, which yields important information concerning the lifetimes of excited states, carrier dynamics, and recombination processes. A short pulse of light excites the sample. which moves electrons from their ground state to an excited state. Excitation pulse durations are typically in the picosecond to nanosecond range, which enables accurate temporal precision. After being excitation, the excited state electrons relax and release photons as they return to the ground state. To track the decline of the photoluminescence signal, the released photons are collected and examined over time. A decay curve representing the photoluminescence lifetime is created by measuring the light intensity over time.

1.7. Lead-free perovskite

The toxicity of lead and stability issues with perovskite solar cells (PSCs) are significant concerns for commercialization. While lead offers superior performance compared to other materials, its toxicity poses substantial limitations. Lead toxicity is a hidden risk that can lead to severe health conditions affecting the hepatic, renal, central nervous and

hematological systems [88]. Lead has been strongly forbidden and ranked among the top 10 most dangerous compounds for the environment and human health by the World Health Organization [88]**.** Nonetheless several strategies can help prevent the environment from lead exposure, including recycling, mitigating techniques, and solar farm fencing. However, the scientific community's replacement strategy for lead paves the way for their work toward lead-free or less hazardous materials for PSCs. Several cations are anticipated to replace Pb in PSCs based on factors such as ionic size, electronic configuration, and tolerance factor, which are known to determine the stability and formability of the perovskite assembly. Group-14 elements Sn^{2+} and Ge^{2+}, Transition Metals (V^{2+}, Co^{2+}, Fe^{2+}, Mn^{2+}, Zn^{2+}, Pd^{2+}, Ni^{2+}, Hg^{2+}, Cu^{2+}, and Cd^{2+}), Alkaline Earth Metals Be^{2+}, Ca^{2+}, Mg^{2+}, Ba^{2+}, and Sr^{2+}, Lanthanides (Yb^{2+}, Tm^{2+}, and Eu^{2+}), and Ga^{2+}, In^{2+}, Bi^{3+}, Sb^{2+} (p-block element) are all suggested to be a substitute for lead. However, Sn^{2+}, Mn^{2+}, Mg^{2+}, Ge^{2+}, Co^{2+}, and Ni^{2+} cations stability appears promising in PSCs [89].

1.7.1. Tin

Tin (Sn) is initially used to replace toxic lead because of its comparable electronic structure and approximately the same ionic radius (1.35 Å). This is in contrast to the Pb-based perovskite, which has greater charge carrier mobility (10^2-10^3 cm^2/Vs) and a smaller band gap [90]**.** Most perovskites have binding energies (2–50 meV), which are comparable to lead and allow for unlimited exciton ionization [91]. Chen *et al.* first used Sn-based perovskite, which has a low band gap (1.3eV) and exciton binding energy (~18meV) and achieved a PCE of 0.9% [92]. Hao *et al.* and Noel *et al.* utilized $MASnI_{3-X}Br_X$ and $MASnI_3$ in PSCs, and a higher PCE of 5.2% and 6.4% was obtained using mesoporous-TiO_2 as the ETL, respectively [93]. The observed shift in PCE may be explained by the addition of Br^- significantly raising the Voc. This could be the result of the subsequent perovskite light absorber having a higher conduction band and a lower series resistance. Though the device performance is good, it was unreliable (deteriorated in less than a day) and not reproducible. The researcher is challenged by the stability and

reproducibility, which offer a way to work on stability using cation and halide ion exchange.

Despite its numerous advantages, including a long diffusion length, high bulk n-type electrical conductivity, low optical band gap, and enhanced electron mobility,, Sn-based perovskite lacks stability due to its facile oxidation, which poses a serious threat to its stability [94]**.** However, the performance of the perovskite layer is limited by the self-doping caused by Sn^{4+} oxidation, which behaves as a p-type dopant. The inhomogeneity and inadequate surface coverage of these Sn-based perovskites are further drawbacks brought on by their quick crystallization. Kanatzidis *et al.* used a variety of solvents to control the fast crystallization, and this solvent variation produced a smooth and pinhole-free surface via utilizing DMSO and NMP and enhancement in the photocurrent observed to 21 mA/cm^2 (Figure 1.12 A, B) [95]. Several deposition techniques (vapor deposition, hybrid vapor deposition) have been used to regulate quick crystallization.

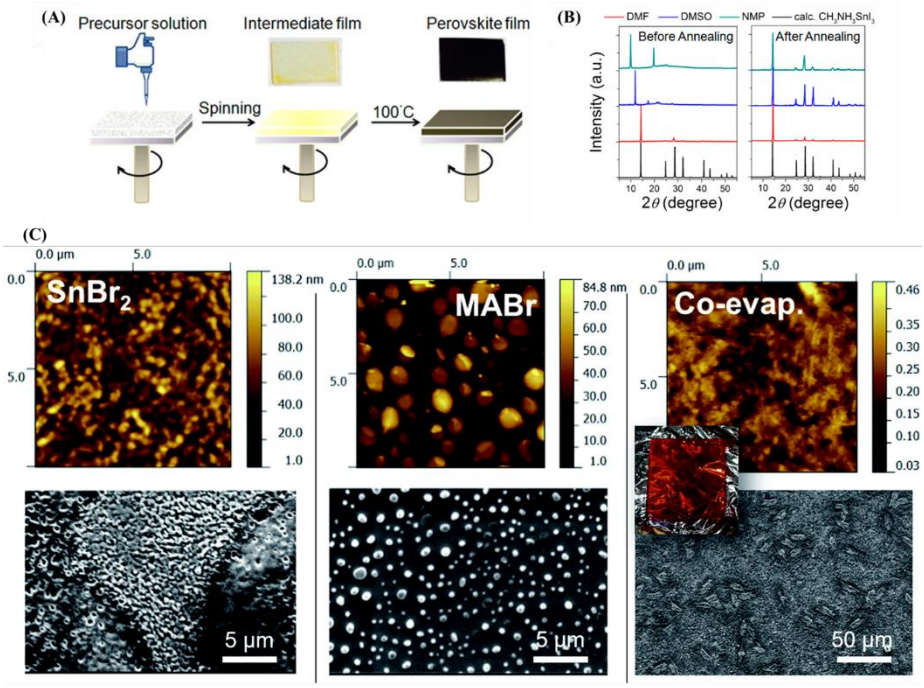

Figure 1.12. (A) spinning-coating process (B) X-ray diffraction. Figure reprinted with permission Ref. [95]. Copyright 2015, The American Chemical Society. (C) AFM and SEM images on Si substrate of samples

($MABr : SnBr_2 = 4 : 1$). Figure reprinted with permission Ref. [96]. Copyright 2016, The Royal Society of Chemistry.

In order to enhance morphology and crystallite size, a two-step deposition approach was employed, wherein SnI_2 was spin-coated onto the MAI solution to engender $MASnI_3$ perovskite precursor (Figure 1.12 C). After being stored in a glove box for 20 days, the perovskite demonstrated exceptional stability, and no further Sn^{+4} peak was seen. However, the $MASnI_3$ perovskite strongly relied on the MAI concentration [97]. Lower performance was observed from the co-evaporation deposition of $MASnBr_3$ perovskite by Qi *et al.,* which generates Sn-Br oxide on the perovskite surface and limits charge transfer and excitons. The sequential evaporation method produced $MASnBr_3$ perovskite, which outperformed co-evaporation and had a higher PCE of 1.12%. This might be attributed to the MABr layer's decreased oxidation [96]. In accordance with the results obtained, it would seem that the two-step deposition method may be better for stabilizing Sn-based perovskite.

Additionally, a mixed cation method was used to increase the Sn-Based PSC stability. The $MASnI_3$ or $FASnI_3$ perovskite was treated with the Cs^+ cation in this approach, and the device efficiency is less than the 2% recorded [98]. Nevertheless, in order to create the $((CH_3(CH_2)_3NH_3)_2(CH_3NH_3)_{n-1}Sn_nI_{3n+1})$ light absorber, Cao *et al.* combined the $CH_3NH_3^+$ (MA^+) and $CH_3(CH_2)_3NH_3^+$ (BA^+). This reduced the dimensionality, and the ideal band gap for n=4 and 3 was measured to be 1.43 and 1.5 eV, respectively. Lower dimensional models perform better than 3D analog models when n = 4. By adding PEA (20%) to $FASnI_3$, Liao and coworkers created $((PEA)_2(FA)_8Sn_9I_{28})$ perovskite, which has more stability than pure $FASnI_3$ perovskite. The author achieved a greater efficiency of 5.94% and stability for up to 1000 hours without encapsulation using the inverted solar cell architecture [99]. The amount of PEA reduced in $FASnI_3$ results in a homogenous growth, strong crystallinity, and a decreased temperature attention on the grain size for $FASnI_3$.

Sn-based perovskite stability may be impacted by charge transport materials, and HTM additives (such as LiTFSI) and spiro-OMeTAD are also used. In the case of the imprint, Hatton *et al.* explored CuI as an HTL and $CsSnI_3$ deposit onto the HTM and fabricated the inverted device structure. Excess SnI_2 was exposed at the $CsSnI_3$/CuI interface, where it acts as an HTL hole extraction efficiency was increased [100]. However, in the instance of PEDOT: PSS as HTL with the $CsSnI_3$ perovskite, no effect on hole extraction efficiency was detected, demonstrating the influence of HTM and phenomena underneath the HTM layer. However, Sun *et al.* used $CsSnI_3$ perovskite in three distinct architectures i.e., planer heterojunction, meso-super, and mesoscopic structure, and they observed the same results [101].

Lead-based perovskites outperform Sn-based perovskites in PCE despite having superior optoelectronic qualities. The combined effects of fast oxidation from +2 to +4, poor film quality, deterioration from HTM, and sensitivity in interfacial layers may be the cause of Sn-based perovskite's low efficiency. The fast oxidation of Sn^{+2} is inhibited by using additives like SnF_2 and $SnCl_2$ in Sn-based perovskite, yet it is unclear what exactly these additives do. Although the effect of halide is unclear, SnF_2 and $SnCl_2$ may, under some assumptions, compensate for the Sn^{+2} vacancies, improving stability. Because SnF_2 is a more potent reducing agent, it may act as another reducing agent in order to stabilize Sn^{+2}. The kind of HTM affects the composition of the perovskite and hole interface; therefore, selecting a proper HTM might enhance the performance and stability of Sn-based perovskite. To investigate additional mixed cation approaches further in order to prolong the stability of Sn-Based perovskite will be useful.

1.7.2. Germanium

With the exception of Sn and Pb, Ge exhibited extremely low toxicity, and none of its elements were mutagenic or carcinogenic. Rats are administered sodium germinate to reduce their likelihood of developing tumors. Furthermore, few Ge complexes, such as organic or inorganic, show antineoplastic effects in people. Similar to Pb and Sn in the same group, Ge garnered interest due to its nearly identical size and electrical

structure when used in PSCs. Due to its divalent nature, Ge with the ABX_3 formula has optical, structural, and electrical characteristics that are comparable to those of Pb and Sn [102]. According to computational studies, Ge-based perovskites exhibit good optoelectronic characteristics for solar applications [103]. In $AGeX_3$, the Eg is influenced by the halide ions; as halide ion size increases, the band gap decreases, as demonstrated in both theoretical and experimental studies. For $CsGeX_3$, the Eg is approximately 3.2 eV, 2.3, and 1.6 when the halide ions are Cl, Br, and I, respectively. In contrast to Pb perovskites, Ge-based perovskite shows a rise in Eg with an increase in cation size (A). Furthermore, adding bigger cations alters the dimensionality and nature of the Eg in perovskite materials, which influences Ge-perovskite absorption in addition to increasing the Eg [104]. The optical, electrical, and structural, characteristics of the $AGeI_3$ perovskite were observed by Stoumpos *et al.* in 2015. Eg is much larger than that of lead, with variations in the A cation ranging the Eg from 1.63 to 2.8 eV. Higher orbital energy in Ge and structural distortion may be the cause of the band gap change [104]**.**

1.7.3. Antimony

Sea spray, volcanic activity, and forest fires are some natural processes that produce Antimony (Sb). Its average daily consumption is predicted to be around 5 mg, with a soil concentration of 0.48 ppm. Low quantities of antimony are thus already present in the general population's interactions. On the other hand, pneumoconiosis, emphysema, and bronchitis may arise from long-term exposure to Sb oxides such as Sb_2O_3 or Sb_2O_5. Sb_2O_3 is categorized as human carcinogenic due to research suggesting that Sb ingestion may encourage spontaneous miscarriages in women (IARC 2B) [105]. Because Sb presented to the same group as arsenic and shows several of the same properties, its location in the periodic table justifies its toxicity. However, Sb is a good substitute for Pb since it is less expensive than Sn and possesses a single pair of $5s^2$ electrons. Sb-based perovskites, denoted by the formula $A_3Sb_2X_9$, where X can be Cl^-, Br^-, or I^- and A can be either Cs^+ or MA^+, exhibit potential for use in solar applications [106, 107]. Sb can be

utilized in PSC perovskites because it poses less toxicity risk than Pb (108). Compared to Pb-based materials, $Cs_3Sb_2I_9$ exhibits superior stability in an ambient environment, with an indirect Eg of 2.05 eV. Jakubas *et al.* (1991) and Bagautdinov *et al.* (1999) examined the structural properties of $(CH_3NH_3)_3Sb_2I_9$ and phase transition properties of $Cs_3Sb_2I_9$ respectively [109, 110].

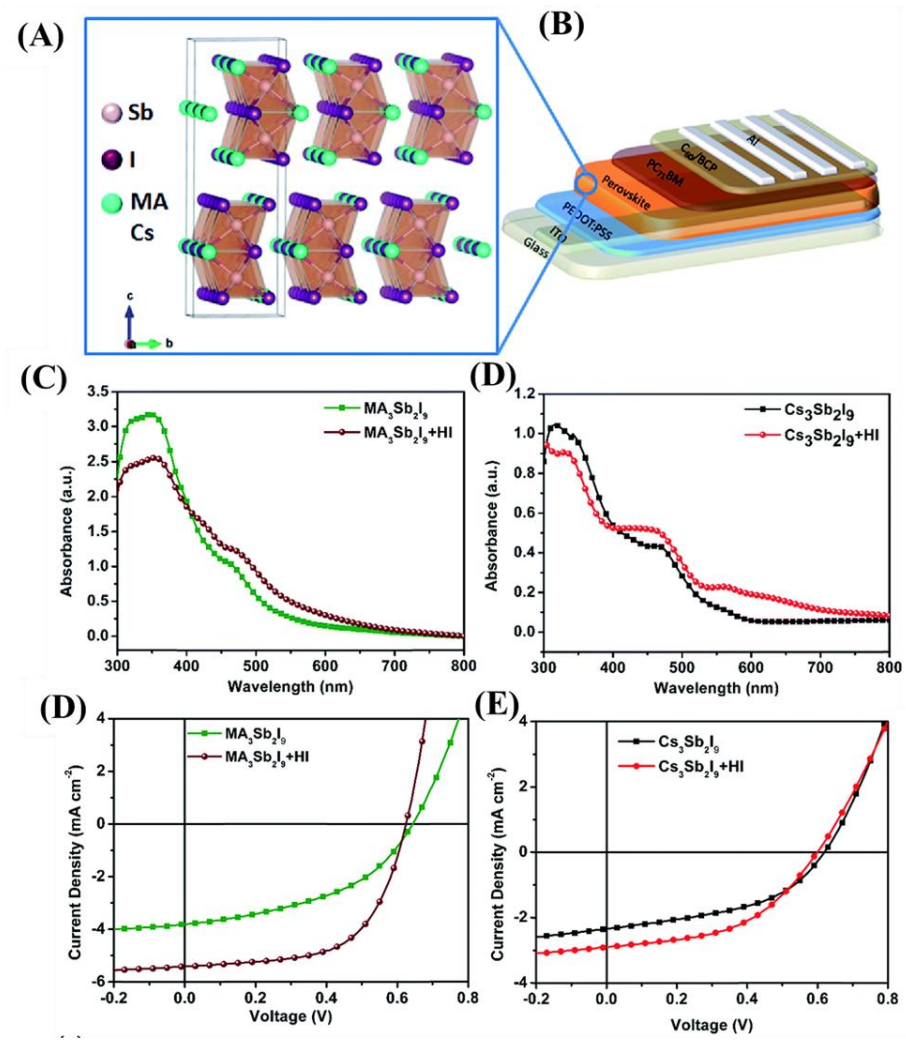

Figure. 1.13. (A) Crystal structures of $A_3Sb_2I_9$ perovskite (B) representation of photovoltaic device (C, D) Absorbance spectra of $MA_3Sb_2I_9$ and $Cs_3Sb_2I_9$, (E, F) J–V characteristics of $MA_3Sb_2I_9$ and $Cs_3Sb_2I_9$. Figure reprinted with permission Ref. [115]. Copyright 2017, The Royal Society of Chemistry.

Saparov *et al.* first proposed substituting Sb for Pb in PSCs after discovering that 2D layered $Cs_3Sb_2I_9$ perovskite has a high absorption coefficient and Eg of 2.05 eV, making it appropriate for solar energy use

[111]. For solution-processable heterojunction utilizing $MA_3Sb_2I_9$, Hebig *et al.* primarily stated a PCE of 0.49% based on p−i−n-type PSCs. Later, it was discovered that PCE for Sb perovskites treated in solution with Rb cations had improved to 0.66% [112, 113]. Umar *et al.* discovered a superior PCE of 1.21% by controlling the dimensionality of $Cs_3Sb_2I_9$ with the aid of HCl-assisted technology [114].

Boopathi *et al.* examined Sb-based light absorber in SCs and observed that those with inorganic Cs^+ cations (i.e., $Cs_3Sb_2I_9$) provided less PCE than those with MA ions (i.e., $MA_3Sb_2I_9$). One step approach was utilized to prepare Sb-based perovskite along with HI as an additive to the active layer. Measured Eg of $Cs_3Sb_2I_9$ and $MA_3Sb_2I_9$ were found to be 2.0 and 1.95 eV, respectively (Figure 1.13), responsible for higher PCE. PCE (2.04%) was achieved by the $MA_3Sb_2I_9$ with HI additive, but $Cs_3Sb_2I_9$ showed only 0.84% (Figure 1.13) [115]. Sb-based PSCs considered non-toxic and have good stability, making them appropriate for combination with other materials, even if their PCE is lower than that of Pb-based PSCs. An Eg of 1.93 eV was obtained in Sb−silver-based double perovskite ($(CH_3NH_3)_2AgSbI_6$) for light absorption [116]. Vargas and colleagues synthesized a distinct copper-antimony halide perovskite material, $Cs_4CuSb_2Cl_{12}$, and calculated an optical band gap (Eg) of 1.02 eV [117].

1.7.4. Bismuth

There are benefits and drawbacks to bismuth (Bi) and its compounds. While prolonged ingestion of some chemicals might cause neurotoxicity and kidney failure, others are employed as therapeutic substances [118, 119]. However, studies conducted in the past have demonstrated that human cells are hardly affected by modest doses of Bi (1 to 100 mM) [119]. Bi(III) may be used as a lead substitute since it had an ionic radius of 1.03 Å and an electronic structure $6s^26p^0$similar to Pb(II) [120]. Bi is understood to be less poisonous and more air-stable than Ge and Sn elements. While Pb and Bi have a +2 and +3 valence state, respectively, by simply replacing 3 Pb^{2+} with 2 Bi^{3+}, the structural formula can be obtained. Consequently, the structural formula for ternary Bi^{3+}-based perovskites is usually $A_3Bi_2X_9$, where X is occupied by I^- or Br^- and A

by Cs^+ or MA^+ [121]. Bi-based materials have great promise for use in solar cell applications because of these properties. Remarkable absorption coefficients and extended carrier diffusion lifetimes have been demonstrated by Bi-based perovskites [122, 123]. More encouragingly, Bi-based perovskite has low toxicity and outstanding environmental stability, guaranteeing their great dependability in upcoming commercial applications [124]. Figure 1.14 concludes that the exceptional features demonstrate Bi is among the most promising choices for replacing Pb alter ants in PSCs. Bi is assumed to take a structure of octahedrally coordinated and a stable 6p block structure. Bi atoms complete two-thirds of the octahedral X_6 voids in the $A_3Bi_2X_9$ structure. This suggests that Bi-based perovskites have high charge transport lifetimes because of their reduced intrinsic defect states and trap densities. Bi structure and properties have been thoroughly investigated in order to fully apprehend its potential in solar cells [122, 125, 126].

The usual perovskite structure of Bi halide derivatives is $A_3Bi_2X_9$ (A = Cs, Rb, K, MA; X = I, Br, Cl). This is also the first Bi-based material to be developed and employed in solar cells. Both two-dimensional (2D) and zero-dimensional (0D) structures are usually for the materials. Compared to the 3D $ABiX_3$ materials, the 0-D $A_3Bi_2X_9$ structure offers greater resilience contrary to phase deterioration due to its reduced dimensionality. Furthermore, compounds with 2D architecture are based on angularly coupled double octahedra, such as $Rb_3Bi_2I_9$ and $K_3Bi_2I_9$. The lattice parameters and Eg can be adjusted by replacing A, B, and X sites in the crystal structure, resulting in a modification of the band energy from ~1.9 eV to ~3.1 eV. The layered Rb and K -based crystals clearly exhibit direct Eg, but $Cs_3Bi_2I_9$ showed an indirect gap, according to computed band structures [127].

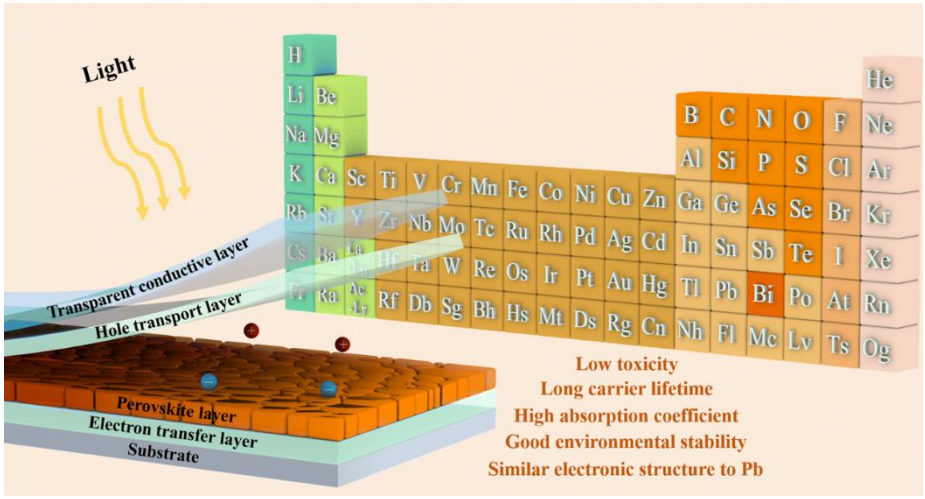

Figure 1.14. Schematic diagram of PSCs device and some owing properties perovskite materials based on Bi. Figure reprinted with permission Ref. [65]. Copyright 2022, The Royal Society of Chemistry.

$A_3Bi_2I_9$ ($A = MA^+, Cs^+$) perovskite structure was synthesized by Park *et al.* and found a $(Bi_2I_9)_3$ clusters, which are surrounded by A cations [122]. Compared with the 3D $MAPbI_3$ perovskite, the synthesized material has a distinct structure. An optimum PCE of 1.09% for $Cs_3Bi_2I_9$ was demonstrated in a PV system that was fabricated using a glass/FTO/TiO_2/perovskite/HTM/Ag configuration [122]. Wider Eg (>2.0 eV) and lower film quality are the causes of the low efficiency [52]. The PCE has only risen to 3.17% despite numerous studies conducted since then to enhance the PV characteristic. Its inefficiency primarily arises from its small dimensions (0D or 2D) and large optical band gap (> 2.1 eV).

Significant development and research have been made in optimizing the composition of materials and film formation. Park and coworkers synthesized $Cs_3Bi_2I_9$ as an active layer in PSCs and obtained a capable PCE of 1.09% [122]. However, a novel Bi-based perovskite configuration of $CsBi_3I_{10}$ with a smaller Eg of 1.77 eV was stated by Johansson *et al.* in 2016 [50]. Subsequently, using $Cs_2AgBiBr_6$, Igbari *et al.* fabricated double perovskite light absorber thin films that produced a champion PCE of 2.51%. Figure 1.15 A shows the synthesis of double perovskite synthesis; one is vacuum sublimation, and the other is solution processing. The device structure, photovoltaic performance,

and EQE are also elaborated (Figure 1.15 B, C, and D). The stability of double perovskite was also examined, and both devices showed an insignificant change up to 350 h (Figure 1.15 E) [128].

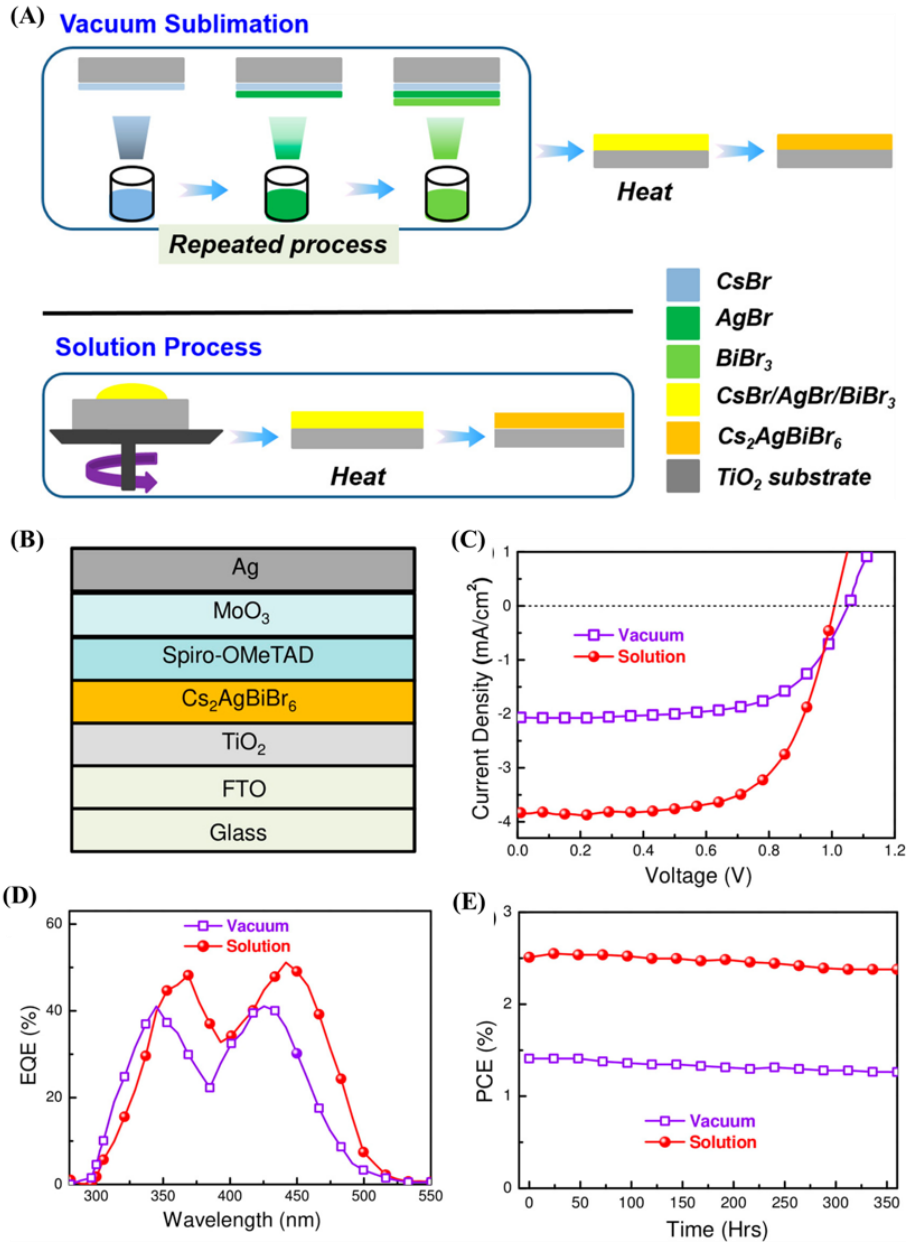

Figure 1.15. (A) Representation of the synthesis of $Cs_2AgBiBr_6$ films by vacuum-sublimation and solution-processing, (B) Device structure, (C) J–V curves, (D) EQE spectra, (E) stability. Figure reprinted with permission Ref. [128]. Copyright 2019, The Royal Society of Chemistry

Bi-based PSCs have recently approached PCE of 3.6% with developing a bulk an heterojunction with the active layer composed of in situ phase-separated $Ag_3Bi_2I_9$ and $Cs_3Bi_2I_9$ [129]. However, this proficiency is

significantly less then to the theoretically predicted efficiency for bi-based PSCs. Although various methods have been devised thus far to enhance PV performance, a basic comprehension of the physical characteristics of pure Bi-based perovskites is still lacking.

Furthermore, challenges remain in identifying the limitations of their optoelectronic properties and developing practical strategies to improve device performance. Trivalent Bi^{3+} frequently exhibits deformed crystal structures in contrast to conventional Pb-based perovskite cubic forms, although having similar electronic and chemical properties as Pb perovskite materials. Recent research indicates that large exciton binding energies, wide optical band gaps, high defect densities, and elevated carrier effective masses are inherent limitations of bismuth-based perovskite materials [51, 130]. Theoretically, tuning the aforesaid abilities and enhancing PV performance can be achieved through chemical composition handling [131].

Cations play a critical role in influencing the optical characteristics of the film. Currently, Cs^+ is the predominant cation used in solar cells, although reports suggest that various inorganic cations can potentially replace Cs^+, offering nearly as intriguing properties. $Cs_3Bi_2I_9$ was synthesized by Park *et al.* via a solution technique, and the material's composition and photoelectric characteristics were examined [122]. They discovered that the crystal assembly of $Cs_3Bi_2I_9$ is made up of clusters (octahedral $(Bi_2I_9)_3$) and encircled by ions (Cs). However, the authors observed that $Cs_3Bi_2I_9$ has a comparatively higher PL yield, indicating reduced nonradiative recombination losses. It has been possible to attain a PCE of 1.09% (Voc = 0.85 V, Jsc = 2.15 mA/cm^2 and FF = 60%). Later, Johansson *et al.* examined the structure of $Cs_3Bi_2I_9$ and its PV potentials in more detail. It was found that the $Cs_3Bi_2I_9$ grew steeply and infiltrated into the mesoporous TiO_2 to produce 2 mm hexagonal lamellar formations. Large voids were created in crystals as a result of $Cs_3Bi_2I_9$ stacking and distinct growth orientation (Figure 1.16) [50].

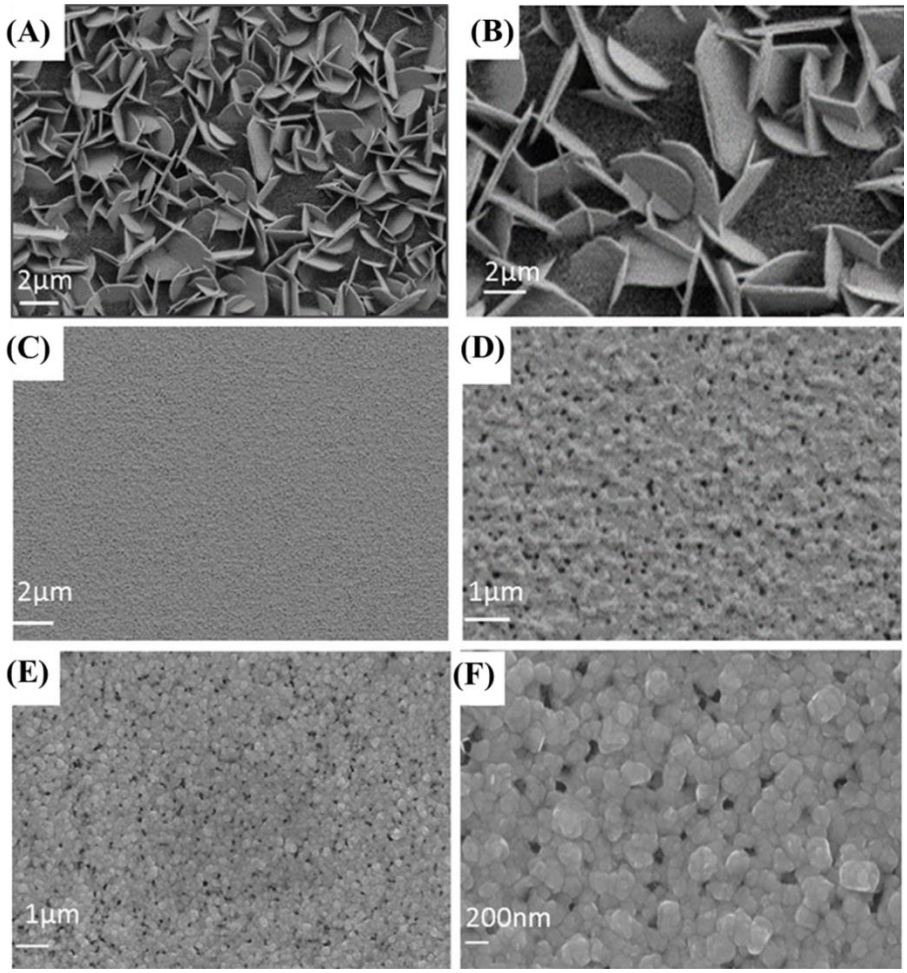

Figure 1.16. SEM images of (A, B) $Cs_3Bi_2I_9$, (C, D) $CsBi_3I_{10}$, (E, F) BiI_3 under high and low magnification. Figure reprinted with permission Ref. [50]. Copyright 2016, The American Chemical Society.

For the light-absorbing layer, a nonuniform film with an irregular absorbent structure is undesirable, as it can lead to significant charge losses and inferior optoelectronic properties. The conventional production method could not adequately evade the vertically grown orientation of $Cs_3Bi_2I_9$ crystals. In addition, low mobility and absorption coefficient cause the low current density of the film's and also restricts the efficiency of $Cs_3Bi_2I_9$ PV systems.

Poor charge collection efficiency primarily caused the lower short-current density, which may be brought on by insufficient charge transfer, severe carrier recombination at interfaces, taking into account the light-harvesting proficiency and absorption spectra of the $Cs_3Bi_2I_9$ perovskite [65]. Therefore, for further enhancement in the Jsc of devices, additional

refining of the characteristics of $Cs_3Bi_2I_9$ films and their interfaces is essential.

The optical and electrical characteristics of $Cs_3Bi_2X_9$ based on three halides (I, Br, and Cl) were fully studied by using a first-principles approach [132]. $Cs_3Bi_2I_9$ and $Cs_3Bi_2Cl_9$ had more subbands than $Cs_3Bi_2Br_9$, because of their weaker symmetry characteristics. According to the calculations, the indirect Eg of each of the three configurations varies depending on the halogen atoms. The primary source of $Cs_3Bi_2X_9$ photo-absorption is the electronic jump that occurs in X and Bi atoms in the 6p orbitals on the Eg. The distribution features conclude that when these crystals are energized to release photons, the electron leap primarily happens between the Bi and X atoms. Scientists modify the ratio of X molecules in $A_3Bi_2X_9$ to obtain a reduced Eg by employing first-principles calculations.

Because of low valance p orbital energy of Br, it is commonly believed that the Eg of the $Cs_3Bi_2I_{9-x}Br_x$ alloy have a tendency to be broader whenever the Br concentration increases. $Cs_3Bi_2I_{9-x}Br_x$ perovskite-based films (x=0, 1, 2, 3, 4, 6, and 9) synthesized by Yu *et al.*, variation in color had been observed for variation in x values (Figure 1.17 A). UV-Vis and XRD spectra support the synthesized materials, and optical Eg is measured by plotting a tauc plot. In contrast to $Cs_3Bi_2I_9$ (2.23 eV), it was found that $Cs_3Bi_2I_6Br_3$ had a smaller Eg of 2.05 eV (Figure 1.17 B, C, D) [75].

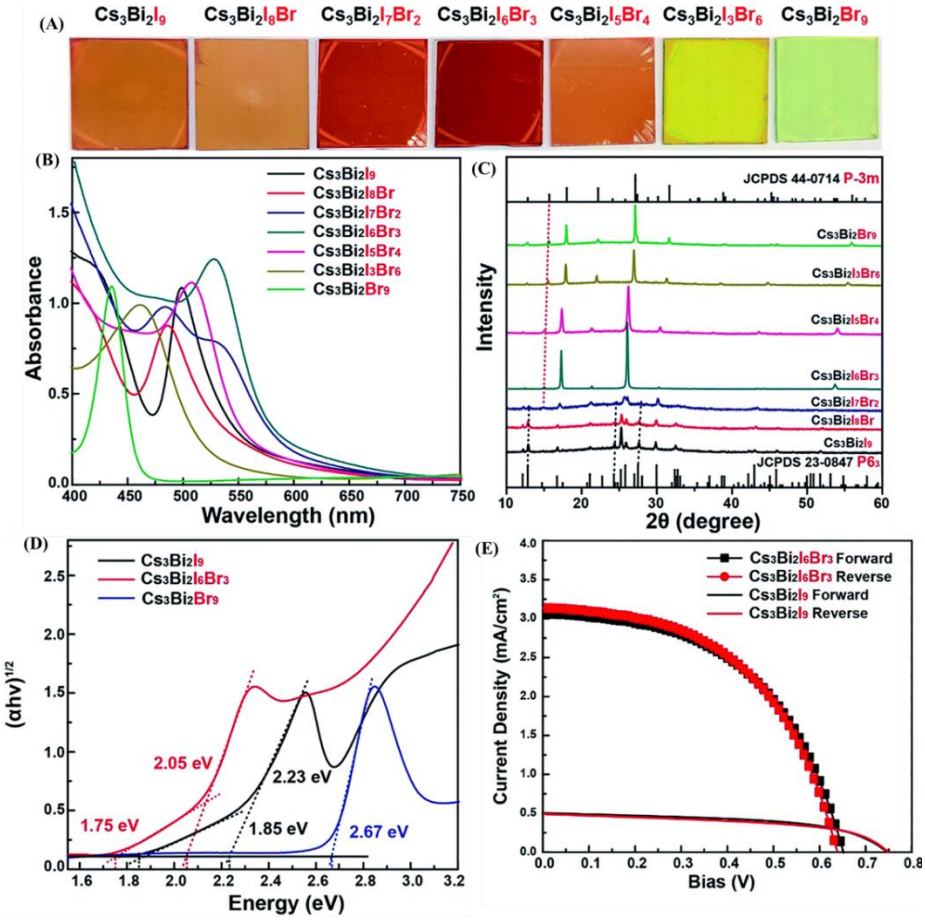

Figure 1.17. (A, B, C) optical images, absorbance spectra, X-RD patterns of $Cs_3Bi_2I_{9-x}Br_x$ films (D) Tauc plots, (E) J–V curves of $Cs_3Bi_2I_9$ and $Cs_3Bi_2I_6Br_3$. Figure reprinted with permission Ref. [75]. Copyright 2019, The Royal Society of Chemistry.

A higher PCE was observed for $Cs_3Bi_2I_6Br_3$ (1.15%) than for $Cs_3Bi_2I_9$ (Figure 1.17 E). Also, double perovskites have gained recognition as viable substitutes for lead-based perovskites since the first report of $Cs_2AgBiBr_6$ and $Cs_2AgBiCl_6$ in PV cell applications in 2016 [133]. Zhang *et al.* presented numbers of intriguing candidate materials with low exciton binding energy, small carrier effective mass, suitable Eg, and intrinsic thermodynamic stability, all of which are frequently necessary for successful light absorbers based on first-principal calculations [134]. Various double perovskite materials with the $A_2M(I)^+M(III)^{3+}X_6$ composition had been formed based on this theory. The A elements used include Cu, MA, and Cs; $M(I)^+$ elements include K^+, Ag^+, Na^+, and In^+;

$M(III)^{3+}$ elements include Bi^{3+}, Sb^{3+}, and In^{3+}; X elements are halogen anions.

Among the various double perovskites chosen for PV investigation, $Cs_2InBiCl_6$ had an Eg of approximately 1.0 eV, and its theoretic higher PCE was similar to that of $CH_3NH_3PbI_3$ [134]. Nevertheless, positively charged monovalent In^+ ions are highly unstable and readily undergoes conversion to elemental indium and In^{3+} ions. As of now, this material has not been formed through chemical synthesis. Ma *et al.* effectively synthesized Cs_2NaBiI_6 double perovskites with an Eg of 1.66 eV using a simple hydrothermal procedure [135]. The resulting perovskites were highly crystalline, uniform, and stable. The Cs_2NaBiI_6 based device demonstrated a PCE of 0.42%, equivalent to that of other Pb-free PSCs [135].

Cu_2AgBiI_6 has been synthesized and employed in solar devices. Cu_2AgBiI_6 exhibits a direct Eg of 2.06 eV, PL lifetime (33ns), an exciton binding energy (25 meV) and a high charge carrier mobility (1.7 $cm^2V^{-1}s^{-1}$) [136]. Peedikakkandy *et al.* conducted an optimization of $Cs_3Bi_2I_9$ by subjecting it to treatment with alkali metal sulfide (Na_2S), resulting in the formation of Cs_3NaBiI_9 [137]. Na-doping pointedly reduced the optical Eg, decreasing it from 2.28 eV to 1.48 eV. Additionally, it improved the phase purity of the thin films, resulting in higher density and smoother surfaces. Among these double perovskites materials, $Cs_2AgBiBr_6$ demonstrated outstanding qualities in simple production, chemical stability, and acceptable Eg. Hence, in the subsequent part, our primary emphasis will be on the advancement and obstacles faced by $Cs_2AgBiBr_6$ in its utilization for solar cell purposes.

For the first time, Greul *et al.* used a one-step solution spin coating approach to create a superior thin film of $Cs_2AgBiBr_6$ double perovskites [53]. Preheating both the substrate and solution might improve the surface distribution of $Cs_2AgBiBr_6$ and enhances film quality. They proposed that annealing at a high temperature (>250℃) is required for full conversion of substrates to $Cs_2AgBiBr_6$. $Cs_2AgBiBr_6$ films exhibit a higher PCE of about 2.5% in SCs following fine-tuning of the synthetic

condition. $Cs_2AgBiBr_6$ based devices exhibited significantly greater light stability compared to $MAPbI_3$ based devices.

1.7.5. Other lead-free perovskite-based elements

A number of various substitutes have been studied in addition to the Pb-free perovskite materials that have already been explained. Silver (Ag), in disparity to lead, is non-toxic and suitable for a variety of uses, such as cutlery and dental fillings [138]. The usage of Ag in double perovskites was investigated by Slavney *et al.* using the formula $AMM'X_6$ (where A = Cs, CH_2NH_3; M′ = Bi, Sb; M = Ag; X = Cl, Br, I), an indirect Eg of 1.95 eV was calculated [133]. Even though lead is more poisonous than Ag, a stable 3D double perovskite with the formula $AMM'X_6$ is not always produced by just substituting any monovalent (M^+) and trivalent (M'^{3+}) cation for Pb^{2+}. Pd^{4+}, Nb^{4+}, Pt^{4+}, or Ti^{4+} in place of M can be used as alternatively [139, 140]. Among these, Cs_2PtI_6 and Cs_2TiBr_6 have demonstrated potential because of their appealing PCE, suitable Eg, extended carrier lifetimes, good stability, and high absorption coefficients [139]. A novel class of lead-free perovskites is represented by double perovskites. While there aren't many streamlined samples with appropriate Eg that have been found, several, such as $(CH_3NH_3)_2AgBiBr_6$, $Cs_2AgBiBr_6$, and $Cs_2AgBiCl_6$ have garnered a lot of interest. Compared to $MAPbI_3$ films, $Cs_2AgBiBr_6$ films have superior stability and longer radiative recombination lifetimes. $Cs_2AgBiBr_6$ and $Cs_2AgBiCl_6$ were synthesized by McClure *et al.*, and an indirect Eg of 2.19 and 2.77 eV were calculated, respectively [141].

1.8. Scope of present work

The preceding discussion highlights the urgency of addressing two major global challenges: environmental degradation and the energy crisis. This thesis project aims to tackle these issues by designing and producing advanced functional materials. The transition from lead-based to lead-free perovskite materials is essential for the sustainable advancement of perovskite solar cells. The aim of this thesis is to explore various lead-free compositions, evaluate their photovoltaic performance parameters, and elucidate their operational principles to advance environmentally friendly and efficient photovoltaic technologies.

The thesis work focuses on the following key points-

1. Synthesis of Antimony and Bismuth based halide perovskite as a light absorber material for photovoltaic application.
2. Utilization of advanced characterization techniques to analyze the physiochemical and optoelectronic properties of the synthesized perovskite materials.
3. Controlling the rapid growth and the morphology of the light absorber.
4. Fabrication of electrodes for photovoltaic devices.

1.9. References

1. International Energy Outlook 2023 - U.S. Energy Information Administration (EIA). Available at: https://www.eia.gov/outlooks/ieo/index.php. Accessed on 23 July 2024.
2. Gielen D., Boshell F., Saygin D., Bazilian M. D., Wagner N., Gorini R. (2019), The role of renewable energy in the global energy transformation, Energy Strategy Reviews, 24, 38–50 (DOI: 10.1016/j.esr.2019.01.006).
3. Wang J., Azam W. (2024), Natural resource scarcity, fossil fuel energy consumption, and total greenhouse gas emissions in top emitting countries, Geoscience Frontiers, 15, 101757 (DOI: 10.1016/j.gsf.2023.101757).
4. Ozdemir A. C. (2023), Decomposition and decoupling analysis of carbon dioxide emissions in electricity generation by primary fossil fuels in Turkey, Energy, 273, 127264 (DOI: 10.1016/j.energy.2023.127264).
5. Stančin H., Mikulčić H., Wang X., Duić, N. (2020 A review on alternative fuels in future energy system, Renewable and Sustainable Energy Reviews, 128, 109927 (DOI: 10.1016/j.rser.2020.109927).
6. Khan S. A. R., Zia-Ul-Haq H. M., Ponce P., Janjua L. (2023), Re-investigating the impact of non-renewable and renewable energy on environmental quality: A roadmap towards sustainable development, Resources Policy, 81, 103411 (DOI: 10.1016/j.resourpol.2023.103411).
7. Zhang Y., Li L., Sadiq M.. Chien F. (2024), The impact of non-renewable energy production and energy usage on carbon emissions: Evidence from China, Energy & Environment, 35, 2248–2269 (DOI: 10.1177/0958305X221150432).
8. Dehghani-Sani A. R., Tharumalingam E., Dusseault M. B., Fraser R. (2019), Study of energy storage systems and environmental challenges of batteries, Renewable and

Sustainable Energy Reviews, 104, 192–208 (DOI: 10.1016/j.rser.2019.01.023).

9. M A., V M. K., Hariharan V. S., Narahari T., P A. K., K M., G, P. K., Prabakaran R. (2023), Fuelling the future: A review of non-renewable hydrogen production and storage techniques, Renewable and Sustainable Energy Reviews, 188, 113791 (DOI: 10.1016/j.rser.2023.113791).
10. Chapin D. M., Fuller C. S., Pearson G. L. (1954), A New Silicon p-n Junction Photocell for Converting Solar Radiation into Electrical Power, Journal of Applied Physics, 25, 676–677 (DOI: 10.1063/1.1721711).
11. Akpan J., Olanrewaju O. (2023), Sustainable Energy Development: History and Recent Advances, Energies, 16, 7049 (DOI: 10.3390/en16207049).
12. Shahbaz M., Siddiqui A., Siddiqui M., Jiao Z., Kautish P. (2023), Exploring the growth of sustainable energy Technologies: A review, Sustainable Energy Technologies and Assessments, 57, 103157 (DOI: 10.1016/j.seta.2023.103157).
13. Hassan Q., Viktor P., J. Al-Musawi T., Mahmood Ali B., Algburi, S., Alzoubi, H. M., Khudhair Al-Jiboory A., Zuhair Sameen A., Salman H. M., Jaszczur M. (2024), The renewable energy role in the global energy Transformations, Renewable Energy Focus, 48, 100545 (DOI: 10.1016/j.ref.2024.100545)
14. Kataray T., Nitesh B., Yarram B., Sinha S., Cuce E., Shaik S., Vigneshwaran P., Roy A. (2023), Integration of smart grid with renewable energy sources: Opportunities and challenges – A comprehensive review, Sustainable Energy Technologies and Assessments, 58, 103363 (DOI: 10.1016/j.seta.2023.103363).
15. Nazim M., Ahmad R. (2023), Chapter 1 - Introduction to advanced electronic materials for clean energy applications. In Advances in Electronic Materials for Clean Energy Conversion and Storage Applications (Edited by Khan A., Nazim M., Asiri A.) Woodhead Publishing Series in Electronic and Optical

Materials, pp. 3–26. Woodhead Publishing (DOI: 10.1016/B978-0-323-91206-8.00012-1).

16. Best Research-Cell Efficiency Chart. Available at: https://www.nrel.gov/pv/cell-efficiency.html. Accessed on 25 September 2023.
17. Belotti A., Liu, J., Curcio, A., Wang, J., Wang, Z., Quattrocchi, E., Effat, M. B., Ciucci, F. (2021), Introducing Ag in Ba0.9La0.1FeO3-δ: Combining cationic substitution with metal particle decoration, Materials Reports: Energy, 1, 100018 (DOI: 10.1016/j.matre.2021.100018).
18. Wang J., Choi S., Kim J., Cha S. W., Lim J. (2020), Recent Advances of First d-Block Metal-Based Perovskite Oxide Electrocatalysts for Alkaline Water Splitting, Catalysts, 10, 770 (DOI: 10.3390/catal10070770).
19. Wang J., Zhao H., Gao Y., Chen D., Chen C., Saccoccio M., Ciucci F. (2016), Ba0.5Sr0.5Co0.8Fe0.2O3−δ on N-doped mesoporous carbon derived from organic waste as a bi-functional oxygen catalyst, International Journal of Hydrogen Energy, 41, 10744–10754 (DOI: 10.1016/j.ijhydene.2016.04.049).
20. Wang Q., Xie Y., Soltani-Kordshuli F., Eslamian M. (2016), Progress in emerging solution-processed thin film solar cells – Part I: Polymer solar cells, Renewable and Sustainable Energy Reviews, 56, 347–361 (DOI: 10.1016/j.rser.2015.11.063).
21. Grätzel M. (2003), Dye-sensitized solar cells, Journal of Photochemistry and Photobiology C: Photochemistry Reviews, 4, 145–153 (DOI: 10.1016/S1389-5567(03)00026-1).
22. Kojima A., Teshima K., Shirai Y., Miyasaka T. (2009), Organometal Halide Perovskites as Visible-Light Sensitizers for Photovoltaic Cells, J. Am. Chem. Soc., 131, 6050–6051 (DOI: 10.1021/ja809598r).
23. Medarde M. L. (1997), Structural, magnetic and electronic properties of perovskites (R = rare earth), Journal of Physics: Condensed Matter, 9(8), 1679.

24. Hu S., Wang J., Zhang J., Lim J., Gao Y., Zhang S. (2021), Engineering the electronic structure of perovskite oxide surface with ionic liquid for enhanced oxygen reduction reaction, Applied Catalysis B: Environmental, 282, 119593 (DOI: 10.1016/j.apcatb.2020.119593).
25. Blasco J., Garcia J., Teresa J. M. de Ibarra M. R., Algarabel P. A. , Marquina C. (1996), A systematic study of structural, magnetic and electrical properties of (La{sub 1-x}Tb{sub x}){sub 2/3}Ca{sub 1/3}MnO{sub 3} perovskites, Journal of Physics. Condensed Matter, 8 (DOI: 10.1088/0953-8984/8/40/008).
26. Wang J., Gao Y., Ciucci F. (2018), Mechanochemical Coupling of MoS2 and Perovskites for Hydrogen Generation, ACS Appl. Energy Mater., 1, 6409–6416 (DOI: 10.1021/acsaem.8b01365).
27. Wei W.-C. J., Huang D.-R., Wang D. (2016), (Bi,Sr)(Fe1−x,Mx)O3−δ (M = Co, Ni and Mn) Cathode Materials with Mixed Electro-Ionic Conductivity, Materials, 9, 922 (DOI: 10.3390/ma9110922).
28. Mishra S., Parida S. K. (2023), Electrical and optical properties of a lead-free complex double perovskite BaNaFeMoO6: Photovoltaic and thermistor applications, Materials Science and Engineering: B, 296, 116629 (DOI: 10.1016/j.mseb.2023.116629).
29. Röder-Roith U., Rettig F., Sahner K., Röder T., Janek J., Moos, R. (2011), Perovskite-type proton conductor for novel direct ionic thermoelectric hydrogen sensor, Solid State Ionics, 192, 101–104 (DOI: 10.1016/j.ssi.2010.05.044).
30. Kodenkandath T. A., Lalena J. N., Zhou W. L., Carpenter E. E., Sangregorio C., Falster A. U., Simmons W. B., O'Connor C. J., Wiley J. B. (1999), Assembly of Metal−Anion Arrays within a Perovskite Host. Low-Temperature Synthesis of New Layered Copper−Oxyhalides, (CuX)LaNb2O7, X = Cl, Br. J, Am. Chem. Soc., 121, 10743–10746 (DOI: 10.1021/ja991566u).
31. Park K., Kim J. (2017), Effect of Nb2O5 content and sintering temperature on the microstructure and bending strength of

porous Ni-YSZ cermets, Ceramics International, 43, 1740–1746 (DOI: 10.1016/j.ceramint.2016.09.049).

32. Lin J., Hu J., Qiu C., Huang H., Chen L., Xie Y., Zhang Z., Lin H., Wang X. (2019), In situ hydrothermal etching fabrication of CaTiO3 on TiO2 nanosheets with heterojunction effects to enhance CO2 adsorption and photocatalytic reduction, Catal. Sci. Technol., 9, 336–346 (DOI: 10.1039/C8CY02142B).
33. Fergus J. W. (2007), Perovskite oxides for semiconductor-based gas sensors, Sensors and Actuators B: Chemical, 123, 1169–1179 (DOI: 10.1016/j.snb.2006.10.051).
34. Grätzel M. (2014), The light and shade of perovskite solar cells, Nature Mater, 13, 838–842 (DOI: 10.1038/nmat4065).
35. Yi Z., Ladi N. H., Shai X., Li H., Shen Y., Wang M. (2019), Will organic–inorganic hybrid halide lead perovskites be eliminated from optoelectronic applications?, Nanoscale Adv., 1, 1276–1289 (DOI: 10.1039/C8NA00416A).
36. Bartel C. J., Sutton C., Goldsmith B. R., Ouyang R., Musgrave C. B., Ghiringhelli L. M., Scheffler M. (2019), New tolerance factor to predict the stability of perovskite oxides and halides, Science Advances, 5, eaav0693 (DOI: 10.1126/sciadv.aav0693).
37. Tao Q., Xu P., Li M., Lu W. (2021), Machine learning for perovskite materials design and discovery, npj Comput Mater, 7, 1–18 (DOI: 10.1038/s41524-021-00495-8).
38. Tress W. (2016), Maximum Efficiency and Open-Circuit Voltage of Perovskite Solar Cells. In Organic-Inorganic Halide Perovskite Photovoltaics: From Fundamentals to Device Architectures (Edited by Park, N.-G., Grätzel, M., and Miyasaka, T.), pp. 53–77. Springer International Publishing, Cham (DOI: 10.1007/978-3-319-35114-8_3).
39. Riordan C., Hulstron R. (1990), What is an air mass 1.5 spectrum? (solar cell performance calculations), In IEEE Conference on Photovoltaic Specialists, pp. 1085–1088 vol.2 (DOI: 10.1109/PVSC.1990.111784).

40. Xie C., You P., Liu Z., Li L., Yan F. (2017), Ultrasensitive broadband phototransistors based on perovskite/organic-semiconductor vertical heterojunctions, Light Sci Appl, 6, e17023–e17023 (DOI: 10.1038/lsa.2017.23).
41. Miyasaka T. (2015), Perovskite Photovoltaics: Rare Functions of Organo Lead Halide in Solar Cells and Optoelectronic Devices, Chemistry Letters 44, 720–729 (DOI: 10.1246/cl.150175).
42. Meng L., You J., Guo T.-F., Yang Y. (2016), Recent Advances in the Inverted Planar Structure of Perovskite Solar Cells, Acc. Chem. Res. 49, 155–165 (DOI: 10.1021/acs.accounts.5b00404).
43. Dou Q., Whatley T., Syed T., Wei W., Wang H. (2022), Carbon nanomaterials–polymer composites for perovskite solar cells: preparation, properties and applications, J. Mater. Chem. A, 10, 19211–19230 (DOI: 10.1039/D2TA02175G).
44. Jeon N. J., Noh J. H., Kim Y. C., Yang W. S., Ryu S., Seok S. I. (2014), Solvent engineering for high-performance inorganic–organic hybrid perovskite solar cells, Nature Mater, 13, 897–903 (DOI: 10.1038/nmat4014).
45. Lee J.-W., Kim H.-S., Park N.-G. (2016), Lewis Acid–Base Adduct Approach for High Efficiency Perovskite Solar Cells, Acc. Chem. Res., 49, 311–319 (DOI: 10.1021/acs.accounts.5b00440).
46. Pinsuwan K., Boonthum C., Supasai T., Sahasithiwat S., Kumnorkaew P., Kanjanaboos P. (2020), Solar perovskite thin films with enhanced mechanical, thermal, UV, and moisture stability via vacuum-assisted deposition, J Mater Sci, 55, 3484–3494 (DOI: 10.1007/s10853-019-04199-9).
47. Lau C. F. J., Deng X., Ma Q., Zheng J., Yun J. S., Green M. A., Huang S., Ho-Baillie A. W. Y. (2016), CsPbIBr2 Perovskite Solar Cell by Spray-Assisted Deposition, ACS Energy Lett., 1, 573–577 (DOI: 10.1021/acsenergylett.6b00341).
48. Bing J., Huang S., Ho-Baillie A. W. Y. (2020), A Review on Halide Perovskite Film Formation by Sequential Solution

Processing for Solar Cell Applications, Energy Technology, 8, 1901114 (DOI: 10.1002/ente.201901114).

49. Im J.-H., Kim H.-S., Park N.-G. (2014), Morphology-photovoltaic property correlation in perovskite solar cells: One-step versus two-step deposition of CH3NH3PbI3, APL Materials, 2, 081510 (DOI: 10.1063/1.4891275).
50. Johansson M. B., Zhu H., Johansson E. M. J. (2016), Extended Photo-Conversion Spectrum in Low-Toxic Bismuth Halide Perovskite Solar Cells, J. Phys. Chem. Lett., 7, 3467–3471 (DOI: 10.1021/acs.jpclett.6b01452).
51. Ghosh B., Wu B., Mulmudi H. K., Guet C., Weber K., Sum T. C., Mhaisalkar S., Mathews N. (2018) Limitations of Cs3Bi2I9 as Lead-Free Photovoltaic Absorber Materials. ACS Appl. Mater. Interfaces, 10, 35000–35007 (DOI: 10.1021/acsami.7b14735).
52. Öz S., Hebig J.-C., Jung E., Singh T., Lepcha A., Olthof S., Jan F., Gao Y., German R., van Loosdrecht P. H. M., Meerholz K., Kirchartz T., Mathur S. (2016), Zero-dimensional (CH3NH3)3Bi2I9 perovskite for optoelectronic applications, Solar Energy Materials and Solar Cells, 158, 195–201 (DOI: 10.1016/j.solmat.2016.01.035).
53. Greul E., Petrus M. L., Binek A., Docampo P., Bein T. (2017), Highly stable, phase pure Cs2AgBiBr6 double perovskite thin films for optoelectronic applications, J. Mater. Chem. A, 5, 19972–19981 (DOI: 10.1039/C7TA06816F).
54. Ahmad K., Ansari S. N., Natarajan K.. Mobin S. M. (2019), A (CH3NH3)3Bi2I9 Perovskite Based on a Two-Step Deposition Method: Lead-Free, Highly Stable, and with Enhanced Photovoltaic Performance, ChemElectroChem, 6, 1192–1198 (DOI: 10.1002/celc.201801322).
55. Deng J., Yang L., Zhang X., Wei K., Du G., Zhu G., Zhang J. (2022), Synergistic effects of morphological control and enhanced charge collection enable efficient and stable lead-free CsBi3I10 thin film solar cells, J. Mater. Chem. A, 10, 9384–9392 (DOI: 10.1039/D1TA10808E).

56. Jain S. M., Phuyal D., Davies M. L., Li M., Philippe B., De Castro C., Qiu Z., Kim J., Watson T., Tsoi W. C., Karis O., Rensmo H., Boschloo G., Edvinsson T., Durrant J. R. (2018), An effective approach of vapour assisted morphological tailoring for reducing metal defect sites in lead-free, (CH3NH3)3Bi2I9 bismuth-based perovskite solar cells for improved performance and long-term stability, Nano Energy, 49, 614–624 (DOI: 10.1016/j.nanoen.2018.05.003).
57. Li Z., Klein T. R., Kim D. H., Yang M., Berry J. J., van Hest M. F. A. M., Zhu, K. (2018), Scalable fabrication of perovskite solar cells, Nat Rev Mater, 3, 1–20 (DOI: 10.1038/natrevmats.2018.17).
58. Zhang Z., Li X., Xia X., Wang Z., Huang Z., Lei B., Gao Y. (2017), High-Quality (CH3NH3)3Bi2I9 Film-Based Solar Cells: Pushing Efficiency up to 1.64%, J. Phys. Chem. Lett., 8, 4300–4307 (DOI: 10.1021/acs.jpclett.7b01952).
59. Wang M., Zeng P., Bai S., Gu J., Li F., Yang Z., Liu M. (2018), High-Quality Sequential-Vapor-Deposited Cs2AgBiBr6 Thin Films for Lead-Free Perovskite Solar Cells, Solar RRL, 2, 1800217 (DOI: 10.1002/solr.201800217).
60. Lan H., Chen X., Fan P., Liang G. (2021), Inorganic and lead-free CsBi3I10 thin-film solar cell prepared by single-source thermal evaporation, J Mater Sci: Mater Electron, 32, 11183–11192 (DOI: 10.1007/s10854-021-05783-z).
61. Adnan M., Lee J. K. (2020), Highly efficient planar heterojunction perovskite solar cells with sequentially dip-coated deposited perovskite layers from a non-halide aqueous lead precursor. RSC Adv., 10, 5454–5461 (DOI: 10.1039/C9RA09607H).
62. Irshad Z., Adnan M., Lee J. K. (2022), Controlling phase and morphology of all-dip-coating processed HC(NH2)2PbI3 perovskite layers from an aqueous halide-free lead precursor, J. Phy. Chem. of Solids, 160, 110374 (DOI: 10.1016/j.jpcs.2021.110374).

63. Irshad Z., Adnan M., Lee J. K. (2022), Simple preparation of highly efficient MAxFA1−xPbI3 perovskite films from an aqueous halide-free lead precursor by all dip-coating approach and application in high-performance perovskite solar cells, J Mater Sci, 57, 1936–1946 (DOI: 10.1007/s10853-022-06867-9).
64. Xiu J., Shao Y., Chen L., Feng Y., Dai J., Zhang X., Lin Y., Zhu Y., Wu Z., Zheng Y., Pan H., Liu C., Shi X., Cheng X., He Z. (2019), Defining the composition and electronic structure of large-scale and single-crystalline like Cs2AgBiBr6 films fabricated by capillary-assisted dip-coating method, Materials Today Energy, 12, 186–197 (DOI: 10.1016/j.mtener.2019.01.010).
65. Cui Y., Yang L., Wu X., Deng J., Zhang X., Zhang J. (2022), Recent progress of lead-free bismuth-based perovskite materials for solar cell applications, J. Mater. Chem. C, 10, 16629–16656 (DOI: 10.1039/D2TC02643K).
66. Bhattarai S., Mhamdi A., Hossain I., Raoui Y., Pandey R., Madan J., Bouazizi A., Maiti M., Gogoi D., Sharma A. (2022), A detailed review of perovskite solar cells: Introduction, working principle, modelling, fabrication techniques, future challenges, Micro and Nanostructures, 172, 207450 (DOI: 10.1016/j.micrna.2022.207450).
67. Wu W.-Q., Chen D., Caruso R. A., Cheng Y.-B. (2017), Recent progress in hybrid perovskite solar cells based on n-type materials. J. Mater. Chem., A 5, 10092–10109 (DOI: 10.1039/C7TA02376F).
68. Zhang X., Wu G., Gu Z., Guo B., Liu W., Yang S., Ye T., Chen, C., Tu W., Chen, H. (2016), Active-layer evolution and efficiency improvement of (CH3NH33Bi2I9-based solar cell on TiO2-deposited ITO substrate. Nano Res., 9, 2921–2930 (DOI: 10.1007/s12274-016-1177-8).
69. Guo X., Dong H., Li W., Li N., Wang L. (2015), Multifunctional MgO Layer in Perovskite Solar Cells. ChemPhysChem, 16, 1727–1732 (DOI: 10.1002/cphc.201500163).

70. Singh T., Kulkarni A., Ikegami M., Miyasaka T. (2016), Effect of Electron Transporting Layer on Bismuth-Based Lead-Free Perovskite (CH3NH3)3 Bi2I9 for Photovoltaic Applications, ACS Appl. Mater. Interfaces, 8, 14542–14547 (DOI: 10.1021/acsami.6b02843).
71. Chen M., Wan L., Kong M., Hu H., Gan Y., Wang J., Chen F., Guo Z., Eder D., Wang S. (2018), Influence of Rutile-TiO2 nanorod arrays on Pb-free (CH3NH3)3Bi2I9-based hybrid perovskite solar cells fabricated through two-step sequential solution process, Journal of Alloys and Compounds, 738, 422–431 (DOI: 10.1016/j.jallcom.2017.12.188).
72. Zhang Z., Sun Q., Lu Y., Lu F., Mu X., Wei S.-H., Sui M. (2022), Hydrogenated Cs2AgBiBr6 for significantly improved efficiency of lead-free inorganic double perovskite solar cell, Nat Commun, 13, 3397 (DOI: 10.1038/s41467-022-31016-w).
73. Zhang Z., Wu C., Wang D., Liu G., Zhang Q., Luo W., Qi X., Guo X., Zhang Y., Lao Y., Qu B., Xiao L., Chen Z. (2019), Improvement of Cs2AgBiBr6 double perovskite solar cell by rubidium doping, Organic Electronics, 74, 204–210 (DOI: 10.1016/j.orgel.2019.06.037).
74. Jia Q., Li C., Tian W., Johansson M. B., Johansson E. M. J., Yang R. (2020), Large-Grained All-Inorganic Bismuth-Based Perovskites with Narrow Band Gap via Lewis Acid–Base Adduct Approach, ACS Appl. Mater. Interfaces, 12, 43876–43884 (DOI: 10.1021/acsami.0c14512).
75. Yu B.-B., Liao M., Yang J., Chen W., Zhu Y., Zhang X., Duan T., Yao W., Wei S.-H., He Z. (2019), Alloy-induced phase transition and enhanced photovoltaic performance: the case of Cs3Bi2I9−xBrx perovskite solar cells, J. Mater. Chem. A, 7, 8818–8825 (DOI: 10.1039/C9TA01978B).
76. Anrango-Camacho C., Pavón-Ipiales K., Frontana-Uribe B. A., Palma-Cando A. (2022), Recent Advances in Hole-Transporting Layers for Organic Solar Cells, Nanomaterials, 12, 443 (DOI: 10.3390/nano12030443).

77. Tonui P., Oseni S. O., Sharma G., Yan Q., Tessema Mola G. (2018), Perovskites photovoltaic solar cells: An overview of current status, Renewable and Sustainable Energy Reviews, 91, 1025–1044 (DOI: 10.1016/j.rser.2018.04.069).
78. Po R., Carbonera C., Bernardi A., Camaioni N. (2011), The role of buffer layers in polymer solar cells, Energy Environ. Sci., 4, 285–310 (DOI: 10.1039/C0EE00273A).
79. Shin S. S., Correa Baena J. P., Kurchin R. C., Polizzotti A., Yoo J. J., Wieghold S., Bawendi M. G., Buonassisi T. (2018), Solvent-Engineering Method to Deposit Compact Bismuth-Based Thin Films: Mechanism and Application to Photovoltaics, Chem. Mater., 30, 336–343 (DOI: 10.1021/acs.chemmater.7b03227).
80. Zhu H., Johansson M. B., Johansson E. M. J. (2018), The Effect of Dopant-Free Hole-Transport Polymers on Charge Generation and Recombination in Cesium–Bismuth–Iodide Solar Cells, ChemSusChem, 11, 1114–1120 (DOI: 10.1002/cssc.201702169).
81. Bai F., Hu Y., Hu Y., Qiu T., Miao X., Zhang S. (2018), Lead-free, air-stable ultrathin Cs3Bi2I9 perovskite nanosheets for solar cells, Solar Energy Materials and Solar Cells, 184, 15–21 (DOI: 10.1016/j.solmat.2018.04.032).
82. Waykar R., Bhorde A., Nair S., Pandharkar S., Gabhale B., Aher R., Rondiya S., Waghmare A., Doiphode V., Punde A., Vairale P., Prasad M., Jadkar S. (2020), Environmentally stable lead-free cesium bismuth iodide (Cs3Bi2I9) perovskite: Synthesis to solar cell application, Journal of Physics and Chemistry of Solids, 146, 109608 (DOI: 10.1016/j.jpcs.2020.109608).
83. Pantaler M., Cho K. T., Queloz V. I. E., García Benito I., Fettkenhauer C., Anusca I., Nazeeruddin M. K., Lupascu D. C., Grancini G. (2018), Hysteresis-Free Lead-Free Double-Perovskite Solar Cells by Interface Engineering, ACS Energy Lett., 3, 1781–1786 (DOI: 10.1021/acsenergylett.8b00871).
84. Wang S., Sina M., Parikh P., Uekert T., Shahbazian B., Devaraj A., Meng Y. S. (2016), Role of 4-tert-Butylpyridine as a Hole

Transport Layer Morphological Controller in Perovskite Solar Cells, Nano Lett., 16, 5594–5600 (DOI: 10.1021/acs.nanolett.6b02158).

85. Li W., Dong H., Wang L., Li N., Guo X., Li J., Qiu Y. (2014), Montmorillonite as bifunctional buffer layer material for hybrid perovskite solar cells with protection from corrosion and retarding recombination, J. Mater. Chem. A, 2, 13587–13592 (DOI: 10.1039/C4TA01550A).
86. Yue Y., Salim N., Wu Y., Yang X., Islam A., Chen W., Liu J., Bi, E., Xie F., Cai M., Han L. (2016), Enhanced Stability of Perovskite Solar Cells through Corrosion-Free Pyridine Derivatives in Hole-Transporting Materials, Advanced Materials, 28, 10738–10743 (DOI: 10.1002/adma.201602822).
87. Verlinden P. J., Swanson R. M., Crane R. A. (1994), 7000 high-eficiency cells for a dream, Progress in Photovoltaics: Research and Applications, 2, 143–152 (DOI: 10.1002/pip.4670020209).
88. Babayigit A., Ethirajan A., Muller M., Conings B. (2016), Toxicity of organometal halide perovskite solar cells, Nature Mater, 15, 247–251 (DOI: 10.1038/nmat4572).
89. Hoefler S. F., Trimmel G., Rath T. (2017), Progress on lead-free metal halide perovskites for photovoltaic applications: a review, Monatsh Chem, 148, 795–826 (DOI: 10.1007/s00706-017-1933-9).
90. Stoumpos C. C., Malliakas C. D., Kanatzidis M. G. (2013), Semiconducting Tin and Lead Iodide Perovskites with Organic Cations: Phase Transitions, High Mobilities, and Near-Infrared Photoluminescent Properties, Inorg. Chem., 52, 9019–9038 (DOI: 10.1021/ic401215x).
91. Manser J. S., Christians J. A., Kamat P. V. (2016), Intriguing Optoelectronic Properties of Metal Halide Perovskites, Chem. Rev., 116, 12956–13008 (DOI: 10.1021/acs.chemrev.6b00136).
92. Chen Z., Wang J. J., Ren Y., Yu C., Shum K. (2012), Schottky solar cells based on CsSnI3 thin-films, Applied Physics Letters, 101, 093901 (DOI: 10.1063/1.4748888).

93. Hao F., Stoumpos C. C., Cao D. H., Chang R. P. H., Kanatzidis M. G. (2014), Lead-free solid-state organic–inorganic halide perovskite solar cells, Nature Photonics, 8, 489–494 (DOI: 10.1038/nphoton.2014.82).
94. Konstantakou M., Stergiopoulos T. (2017), A critical review on tin halide perovskite solar cells, J. Mater. Chem. A, 5, 11518–11549 (DOI: 10.1039/C7TA00929A).
95. Hao F., Stoumpos C. C., Guo P., Zhou N., Marks T. J., Chang R. P. H., Kanatzidis M. G. (2015), Solvent-Mediated Crystallization of CH3NH3SnI3 Films for Heterojunction Depleted Perovskite Solar Cells, J. Am. Chem. Soc., 137, 11445–11452 (DOI: 10.1021/jacs.5b06658).
96. Jung M.-C., Raga S. R., Qi Y. (2016), Properties and solar cell applications of Pb-free perovskite films formed by vapor deposition, RSC Adv., 6, 2819–2825 (DOI: 10.1039/C5RA21291J).
97. Weiss M., Horn J., Richter C., Schlettwein D. (2016), Preparation and characterization of methylammonium tin iodide layers as photovoltaic absorbers, physica status solidi (a), 213, 975–981 (DOI: 10.1002/pssa.201532594).
98. Zhu Z., Li N., Zhao D., Wang L., Jen A. K.-Y. (2019), Improved Efficiency and Stability of Pb/Sn Binary Perovskite Solar Cells Fabricated by Galvanic Displacement Reaction, Advanced Energy Materials, 9, 1802774 (DOI: 10.1002/aenm.201802774).
99. Liao Y., Liu H., Zhou W., Yang D., Shang Y., Shi Z., Li B., Jiang X., Zhang L., Quan L. N., Quintero-Bermudez R., Sutherland B. R., Mi Q., Sargent E. H., Ning Z. (2017), Highly Oriented Low-Dimensional Tin Halide Perovskites with Enhanced Stability and Photovoltaic Performance, J. Am. Chem. Soc., 139, 6693–6699 (DOI: 10.1021/jacs.7b01815).
100. Marshall K. P., Walton R. I., Hatton R. A. (2015), Tin perovskite/fullerene planar layer photovoltaics: improving the efficiency and stability of lead-free devices. J. Mater. Chem. A, 3, 11631–11640 (DOI: 10.1039/C5TA02950C).

101. Wang N., Zhou Y., Ju M.-G., Garces H. F., Ding T., Pang S., Zeng X. C., Padture N. P., Sun X. W. (2016), Heterojunction-Depleted Lead-Free Perovskite Solar Cells with Coarse-Grained B-γ-CsSnI3 Thin Films, Adv. Energy Mater., 6, 1601130 (DOI: 10.1002/aenm.201601130).

102. Krishnamoorthy T., Ding H., Yan C., Leong W. L., Baikie T., Zhang Z., Sherburne M., Li S., Asta M., Mathews N., Mhaisalkar S. G. (2015), Lead-free germanium iodide perovskite materials for photovoltaic applications, J. Mater. Chem. A, 3, 23829–23832 (DOI: 10.1039/C5TA05741H).

103. Tang L.-C., Chang Y.-C., Huang J.-Y., Lee M.-H., Chang C.-S. (2009), First Principles Calculations of Linear and Second-Order Optical Responses in Rhombohedrally Distorted Perovskite Ternary Halides, CsGeX3 (X = Cl, Br, and I), Jpn. J. Appl. Phys., 48, 112402 (DOI: 10.1143/JJAP.48.112402).

104. Stoumpos C. C., Frazer L., Clark D. J., Kim Y. S., Rhim S. H., Freeman A. J., Ketterson J. B., Jang J. I., Kanatzidis M. G. (2015), Hybrid Germanium Iodide Perovskite Semiconductors: Active Lone Pairs, Structural Distortions, Direct and Indirect Energy Gaps, and Strong Nonlinear Optical Properties, J. Am. Chem. Soc., 137, 6804–6819 (DOI: 10.1021/jacs.5b01025).

105. Sundar S., Chakravarty, J. (2010), Antimony Toxicity, Int. J. Environ. Res. Public Health ,7, 4267–4277 (DOI: 10.3390/ijerph7124267).

106. Jena A. K., Kulkarni A., Miyasaka T. (2019), Halide Perovskite Photovoltaics: Background, Status, and Future Prospects, Chem. Rev., 119, 3036–3103 (DOI: 10.1021/acs.chemrev.8b00539).

107. Hu H., Dong B., Zhang W. (2017), Low-toxic metal halide perovskites: opportunities and future challenges, J. Mater. Chem. A, 5, 11436–11449 (DOI: 10.1039/C7TA00269F).

108. Ahmad K., Kumar P., Mobin S. M. (2020), A Two-Step Modified Sequential Deposition Method-based Pb-Free (CH3NH3)3Sb2I9 Perovskite with Improved Open Circuit

Voltage and Performance, ChemElectroChem, 7, 946–950 (DOI: 10.1002/celc.201902107).

109. Bagautdinov B. Sh., Novikova M. S., Aleksandrova I. P., Blomberg M. K., Chapuis G. (1999), X-ray study of phase transitions in Cs3Sb2I9 crystal, Solid State Communications, 111, 361–366 (DOI: 10.1016/S0038-1098(99)00217-3).

110. Jakubas R., Decressain R., Lefebvre J. (1992), NMR and dilatometric studies of the structural phase transitions of (CH3NH3)3Sb2I9 and (CH3NH3)3Bi2I9 crystals, Journal of Physics and Chemistry of Solids, 53, 755–759 (DOI: 10.1016/0022-3697(92)90185-G).

111. Saparov B., Hong F., Sun J.-P., Duan H.-S., Meng W., Cameron S., Hill I. G., Yan Y., Mitzi D. B. (2015), Thin-Film Preparation and Characterization of Cs3Sb2I9: A Lead-Free Layered Perovskite Semiconductor, Chem. Mater., 27, 5622–5632 (DOI: 10.1021/acs.chemmater.5b01989).

112. Hebig J.-C., Kühn I., Flohre J., Kirchartz T. (2016), Optoelectronic Properties of (CH3NH3)3Sb2I9 Thin Films for Photovoltaic Applications, ACS Energy Lett., 1, 309–314 (DOI: 10.1021/acsenergylett.6b00170).

113. Zuo C., Ding L. (2017), Lead-free Perovskite Materials (NH4)3Sb2IxBr9−x, Angewandte Chemie, 129, 6628–6632 (DOI: 10.1002/ange.201702265).

114. Umar F., Zhang J., Jin Z., Muhammad I., Yang X., Deng H., Jahangeer K., Hu Q., Song H., Tang J. (2019), Dimensionality Controlling of Cs3Sb2I9 for Efficient All-Inorganic Planar Thin Film Solar Cells by HCl-Assisted Solution Method, Advanced Optical Materials, 7, 1801368 (DOI: 10.1002/adom.201801368).

115. Boopathi K. M., Karuppuswamy P., Singh A., Hanmandlu C., Lin L., Abbas S. A., Chang C. C., Wang P. C., Li, G., Chu C. W. (2017), Solution-processable antimony-based light-absorbing materials beyond lead halide perovskites, J. Mater. Chem. A, 5, 20843–20850 (DOI: 10.1039/C7TA06679A).

116. Wei F., Deng Z., Sun S., Zhang F., Evans D. M., Kieslich G., Tominaka S., Carpenter M. A., Zhang J., Bristowe P. D., Cheetham A. K. (2017), Synthesis and Properties of a Lead-Free Hybrid Double Perovskite: (CH3NH3)2AgBiBr6, Chem. Mater., 29, 1089–1094 (DOI: 10.1021/acs.chemmater.6b03944).

117. Vargas B., Ramos E., Pérez-Gutiérrez E., Alonso J. C., Solis-Ibarra D. (2017), A Direct Bandgap Copper–Antimony Halide Perovskite, J. Am. Chem. Soc., 139, 9116–9119 (DOI: 10.1021/jacs.7b04119).

118. Borbinha C., Serrazina F., Salavisa M., Viana-Baptista M. (2019), Bismuth encephalopathy- a rare complication of long-standing use of bismuth subsalicylate. BMC Neurol 19, 212 (DOI: 10.1186/s12883-019-1437-9).

119. Rodilla V., Miles A. T., Jenner W., Hawksworth G. M. (1998), Exposure of cultured human proximal tubular cells to cadmium, mercury, zinc and bismuth: toxicity and metallothionein induction, Chemico-Biological Interactions, 115, 71–83 (DOI: 10.1016/S0009-2797(98)00059-3).

120. Jin Z., Zhang Z., Xiu J., Song H., Gatti T., He Z. (2020), A critical review on bismuth and antimony halide based perovskites and their derivatives for photovoltaic applications: recent advances and challenges, J. Mater. Chem. A, 8, 16166–16188 (DOI: 10.1039/D0TA05433J).

121. Lyu M., Yun J.-H., Chen P., Hao M., Wang L. (2017), Addressing Toxicity of Lead: Progress and Applications of Low-Toxic Metal Halide Perovskites and Their Derivatives, Advanced Energy Materials, 7, 1602512 (DOI: 10.1002/aenm.201602512).

122. Park B.-W., Philippe B., Zhang X., Rensmo H., Boschloo G., Johansson E. M. J. (2015), Bismuth Based Hybrid Perovskites A3Bi2I9 (A: Methylammonium or Cesium) for Solar Cell Application, Advanced Materials, 27, 6806–6813 (DOI: 10.1002/adma.201501978).

123. Hoye R. L. Z., Brandt R. E., Osherov A., Stevanović V., Stranks S. D., Wilson M. W. B., Kim H., Akey A. J., Perkins J.

D., Kurchin R. C., Poindexter J. R., Wang E. N., Bawendi M. G., Bulović, V., Buonassisi T. (2016), Methylammonium Bismuth Iodide as a Lead-Free, Stable Hybrid Organic–Inorganic Solar Absorber, Chemistry – A European Journal, 22, 2605–2610 (DOI: 10.1002/chem.201505055).

124. Hoefler S. F., Rath T., Fischer R., Latal C., Hippler D., Koliogiorgos A., Galanakis I., Bruno A., Fian A., Dimopoulos T., Trimmel G. (2018), A Zero-Dimensional Mixed-Anion Hybrid Halogenobismuthate(III) Semiconductor: Structural, Optical, and Photovoltaic Properties, Inorg. Chem., 57, 10576–10586 (DOI: 10.1021/acs.inorgchem.8b01161).

125. Popoola I. K., Gondal M. A., Popoola A., Oloore L. E. (2022), Bismuth-based organometallic-halide perovskite photo-supercapacitor utilizing novel polymer gel electrolyte for hybrid energy harvesting and storage applications, Journal of Energy Storage, 53, 105167 (DOI: 10.1016/j.est.2022.105167).

126. Eckhardt K., Bon V., Getzschmann J., Grothe J., Wisser F. M., Kaskel S. (2016), Crystallographic insights into (CH3NH3)3(Bi2I9): a new lead-free hybrid organic–inorganic material as a potential absorber for photovoltaics, Chem. Commun., 52, 3058–3060 (DOI: 10.1039/C5CC10455F).

127. Lehner A. J., Fabini D. H., Evans H. A., Hébert C.-A., Smoc, S. R., Hu J., Wang H., Zwanziger J. W., Chabinyc M. L., Seshadri R. (2015), Crystal and Electronic Structures of Complex Bismuth Iodides A3Bi2I9 (A = K, Rb, Cs) Related to Perovskite: Aiding the Rational Design of Photovoltaics, Chem. Mater., 27, 7137–7148 (DOI: 10.1021/acs.chemmater.5b03147).

128. Igbari F., Wang R., Wang Z.-K., Ma X.-J., Wang Q., Wang K.-L., Zhang Y., Liao L.-S., Yang Y. (2019), Composition Stoichiometry of Cs2AgBiBr6 Films for Highly Efficient Lead-Free Perovskite Solar Cells, Nano Lett., 19, 2066–2073 (DOI: 10.1021/acs.nanolett.9b00238).

129. Hu W., He X., Fang Z., Lian W., Shang Y., Li X., Zhou W., Zhang M., Chen T., Lu Y., Zhang L., Ding L., Yang S. (2020),

Bulk heterojunction gifts bismuth-based lead-free perovskite solar cells with record efficiency, Nano Energy, 68, 104362 (DOI: 10.1016/j.nanoen.2019.104362).

130. Sebastia-Luna P., Gélvez-Rueda M. C., Dreessen C., Sessolo M., Grozema F. C., Palazon F., Bolink H. J. (2020), Potential and limitations of CsBi3I10 as a photovoltaic material, J. Mater. Chem. A, 8, 15670–15674 (DOI: 10.1039/D0TA02237C).

131. Cong W.-Y., Guan C., Lu Y.-B., Zhang P., Xue S., Wu Q. (2021), Investigations of modulation effect of co-metal ions on the optical properties of the hybrid double perovskites (MA)2AgBi1−xSbxBr6, J. Phys.: Condens. Matter, 33, 495501 (DOI: 10.1088/1361-648X/ac25ac).

132. Luo T., Wei J. (2020), First principles study of electronic and optical properties of inorganic and lead-free perovskite: Cs3Bi2X9 (X: Cl, Br, I), Materials Chemistry and Physics, 253, 123374 (DOI: 10.1016/j.matchemphys.2020.123374).

133. Slavney A. H., Hu T., Lindenberg A. M., Karunadasa H. I. (2016), A Bismuth-Halide Double Perovskite with Long Carrier Recombination Lifetime for Photovoltaic Applications, J. Am. Chem. Soc., 138, 2138–2141 (DOI: 10.1021/jacs.5b13294).

134. Zhao X.-G., Yang J.-H., Fu Y., Yang D., Xu Q., Yu L., Wei S.-H., Zhang L. (2017), Design of Lead-Free Inorganic Halide Perovskites for Solar Cells via Cation-Transmutation, J. Am. Chem. Soc., 139, 2630–2638 (DOI: 10.1021/jacs.6b09645).

135. Zhang C., Gao L., Teo S., Guo Z., Xu Z., Zhao S., Ma T. (2018), Design of a novel and highly stable lead-free Cs2NaBiI6 double perovskite for photovoltaic application, Sustainable Energy Fuels, 2, 2419–2428 (DOI: 10.1039/C8SE00154E).

136. Sansom H. C., Longo G., Wright A. D., Buizza L. R. V., Mahesh S., Wenger B., Zanella M., Abdi-Jalebi M., Pitcher M. J., Dyer M. S., Manning T. D., Friend R. H., Herz L. M., Snaith H. J., Claridge J. B., Rosseinsky M. J. (2021), Highly Absorbing

Lead-Free Semiconductor Cu2AgBiI6 for Photovoltaic Applications from the Quaternary CuI–AgI–BiI3 Phase Space, J. Am. Chem. Soc., 143, 3983–3992 (DOI: 10.1021/jacs.1c00495).

137. Peedikakkandy L., Chatterjee S., Pal A. J. (2020), Bandgap Engineering and Efficient Conversion of a Ternary Perovskite (Cs3Bi2I9) to a Double Perovskite (Cs2NaBiI6) with the Aid of Alkali Metal Sulfide, J. Phys. Chem. C, 124, 10878–10886 (DOI: 10.1021/acs.jpcc.0c02786).

138. Asakura K., Satoh H., Chiba M., Okamoto M., Serizawa K., Nakano M., Omae K. (2009), Genotoxicity Studies of Heavy Metals: Lead, Bismuth, Indium, Silver and Antimony, Journal of Occupational Health, 51, 498–512 (DOI: 10.1539/joh.L9080).

139. Chen M., Ju M.-G., Carl A. D., Zong Y., Grimm R. L., Gu J., Zeng X. C., Zhou Y., Padture N. P. (2018), Cesium Titanium(IV) Bromide Thin Films Based Stable Lead-free Perovskite Solar Cells, Joule, 2, 558–570 (DOI: 10.1016/j.joule.2018.01.009).

140. Zhou J., Xia Z., Molokeev M. S., Zhang X., Peng D. , Liu Q. (2017), Composition design, optical gap and stability investigations of lead-free halide double perovskite Cs2AgInCl6. J. Mater. Chem. A, 5, 15031–15037 (DOI: 10.1039/C7TA04690A).

141. McClure E. T., Ball M. R., Windl W., Woodward P. M. (2016), Cs_2AgBiX_6 (X = Br, Cl): New Visible Light Absorbing, Lead-Free Halide Perovskite Semiconductors, Chem. Mater., 28, 1348–1354 (DOI: 10.1021/acs.chemmater.5b04231).

CHAPTER 2

Two-Step Deposition Approach for Lead Free $(NH_4)_3Sb_2I_9$ Perovskite Solar Cells with Enhanced Open Circuit Voltage and Performance

2.1. Introduction

Production of green energy units including hydrogen [1-6], batteries [7-11], supercapacitors [12-14] and solar cells [15] by low-cost methods is of great importance. Solar energy harvesting using perovskite or perovskite-like materials is trending due to cost-effective and simple fabrication techniques [15-29]. Perovskite materials have been mostly used in the study of energy storage and energy conversion applications [18-46]. Previously, different kinds of solar cells were developed but $MAPbX_3$ (MA= $CH_3NH_3^+$, and X= Br^- or I^-) based PSCs have achieved a highest PCE of more than 25% [17]. Although, $MAPbX_3$ based PSCs achieved excellent PCE but the presence of toxic Pb restrict its commercialization [22]. Thus, it will be of great importance to find out the other non-toxic or less-toxic perovskite and perovskite-like material for the construction of Pb free PSCs. In this regard, $CH_3NH_3SnI_3$ perovskite structure was introduced as light absorber for the development of Pb free PSCs which showed the PCE of 6.3% [23]. Further, strategies improved the PCE to 7.13% as claimed by Li *et al*. [24]. The band gap implementation and engineering was also introduced by Hao *et al*. [25] to develop the new perovskite material ($CH_3NH_3SnIBr_2$) for Pb free PSCs. The obtained PCE for $CH_3NH_3SnIBr_2$ based PSCs was reported as 5.73%. Gupta *et al*. [26] obtained an PCE of 2.1% by tuning the halide composition. In further investigations, Kumar *et al*. [27], Song *et al*. [28] and another research group of Heo *et al*. [29] tuned the cationic composition e.g. replaced the $CH_3NH_3^+$ cation part with Cs^+ ion and finally achieved the PCE of 2.02%, 3.83%, and 4.3%, respectively. Sn (II) can be rapidly oxidized to Sn (IV) in air which abandon the limitations of its application in PSCs. Therefore, it is a challenge for the scientific community to find out the air stable perovskite or perovskite material.

Bismuth (Bi) and antimony (Sb) exhibit promising characteristics, including air stability and reduced toxicity, making them potential candidates to replace lead (Pb). The perovskite-like materials with general formula of $A_3B_2X_9$ (A= Cs, CH_3NH_3, NH_3; B= Bi^{3+} or Sb^{3+}, X= Cl^-, Br^-, I^-) can be utilized in photovoltaic applications [30, 31]. Previously, some reported perovskite-like materials such as $(CH_3NH_3)_3Sb_2I_9$, $Cs_3Bi_2I_9$, $Cs_3Sb_2I_9$, $(CH_3NH_3)_3Bi_2I_9$ and $(NH_4)_3Sb_2I_9$ have been introduced as light absorbers for the fabrication of stable Pb free PSCs [30-32]. The reported literature reveals that the morphological features of the perovskite film influence the photovoltaic performance [32]. Thus, it is necessary to introduce and utilize the novel strategies to obtain the high-quality films of perovskite materials. In this context, Henawey *et al*. [33] and Ahmad *et al*. [22] employed two step approaches to prepare the high quality thin films of the perovskite light absorbers to further enhance the photovoltaic performance of the PSCs. An interesting work have been reported by Henawey *et al*. [33] and Ahmad *et al*. [22] indicating that perovskite films exhibited smooth and uniform surfaces, leading to an enhanced Voc. The authors stated that enhancement in photovoltaic performance especially improved Voc which may be due to the presence of smooth and high-quality thin films with large grain sizes of perovskite light absorber layer obtained by two-step deposition approach.

Herein, we have utilized ammonium antimony halide ($(NH_4)_3Sb_2I_9$) perovskite-like material as light absorber and employed two different approaches for the preparation of $(NH_4)_3Sb_2I_9$ perovskite-like material. For two step approach, we have dissolved ammonium iodide (NH_4I; 3 M) and antimony iodide (SbI_3; 2M) in a mixture of gamma-butyrolactone (GBL) + dimethyl sulphoxide (DMSO) and stirred at 70 ^oC overnight. The weight ratio of the GBL and DMSO was 50:50 (2 mL).

2.2. Experimental section

2.2.1. Materials

All the chemicals, reagents and solvents were purchased from SRL, Sigma Aldrich, Merck, Alfa Aesar and Solaronix (India) and used as

received. FTO glass substrates were purchased from Sigma Aldrich (India).

2.2.2. Characterization methods

The X-ray diffraction patterns (XRD) patterns of the prepared films were analyzed by Rigaku, Japan (RINT 2500 V) x-ray diffractometer (Cu Kα irradiation (λ = 1.5406 Å). Optical absorption spectra were recorded on Varian UV–*vis* spectrophotometer (model: Carry 100). The surface morphology of the $(NH_4)_3Sb_2I_9$ thin films were checked on Supra 55 Zeiss Field Emission Scanning Electron microscope (FE-SEM). Cyclic voltammetry and Impedance spectroscopy measurements were performed on Metrohm Autolab (PGSTAT 204N) using NOVA software version 1.10. The photocurrent-voltage (*J-V*) analysis were performed on Photo Emission Tech. Instrument (solar simulator) under the AM 1.5 G condition of 100 mW/cm^2 illumination.

2.2.3. Device fabrication

2.2.3.1. Preparation of electrode

The fluorine doped tin oxide (FTO) glass substrate was etched using zinc powder and HCl (2 M) which was further washed with detergent and subsequently cleaned with acetone, 2-propanol, deionized water using ultrasonicator. The compact TiO_2 layer (CL) was deposited by spin coating of titanium diisopropoxide bis(acetylacetonate) solution (diluted in ethanol) and annealed at 500°C for 30min. The mesoporous layer (m-TiO_2) for electron transport (18NRT;Dyesol; diluted in ethanol (2:7 weight ratio)) was also spin coated onto the blocking layer (BL-TiO_2) at 4000 rpm for 30 sec and annealed at 500°C for 30 min.

2.2.3.2. Preparation of $(NH_4)_3Sb_2I_9$ films

The $(NH_4)_3Sb_2I_9$ thin films were prepared by two different approaches (one-step and two-step sequential deposition). For one-step approach, 35 wt% ratio of NH_4I and SbI_3 were mixed in 2 mL GBL+DMSO solution and a thin film of $(NH_4)_3Sb_2I_9$ was spin coated on the prepared electrode (FTO/CL-TiO_2/m-TiO_2) at an applied spin speed of 3000 rpm for 30 sec and annealed at 70 °C for 30 min.

For two-step deposition approach, 35wt% ratio of NH_4I and SbI_3 were mixed in 2 mL GBL+DMSO solution and a thin film of $(NH_4)_3Sb_2I_9$ was

spin coated on the prepared electrode (FTO/CL-TiO_2/m-TiO_2) at an applied spin speed of 3000 rpm for 30 sec. Further, the toluene drop was spin coated on the last few second of spin coating process and annealed at 70°C for 30 min. The hole transport layer (HTL) of spiro-MeOTAD dissolved in chlorobenzene; 30 mg/mL with additives bis(trifiuoromethane) sulfonimide lithium salt (LiTFSI; 99.95%), 4-tert-butylpyridine was spin coated and subsequently gold (Au) layer was deposited using thermal evaporation. This step of HTL and Au layer was same for both the devices.

2.2.4. Cyclic voltammetry of $(NH_4)_3Sb_2I_9$

The electrochemical approach was used to calculate the HOMO-LUMO of the $(NH_4)_3Sb_2I_9$. The cyclic voltammetry (CV) was recorded at an applied scan rate of 20 mV/s. The working electrode (glassy carbon electrode) was used to determine the potential of ferrocene/ferrocenium (Fc/Fc^+), using Ag/AgCl as reference electrode whereas Pt electrode acted as counter electrode. The prepared $(NH_4)_3Sb_2I_9$ film on FTO glass substrate was dissolved in tetrabutylammonium hexafuorophosphate ($TBAPF_6$; conc.=0.1 M) in acetonitrile having ferrocene (conc.=0.001 M).

2.2.5. Photoluminescence (PL) measurements

The photoluminescence measurements were carried out with a home-made PL system (Lum Y Pro). Samples were then excited with a laser light at 532 nm emission wavelength. Non-absorbed laser light and emitted photoluminescence fluxes were subsequently detected by the spectrometer of the QuantY Pro LumY Pro, which in combination with the integrating sphere is calibrated to absolute photon numbers.

2.3 Results and discussion

The $(NH_4)_3Sb_2I_9$ thin film was prepared on to the patterned FTO substrate using spin coating process (speed=3000 rpm; time 30 sec) and a toluene drop was also spin coated on to the prepared $(NH_4)_3Sb_2I_9$ thin film and annealed at 70 °C for 30 min. In case of one step process, similar strategies were applied except addition of toluene. The fabrication of the

$(NH_4)_3Sb_2I_9$ thin films by one and two step approaches has been illustrated in Scheme 2.1.

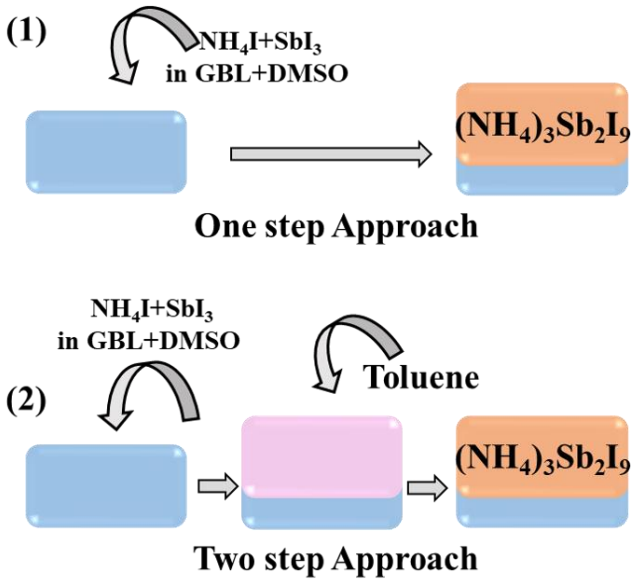

Scheme 2.1. Schematic representation of the fabrication of $(NH_4)_3Sb_2I_9$ perovskite film using one step (1) and two-step (2) deposition approaches.

The powder X-ray diffraction (PXRD) patterns of the $(NH_4)_3Sb_2I_9$ thin films prepared by one step (black) and two step (blue) approaches were recorded to confirm the formation of $(NH_4)_3Sb_2I_9$.

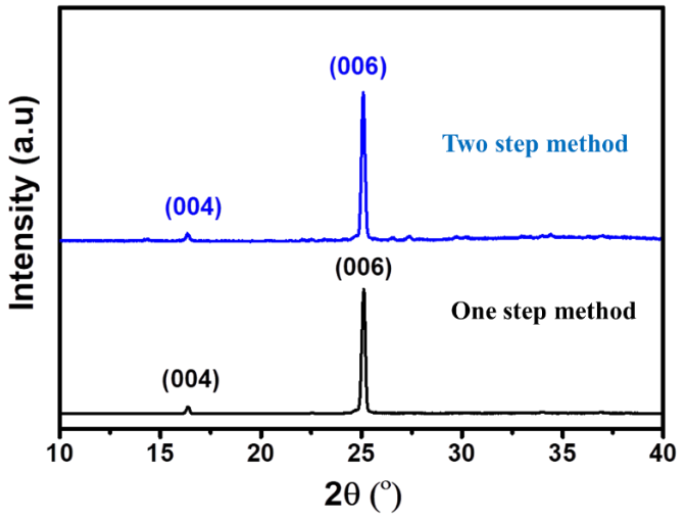

Figure 2.1. PXRD of the $(NH_4)_3Sb_2I_9$ prepared using one step (black) and two step (blue) method (Solvent DMSO and GBL, thin film on FTO glass, Room Temperature).

The PXRD spectra of the $(NH_4)_3Sb_2I_9$ showed the presence of two strong diffraction peaks corresponded to the (004) and (006) diffraction planes (Figure 2.1). As reported by Zuo *et al*. [34], $(NH_4)_3Sb_2I_9$ crystallized in the monoclinic space group $P12_1/n$ and obtained PXRD pattern of the $(NH_4)_3Sb_2I_9$ was well-matched with previous report [34].

Since, the stability of the perovskite materials is of great significance, we have kept the prepared thin film of $(NH_4)_3Sb_2I_9$ in air with controlled humidity (40-50%) for 10 days. The PXRD of the air-exposed thin film of $(NH_4)_3Sb_2I_9$ was recorded, and the corresponding spectra is presented in Figure 2.2.The PXRD data showed insignificant changes in the PXRD spectra without appearing new diffraction plane which suggested its good stability in air.

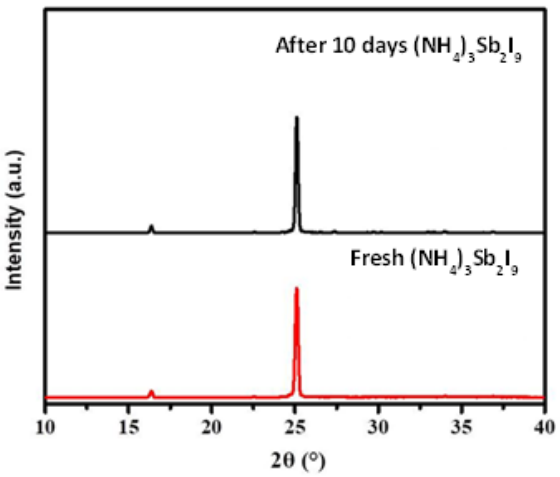

Figure 2.2. PXRD of freshly prepared $(NH_4)_3Sb_2I_9$ (Red) and air exposed $(NH_4)_3Sb_2I_9$ (Black) (kept in aerobic conditions for 10 days) perovskite film (Solvent DMSO and GBL, thin film on FTO glass, Room Temperature).

Further, optical properties of the $(NH_4)_3Sb_2I_9$ films prepared by two different deposition methods have been studied by employing using ultraviolet-visible (UV-vis) spectroscopy. The recorded UV-*vis* absorption spectra of the $(NH_4)_3Sb_2I_9$ films prepared by one step (black) and two step (blue) method have been presented in Figure 2.3.

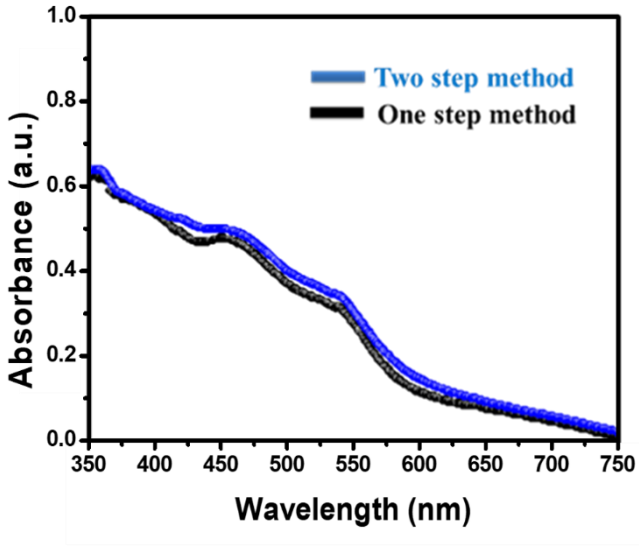

Figure 2.3. UV-vis spectra of the $(NH_4)_3Sb_2I_9$ prepared using one step (black) and two step (blue) method (Solvent DMSO and GBL, thin film on FTO glass, Room Temperature).

The prepared thin films of $(NH_4)_3Sb_2I_9$ by two different approaches showed the similar optical properties and a broad absorption band was appeared between 500-600 nm. The band gap was found to be 2.05 eV as calculated by Tauc plot (Figure 2.4).

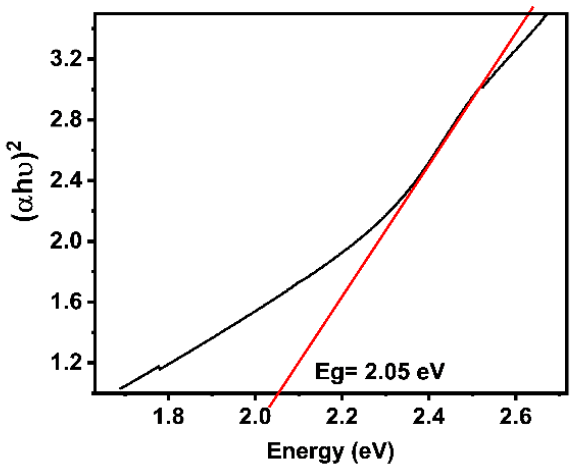

Figure 2.4. Tauc plot of the $(NH_4)_3Sb_2I_9$ (the linear fitting region of the Tauc plot is extrapolated to the energy axis (X-axis) to estimate the optical band gap Eg).

The morphological characteristics of the $(NH_4)_3Sb_2I_9$ by two different approaches were also investigated by recording microscopic images. The scanning electron microscopic images of the $(NH_4)_3Sb_2I_9$ prepared

by one step approach showed the presence of hexagonal flower like structure (Figures 2.5 A, B) whereas the non-hexagonal shaped surface morphology was observed in case of $(NH_4)_3Sb_2I_9$ prepared by two step approach (Figures 2.5 C, D). Generally, perovskite materials rapidly crystallized which lead to the formation of non-uniform surface morphology[35]. Thus, it has been observed from the reported literature that some antisolvents such as toluene or chlorobenzene may control the crystallization process[22]. We have employed toluene as antisolvent to control the crystallization process.

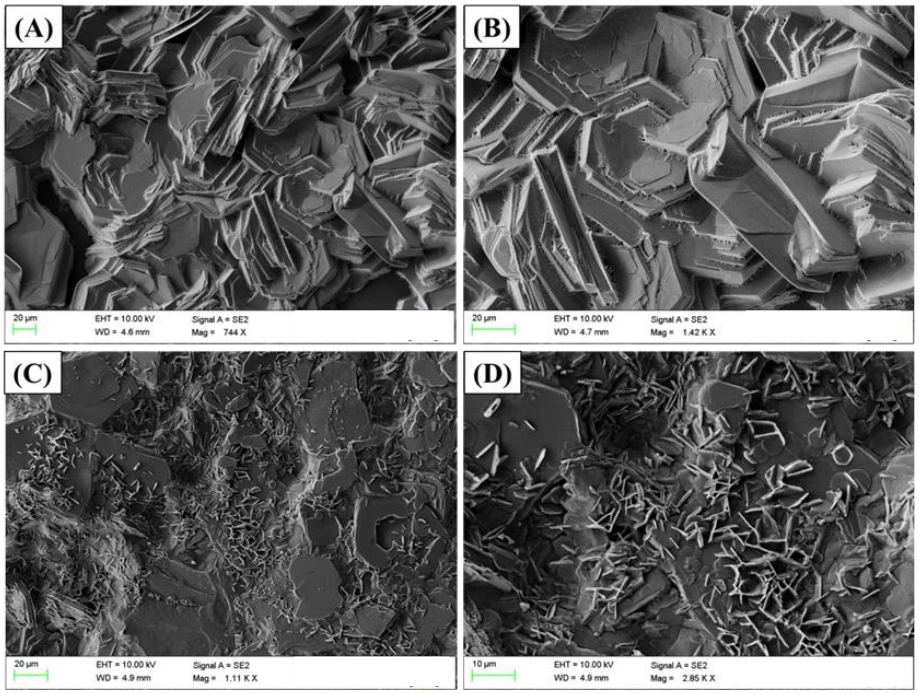

Figure 2.5. FESEM images of the $(NH_4)_3Sb_2I_9$ prepared using one step (A, B) and two step (C, D) method (Solvent DMSO and GBL, thin film on FTO glass, Room Temperature).

Thus, we believe that the presence of non-hexagonal shaped surface may be due to the controlled growth of the $(NH_4)_3Sb_2I_9$. This non-hexagonal surface may provide good interfacial contacts between m-TiO_2 and spiro-MeOTAD which can be beneficial to improve the photovoltaic performance of the PSCs[36-38]. The elemental composition of the $(NH_4)_3Sb_2I_9$ was also investigated by energy-dispersive X-ray spectroscopy (EDX). The EDX results have been presented in Figure 2.6 which observed the presence of N, Sb and I elements and confirmed the formation of $(NH_4)_3Sb_2I_9$ without any impurity.

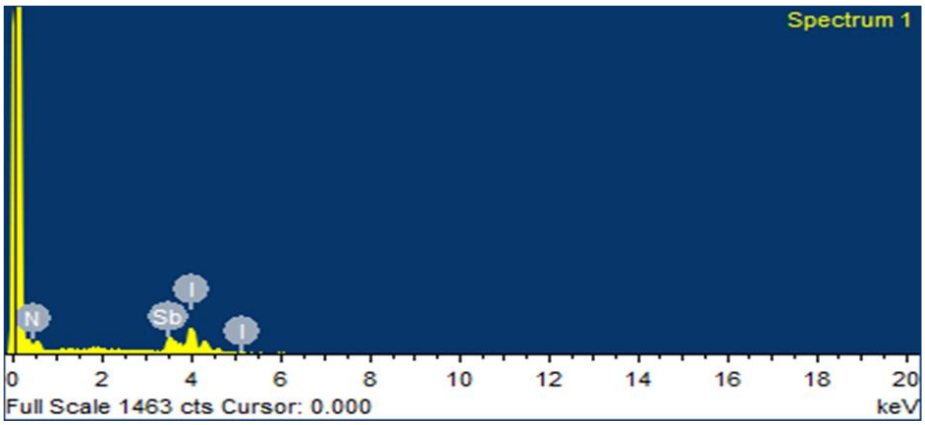

Figure 2.6. EDX spectra of $(NH_4)_3Sb_2I_9$ (Solvent DMSO and GBL, thin film on FTO glass, Room Temperature).

Furthermore Pb free PSCs were developed by two different appraches with device structure of FTO/CL-TiO_2/m-TiO_2/$(NH_4)_3Sb_2I_9$/HTM/Au. The Pb free PSCs developed by one step and two step approaches have been denoted as PSC-1 and PSC-2 respectively. The photovoltaic performance of the PSC-1 and PSC-2 were evaluated by recording photocurrent–voltage (J-V) curves under 1 sun conditions (1.5 AM;100 mW/cm^2). The J-V curves of the PSC-1 (black) and PSC-2 (blue) have been presented in Figure 2.7.

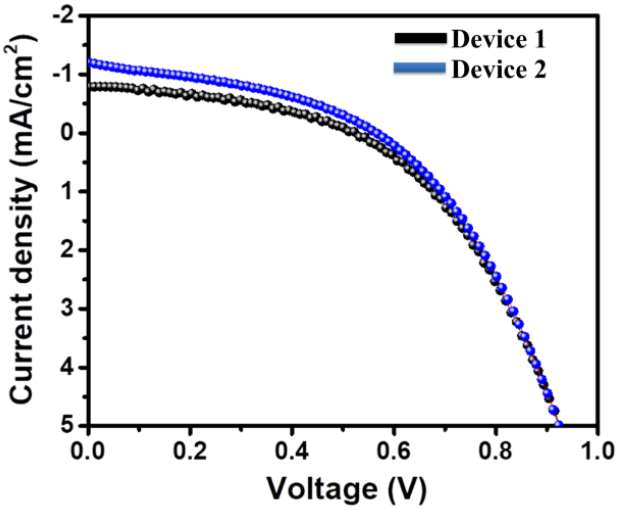

Figure 2.7. J-V curves of the fabricated PSCs devices prepared using $(NH_4)_3Sb_2I_9$ one step (PSC-1) (device 1) and $(NH_4)_3Sb_2I_9$ two step (PSC-2) (device 2) method (Forward Bias, AM 1.5 G; 100 mW/cm^2, Active Area 0.1 cm^2, Room Temperature).

The observations revealed that PSC-1 has a PCE of 0.2% whereas PSC-2 has shown an enahnced PCE of 0.42%. The decent open circuit voltage

(Voc) of 942 mV and 945 mV were observed for PSC-1 and PSC-2 respectively. It was observed that Voc for PSC-1 and PSC-2 was almost same but the photocurrent density (Jsc) was higher for PSC-2 (1.16 mA/cm^2) compared to the PSC-1 (0.80 mA/cm^2). The fill factor (FF) was also high for PSC-2 (42%) compared to the PSC-1 (34%). Thus,we can say that the enhanced PCE of 0.42% for PSC-2 may be due to the high FF and Jsc compared to the PSC-1. The J-V curve of the best performing PSC-1 and PSC-2 have been presented in Figure 2.8. The observed photovoltaic performance of devices was compared to the reported light absorber and the Table A1 showed compared results.

Moreover the non-hexagonal surface morphology of the $(NH_4)_3Sb_2I_9$ provide better contacts between the m-TiO_2 and hole transport layer (spiro-MeOTAD) which improved the charge extraction and enhanced the PCE of PSC-2 [36,37]. The box graph of the Voc, Jsc, FF and PCE for PSC-1 and PSC-2 has also been given in Figure 2.8.

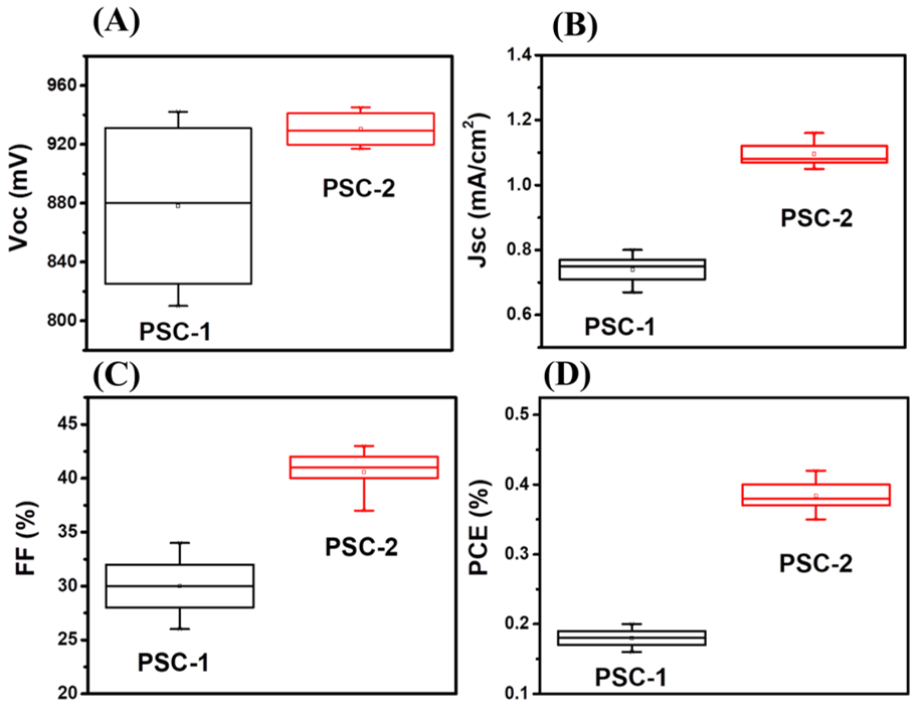

Figure 2.8. Box charts of V_{oc} (A), J_{sc} (B), FF (C) and PCE (D) of the PSC-1 ($(NH_4)_3Sb_2I_9$ one step) and PSC-2 ($(NH_4)_3Sb_2I_9$ two step) (Forward Bias, AM 1.5 G; 100 mW/cm^2, Active Area 0.1 cm^2, Room Temperature).

Furthermore we have recorded the incident-photon-to-current-conversion efficiency (IPCE) of the PSC-1 and PSC-2. The recorded IPCE curves of the PSC-1 and PSC-2 have been presented in Figure 2.9. The higher IPCE was obtained for PSC-2 compared to the PSC-1.

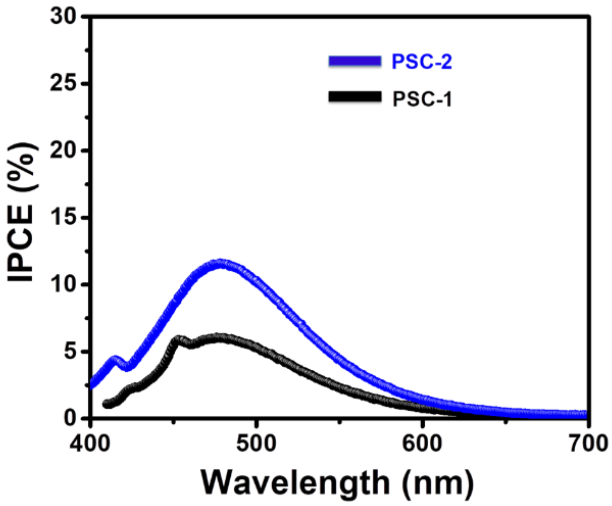

Figure 2.9. IPCE curves of the **PSC-1** $(NH_4)_3Sb_2I_9$ one step and **PSC-2** $(NH_4)_3Sb_2I_9$ two step (thin film on FTO glass, Room Temperature)

The photo-luminescence (PL) of the PSC-1 (FTO/CL-TiO_2/m-TiO_2/$(NH_4)_3Sb_2I_9$/HTM) and PSC-2 (FTO/CL-TiO_2/m-TiO_2/$(NH_4)_3Sb_2I_9$/HTM) have been presented in Figure 2.10. The obtained results showed that PSC-1 has high PL intensity compared to the PSC-2.

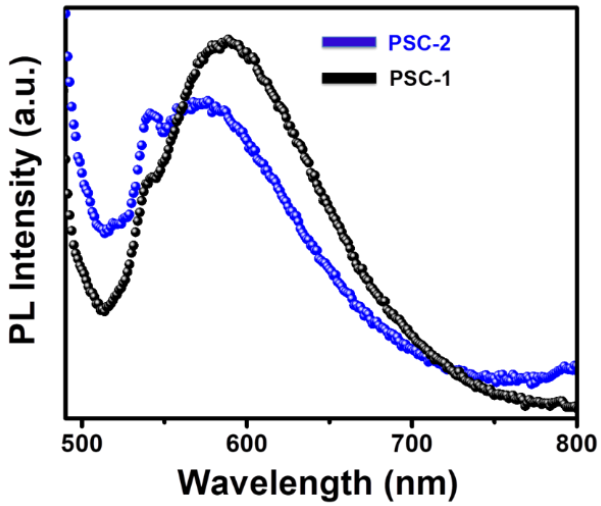

Figure 2.10. PL spectra of the PSC-1 $(NH_4)_3Sb_2I_9$ one step and PSC-2 $(NH_4)_3Sb_2I_9$ two step (thin film on FTO glass, Room Temperature)

The PL intesnity is directly related to the radiative recombination process and suggested that recombination rate is higher in PSC-1 compared to the PSC-2. Therefore, PSC-2 exhibited enhanced photovoltaic performance compared to the PSC-1. Further, time resolved photo-luminescence (TRPL) spectroscopy was also employed to investigate the charge carrier transport characteristics of the $(NH_4)_3Sb_2I_9$ films. The recorded TRPL spectra of the PSC-1 (FTO/CL-TiO_2/m-TiO_2/$(NH_4)_3Sb_2I_9$/HTM) and PSC-2 (FTO/CL-TiO_2/m-TiO_2/$(NH_4)_3Sb_2I_9$/HTM) have been presented in Figure 2.11. The PSC-1 showed a electron lifetime of 0.39 ns whereas PSC-2 exhibited the electron lifetime of 0.47 ns.

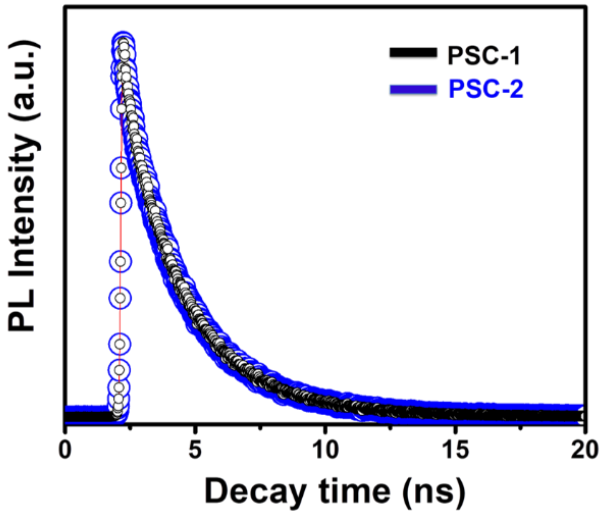

Figure 2.11. TRPL of the PSC-1 $(NH_4)_3Sb_2I_9$ one step and PSC-2 $(NH_4)_3Sb_2I_9$ two step (thin film on FTO glass, Room Temperature)

This showed that PSC-2 has better charge transport carrier properties compared to the PSC-1 which may be associated to the better surface of the $(NH_4)_3Sb_2I_9$ film prepared by two step approach. The cross-sectional SEM images of the PSC-1 and PSC-2 have been presnted in Figure 2.12 which showed the interfacial contacts between different layers.

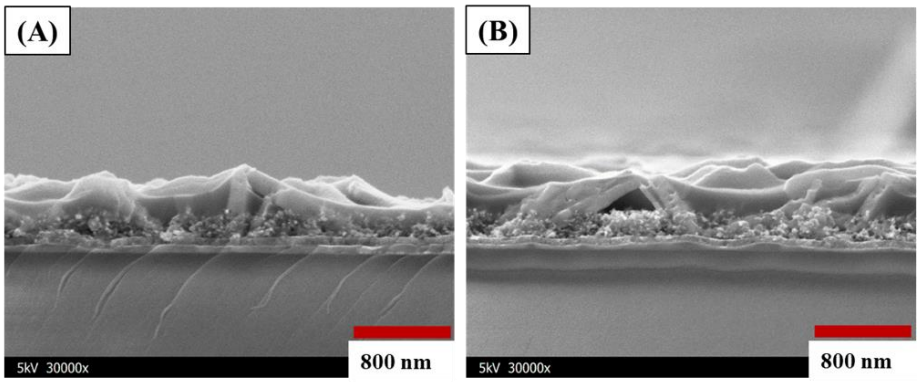

Figure 2.12. Cross-sectional SEM images of the PSC-1 $(NH_4)_3Sb_2I_9$ one step (A) and PSC-2 $(NH_4)_3Sb_2I_9$ two step (B) (thin film on FTO glass, Room Temperature)

Although, PSC-2 exhibited enhanced PCE but this PCE is still far away from the $MAPbX_3$ based PSCs. We have recorded the SEM images of the $(NH_4)_3Sb_2I_9$ films prepared by one step and two step approaches at different scales. We have observed that the morphological features of the $(NH_4)_3Sb_2I_9$ further need to be improved by using other strategies such as vapor deposition or sequential deposition methods which may be helpful to enhanced the PCE of the $(NH_4)_3Sb_2I_9$ based PSCs. Thus, further deep investigations are required to improve the PCE of the $(NH_4)_3Sb_2I_9$ based PSCs.

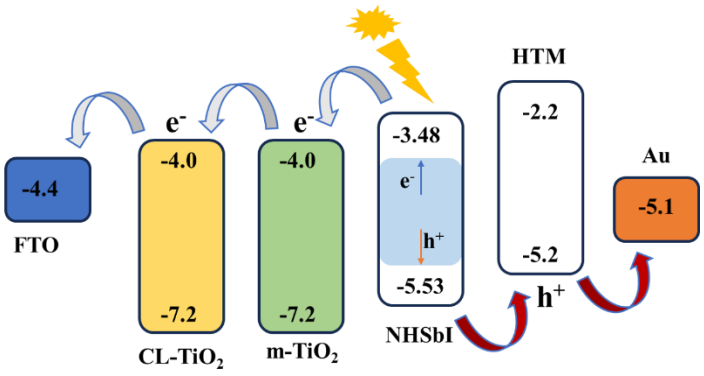

Scheme 2.2 Showed the energy level diagram of PSCs contains $(NH_4)_3Sb_2I_9$ as perovskite material.

The energy level diagram of the PSCs has been presented in Scheme 2.2. The energy level values of the TiO_2, spiro-MeOTAD and Au were taken from the reported [22] literature whereas highest occupied molecular orbital (HOMO) and lowest unoccupied molecular orbital (LUMO)

values of the $(NH_4)_3Sb_2I_9$ were calculated by employing cyclic voltammetry (CV) and UV-vis absorption spectroscopy as reported by Chen *et al*.[39]. The CV graph of the $(NH_4)_3Sb_2I_9$ was recorded in the potential range of 0 to -2 V and have been presented in Figure 2.13 A. The valence band (E_{VB}) and conduction band (E_{CB}) energy level were calculated using equation 2.1 and 2.2 respectively [22,39].

E_{HOMO} (E_{VB}) = (E_{CB}-E_g) eV …….... (Equation 2.1)

(E_g = band gap calculated from UV-vis absorption spectroscopy)

E_{LUMO} (E_{CB}) = -(E_{red}+4.725) eV……. (Equation 2.2)

(E_{red} represent the onset reduction potential)

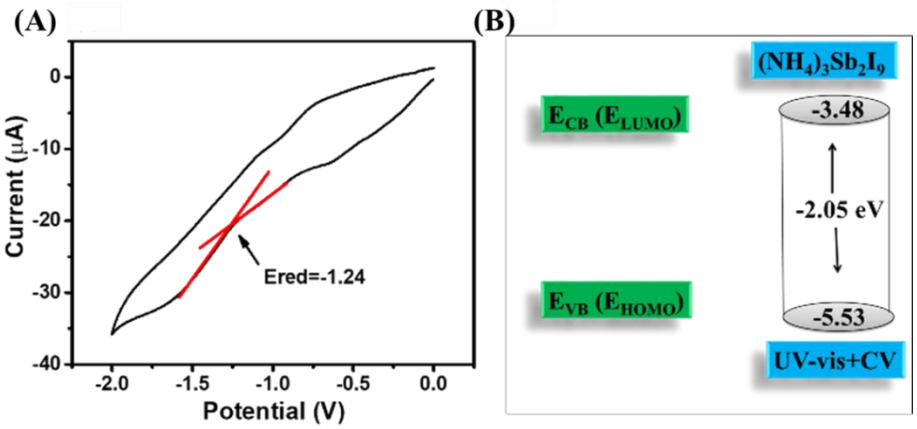

Figure 2.13. CV (A) and energy level values (B) of $(NH_4)_3Sb_2I_9$ (Glassy carbon electrodes, Ag/AgCl and Pt wire utilized as working electrode, the reference and counter electrodes respectively. The potential of the ferrocene/ferrocenium (Fc/Fc^+) in the three-electrode system has been determined using the GCE. $(NH_4)_3Sb_2I_9$ was dissolved in 0.1M tetrabutylammonium hexafluorophosphate ($TBAPF_6$) in acetonitrile containing 0.001M ferrocene at a scan rate of 20 mV/s to record the $(NH_4)_3Sb_2I_9$ CV curve)

The HOMO and LUMO energy values of the $(NH_4)_3Sb_2I_9$ was found to be -5.53 eV and -3.48 eV respectively. The calculated HOMO and LUMO energy values of the $(NH_4)_3Sb_2I_9$ has been presented in Figure 2.13 B. The PSCs device absorbs the sunlight which created the electron and hole pairs in the perovskite structure. This generated electron transferred to conduction band of the electron transport layer (ETL) and leaved a hole in the perovskite structure. This hole to transferred by hole

transport materials (HTM). The transferred electron travelled to the FTO glass substrates and generated electrical energy.

2.3.1. Calculations of HOMO and LUMO energy values

The recorded CV of the $(NH_4)_3Sb_2I_9$ film exhibited three different onset potential values. We have calculated the HOMO and LUMO energy values using three different onset potentials, respectively.

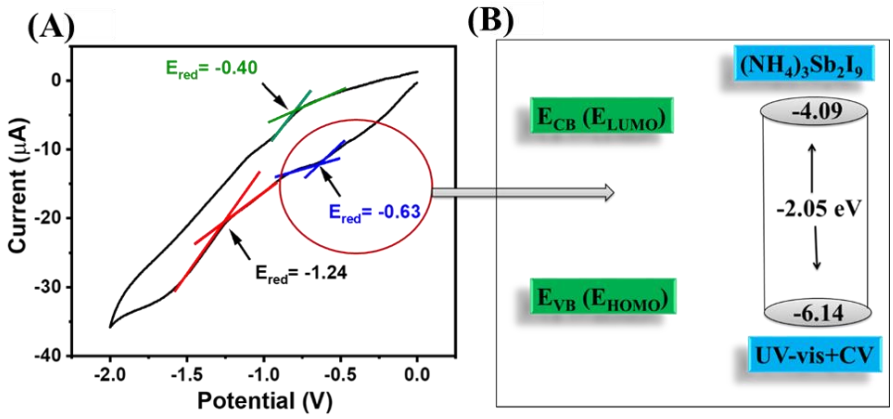

Figure 2.14. CV (A) and energy level values (B) of $(NH_4)_3Sb_2I_9$ (Ered=-0.63) (Glassy carbon electrodes, Ag/AgCl and Pt wire utilized as working electrode, the reference and counter electrodes respectively. The potential of the ferrocene/ferrocenium (Fc/Fc^+) in the three-electrode system has been determined using the GCE. $(NH_4)_3Sb_2I_9$ was dissolved in 0.1M tetrabutylammonium hexafluorophosphate ($TBAPF_6$) in acetonitrile containing 0.001M ferrocene at a scan rate of 20 mV/s to record the $(NH_4)_3Sb_2I_9$ CV curve)

The HOMO and LUMO energy values of -6.14 and -4.09 eV were obtained using onset potential of -0.63 V (Figure 2.14). In case of onset potential of -0.40 V, the HOMO and LUMO energy values of -6.37 and -4.32 eV were observed (Figure 2.15). The HOMO and LUMO energy values of -5.53 and -3.48 eV were obtained with respect to the onset potential of -1.24 V. The HOMO and LUMO energy values of -5.53 and -3.48 eV at onset potential of -1.24 V were consistent with previously reported similar perovskite light absorbing materials [52-54].

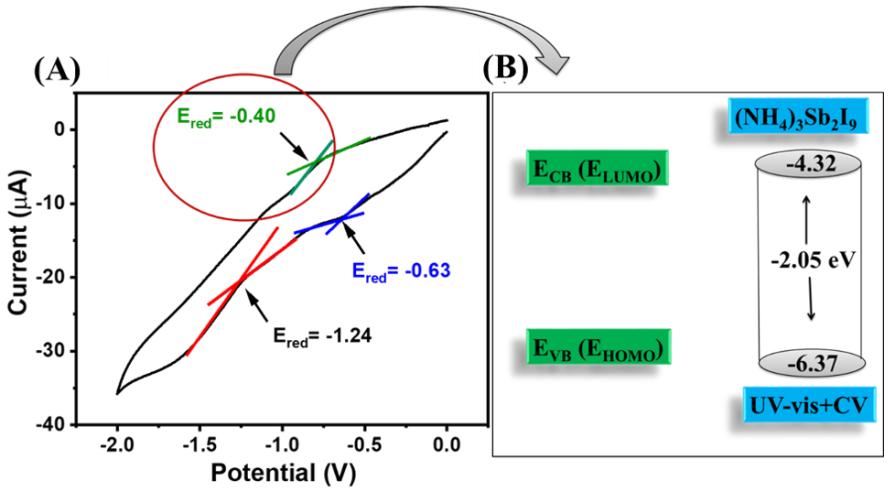

Figure 2.15. CV (a) and energy level values (b) of $(NH_4)_3Sb_2I_9$ (Ered=-0.4) (Glassy carbon electrodes, Ag/AgCl and Pt wire utilized as working electrode, the reference and counter electrodes respectively. The potential of the ferrocene/ferrocenium (Fc/Fc^+) in the three-electrode system has been determined using the GCE. $(NH_4)_3Sb_2I_9$ was dissolved in 0.1M tetrabutylammonium hexafluorophosphate ($TBAPF_6$) in acetonitrile containing 0.001M ferrocene at a scan rate of 20 mV/s to record the $(NH_4)_3Sb_2I_9$ CV curve)

This was also proven by the photovoltaic performance and PL measurements that electron has been generated and transferred efficiently. If we consider the HOMO and LUMO energy values at two other onset potential values, it will be difficult to transfer electron to the conduction band of TiO_2 due un-match of energy values. In recent years, numerous efforts and strategies were applied to find out the stable and Pb free perovskite light absorbers for photovoltaic applications. In this regard, some Pb free perovskite or perovskite like-materials have been introduced in photovoltaic applications. Ahmad *et al.*[22] prepared a lead free methyl ammonium antimony iodide perovskite-like material for the development of PSCs and obtained a high open circuit voltage of 740 mV with an efficiency of 0.5%. In other work, Zhang *et al.*[47] also fabricated bismuth based halide PSCs and achieved an excellent PCE of 1.64% with an open circuit voltage of 810 mV. Gao and co-workers [48] utilized double halide perovskite and obtained a PCE 0.42% with open circuit voltage of 470 mV. Li *et al.* [49] reported lower band gap of 1.8

eV for $(C_6H_5CH_2NH_3)_2CuBr_4$ perovskite, and an efficiency of 0.2%. In another report, Johansson *et al.* [50] and Boopathi *et al.* [51] also developed the Pb free PSCs and reported a PCE of 0.62 and 0.67%, respectively.

2.4. Summary

This work demonstrated the fabrication of $(NH_4)_3Sb_2I_9$ thin films using one step and two step deposition approaches for photovoltaic applications. The fabricated $(NH_4)_3Sb_2I_9$ thin films showed good stability and optoelectronic properties which suggested their potential in photovoltaic applications. The $(NH_4)_3Sb_2I_9$ based PSCs devices exhibited good open circuit voltage and decent photocurrent density. The efficiency of the $(NH_4)_3Sb_2I_9$ based PSCs devices was still lower which need to be improved. We believe that the incorporation of some novel electron transport and charge extraction layers would be beneficial to enhance the efficiency of the $(NH_4)_3Sb_2I_9$ based PSCs. The insertion or doping of $(NH_4)_3Sb_2I_9$ structures with less toxic metals would also be helpful to enhance the optical properties of the $(NH_4)_3Sb_2I_9$. Further in-depth investigations are necessary to study the structural properties of $(NH_4)_3Sb_2I_9$ to enhanced the photovoltaic performance of the Sb-based PSCs.

2.5. References

1. Yang P., Zhao H., Yang Y., Zhao P., Zhao X., Yang L. (2020), Fabrication of N, P-codoped Mo_2C/Carbon Nanofibers via Electrospinning as Electrocatalyst for Hydrogen Evolution Reaction ES Materials & Manufacturing, 7, 34–39 (DOI: 10.30919/esmm5f618).
2. Wei L., Lozano K., Mao, Y. (2018), Microwave Popped Co(II)-Graphene Oxide Hybrid: Bifunctional Catalyst for Hydrogen Evolution Reaction and Hydrogen Storage, Engineered Science, 3, 62–66 (DOI: 10.30919/es8d723).
3. Vairale P., Sharma V., Bade B., Waghmare A., Shinde P., Punde A., Doiphode V., Aher R., P S., harkar Nair S., Jadkar, V. (2020), Melanin Sensitized Nanostructured ZnO Photoanodes for Efficient Photoelectrochemical Splitting of Water: Synthesis and Characterization, Engineered Science, 11, 76–84 (DOI: 10.30919/es8d0023).
4. Yuan Q., Wang R., Wang Q., Sun P., Nie R., Wang X. (2018), Ultrathin $MoSe_2$ Nanosheets Coated on Hollow Carbon Spheres as Efficient Hybrid Catalyst for Hydrogen Evolution Reaction, ES Materials & Manufacturing, 2, 9–15 (DOI: 10.30919/esmm5f112).
5. Yu H., Xu C., Li Y., Jin F., Ye F., Li X. (2020), Performance Enhancement of CuO/ZnO by Deposition on the Metal-Organic Framework of Cu-BTC for Methanol Steam Reforming Reaction, ES Energy & Environment, 8, 65–77 (DOI: 10.30919/esee8c415).
6. Caia Z., Wanga P., Yanga J., Wanga X. (2019), Update on Recent Designing Strategies of Transition Metal-Based Layered Double Hydroxides Bifunctional electrocatalysts, ES Energy & Environment, 5, 22–36 (DOI: 10.30919/esee8c320).
7. Idrees M., Liu L., Batool S., Luo H., Liang J., Xu B., Wang S., Kong J. (2019), Cobalt-doping Enhancing Electrochemical Performance of Silicon/Carbon Nanocomposite as Highly Efficient Anode Materials in Lithium-Ion Batteries, Engineered Science, 6, 64–76 (DOI: 10.30919/es8d798).

8. Li Y., Wang X., Wang Z., Chen L. (2019), Facile Synthesis of SnO_2 Nanorods for Na-Ion Batteries, ES Energy & Environment, 3, 55–59 (DOI: 10.30919/esee8c198).
9. Wang H. T. Z. Z., Yao Y. (2019), A Novel Core-shell Structured Nickel-rich Layered Cathode Material for High-energy Lithium-ion Batteries, Engineered Science, 8, 25–32 (DOI: 10.30919/es8d502).
10. Fu Y., Pei X., Dai Y., Mo D., Lyu S. (2019), Three-Dimensional Graphene-Like Carbon Prepared from CO2 as Anode Material for High-Performance Lithium-Ion Batteries, ES Energy & Environment, 4, 66–73 (DOI: 10.30919/esee8c292).
11. Li G., Dang C., Hou Y., Dang F., Fan Y., Guo, Z. (2020), Experimental and Theoretical Characteristic of Single Atom Co-N-C Catalyst for Li-O2 Batteries, Engineered Science, 10, 85–94 (DOI: 10.30919/es8d1005).
12. Liu Y., Lu N., Liu F., Na R., Wang G., Guan S., Liu F. (2020), Highly Strong and Tough Double-Crosslinked Hydrogel Electrolyte for Flexible Supercapacitors, ChemElectroChem, 7, 1007–1015 (DOI: 10.1002/celc.201902134).
13. Mishra A., Shetti N., Basu S., Reddy K., Aminabhavi T. (2019), Carbon Cloth-based Hybrid Materials as Flexible Electrochemical Supercapacitors, ChemElectroChem, 6, 5771–5786 (DOI: 10.1002/celc.201901122).
14. Guo J., Ma Y., Zhao K., Wang Y., Yang B., Cui J., Yan X. (2019), High-Performance and Ultra-Stable Aqueous Supercapacitors Based on a Green and Low-Cost Water-In-Salt Electrolyte, ChemElectroChem, 6, 5433–5438 (DOI: 10.1002/celc.201901591).
15. Ahmad K., M. Mobin, S. (2017), Graphene oxide based planar heterojunction perovskite solar cell under ambient condition, New Journal of Chemistry, 41, 14253–14258 (DOI: 10.1039/C7NJ02847D).
16. Kanda H., Shibayama N., Joel Huckaba A., Lee Y., Paek S., Klipfel N., Roldán-Carmona C., Emmanuel Queloz V. I., Grancini G., Zhang Y., Abuhelaiqa M., Taek Cho K., Li M., Driss Mensi M., Kinge S., Khaja Nazeeruddin, M. (2020), Band-bending induced

passivation: high performance and stable perovskite solar cells using a perhydropoly(silazane) precursor, Energy & Environmental Science, 13, 1222–1230 (DOI: 10.1039/C9EE02028D).

17. Kim G., Min H., Lee K. S., Lee D. Y., Yoon S. M., Seok S. I. (2020), Impact of strain relaxation on performance of α-formamidinium lead iodide perovskite solar cells, Sci., 370, 108–112 (DOI: 10.1126/science.abc4417).
18. Wang D., Guo Z. (2020), Ten years' Glory of Halide Perovskite Materials, Engineered Science, 11, 1–2 (DOI: 10.30919/es5e1026).
19. Jiang Q., Wang L., Yan C., Liu C., Guo Z., Wang N. (2018), Nano-mesoporous TiO_2 Vacancies Modification for Halide Perovskite Solar Cells, Engineered Science, 1, 64–68 (DOI: 10.30919/es.180329).
20. Wang W., Li J., Ni P., Liu B., Chen Q., Lu Y., Wu H., Cao B., Liu, Z. (2019), Improved Synthesis of Perovskite $CsPbX_3@SiO_2$ (X = Cl, Br, and I) Quantum Dots with Enhanced Stability and Excellent Optical Properties, ES Materials & Manufacturing, 4, 66–73 (DOI: 10.30919/esmm5f219).
21. Tavakoli M. M., Prochowicz D., Yadav P., Tavakoli R., Saliba M. (2018), Zinc Stannate Nanorod as an Electron Transporting Layer for Highly Efficient and Hysteresis-less Perovskite Solar Cells, Engineered Science, 3, 48–53 (DOI: 10.30919/es8d749).
22. Ahmad K., Kumar P., Mobin S. M. (2020), A Two-Step Modified Sequential Deposition Method-based Pb-Free $(CH_3NH_3)_3Sb_2I_9$ Perovskite with Improved Open Circuit Voltage and Performance, ChemElectroChem, 7, 946–950 (DOI: 10.1002/celc.201902107).
23. K. Noel N., D. Stranks S., Abate A., Wehrenfennig C., Guarnera S., Haghighirad A.-A., Sadhanala A., E. Eperon G., K. Pathak S., B. Johnston M., Petrozza A., M. Herz L., J. Snaith H. (2014), Lead-free organic–inorganic tin halide perovskites for photovoltaic applications, Energy & Environmental Science, 7, 3061–3068 (DOI: 10.1039/C4EE01076K).
24. Li F., Zhang C., Huang J.-H., Fan H., Wang H., Wang P., Zhan C., Liu C.-M., Li X., Yang L.-M., Song Y., Jiang K.-J. (2019), A Cation-

Exchange Approach for the Fabrication of Efficient Methylammonium Tin Iodide Perovskite Solar Cells, Angew. Chem. Int. Ed., 58, 6688–6692 (DOI: 10.1002/anie.201902418).

25. Hao F., Stoumpos C. C., Cao D. H., Chang R. P. H., Kanatzidis M. G. (2014), Lead-free solid-state organic–inorganic halide perovskite solar cells, Nat. Photo., 8, 489–494 (DOI: 10.1038/nphoton.2014.82).
26. Gupta S., Bendikov T., Hodes G., Cahen D. (2016), $CsSnBr_3$, A Lead-Free Halide Perovskite for Long-Term Solar Cell Application: Insights on SnF_2 Addition, ACS Energy Lett., 1, 1028–1033 (DOI: 10.1021/acsenergylett.6b00402).
27. Kumar M. H., Dharani S., Leong W. L., Boix P. P., Prabhakar R. R., Baikie T., Shi C., Ding H., Ramesh R., Asta M., Graetzel M., Mhaisalkar S. G., Mathews N. (2014), Lead-Free Halide Perovskite Solar Cells with High Photocurrents Realized Through Vacancy Modulation, Adv. Mater., 26, 7122–7127 (DOI: 10.1002/adma.201401991).
28. Song T.-B., Yokoyama T., Logsdon J., Wasielewski M. R., Aramaki S., Kanatzidis M. G. (2018), Piperazine Suppresses Self-Doping in $CsSnI_3$ Perovskite Solar Cells, ACS Appl. Energy Mater., 1, 4221–4226 (DOI: 10.1021/acsaem.8b00866).
29. Heo J. H., Kim J., Kim H., Moon S. H., Im S. H., Hong K.-H. (2018), Roles of SnX_2 (X = F, Cl, Br) Additives in Tin-Based Halide Perovskites toward Highly Efficient and Stable Lead-Free Perovskite Solar Cells, J. Phys. Chem. Lett., 9, 6024–6031 (DOI: 10.1021/acs.jpclett.8b02555).
30. Ahmad K., Ansari S. N., Natarajan K., Mobin S. M. (2018), Design and Synthesis of 1D-Polymeric Chain Based $[(CH_3NH_3)_3Bi_2Cl_9]_n$ Perovskite: A New Light Absorber Material for Lead Free Perovskite Solar Cells, ACS Appl. Energy Mater., 1, 2405–2409 (DOI: 10.1021/acsaem.8b00437).
31. Ahmad K., Kumar P., Mobin S. M. (2020), Inorganic Pb-Free Perovskite Light Absorbers for Efficient Perovskite Solar Cells with

Enhanced Performance, Chem. Asian J., 15, 2859–2863 (DOI: 10.1002/asia.202000680).

32. Ahmad K., Mobin S. M. (2020), Recent Progress and Challenges in $A_3Sb_2X_9$-Based Perovskite Solar Cells, ACS Omega, 5, 28404–28412 (DOI: 10.1021/acsomega.0c04174).
33. I. El-Henawey M., S. Gebhardt R., M. El-Tonsy M., Chaudhary S. (2016), Organic solvent vapor treatment of lead iodide layers in the two-step sequential deposition of CH 3 NH 3 PbI 3 -based perovskite solar cells, J. Mater. Chem. A, 4, 1947–1952 (DOI: 10.1039/C5TA08656F).
34. Zuo C., Ding L. (2017), Lead-free Perovskite Materials $(NH_4)_3Sb_2I_xBr_{9-x}$, Angew. Chem., 129, 6628–6632 (DOI: 10.1002/ange.201702265).
35. Sakai N., Pathak S., Chen H.-W., A. Haghighirad A., D. Stranks S., Miyasaka T., J. Snaith H. (2016), The mechanism of toluene-assisted crystallization of organic–inorganic perovskites for highly efficient solar cells, J. Mater. Chem. A, 4, 4464–4471 (DOI: 10.1039/C6TA01087C).
36. Lyu M., Yun J.-H., Cai M., Jiao Y., Bernhardt P. V., Zhang M., Wang Q., Du A., Wang H., Liu G., Wang L. (2016), Organic–inorganic bismuth (III)-based material: A lead-free, air-stable and solution-processable light-absorber beyond organolead perovskites, Nano Res., 9, 692–702 (DOI: 10.1007/s12274-015-0948-y).
37. Ran C., Wu Z., Xi J., Yuan F., Dong H., Lei T., He X., Hou X. (2017), Construction of Compact Methylammonium Bismuth Iodide Film Promoting Lead-Free Inverted Planar Heterojunction Organohalide Solar Cells with Open-Circuit Voltage over 0.8 V, J. Phys. Chem. Lett., 8, 394–400 (DOI: 10.1021/acs.jpclett.6b02578).
38. Singh T., Kulkarni A., Ikegami M., Miyasaka T. (2016), Effect of Electron Transporting Layer on Bismuth-Based Lead-Free Perovskite $(CH_3NH_3)_3$ Bi_2I_9 for Photovoltaic Applications, ACS Appl. Mater. Interfaces, 8, 14542–14547 (DOI: 10.1021/acsami.6b02843).

39. Chen X., Myung Y., Thind A., Gao Z., Yin B., Shen M., Beom Cho S., Cheng P., Sadtler B., Mishra R., Banerjee P. (2017), Atmospheric pressure chemical vapor deposition of methylammonium bismuth iodide thin films, J. Mater. Chem., A 5, 24728–24739 (DOI: 10.1039/C7TA06578G).
40. Luo Q., Wu R., Ma L., Wang C., Liu H., Lin H., Wang N., Chen Y., Guo Z. (2021), Recent Advances in Carbon Nanotube Utilizations in Perovskite Solar Cells, Advanced Functional Materials, 31, 2004765 (DOI: 10.1002/adfm.202004765).
41. Luo Q., Ma H., Hou Q., Li Y., Ren J., Dai X., Yao Z., Zhou Y., Xiang L., Du H., He H., Wang N., Jiang K., Lin H., Zhang H., Guo Z. (2018), All-Carbon-Electrode-Based Endurable Flexible Perovskite Solar Cells, Adv. Fun. Mater., 28, 1706777 (DOI: 10.1002/adfm.201706777).
42. Zhang Y., Kirs A., Ambroz F., Lin C.-T., Bati A. S. R., Parkin I. P., Shapter J. G., Batmunkh M., Macdonald T. J. (2021), Ambient Fabrication of Organic–Inorganic Hybrid Perovskite Solar Cells, Small Methods, 5, 2000744 (DOI: 10.1002/smtd.202000744).
43. Zuo C., Ding L. (2017), Lead-free Perovskite Materials $(NH_4)_3Sb_2I_xBr_{9-x}$, Angew. Chem. Inter. Ed., 56, 6528–6532 (DOI: 10.1002/anie.201702265).
44. Giustino F., Snaith H. J. (2016), Toward Lead-Free Perovskite Solar Cells, ACS Energy Lett., 1, 1233–1240 (DOI: 10.1021/acsenergylett.6b00499).
45. Jain S. M., Edvinsson T., Durrant J. R. (2019), Green fabrication of stable lead-free bismuth based perovskite solar cells using a non-toxic solvent, Comm. Chem., 2, 1–7 (DOI: 10.1038/s42004-019-0195-3).
46. Sun S., Tominaka S., Lee J.-H., Xie F., Bristowe P. D., Cheetham A. K. (2016), Synthesis, crystal structure, and properties of a perovskite-related bismuth phase, (NH4)3Bi2I9, APL Materials, 4, 031101 (DOI: 10.1063/1.4943680).
47. Zhang Z., Li X., Xia X., Wang Z., Huang Z., Lei B., Gao Y. (2017), High-Quality $(CH_3NH_3)_3Bi_2I_9$ Film-Based Solar Cells: Pushing

Efficiency up to 1.64%, J. Phys. Chem. Lett., 8, 4300–4307 (DOI: 10.1021/acs.jpclett.7b01952).

48. Zhang C., Gao L., Teo S., Guo Z., Xu Z., Zhao S., Ma T. (2018), Design of a novel and highly stable lead-free Cs_2NaBiI_6 double perovskite for photovoltaic application, Sustainable Energy & Fuels, 2, 2419–2428 (DOI: 10.1039/C8SE00154E).
49. Li X., Li B., Chang J., Ding B., Zheng S., Wu Y., Yang J., Yang G., Zhong X., Wang J. (2018), $(C_6H_5CH_2NH_3)_2CuBr_4$: A Lead-Free, Highly Stable Two-Dimensional Perovskite for Solar Cell Applications, ACS Appl. Energy Mater., 1, 2709–2716 (DOI: 10.1021/acsaem.8b00372).
50. Johansson M. B., Philippe B., Banerjee A., Phuyal D., Mukherjee S., Chakraborty S., Cameau M., Zhu H., Ahuja R., Boschloo G., Rensmo H., Johansson E. M. J. (2019), Cesium Bismuth Iodide Solar Cells from Systematic Molar Ratio Variation of CsI and BiI_3, Inorg. Chem., 58, 12040–12052 (DOI: 10.1021/acs.inorgchem.9b01233).
51. Moorthy Boopathi K., Karuppuswamy P., Singh A., Hanmandlu C., Lin L., Ali Abbas S., Cheng Chang C., Cheng Wang P., Li, G., Wei Chu C. (2017), Solution-processable antimony-based light-absorbing materials beyond lead halide perovskites, Journal of Materials Chemistry A, 5, 20843–20850 (DOI: 10.1039/C7TA06679A).
52. Singh A., Boopathi K. M., Mohapatra A., Chen Y. F., Li G., Chu C. W. (2018), Photovoltaic Performance of Vapor-Assisted Solution-Processed Layer Polymorph of $Cs_3Sb_2I_9$, ACS Appl. Mater. Interfaces, 10, 2566–2573 (DOI: 10.1021/acsami.7b16349).
53. Yu B.-B., Liao M., Yang J., Chen W., Zhu Y., Zhang X., Duan T., Yao W., Wei S.-H., He Z. (2019), Alloy-induced phase transition and enhanced photovoltaic performance: the case of $Cs_3Bi_2I_{9-x}Br_x$ perovskite solar cells, J. Mater. Chem., A 7, 8818–8825 (DOI: 10.1039/C9TA01978B).

54. Stroyuk O. (2018), Lead-free hybrid perovskites for photovoltaics, Beilstein J. Nanotechnol., 9, 2209–2235 (DOI: 10.3762/bjnano.9.207).

CHAPTER 3

Optoelectronic and Photovoltaic Properties of $(NH_4)_3Bi_2I_9$: a Perovskite-Like Energy Material for Pb Free Perovskite Solar Cells

3.1. Introduction

Organic-inorganic lead halide perovskite solar cells (PSCs) have drawn tremendous attention due to their cost effective, simple fabrication and high performance [1-3]. Perovskite solar cells were originated in 2009 with 3% efficiency by Kojima *et al*. [4] Further, numerous efforts were made to enhance this PCE and finally more that 25% efficiency has been reported [5]. Although, PSCs having methyl ammonium lead halide perovskite light absorber has been proven most efficient photovoltaic device but suffers from the poor stability and hazardous nature of lead (Pb) [6,7] In this regard, Noel *et al*. [8] and Hao *et al*. [9] have developed Pb free PSCs using $CH_3NH_3SnI_3$ light absorber which showed the PCE of ~6%. Liu *et al*. [10] also designed mixed cationic tin halide perovskite for Pb free PSCs but the obtained PCE was less than 0.5%. Song *et al*. [11] further employed $CsSnI_3$ and $CsSnBr_3$ perovskite light absorbers and the obtained PCE was found to be 1.83%, and 3.04% respectively. Ke *et al*. [12] developed the PSCs using novel hollow 3D perovskite {en}$FASnI_3$ perovskite. The developed PSCs exhibited the PCE of 7.1%. Mhaisalkar and co-workers reported $AGeI_3$ (A= Cs^+, $CH_3NH_3^+$ or $HC(NH_2)_2$)) perovskite materials for Pb free PSCs [13].

Remarkably, Tin and germanium-based perovskite materials have shown good performance but require inert atmosphere due to the air sensitivity. The Sn^{2+} or Ge^{2+} rapidly changed to the Sn^{4+} or Ge^{4+} which diminished the stability of the perovskite structures. Mathews and co-workers utilized $MA_2CuCl_xBr_{4-x}$ hybrid perovskites for photovoltaic applications however its PCE was found to be poor [14]. Li *et al*. [15] and Ahmad *et al*. [16] also employed $C_6H_4NH_2CuBr_2I$ perovskite materials for photovoltaic applications. The $C_6H_4NH_2CuBr_2I$ perovskite materials exhibited excellent stability but the obtained PCE was less than

1% [15,16]. Li *et al.* [17,18] investigated the optoelectronic properties of the $(C_6H_5CH_2NH_3)_2CuBr_4$ and $[H_3NC_6H_4NH_3]CuBr_4$ whereas Vargas *et al*. [19] employed $Cs_4CuSb_2Cl_{12}$ as light absorber for Pb free PSCs applications. According to the recent reports, it has been observed antimony (Sb) and bismuth (Bi) based perovskite materials have excellent stability under atmospheric conditions. Ding *et al*. [20] fabricated planar PSCs using $(NH_4)_3Sb_2I_xBr_{9-x}$ perovskite and obtained the PCE of 0.51%. Hebig *et al*. [21] investigated the optoelectronic properties of the $(CH_3NH_3)_3Sb_2I_9$ and fabricated the planar hetero-junction PSCs which exhibited the PCE of 0.5%. Harikesh *et al*. [22] proposed $Rb_3Sb_2I_9$ as suitable energy material for photovoltaic applications and achieved the PCE of 0.66%. On the other hand, Bi is a non-toxin element which has the potential to replace the Pb from the Pb based PSCs. Okano *et al*. has introduced gas-assisted approach to prepare the $(CH_3NH_3)_3Bi_2I_9$ thin films for PSCs [23]. Kulkarni *et al*. [24] prepared the N-methyl pyrrolidone-assisted $(CH_3NH_3)_3Bi_2I_9$ thin films and obtained the PCE of 0.31%. Huang *et al*. [25] applied FPDI electron transport layer for $(CH_3NH_3)_3Bi_2I_9$ PSCs. However, the obtained PCE was 0.06%. This may be due to the poor charge extraction properties of the FPDI or poor surface. Mathur and co-workers fabricated the planar heterojunction PSCs using $(CH_3NH_3)_3Bi_2I_9$ perovskite material and obtained the PCE of 0.1% [26]. Abulikemu *et al*. [27] crystallized the structure of $(CH_3NH_3)_3Bi_2I_9$ perovskite and developed the PSCs and the highest obtained PCE was found to be 0.11%. Filip *et al*. [28] proposed $Cs_2BiAgCl_6$ and $Cs_2BiAgBr_6$ perovskites whereas Shao *et al*. [29] investigated the photovoltaic properties of $AgBi_2I_7$. The highest PCE of 0.83% was achieved by using $AgBi_2I_7$ in mesoscopic PSCs [29]. It has been observed that various Pb free perovskite structures have been developed by utilizing novel strategies and non/less toxic metal. It is of great importance to find out or investigate the optoelectronic properties of the new perovskite materials. Sun *et al*. [30] have investigated the crystallographic features of the $(NH_4)_3Bi_2I_9$. In 2019, Zhuang *et al*. [31] have developed the X-ray detector made of perovskite-like $(NH_4)_3Bi_2I_9$

material. To date, there have been no reports on the use of $(NH_4)_3Bi_2I_9$ (ABI) as a light absorber in lead-free perovskite solar cells (PSCs).

3.2. Experimental section

3.2.1. Materials

We have purchased all the chemicals (BiI_3, NH_4I, Spiro-MeOTAD, 4-tertbutylpyridine, TiO_2 precursors, bis(trifluoromethylsulfonyl)imide lithium salt, etc.), solvents (chlorobenzene, DMSO and DMF), FTO glass substrates and other precursors from Merck, SRL, Dyesol, Loba, Sigma Aldrich, BAT-SOL, Alfa Aesar and Solaronix. The precursors and chemicals were used without any further purification.

3.2.2. Characterization methods

The Powder X-ray diffraction (PXRD) investigations were carried out on RINT 2500 V x-ray diffractometer (Rigaku, Japan), (Source=Cu Kα irradiation; $\lambda = 1.5406$ Å). Field Emission Scanning Electron microscopic (FE-SEM) images were taken on Supra 55 Zeiss Field Emission Scanning Electron microscope. The Energy Dispersive X-ray (EDX) spectroscopy was used to investigate the element composition using Oxford Instrument' X-max, Aztec. Optical band gap was calculated using UV-vis absorption spectroscopy on a Varian UV–*vis* spectrophotometer (model: Carry 100). The photocurrent-voltage (*J-V*) curves were recorded under AM 1.5 G condition (100 mW/cm^2 illumination). Cyclic voltammetry (CV) measurements were carried out on Metrohm Potentiostat/Galvanostat using Nova software.

3.2.3. Electrochemical investigations

The highest occupied molecular orbital (HOMO) and lowest unoccupied molecular orbital (LUMO) energy values of the ABI were determined by employing by UV-vis and CV approach. The CV curve of the ABI was recorded using a 3-electrode assembly (where glassy carbon electrode acted as working electrode whereas Ag/AgCl and Pt wire electrode worked as reference and counter electrode respectively). The GCE has been used to determine the potential of the ferrocene/ferrocenium (Fc/Fc^+) in the three electrode system. The CV curve of the ABI was recorded by dissolving ABI in 0.1M tetrabutylammonium

hexafuorophosphate ($TBAPF_6$) in acetonitrile having 0.001M ferrocene at scan rate=20mV/s.

3.2.4. Perovskite film preparations

0.7M BiI_3 was dissolved in 1 mL of N,N-dimethylformamide (DMF) using ultra-sonicator for 1h. Further, NH_4I was dissolved in the resulting solution. The molar ratio of the NH_4I and BiI_3 was fixed to 3:2. The obtained reaction mixture was filtered through a 0.22 μm PTFE filter. The obtained reaction mixture was denoted as ABI-1. For ABI-1, ABI-2 and ABI-3, we have employed two-step deposition method by utilizing solvent engineering approach to prepare the ABI ($(NH_4)_3Bi_2I_9$) films. The BiI_3 and NH_4I were dissolved in the mixture of DMSO (0.2mL) and DMF (0.8mL) and spin coated (1500 rpm 30sec) on to the FTO glass electrode. 200 μL of chlorobenzene (acted as anti-solvent) was dropped (~10 s) before the second deposition (4500 rpm). This prepared film was denoted as ABI-2. For ABI-3, the ratio of DMSO and DMF was fixed to 0.4:0.6 (V:V) whereas other conditions were similar to the ABI-2.The deposited films were annealed at 100°C for 15 min.

3.2.5. Device fabrication

The fluorine-doped tin oxide (FTO) was patterned and cleaned with detergent, water, acetone and 2-propanol using ultra-sonicator for 15 min. The blocking layer of TiO_2 (bl-TiO_2) was deposited using 20 mM titanium diisopropoxide bis(acetylacetonate) solution and annealed at 450°C for 30min. Thereafter, a mesoporous film of TiO_2 (mp-TiO_2) was also deposited on to the FTO/bl-TiO_2 and sintered at 500°C for 45 min. Further, the perovskite film (ABI-1, ABI-2 or ABI-3) was deposited on to the FTO/bl-TiO_2/mp-TiO_2 as described above. Furthermore, hole transport material (HTM) layer was deposited on to the FTO/bl-TiO_2/mp-TiO_2/perovskite. The HTM was prepared using spiro-OMeTAD in chlorobenzene (90mg/mL) with bis(trifluoromethylsulfonyl)imide lithium salt (Li-TFSI; 99.95%), tris(2-(1H-pyrazol-1-yl)-4-tert-butylpyridine)-cobalt(III) tris-(bis(trifluoromethylsulfonyl)imide=FK209) and 4-tert-butylpyridine (4-tBP). The molar ratio of the Li-TFSI, FK209 and 4-tBP was fixed to 0.45;0.035;3.1. Finally, Au counter electrode was deposited on to the

FTO/bl-TiO_2/mp-TiO_2/perovskite/HTM using thermal evaporation method.

3.3. Results and discussion

Herein, we have investigated the optoelectronic and photovoltaic properties of the perovskite-like ABI material for photovoltaic applications. Moreover, we have employed solvent engineering and anti-solvent crystallization approach to improve the photovoltaic performance of the PSCs. To the best of our knowledge, this is the first report on the fabrication of Pb free PSCs using ABI perovskite light absorber. Two-step approach was adopted along with solvent engineering method to obtain the high performance Pb free PSCs. The BiI_3 and NH_4I were dissolved in the mixture of DMSO and DMF and spin coated (1500 rpm, 30 sec) on to the FTO glass electrode (Scheme 3.1). The molar ratio of the NH_4I and BiI_3 was fixed to 3:2. 200 µL of chlorobenzene (acted as anti-solvent) was dropped (~10 s) before the second deposition (4500 rpm).

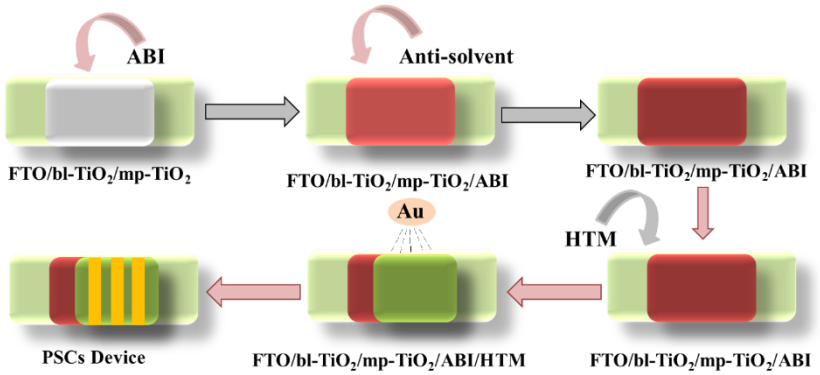

Scheme 3.1. Schematic diagram shows the fabrication procedure.

The powder X-ray diffraction method (PXRD) was employed to investigate the formation and phase purity of the fabricated thin films of ABI-1 (DMSO:DMF= 0:1), ABI-2 (DMSO:DMF=0.2:0.8) and ABI-3 (DMSO:DMF=0.4:0.6). The PXRD patterns of the ABI-1, ABI-2 and ABI-3 have been presented in Figure 3.1. The PXRD patterns of the ABI-1 (black), ABI-2 (blue) and ABI-3 (red) exhibited the strong diffraction peak at ~24.6° which suggested the presence of (006) diffraction plane.

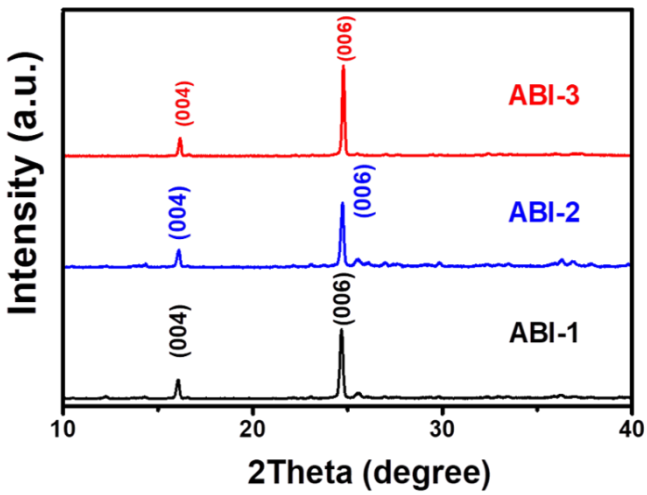

Figure 3.1. PXRD patterns of $(NH_4)_3Bi_2I_9$, ABI-1 (DMSO:DMF= 0:1), ABI-2 (DMSO:DMF=0.2:0.8) and ABI-3 (DMSO:DMF=0.4:0.6), (thin film on FTO, room temperature).

However, the diffraction peak at ~16.7° showed the presence of (004) diffraction plane in the structure of ABI-1, ABI-2 and ABI-3 perovskites. The PXRD patterns of the ABI-1, ABI-2 and ABI-3 were consistent with recent report [31]. The preparation of ABI-1, ABI-2 and ABI-3 perovskite thin films were carried out in aerobic conditions with controlled humidity (30-40%). The stability of the perovskite structures can be estimated by Goldschmidt tolerance factor (*t*) [1]. The Goldschmidt tolerance factor (*t*) is given below:

$$(t)=\frac{(rA+rX)}{\sqrt{2}(rB+rX)} \qquad \text{..... (Equation 3.1)}$$

(Herein, rA and rB= ionic radii of the A and B while rX is the ionic radii of the X present in the ABX_3 structure. An ideal cubic perovskite structure is expected when t=1.

This is also suggested that the ionic size of A is larger than B. The stable perovskite structures can be obtained when t lies between 0.8 and 1. It is also widely studied that If *t* less than 0.8 the cation A is too small or if more than 1 than it's too large to fit into BX_6 octahedron, thereby favoring the formation of alternative perovskite structures.

The octahedral factor (μ) should be lies between 0.44 and 0.72 for B and X to form a stable BX_6 octahedron. The octahedral factor (μ) is given below:[1]

$(\mu)=\frac{rB}{rX}$ ……. (Equation 3.2)

The effective ionic radii of the Ammonium $[NH_4]^+$ and Bi^{3+} is 146 pm and 103 pm which suggested its potential to form the stable perovskite like structure [1]. Therefore, it can be considered that ABI is a stable perovskite like material which can be employed in photovoltaic applications.

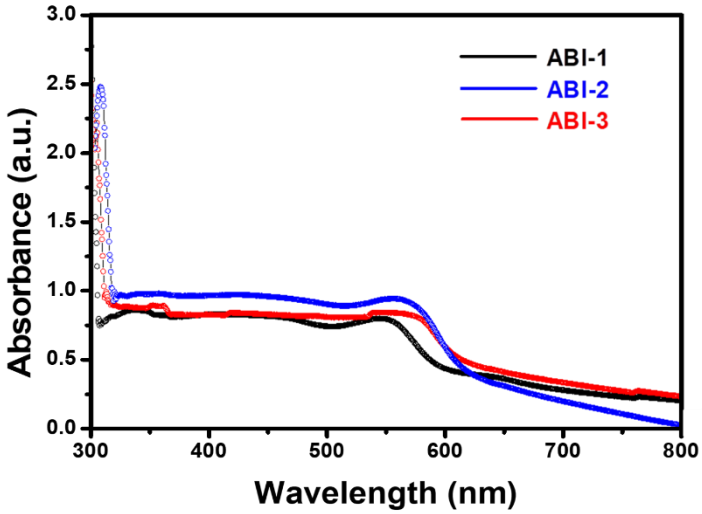

Figure 3.2. UV-vis absorption spectra of $(NH_4)_3Bi_2I_9$ ABI-1 (DMSO:DMF= 0:1), ABI-2 (DMSO:DMF=0.2:0.8) and ABI-3 (DMSO:DMF=0.4:0.6), (thin film on FTO, room temperature).

The ultraviolet-visible (UV-vis) spectroscopic investigations were carried out to obtain the optical band gap of the prepared ABI-1, ABI-2 and ABI-3 perovskites. The UV-vis spectra of the ABI-1, ABI-2 and ABI-3 were recorded on UV-vis spectrophotometer and the recorded UV-vis spectra have been presented in Figure 3.2.

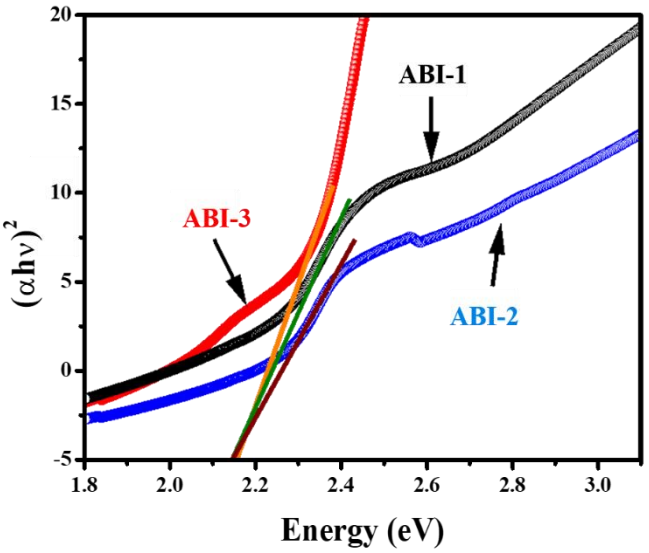

Figure 3.3. Tauc plot of $(NH_4)_3Bi_2I_9$, ABI-1 (DMSO:DMF= 0:1), ABI-2 (DMSO:DMF=0.2:0.8) and ABI-3 (DMSO:DMF=0.4:0.6) (the linear fitting region of the Tauc plot is extrapolated to the energy axis (X-axis) to estimate the optical band gap Eg).

The band gap of ~2.1 eV was found for the prepared ABI films using Tauc relation (Figure 3.3). The perovskite or perovskite like materials with such band gap are more suitable for tandem solar cells. In last few years, perovskite materials with band gap 1.5-2.2 eV have been widely employed as light absorbing material for the development of highly stable and Pb free PSCs. The previous reports showed that the structural surface morphology of such perovskite materials has large impact on the performance of the fabricated Pb free PSCs devices. We have recorded the field emission scanning electron microscopic (FE-SEM) pictures of the prepared thin films of ABI-1, ABI-2 and ABI-3 perovskites. The FE-SEM results have been presented in Figure 3.4. The FE-SEM picture showed that ABI-1 crystalized rapidly which may be due to the high vapor pressure (~2.7 Torr) and weak Lewis basicity of DMF. However, the introduction of DMSO may suppress the fast crystallization process due to its strong Lewis basicity (due to the presence of electron-donating methyl group) and lower vapor pressure (~0.42 Torr).

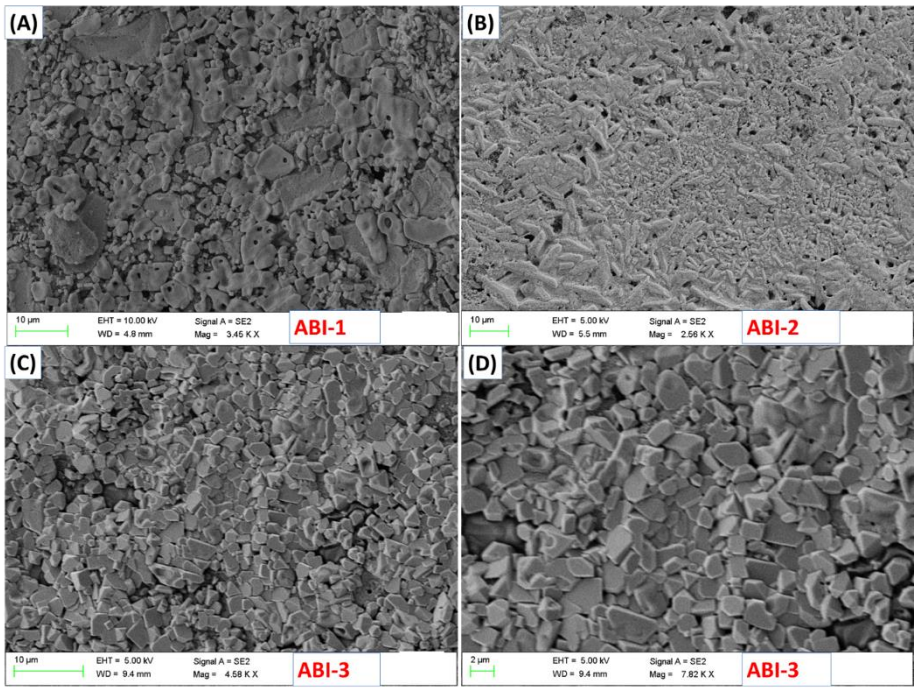

Figure 3.4. FE-SEM images of $(NH_4)_3Bi_2I_9$, ABI-1 (DMSO:DMF= 0:1) (A), ABI-2 (DMSO:DMF=0.2:0.8) (B) and ABI-3 (DMSO:DMF=0.4:0.6) (C–D), (thin film on FTO, room temperature).

Thus, it can be clearly seen from the FE-SEM images of the ABI-2 and ABI-3 that the introduction of DMSO controls the nucleation growth by controlling the fast crystallization process which resulted to the better and improved surface morphology of the ABI-2 and ABI-3 over ABI-1. The high quality and improved film of ABI-3 was obtained compare to the ABI-1 and ABI-2 (Figures 3.4 A-D).

This suggested that the use of DMSO: DMF with 0.4:0.6 ratio suppress the rapid crystallization process more effectively. Furthermore, the elemental composition of the ABI was confirmed by energy dispersive X-ray (EDX) spectroscopy. The EDX investigations showed the presence of N, Bi and I elements in the ABI structure. The weight percentage and atomic percentage of the N, Bi and I have been presented in Figure 3.5A whereas EDX spectrum has been depicted in Figure 3.5B. Further we have fabricated the Pb free PSCs using ABI-1, ABI-2 and ABI-3 perovskite light absorbers. The schematic picture of the fabricated Pb free PSCs has been displayed in Scheme 3.2 A. The energy level diagram of the proposed Pb free PSCs has been presented in Scheme 3.2 B.

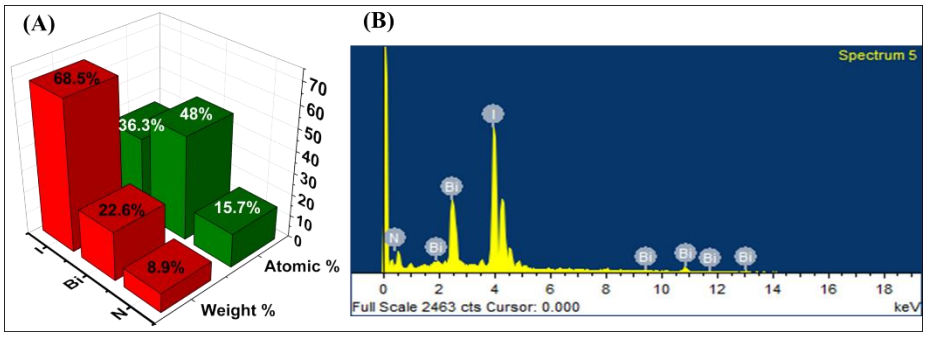

Figure 3.5. EDX data of the $(NH_4)_3Bi_2I_9$ ABI-2 (DMSO:DMF=0.2:0.8) (A-B).

It is understood that the electron-hole pairs generated in the ABI perovskite material. The generated electron has to be transported to the working glass substrate via electron transporter. The remaining hole in the ABI perovskite material has to be transported via hole transporter to complete the working mechanism of the Pb free PSCs. The overall working mechanism of the Pb free PSCs can be easily understood by Scheme 3.2 B.

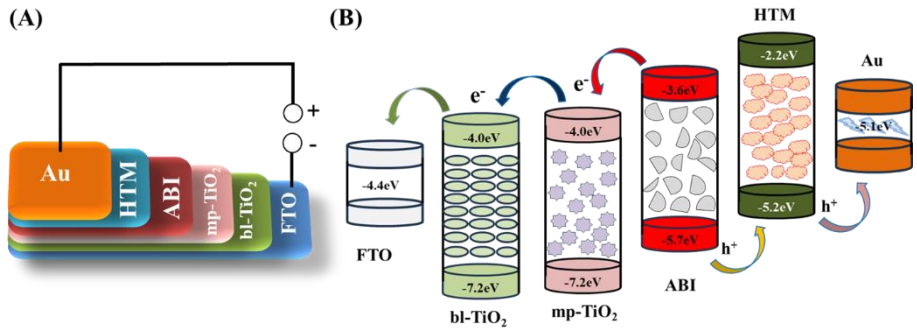

Scheme 3.2. Schematic picture (A) and energy level diagram (B) of the $(NH_4)_3Bi_2I_9$ based PSCs.

The energy level values of the working substrate (FTO), blocking/mesoporous TiO_2, hole transport material (Spiro-MeOTAD) and Au were adopted from the previous literature. However, the probable HOMO and LUMO energy level values of the ABI were determined according to previous reports. The cyclic voltammetry (CV) was employed to determine the onset reduction potential (E_{red}) of the ABI. The recorded CV curve of the ABI has been presented in Figure 3.6 A. The conduction band energy (E_{CB}) of the ABI was calculated using equation (a) whereas the valence band energy (E_{VB}) was

determined by employing equation (b). The equation (Equation 3.3, 3.4) are given below:

E_{CB} (E_{LUMO}) = - (E_{red} + 4.725) eV ……(Equation 3.3)

E_{VB} (E_{HOMO}) = -(E_{CB} - E_g) eV …….. (Equation 3.4)

(Herein, E_g=band gap calculated from UV-vis spectra and E_{CB}= conduction band energy value determined by equation (a)).

The calculated energy values of the E_{CB} (E_{LUMO}) and E_{VB} (E_{HOMO}) of the ABI perovskite material has been presented in Figure 3.6 B. The obtained energy values of the E_{CB} (E_{LUMO}) and E_{VB} (E_{HOMO}) of the ABI perovskite material are well matched with the energy level values of the electron transport layer and hole transport material. This suggested the potential of the ABI as light absorber for Pb free PSCs.

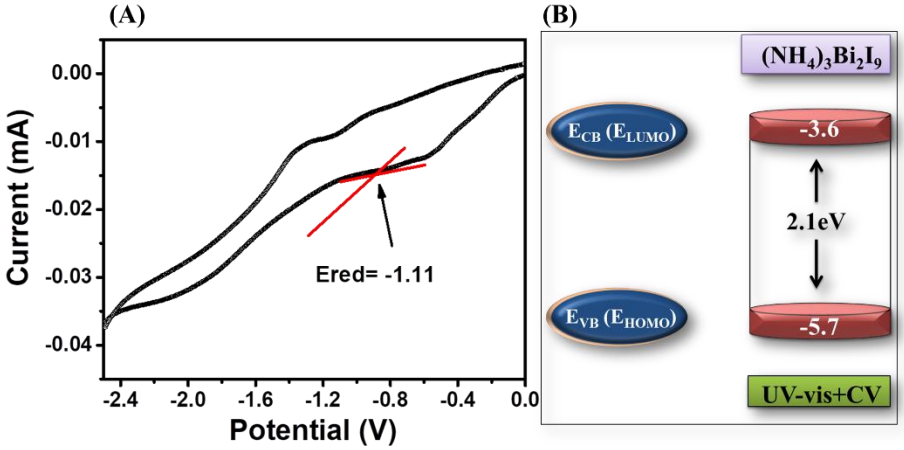

Figure 3.6. CV curve (A) and energy level diagram (B) of $(NH_4)_3Bi_2I_9$. (Glassy carbon electrodes, Ag/AgCl and Pt wire utilized as working electrode, the reference and counter electrodes respectively. The potential of the ferrocene/ferrocenium (Fc/Fc^+) in the three-electrode system has been determined using the GCE. $(NH_4)_3Bi_2I_9$ was dissolved in 0.1M tetrabutylammonium hexafluorophosphate ($TBAPF_6$) in acetonitrile containing 0.001M ferrocene at a scan rate of 20 mV/s to record the $(NH_4)_3Bi_2I_9$ CV curve).

The short circuit photocurrent density (J)-voltage (V) curves of the fabricated PSCs devices were recorded to investigate the photovoltaic performance. The J-V curves of the PSCs devices using ABI-1, ABI-2 and ABI-3 perovskite light absorbers have been presented in Figure 3.7.

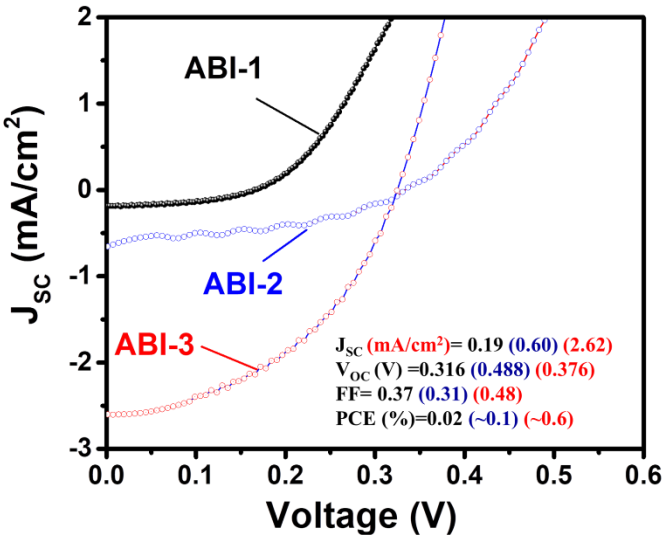

Figure 3.7. J–V curves of $(NH_4)_3Bi_2I_9$ ABI-1 (DMSO:DMF= 0:1), ABI-2 (DMSO:DMF=0.2:0.8) and ABI-3 (DMSO:DMF=0.4:0.6) perovskite light absorbers-based PSCs (Forward Bias, AM 1.5 G; 100 mW/cm^2, Active Area 0.1 cm^2, Room temperature).

The highest PCE of ~0.6% was obtained for ABI-3 based PSCs whereas the lowest PCE of 0.02% was observed for ABI-1 based PSCs device. Moreover, the developed PSCs devices exhibited descent open circuit voltage. The highest short-circuit photocurrent density was observed for the ABI-3 based PSCs device.

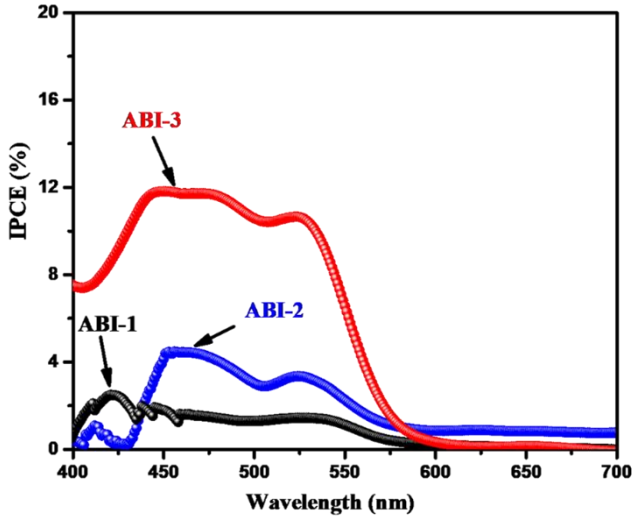

Figure 3.8. IPCE of $(NH_4)_3Bi_2I_9$ ABI-1 (DMSO:DMF= 0:1), ABI-2 (DMSO:DMF=0.2:0.8) and ABI-3 (DMSO:DMF=0.4:0.6) perovskite light absorbers-based PSCs (Room temperature).

Further, incident-photon-current-conversion (IPCE) of ABI-1, ABI-2 and ABI-3 based PSCs were also obtained (Figure 3.8). The observations

clearly show the highest IPCE value for ABI-3 based PSCs device which may be responsible for improved Jsc value of ABI-3 based PSCs. The J-V curves and IPCE results showed that solvent engineering approach is effective to enhance the short-circuit photocurrent density and PCE. Subsequently, we have obtained steady-state photoluminescence (PL) spectra of the ABI-1, ABI-2 and ABI-3 based PSCs, and results have been summarized in Figure 3.9. The PL spectrum of ABI-3 showed lower intensity compared ABI-1 or ABI-2 which suggested better charge extraction in ABI-3.

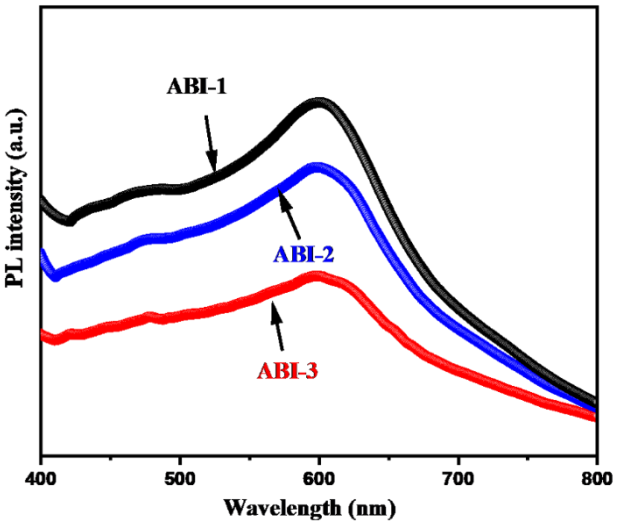

Figure 3.9. Steady-state PL of of $(NH_4)_3Bi_2I_9$, ABI-1 (DMSO:DMF= 0:1), ABI-2 (DMSO:DMF=0.2:0.8) and ABI-3 (DMSO:DMF=0.4:0.6) perovskite light absorbers-based PSCs (Room temperature).

The time-resolved PL (TRPL) of the ABI-1, ABI-2 and ABI-3 based PSCs were also obtained to examine the electron life time. The TRPL of the ABI-1, ABI-2 and ABI-3 based PSCs have been presented in Figure 3.10. ABI-1 and ABI-2 based PSCs device showed the electron life time of 0.15 ns and 0.24 ns whereas ABI-3 based PSCs device exhibited life time of 0.49 ns. This showed that ABI-3 based PSCs has better charge-transport carrier properties compared to the ABI-1 or ABI-2 based PSCs. This may be attributed to the relatively improved/uniform surface of ABI-3 film compared to the ABI-2 or ABI-1 film. The photovoltaic parameters of the fabricated PSCs devices have been presented in Table A2.

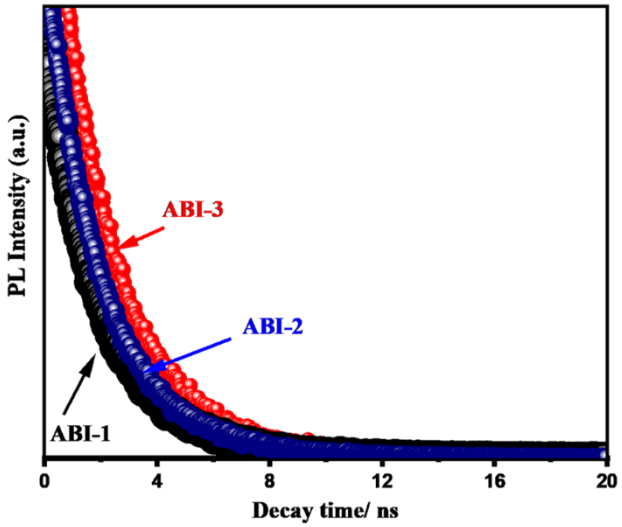

Figure 3.10. Time-resolved PL of $(NH_4)_3Bi_2I_9$, ABI-1 (DMSO:DMF= 0:1), ABI-2 (DMSO:DMF=0.2:0.8) and ABI-3 (DMSO:DMF=0.4:0.6) perovskite light absorbers-based PSCs (Room temperature).

The development of high performance Pb free PSCs is a need of today's world. In this regard, numerous efforts were made by the scientific community. Previously different kind of light absorbers have been adopted to construct the Pb free PSCs. Lan *et al*. [32]and Fabian *et al*. [33] utilized photovoltaic activity of the formamidinium bismuth iodide ($(FA)_3Bi_2I_9$) and 1,6-hexanediammonium bismuth iodide ($(HDABiI_5)$) perovskite-like materials for photovoltaic applications respectively.

In other case, $(CH_3NH_3)_3Bi_2I_9$ has also been employed in PSCs applications[34-37]. The developed PSCs using Bi based perovskite materials showed excellent stability compare to the Pb based PSCs but the performance was extremely poor. In other efforts, $(CH_3NH_3)_3Sb_2I_9$ has also been explored in photovoltaic devices but overall performance was poor [21,38]. In other reports, Sn and Cu based perovskite structures have also been employed for the development of Pb free PSCs [10,15,40]. In another work, Pb-free bulk heterojunction photovoltaic cell was also reported [41]. Recently, our groups also developed Pb free PSCs using bismuth, antimony and copper halide perovskite-like materials which showed decent Voc [42-44]. In present work, we have explored the optoelectronic and photovoltaic properties of the ABI. The performance of the ABI-3 was found to be comparable with the recent

reports (Table A3). We believe the photovoltaic activity of the ABI based PSCs can be further enhanced by adopting different device structures and better charge extraction or electron transport layers.

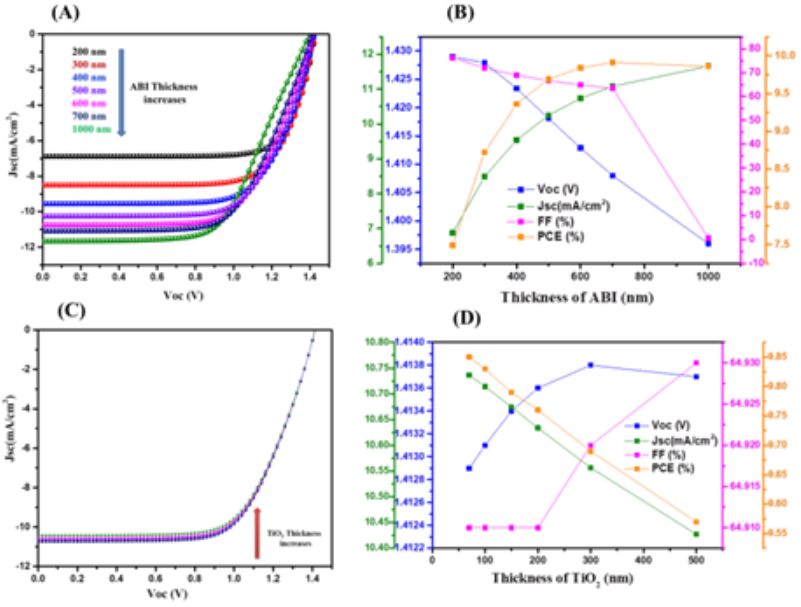

Figure 3.11. (A) JV curves and (B) photovoltaic parameters of FTO(500 nm)/TiO_2(70 nm)/ABI(varying)/Spiro-OMeTAD(20 0nm). JV curves (C) and photovoltaic parameters (D) of FTO(500 nm)/TiO_2(varying)/ABI(600 nm)/Spiro-OMeTAD(200 nm).

The $(NH_4)_3Bi_2I_9$ perovskite has the potential for photovoltaic applications. Recently simulation investigations have received enormous attention for optimizing PCE of the PSCs. Thus, we have employed numerical simulation approach for theoretical investigation using SCAPS-1D software [45]. The simulated J-V characteristics of the ABI device with varying absorber thickness are shown in Figure 3.11A. According to the simulated data, it was observed that with an increase in Jsc, a maximum PCE of more than 10% may be achieved with a 600 nm absorber thickness. Figure 3.11 B displayed the photovoltaic performance of the ABI device, including FF, Voc, Jsc, and PCE.

Furthermore, the impact of TiO_2 thickness was studied, and it was discovered that a 70 nm thick TiO_2 layer showed ~9.9% efficiency (Figure 3.11 C, D) whereas, Voc and FF increases with an increase in layer of TiO_2. The influence of thickness of Spiro-OMeTAD was also investigated and it was observed that at 200 nm thickness of Spiro-

OMeTAD layer, a considerable increase in PCE of up to 9.8% is seen (Figure 3.12 A, B). It might be because the Spiro-OMeTAD and the HOMO level of the perovskite absorber have superior band matching.

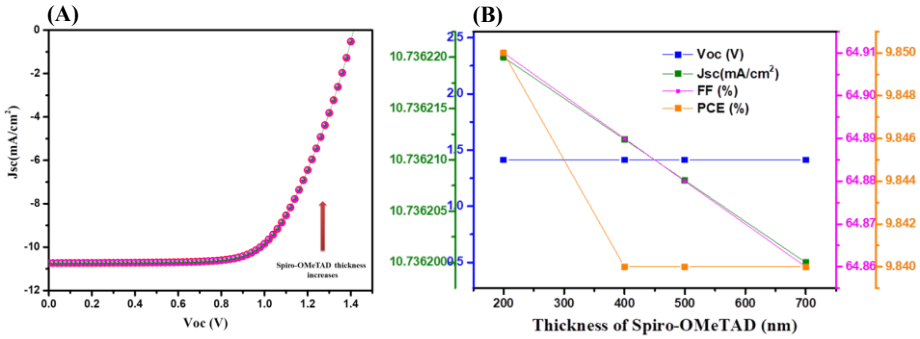

Figure 3.12. (A) JV curves and (B) Photovoltaic parameters of JV curves of FTO(500 nm)/TiO_2(70 nm)/ABI(600 nm)/Spiro-OMeTAD(varying).

3.4. Summary

In summary, for the first time, we have prepared the thin films of $(NH_4)_3Bi_2I_9$ perovskite using solvent engineering approach. The optoelectronic properties of the $(NH_4)_3Bi_2I_9$ perovskite were investigated. The solvent engineering approach and the utilization of anti-solvent (chlorobenzene) influences the crystallization process. Furthermore, perovskite solar cells were developed by utilizing $(NH_4)_3Bi_2I_9$ perovskite light absorber. The developed perovskite solar cells exhibited better open circuit voltage and suggested the potential of $(NH_4)_3Bi_2I_9$ perovskite as energy material for photovoltaic applications.

3.5. References

1. Kour R., Arya S., Verma S., Gupta J., Bandhoria P., Bharti V., Datt R., Gupta V. (2019), Potential Substitutes for Replacement of Lead in Perovskite Solar Cells: A Review, Global Challenges, 3, 1900050 (DOI: 10.1002/gch2.201900050).
2. Jeon N. J., Lee H. G., Kim Y. C., Seo J., Noh J. H., Lee J., Seok S. I. (2014), o-Methoxy Substituents in Spiro-OMeTAD for Efficient Inorganic–Organic Hybrid Perovskite Solar Cells, J. Am. Chem. Soc., 136, 7837–7840 (DOI: 10.1021/ja502824c).
3. Ahmad K., M. Mobin S. (2017), Graphene oxide based planar heterojunction perovskite solar cell under ambient condition, New Journal of Chemistry, 41, 14253–14258 (DOI: 10.1039/C7NJ02847D).
4. Kojima A., Teshima K., Shirai Y., Miyasaka T. (2009), Organometal Halide Perovskites as Visible-Light Sensitizers for Photovoltaic Cells, J. Am. Chem. Soc., 131, 6050–6051 (DOI: 10.1021/ja809598r).
5. Gao X.-X., Luo W., Zhang Y., Hu R., Zhang B., Züttel A., Feng Y., Nazeeruddin M. K. (2020), Stable and High-Efficiency Methylammonium-Free Perovskite Solar Cells, Advanced Materials, 32, 1905502 (DOI: 10.1002/adma.201905502).
6. Ahmad K., Ansari S. N., Natarajan K., Mobin S. M. (2018), Design and Synthesis of 1D-Polymeric Chain Based $[(CH_3NH_3)_3Bi_2Cl_9]_n$ Perovskite: A New Light Absorber Material for Lead Free Perovskite Solar Cells, ACS Appl. Energy Mater., 1, 2405–2409 (DOI: 10.1021/acsaem.8b00437).
7. Ahmad K., Ansari S. N., Natarajan K., Mobin S. M. (2019), A $(CH_3NH_3)_3Bi_2I_9$ Perovskite Based on a Two-Step Deposition Method: Lead-Free, Highly Stable, and with Enhanced Photovoltaic Performance, ChemElectroChem, 6, 1192–1198 (DOI: 10.1002/celc.201801322).
8. K. Noel N., D. Stranks S., Abate A., Wehrenfennig C., Guarnera S., Haghighirad A.-A., Sadhanala A., E. Eperon G., K. Pathak S.,

B. Johnston M., Petrozza A., M. Herz L., J. Snaith H. (2014), Lead-free organic–inorganic tin halide perovskites for photovoltaic applications, Energy & Environmental Science, 7, 3061–3068 (DOI: 10.1039/C4EE01076K).

9. Hao F., Stoumpos C. C., Cao D. H., Chang R. P. H., Kanatzidis M. G. (2014), Lead-free solid-state organic–inorganic halide perovskite solar cells, Nature Photonics, 8, 489–494 (DOI: 10.1038/nphoton.2014.82).
10. Liu X., Yang, Z., Chueh C.-C., Rajagopal A., T. Williams S., Sun Y., K.-Y. Jen A. (2016), Improved efficiency and stability of Pb–Sn binary perovskite solar cells by Cs substitution, Journal of Materials Chemistry A, 4, 17939–17945 (DOI: 10.1039/C6TA07712A).
11. Song T.-B., Yokoyama T., Stoumpos C. C., Logsdon J., Cao D. H., Wasielewski M. R., Aramaki S., Kanatzidis M. G. (2017), Importance of Reducing Vapor Atmosphere in the Fabrication of Tin-Based Perovskite Solar Cells, J. Am. Chem. Soc., 139, 836–842 (DOI: 10.1021/jacs.6b10734).
12. Ke W., Stoumpos C. C., Zhu M., Mao L., Spanopoulos I., Liu J., Kontsevoi O. Y., Chen M., Sarma D., Zhang Y., Wasielewski M. R., Kanatzidis M. G. (2017), Enhanced photovoltaic performance and stability with a new type of hollow 3D perovskite {en}FASnI3, Science Advances, 3, e1701293 (DOI: 10.1126/sciadv.1701293).
13. Krishnamoorthy T., Ding H., Yan C., Leong W. L., Baikie T., Zhang Z., Sherburne M., Li S., Asta M., Mathews N., Mhaisalkar S. G. (2015), Lead-free germanium iodide perovskite materials for photovoltaic applications, J. Mater. Chem. A, 3, 23829–23832 (DOI: 10.1039/C5TA05741H).
14. Cortecchia D., Dewi H. A., Yin J., Bruno A., Chen S., Baikie T., Boix P. P., Grätzel M., Mhaisalkar S., Soci, C., Mathews, N. (2016), Lead-Free MA2CuClxBr4–x Hybrid Perovskites, Inorg. Chem., 55, 1044–1052 (DOI: 10.1021/acs.inorgchem.5b01896).
15. Li X., Zhong X., Hu Y., Li B., Sheng Y., Zhang Y., Weng C., Feng M., Han H., Wang J. (2017), Organic–Inorganic Copper(II)-Based Material: A Low-Toxic, Highly Stable Light Absorber for

Photovoltaic Application, J. Phys. Chem. Lett., 8, 1804–1809 (DOI: 10.1021/acs.jpclett.7b00086).

16. Ahmad K., Mobin S. M. (2020), Organic–Inorganic Copper (II)-Based Perovskites: A Benign Approach toward Low-Toxicity and Water-Stable Light Absorbers for Photovoltaic Applications, Energy Technology, 8, 1901185 (DOI: 10.1002/ente.201901185).
17. Li X.-L., Li Z., Zhang G., Yang G.-J. (2020), Lead-free perovskite $[H_3NC_6H_4NH_3]CuBr_4$ with both a bandgap of 1.43 eV and excellent stability, J. Mater. Chem. A, 8, 5484–5488 (DOI: 10.1039/C9TA12872G).
18. Li X., Li B., Chang J., Ding B., Zheng S., Wu Y., Yang J., Yang G., Zhong X., Wang J. (2018), $(C_6H_5CH_2NH_3)_2CuBr_4$: A Lead-Free, Highly Stable Two-Dimensional Perovskite for Solar Cell Applications, ACS Appl. Energy Mater., 1, 2709–2716 (DOI: 10.1021/acsaem.8b00372).
19. Vargas B., Ramos E., Pérez-Gutiérrez E., Alonso J. C., Solis-Ibarra D. (2017), A Direct Bandgap Copper–Antimony Halide Perovskite, J. Am. Chem. Soc., 139, 9116–9119 (DOI: 10.1021/jacs.7b04119).
20. Zuo C., Ding, L. (2017), Lead-free Perovskite Materials $(NH_4)_3Sb_2I_xBr_{9-x}$, Angewandte Chemie International Edition, 56, 6528–6532 (DOI: 10.1002/anie.201702265).
21. Hebig J.-C., Kühn I., Flohre J., Kirchartz T. (2016), Optoelectronic Properties of $(CH_3NH_3)_3Sb_2I_9$ Thin Films for Photovoltaic Applications, ACS Energy Lett., 1, 309–314 (DOI: 10.1021/acsenergylett.6b00170).
22. Harikesh P. C., Mulmudi H. K., Ghosh B., Goh T. W., Teng Y. T., Thirumal K., Lockrey M., Weber K., Koh T. M., Li S., Mhaisalkar S., Mathews N. (2016), Rb as an Alternative Cation for Templating Inorganic Lead-Free Perovskites for Solution Processed Photovoltaics, Chem. Mater., 28, 7496–7504 (DOI: 10.1021/acs.chemmater.6b03310).
23. Okano T., Suzuki Y. (2017), Gas-assisted coating of Bi-based (CH3NH3)3Bi2I9 active layer in perovskite solar cells, Materials Letters, 191, 77–79 (DOI: 10.1016/j.matlet.2017.01.047).

24. Kulkarni A., Singh T., Ikegami M., Miyasaka T. (2017), Photovoltaic enhancement of bismuth halide hybrid perovskite by N-methyl pyrrolidone-assisted morphology conversion, RSC Adv., 7, 9456–9460 (DOI: 10.1039/C6RA28190G).
25. Huang J., Gu Z., Zhang X., Wu G., Chen, H. (2018), Lead-free $(CH_3NH_3)_3Bi_2I_9$ perovskite solar cells with fluorinated PDI films as organic electron transport layer, Journal of Alloys and Compounds, 767, 870–876 (DOI: 10.1016/j.jallcom.2018.07.185).
26. Öz S., Hebi, J.-C., Jung E., Singh T., Lepcha A., Olthof S., Jan F., Gao Y., German R., van Loosdrecht P. H. M., Meerholz K., Kirchartz T., Mathur S. (2016), Zero-dimensional $(CH_3NH_3)_3Bi_2I_9$ perovskite for optoelectronic applications, Solar Energy Materials and Solar Cells, 158, 195–201 (DOI: 10.1016/j.solmat.2016.01.035).
27. Abulikemu M., Ould-Chikh S., Miao X., Alarousu E., Murali B., Ndjawa G. O. N., Barbé J., Labban A. E., Amassian A., Gobbo, S. D. (2016), Optoelectronic and photovoltaic properties of the air-stable organohalide semiconductor $(CH_3NH_3)_3Bi_2I_9$, J. Mater. Chem. A, 4, 12504–12515 (DOI: 10.1039/C6TA04657F).
28. Filip M. R., Hillman S., Haghighirad A. A., Snaith H. J., Giustino F. (2016), Band Gaps of the Lead-Free Halide Double Perovskites $Cs_2BiAgCl_6$ and $Cs_2BiAgBr_6$ from Theory and Experiment, J. Phys. Chem. Lett., 7, 2579–2585 (DOI: 10.1021/acs.jpclett.6b01041).
29. Shao Z., Le Mercier T., Madec M. B., Pauporté T. (2018), $AgBi_2I_7$ layers with controlled surface morphology for solar cells with improved charge collection, Materials Letters, 221, 135–138 (DOI: 10.1016/j.matlet.2018.03.085).
30. Sun S., Tominaka S., Lee J.-H., Xie F., Bristowe P. D., Cheetham A. K. (2016), Synthesis, crystal structure, and properties of a perovskite-related bismuth phase, $(NH_4)_3Bi_2I_9$, APL Materials, 4, 031101 (DOI: 10.1063/1.4943680).
31. Zhuang R., Wang X., Ma W., Wu Y., Chen X., Tang L., Zhu H., Liu J., Wu L., Zhou W., Liu X., Yang Y. (Michael) (2019), Highly sensitive X-ray detector made of layered perovskite-like

$(NH_4)_3Bi_2I_9$ single crystal with anisotropic response, Nat. Photonics, 13, 602–608 (DOI: 10.1038/s41566-019-0466-7).

32. Lan C., Liang G., Zhao S., Lan H., Peng H., Zhang D., Sun H., Luo J., Fan P. (2019), Lead-free formamidinium bismuth perovskites $(FA)_3Bi_2I_9$ with low bandgap for potential photovoltaic application, Solar Energy, 177, 501–507 (DOI: 10.1016/j.solener.2018.11.050).
33. Fabian D. M., Ardo, S. (2016), Hybrid organic–inorganic solar cells based on bismuth iodide and 1,6-hexanediammonium dication, J. Mater. Chem., A 4, 6837–6841 (DOI: 10.1039/C6TA00517A).
34. Hoefler S. F., Rath T., Fischer R., Latal C., Hippler D., Koliogiorgos A., Galanakis I., Bruno A., Fian A., Dimopoulos T., Trimmel, G. (2018), A Zero-Dimensional Mixed-Anion Hybrid Halogenobismuthate(III) Semiconductor: Structural, Optical, and Photovoltaic Properties, Inorg. Chem., 57, 10576–10586 (DOI: 10.1021/acs.inorgchem.8b01161).
35. Tang M.-C., Barrit D., Munir R., Li R., Barbé J. M., Smilgies D.-M., Gobbo S. D., Anthopoulos T. D., Amassian A. (2019), Bismuth-Based Perovskite-Inspired Solar Cells: In Situ Diagnostics Reveal Similarities and Differences in the Film Formation of Bismuth- and Lead-Based Films, Solar RRL, 3, 1800305 (DOI: 10.1002/solr.201800305).
36. Sanders S., Stümmler D., Pfeiffer P., Ackermann N., Simkus G., Heuken M., Baumann P. K., Vescan A., Kalisch H. (2019), Chemical Vapor Deposition of Organic-Inorganic Bismuth-Based Perovskite Films for Solar Cell Application, Sci Rep, 9, 9774 (DOI: 10.1038/s41598-019-46199-4).
37. Park B.-W., Philippe B., Zhang X., Rensmo H., Boschloo G., Johansson E. M. J. (2015), Bismuth Based Hybrid Perovskites $A_3Bi_2I_9$ (A: Methylammonium or Cesium) for Solar Cell Application, Advanced Materials, 27, 6806–6813 (DOI: 10.1002/adma.201501978).
38. Chatterjee S., Pal A. J. (2018), Tin(IV) Substitution in $(CH_3NH_3)_3Sb_2I_9$: Toward Low-Band-Gap Defect-Ordered Hybrid

Perovskite Solar Cells, ACS Appl. Mater. Interfaces, 10, 35194–35205 (DOI: 10.1021/acsami.8b12018).

39. Elseman A. M., Shalan A. E., Sajid S., Rashad M. M., Hassan A. M., Li M. (2018), Copper-Substituted Lead Perovskite Materials Constructed with Different Halides for Working $(CH_3NH_3)_2Cu_{X4}$-Based Perovskite Solar Cells from Experimental and Theoretical View, ACS Appl. Mater. Interfaces, 10, 11699–11707 (DOI: 10.1021/acsami.8b00495).
40. Ahmad K., Kumar P., Mobin, S. M. (2020), A Two-Step Modified Sequential Deposition Method-based Pb-Free $(CH_3NH_3)_3Sb_2I_9$ Perovskite with Improved Open Circuit Voltage and Performance, ChemElectroChem, 7, 946–950 (DOI: 10.1002/celc.201902107).
41. Hu W., He X., Fang Z., Lian W., Shang Y., Li X., Zhou W., Zhang M., Chen T., Lu Y., Zhang L., Ding L., Yang, S. (2020), Bulk heterojunction gifts bismuth-based lead-free perovskite solar cells with record efficiency, Nano Energy, 68, 104362 (DOI: 10.1016/j.nanoen.2019.104362).
42. Ahmad K., Kumar P., Shrivastava P., Mobin S. M. (2022), Sn(IV) Inserted Lead-Free Perovskite Materials $(MA_3(Bi_{1-x}Sn_x)_2I_9)$ as Light Absorbers: Bandgap Engineering and Enhanced Photovoltaic Performance, Energy Technology, 10, 2100717 (DOI: 10.1002/ente.202100717).
43. Kumar P., Ahmad K., Dagar J., Unger E., Mobin S. M. (2021), Two-Step Deposition Approach for Lead Free $(NH_4)_3Sb_2I_9$ Perovskite Solar Cells with Enhanced Open Circuit Voltage and Performance, ChemElectroChem, 8, 3150–3154 (DOI: 10.1002/celc.202100957).
44. Ahmad K., Kumar P., Mobin S. M. (2020), Inorganic Pb-Free Perovskite Light Absorbers for Efficient Perovskite Solar Cells with Enhanced Performance, Chemistry – An Asian Journal, 15, 2859–2863 (DOI: 10.1002/asia.202000680).
45. Burgelman M., Nollet P., Degrave, S. (2000), Modelling polycrystalline semiconductor solar cells, Thin Solid Films, 361–362, 527–532 (DOI: 10.1016/S0040-6090(99)00825-1).

CHAPTER 4

Improved Photovoltaic Performance of Pb-Free $AgBi_2I_7$ based Photovoltaics

4.1. Introduction

Due to their exceptional semiconducting characteristics, such as a relatively low carrier recombination rates, [1,2] long carrier diffusion lengths,[2] low charge carrier mobilities, [3,4] stoichiometry-tunable band gap,[5,6] and high absorption coefficients, lead-based halide perovskites have recently attracted a lot of attention [7]. Formamidinium lead iodide ($FAPbI_3$), one of the perovskite systems, has drawn the most interest because of its outstanding performance in thin-film solar cells, where it can achieve power conversion efficiencies (PCEs) of 25.7% till 2022 [8]. However, the presence of noxious Pb and the product's fragility when exposed to moisture and temperatures have led to grave worries about its viability for commercial use. There has been a lot of interest in developing halide perovskite solar cells that are non or low-toxic and air stable. As a result, efforts have been made to develop perovskite solar cells and seek alternatives to lead. Many perovskites based on tin (Sn) [9] and germanium (Ge) [10] have been investigated to address the issue of toxicity. Song *et al.* [11] designed and manufactured Sn-based perovskite materials containing Caesium (Cs) as a cation, with $CsSnI_3$ and $CsSnBr_3$ perovskite with efficiency of 3.04% and 1.83%, respectively. In addition, Ke *et al.* [12] used an unique hollow 3-D perovskite [$enFASnI_3$] as a light absorber material in perovskite solar cells (PSCs), with a 7.1% efficiency. Mhaisalkar and colleagues used a Ge-based $AGeI_3$ perovskite-like material [13]. These Sn and Ge based perovskite-like materials have a high efficiency, but they must be handled with caution since they are air sensitive and need inert environment to be stable. The perovskite structure is distorted by the quick shift in oxidation state of Sn and Ge by +2 oxidation number. Moreover, when compared to Pb, these Sn and Ge based perovskites are unable to reach high efficiency. However, instability and poor

performance of Sn and Ge based devices in ambient conditions owing to disproportionation are disappointing.

There have been several reports on the use of copper (Cu) as a metal ion in PSCs, utilizing a lead-free approach. Cu as $MA_2CuCl_xBr_{4-x}$, $C_6H_4NH_2CuBr_2I$ perovskite material was used as a light absorber in photovoltaic applications by Methews *et al.* [14], Ahmad *et al.* [15], and Li *et al*. [16] Although these Cu-based perovskites have high stability, they are inefficient in producing good PCE. Yang *et al.* [17], Wang *et al.* [18], and Vargas *et al.* [19] study the optoelectronic activity of $(C_6H_5CH_2NH_3)_2CuBr_4$, $(H_3NC_6H_4NH_3)CuBr_4$, and $Cs_4CuSb_2Cl_{12}$ perovskite materials, respectively. Further, lead (II), bismuth (Bi^{3+}), and antimony (Sb^{3+}) ions are isoelectronic ($6s^2$), and they may be stable and safe substitutes in thin-film photovoltaic (PV) systems. Bismuth (Bi^{+3}) may be used to manufacture the PSCs device as a non-toxic metal ion, which is promising for replacing Pb and Sn metals. The $A_3Bi_2I_9$ basic formula (A= Cs^+, MA^+, NH_4^+, B=Bi^{+3}, Sb^{+3}, X= Cl^-, Br^-, I^-) has been widely employed in the design and manufacture of lead-free perovskite solar cells. Mobin *et al.* [20] create $Cs_3Sb_2I_9$ and $Cs_3Bi_2I_9$ perovskites with a PCE of above 1%. Hebig *et al.* [21] and Ahmad *et al.* [22] used $MA_3Sb_2I_9$ for photovoltaic applications, whereas Kumar *et al.* [23] and Zuo *et al.* [24] used $(NH_4)_3Sb_2I_9$ perovskite as the light absorber and developed a device that demonstrated the potential of Bi^{+3} in PSC. Okano *et al.* [25] and Ahmad *et al.* [26] employed a gas-assisted and two-step manufacturing technique to prepare $(CH_3NH_3)_3Bi_2I_9$ for PSC, respectively. Kulkarni *et al.* [27] used an N-methyl pyrrolidone-assisted method and achieved 0.31% PCE. Huang *et al.* [28] obtained 0.06% PCE using fluorinated perylene diimide (FPDI) as an ETL (electron transport layer) in $(CH_3NH_3)_3Bi_2I_9$ PSC. This low PCE might be due to the FPDI's weak surface or charge extraction issue. Sun *et al.* [29], and Zhuang *et al.* [30] on the other hand, look into the crystalline properties of $(NH_4)_3Bi_2I_9$ perovskite and use them in X-ray and PSCs, respectively. Furthermore, their broad band gap and low PCE reduce the likelihood of commercialization. To improve photovoltaic efficiency, 3D structures based on silver-bismuth iodide are used. Filip *et al.* suggested double

halide perovskites like $Cs_2BiAgCl_6$ and $Cs_2BiAgBr_6$ in 2016 [31]. $AgBi_2I_7$ perovskite has recently attracted interest because to its efficiency and narrow band gap (<2.0 eV), which improve light harvesting characteristics. Kim *et al.* [32] reported the first Ag-based PSC using Bi as the metal ion in 2016 and attained a PCE of 1.2%. However, when Shao *et al.* [33,34] and Johansson *et al.* [35] employed the same methodology, the performance of $AgBi_2I_7$ perovskite changed with photovoltaic efficiency. Reproducing the solar cell yielded just 0.52% and 0.4% efficiency [33,34,35]. $AgBi_2I_7$ perovskite's sensitivity can make up for its lack of repeatability, or it could be caused by the annealing temperature. To comprehend and modify the attributes of Ag-based Bi PSCs, we synthesised the $AgBi_2I_7$ (SBI).

4.2. Experimental section

4.2.1. Materials

We have purchased all the chemicals (BiI_3, AgI, Spiro-MeOTAD, 4-tertbutylpyridine, TiO_2 precursors, bis(trifluoromethylsulfonyl)imide lithium salt, etc.), solvents (chlorobenzene, Methanol and DMF), FTO glass substrates and other precursors from Merck, SRL, Dyesol, Loba, Sigma Aldrich, BAT-SOL, Alfa Aesar and Solaronix. The precursors and chemicals were used without any further purification.

4.2.2. Characterization methods

The Powder x-ray diffraction (PXRD) investigations were carried out on RINT 2500 V x-ray diffractometer (Rigaku, Japan), (Source=Cu Kα irradiation; $\lambda = 1.5406$ Å). Field Emission Scanning Electron microscopic (FE-SEM) images were taken on Supra 55 Zeiss Field Emission Scanning Electron microscope. Optical band gap was calculated using UV-vis absorption spectroscopy on a Varian UV–*vis* spectrophotometer (model: Carry 100). The photocurrent-voltage (*J-V*) curves were recorded under AM 1.5 G condition (100 mW/cm^2 illumination). Cyclic voltammetry (CV) measurements were carried out on Metrohm Potentiostat/Galvanostat using Nova software.

4.2.3. Electrochemical investigations

The highest occupied molecular orbital (HOMO) and lowest unoccupied molecular orbital (LUMO) energy values of the $AgBi_2I_7$ were determined by employing a UV-vis and CV approach. The CV curve of the $AgBi_2I_7$ was recorded using a 3 electrode assembly (where glassy carbon electrode acted as working electrode whereas Ag/AgCl and Pt wire electrode worked as reference and counter electrode respectively). The GCE has been used to determine the potential of the ferrocene/ferrocenium (Fc/Fc^+) in the 3 electrode system. The CV curve of the $AgBi_2I_7$ was recorded by dissolving $AgBi_2I_7$ in 0.1M tetrabutylammonium hexafuorophosphate ($TBAPF_6$) in acetonitrile having 0.001M ferrocene at scan rate=20mV/s.

4.3.4. Perovskite film preparations

0.7M BiI_3 was dissolved in 1 mL of N,N-dimethylformamide (DMF) using ultra-sonicator for 1h. Further, AgI was dissolved in the resulting solution. The molar ratio of the AgI and BiI_3 was fixed to 1:2. The obtained reaction mixture was filtered through a 0.22 μm PTFE filter. The obtained reaction mixture was denoted as SBI-D ($AgBi_2I_7$, DMF). For SBI-DM ($AgBi_2I_7$, DMF: MeOH), we have employed two-step deposition method by utilizing solvent engineering approach to prepare the $AgBi_2I_7$ films. The BiI_3 and AgI were dissolved in the mixture of DMF (0.5mL) and MeOH (0.5mL) and spin coated (1500 rpm 30sec) on to the FTO glass electrode. This prepared film was denoted as SBI-DM. The deposited films were annealed at 100°C for 15 min.

4.3.5. Device fabrication

The fluorine-doped tin oxide (FTO) was patterned and cleaned with detergent, water, acetone and 2-propanol using ultra-sonicator for 15 min. The blocking layer of TiO_2 (bl-TiO_2) was deposited using 20 mM titanium diisopropoxide bis(acetylacetonate) solution and annealed at 450°C for 30 min. Further a mesoporous film of TiO_2 (mp-TiO_2) was also deposited on to the FTO/bl-TiO_2 and sintered at 500°C for 45 min. Further, the perovskite film (SBI-D, and SBI-DM) was deposited on to the FTO/bl-TiO_2/mp-TiO_2 as described above. Further, hole transport material (HTM) layer was deposited on to the FTO/bl-TiO_2/mp-TiO_2/perovskite. The HTM was prepared using spiro-OMeTAD in

chlorobenzene (90 mg/mL) with bis(trifluoromethylsulfonyl)imide lithium salt (Li-TFSI; 99.95%), tris(2-(1H-pyrazol-1-yl)-4-tert-butylpyridine)-cobalt (III)tris-(bis(trifluoromethylsulfonyl) imide= FK209) z and 4-tert-butylpyridine (4-tBP). The molar ratio of the Li-TFSI, FK209 and 4-tBP was fixed to 0.45, 0.035 and 3.1. Finally, Au counter electrode was deposited on to the FTO/bl-TiO_2/mp-TiO_2/perovskite/HTM using thermal evaporation method.

4.3. Results and discussion

We have studied the solution engineering approach to improve the photovoltaic performance of silver- based bismuth iodide perovskite as light absorber. To our knowledge, this is the first report on the use of SBI perovskite as a light absorber in the presence of DMF and DMF: MeOH. The impact of the solvent engineering strategy on the fabrication of SBI perovskite solar cells may be immediately seen in their efficiency and photovoltaic properties. In the present work, we employed DMF and MeOH, two different solvents within an appropriate ratio, with molar ratio 1:2 of AgI and BiI_3 respectively. The $AgBi_2I_7$ DMF (SBI-D) and $AgBi_2I_7$ DMF: MeOH (SBI-DM) was spin coated on to the conductive glass electrode (FTO) at 1500 rpm for 30 seconds (Scheme 4.1).

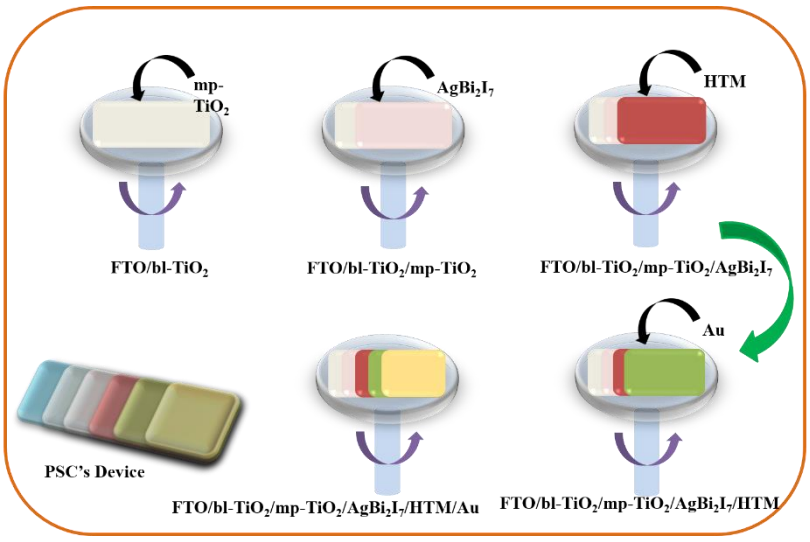

Scheme 4.1. Schematic of fabrication procedure of the perovskite solar cell.

A convincing demonstration of the equimolar ratio of both the solvent (DMF: MeOH) give highest PCE as compared to DMF only of 0.96% under illumination 1 sun condition and 30-40% humidity.

The PXRD was used to characterize the phase purity and formation of the SBI perovskite material synthesized with both DMF and DMF: MeOH solvents, with the findings shown in Figure 4.1. The formation and crystalline nature of SBI-D (DMF: MeOH=1:0) and SBI-DM (DMF: MeOH=0.5:0.5) perovskite materials were revealed by PXRD peak patterns. The growth of SBI-D and SBI-DM is supported by the appearance of a prominent diffraction peak in the (333) plane.

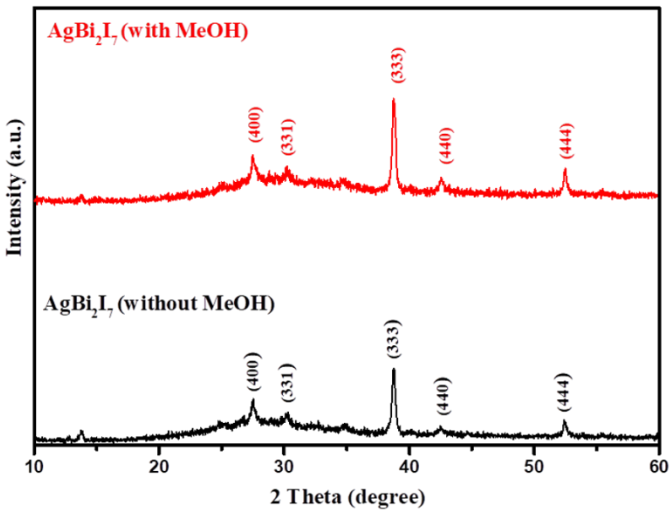

Figure 4.1. (A) PXRD peak pattern, (B) UV-vis absorption spectra of $AgBi_2I_7$ perovskite with MeOH (red), without MeOH (black) (Solvent DMF and MeOH, thin film on FTO glass, Room Temperature).

The stability of perovskite may be assessed using the Goldschmidt tolerance factor (t); when the value of "t" is between 0.8 and 1, it implies that the perovskite structure is stable [36]. Another important component in cubic crystal is the A's ionic radii, which should not be either large (then, t>1) or too small (then, t<0.8) in comparison to the B's ionic radii. If A's ionic radii are substantially bigger than B, it will not fit inside the BX_8 octahedron. It could originate from a distinct perovskite structure. The tolerance factor and octahedron ratio are described by equations 4.1, 4.2 :

$$(t)=\frac{(rA+rX)}{\sqrt{2}\,(rB+rX)} \qquad \text{……. (Equation 4.1)}$$

$(\mu)=\frac{rB}{rX}$ ……. (Equation 4.2)

(where, rA, rB, and rX stands for ionic radii of the A, B, and X presented in the perovskite (ABX_3) structure)

At t=1, the predicted perfect cubic structure was seen. In order to produce a stable octahedron for a cubic cell, the octahedron factor(μ) should be between 0.44 and 0.72. The effective ionic radii of silver (Ag) and bismuth (Bi) are 1.26 Å and 1.03 Å, respectively, which is appropriate for the creation of a stable cubic perovskite structure. We may infer and remark on the stability of our perovskite based on this finding, and therefore, it can also be employed as a light absorber material in photovoltaic application. UV/Vis spectroscopy was used to determine the optical characteristics of SBI-D and SBI-DM thin films (Figure 4.2). The absorption spectra of these perovskite materials were nearly identical.

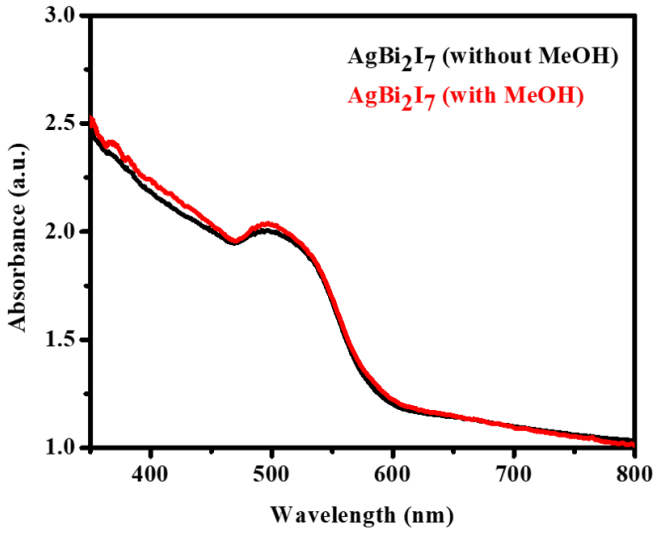

Figure 4.2. UV-vis absorption spectra of $AgBi_2I_7$ perovskite with MeOH (red), without MeOH (black) (Solvent DMF and MeOH, thin film on FTO glass, Room Temperature).

The optical band gaps for SBI-D and SBI-DM may be calculated using UV absorption spectra and linear extrapolation of Tauc plots (Figure 4.3) [37].

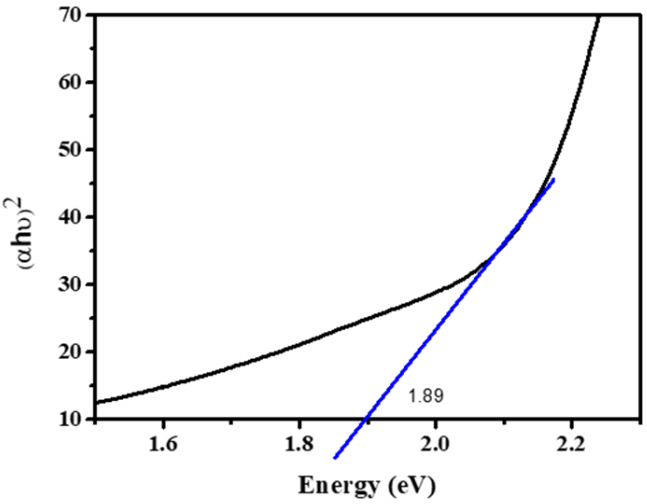

Figure 4.3. Tauc Plot of $AgBi_2I_7$ (the linear fitting region of the Tauc plot is extrapolated to the energy axis (X-axis) to estimate the optical band gap Eg).

The optical band gap was calculated to be 1.89 eV using the tauc plot $((\alpha h\nu)^n$ against $h\nu)$, where α, h and ν is the absorption coefficient, Planck's constant, and excitation frequency respectively. The computed optical band gap reveals that the produced perovskite has high absorbance and has the potential to be used as a light absorber in solar cells.

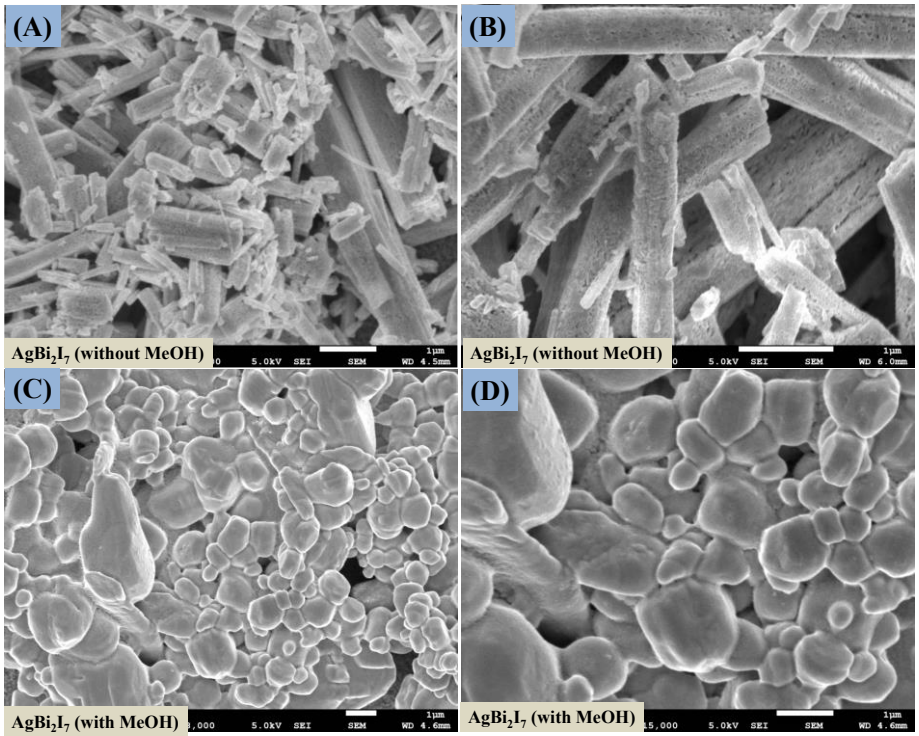

Figure 4.4. FE-scanning electron microscopy images of $AgBi_2I_7$

perovskite without MeOH (A, B), with MeOH (C, D) (Solvent DMF and MeOH, thin film on FTO glass, Room Temperature).

Surface morphology investigation was done using FE-SEM to assess the influence of participation and solvent composition on the perovskite SBI material. The surface morphology of SBI-D and SBI-DM was shown in Figure 4.4 A-D, and it was obvious that only the DMF solvent produced a rod-like shape, whereas the DMF: MeOH combination produced a distorted rod-like morphology that was converted to a uniform surface morphology. It might be due to perovskite suppressing and regulating the quick crystallization process. It has been discovered that a pinhole-free, smooth layer can improve the photovoltaic efficiency of perovskite solar cells.

When a photon strikes a perovskite material, it generates an electron and hole pair. The produced electron was excited and moved towards the LUMO (lowest unoccupied molecular orbital) level, from where it was transferred to conductive glass (FTO) through mesoporus-TiO_2 and blocking-TiO_2 LUMO levels. The produced electrons are contained in FTO glass, and while the remaining hole on perovskite materials is carried via HTM (hole transport material) to complete the circuit.

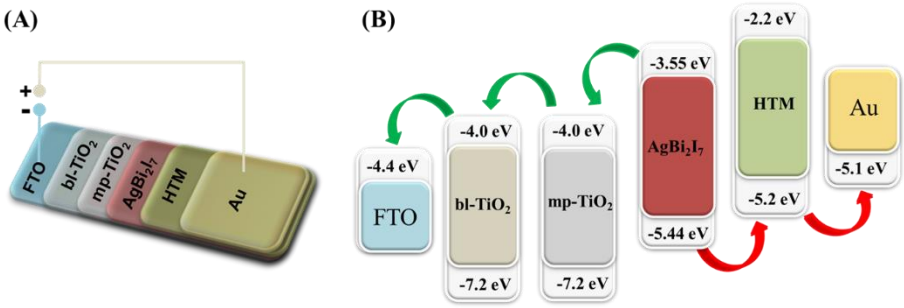

Scheme 4.2. Schematic Device structure (A) and materials energy level diagram (B) of the SBI based PSCs. Energy lavels values as per reported literature.

Scheme 4.2 explains the entire electron transfer mechanism in simple terms. All of the energy levels of conductive glass, ETL, and HTM, such as bl-TiO_2, mp-TiO_2, Spiro-MeOTAD, and Au, have been extracted from previously published literature. In addition, using UV-Visible and cyclic

voltammetry (CV) techniques, the HOMO-LUMO energy levels of our perovskite materials SBI were estimated similar to prior reports.

The optical band gap of SBI was determined using a tauc plot, whereas the onset reduction potential (E_{red}) was determined using a CV graph (Figure 4.5). We determine the energy levels of SBI perovskite material using equations 4.3, 4.4 [38].

E_{CB} (E_{LUMO}) = - (E_{red} + 4.725) eV ……(Equation 4.3)

E_{VB} (E_{HOMO}) = -(E_{CB} - E_g) eV …….. (Equation 4.4)

(Here, E_g and E_{red} stand for optical band gap and onset reduction potential, E_{CB} and E_{VB} are conduction and valance band energy levels). Henceforth, we compared our computed SBI perovskite energy levels (E_{CB} and E_{VB}) to the ETL and HTM for smooth charge transfer. The results indicate an excellent correlation between the HOMO and LUMO levels, implying that SBI perovskite has potential as a light absorber material.

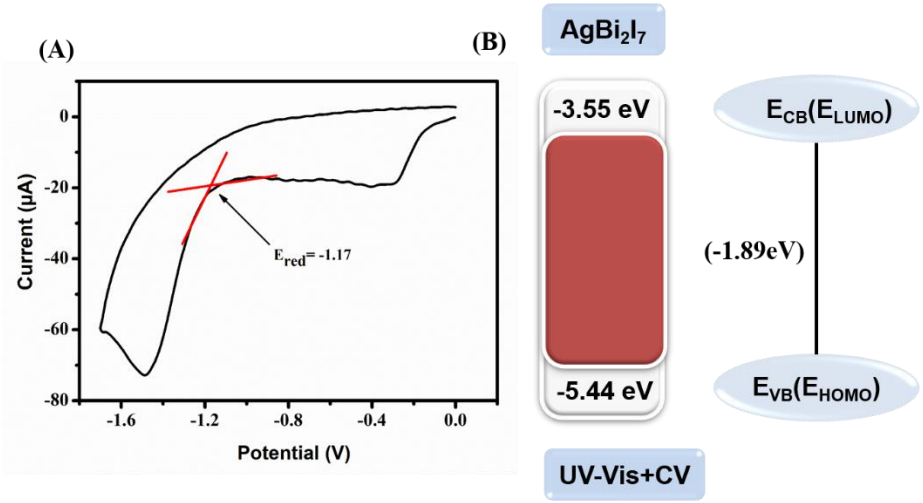

Figure 4.5. CV curve (A) and energy level diagram (B) of $AgBi_2I_7$. (Glassy carbon electrodes, Ag/AgCl and Pt wire utilized as working electrode, the reference and counter electrodes respectively. The potential of the ferrocene/ferrocenium (Fc/Fc^+) in the three-electrode system has been determined using the GCE. $AgBi_2I_7$ was dissolved in 0.1M tetrabutylammonium hexafluorophosphate ($TBAPF_6$) in acetonitrile containing 0.001M ferrocene at a scan rate of 20 mV/s to record the $AgBi_2I_7$ CV curve).

Moreover, a PSC device was designed using $AgBi_2I_7$ as a perovskite light absorber. The device's photovoltaic performance was measured after it was fabricated in ambient conditions (30–40% humidity). The short circuit photocurrent density-voltage curve used to assess the device's photovoltaic performance. Figure 4.6 shows the photovoltaic performance of SBI-D and SBI-DM under one sun condition (1.5 AM; 100 mW/cm^2). Table A4 contains all of the photovoltaic parameters recorded by the devices.

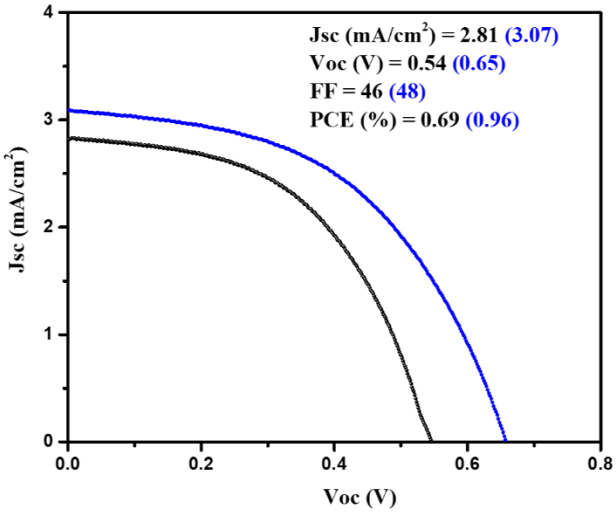

Figure 4.6. Showing the photovoltaic performance of $AgBi_2I_7$ perovskite without MeOH (Black), with MeOH (Blue) under 1 sun conditions (Forward Bias, AM 1.5 G; 100 mW/cm^2, Active Area 0.1 cm^2, Room temperature).

The maximum PCE of 0.96% was reached using SBI-DM PSCs, which is higher than the PCE of PSCs manufactured with SBI-D as a light absorber. Additionally, Figure 4.7 provides the box charts of the Jsc, FF, Voc, and PCE for SBI-D and SBI-DM. Moreover, SBI-DM perovskite as a light absorber attained a higher open circuit voltage than SBI-D PSCs.

However, $AgBi_2I_7$ synthesized from DMF and MeOH solutions revealed homogenous grains and a thin uniform layer. Providing an easy interaction with surrounding charge transfer layers. It is observed from the XRD and SEM results that the solvent in the precursor solution significantly affects the crystallization and morphology of $AgBi_2I_7$.This

solvent engineering approach showed the improvement in morphology without affecting the perovskite structure, which resulted in an increase in efficiency.

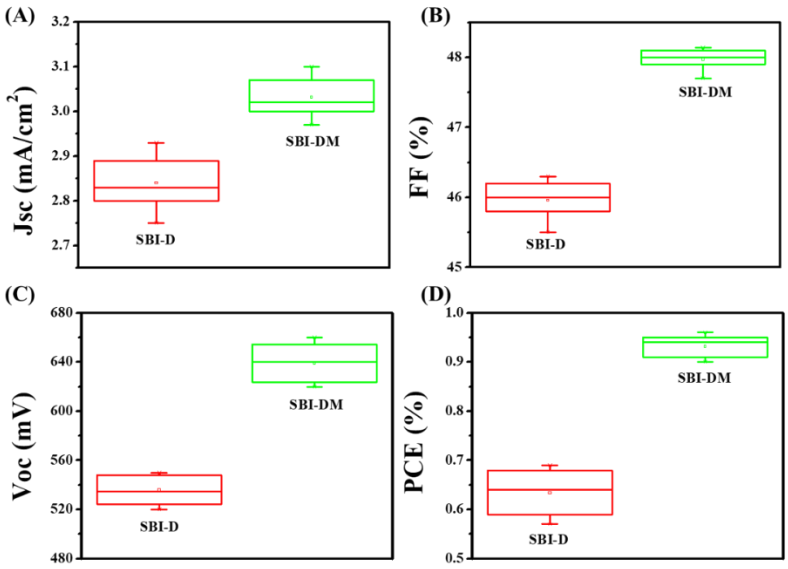

Figure 4.7. Box charts of Jsc (A), FF (B) Voc (C), and PCE (D) of $AgBi_2I_7$ perovskite without MeOH (Black), with MeOH (Blue) under 1 sun conditions (Forward Bias, AM 1.5 G; 100 mW/cm^2, Active Area 0.1 cm^2, Room temperature).

We summarized all data in Table A4 for comparison with other reported photovoltaic performance of Pb free PSCs. Recently, there has been a tremendous increase in the production of Pb-free PSCs. The research and development of non-toxic perovskite materials for photovoltaic applications has garnered considerable interest from researchers. 0-D $(CH_3NH_3)_3Sb_2I_9$ perovskite was introduced by Hebig *et al.* [21] as a potential contender for lead-free perovskite solar cells. Additionally, a PCE of 0.49% was obtained by using solvent engineering techniques that included a toluene drop during the spin-coating procedure. Li *et al.* [16] created a novel form of photovoltaic material with a band gap of 1.64 eV, although they only managed to obtain a 0.46% efficiency. For PSCs, Qiu *et al.* [39] used a Cs_2SnI_6 light absorber, but the manufactured device had a subpar PCE of 0.86%. A thin file of $AgBi_2I_7$ perovskite with a direct band gap of 1.93 eV was designed by Shao *et al.* [34], although the efficiency was only 0.83%. 2018 had seen the utilization of

$(CH_3NH_3)_3Sb_2I_9$ perovskite material in solar cells by Chatterjee *et al.* [40], and the manufactured PSCs device had the best PCE of 0.57% without any dopant. In earlier research, Zhang *et al.* [41] designed a novel perovskite structure; the light absorber (Cs_2NaBiI_6) had good optoelectronic properties, however its PCE was less than 1%. The very stable Pb free PSCs have also been developed using all inorganic perovskite structures, although only 0.62% efficiency was attained [42]. Zuo *et al.* [43] had used variation in halide ion using iodide and bromide ions, with $(NH_4)_3Sb_2I_9$ having the maximum PCE of 0.5%. However, Yokoyama *et al.* [44] and Ahmad *et al.* [45] respectively designed Sn-based perovskites ($CH_3NH_3SnBr_3$) and Sn-incorporated materials ($MA_3(Bi_{1-x}Snx)_2I_9$), where the PCE was higher with the doped light absorber ($MA_3(Bi_{1-x}Sn_x)_2I_9$). When compared to previous reported lead-free perovskite devices, the photovoltaic performance of our SBI-D and SBI-DM based PSCs devices was superior.

Research is still underway to develop a high-performance, stable device that can meet all energy demands. In this viewpoint, various attempts such as encapsulation, insertion of metal ions, doping of metal ions, and multistep fabrication was done. Different Pb-free PSCs have been developed and manufactured. We also looked at the electrical and optical properties of perovskite light absorbers and charge transport layers, which are important for improving the efficiency of perovskite solar cells. Computational studies were conducted to determine the influence of ETL, HTM, and perovskite material thickness during solar cell fabrication. Understanding the variable performance characteristics of PSCs (FF, V_{oc}, J_{sc}, PCE) in terms of thickness variation was important. The SCAPS-1D programme was used to simulate the $AgBi_2I_7$ lead-free perovskite [46].

The J-V curve and performance metrics for the FTO (500 nm)/TiO_2 (100 nm)/ $AgBi_2I_7$ (varying)/Spiro-MeOTAD (100 nm)/Au device architecture was shown in Figure 4.8 A, B. According to the numerical simulation, the $AgBi_2I_7$ lead-free perovskite's greatest PCE, with a perovskite layer thickness of 500 nm, was 13.26%. When the perovskite material's thickness is extended from 100 nm to 500 nm, the J_{sc} value

rises while the V_{oc} value somewhat declines but not enough to have an impact on performance. The outstanding $AgBi_2I_7$ perovskite PCE of 13.26% at optimum 500 nm thickness was employed for simulation purposes.

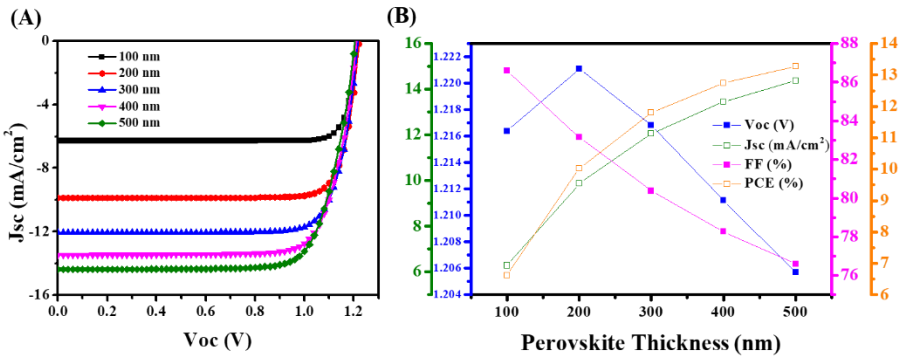

Figure 4.8. (A) J-V curves and (B) Photovoltaic parameters of the simulated Pb-free PSCs with device architecture of FTO(500 nm)/TiO_2(100 nm)/ $AgBi_2I_7$ (varying)/spiro-MeOTAD(100 nm)/Au.

ETL and HTM effects on performance had been examined to note the impact of perovskite material thickness. The J-V curve of a simulation with increasing TiO_2 thickness was shown in Figure 4.9 A. A little drop in J_{sc} was seen when TiO_2 thickness increased from 100 nm to 500 nm. Additionally, this drop in J_{sc} impacts the device PCE as TiO_2 thickness increases, with only a minimal impact on V_{oc} and FF (Figure 4.9 B).

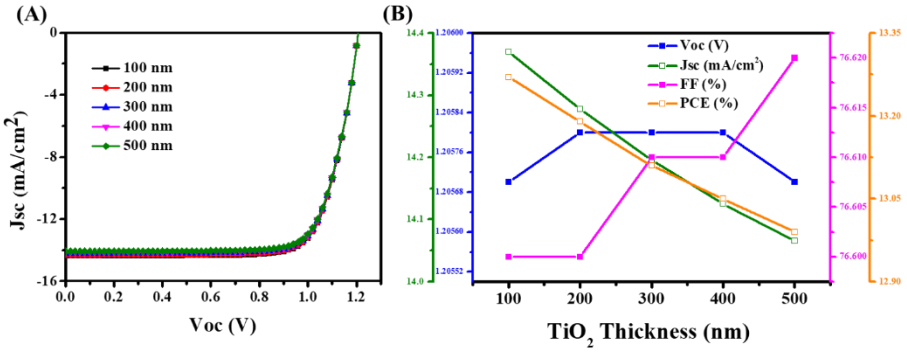

Figure 4.9. (A) J-V curves and (B) Photovoltaic parameters of the simulated Pb-free PSCs with device architecture of FTO(500 nm)/TiO_2(varying)/ $AgBi_2I_7$ (500 nm)/spiro-MeOTAD(100 nm)/Au.

As a consequence, simulation findings show that TiO_2 at a thickness of 100 nm is far more effective than ETL. Figure 4.10 A, the J-V curves of $AgBi_2I_7$ perovskite with various thickness of HTMs (Spiro-MeOTAD),

which exhibited almost little change in J_{sc} and V_{oc}. The simulated results of the perovskite parameter demonstrate that, with the exception of V_{oc}, all other parameters showed a declining tendency as the thickness of the HTM increased (Figure 4.10 B). As a result of its superior performance, modelling of the $AgBi_2I_7$ perovskite was done at a 100 nm TiO_2 and HTM thickness. Recently, computational studies on lead-free perovskite solar cells were also carried out, by Mobin *et al.* [36] and reporting relative efficiencies of approximately 12% for the perovskite materials $MA_3(Bi_{1-x}Sn_x)_2I_9$.

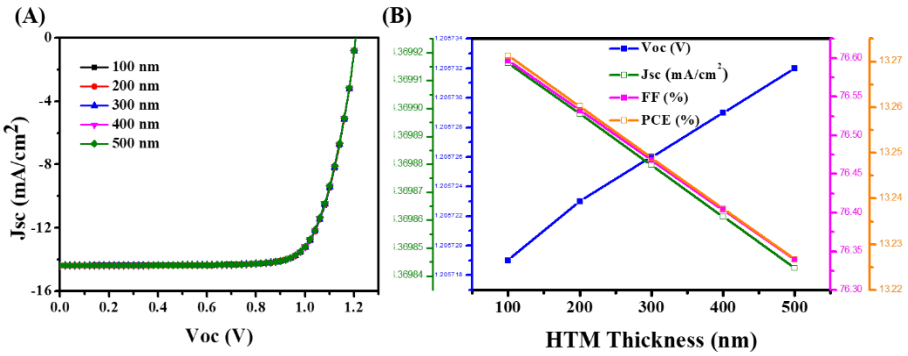

Figure 4.10. (A) J-V curves and (B) Photovoltaic parameters of the simulated Pb-free PSCs with device architecture of FTO(500 nm)/TiO_2(100 nm)/ $AgBi_2I_7$ (500 nm)/spiro-MeOTAD(varying)/Au.

4.4. Summary

To summarize our work, we used a solvent engineering technique to fabricate silver-based bismuth perovskite ($AgBi_2I_7$) material as a light absorber for PSCs. The photovoltaic efficiency was improved by combining DMF and MeOH in an optimum ratio. The obtained device performance results demonstrate the efficiency of the solvent engineering method. Likewise, using $AgBi_2I_7$ as a light absorber in the device construction of PSCs resulted in good PCE (0.96%) and V_{oc} (650mV). In the future perspective, improving system performance may be achieved by comprehending the crystallization process as well as by investigating appropriate charge transport layers and solvents. To improve the optical characteristics of the $AgBi_2I_7$, less noxious metals might be inserted or doped into the structure. Additionally, $AgBi_2I_7$ can be applied in different energy-harvesting scenarios.

4.5. References

1. Xing G., Mathews N., Sun S., Lim S. S., Lam Y. M., Grätzel M., Mhaisalkar S., Sum T. C. (2013), Long-Range Balanced Electron- and Hole-Transport Lengths in Organic-Inorganic $CH_3NH_3PbI_3$, Science, 342, 344–347 (DOI: 10.1126/science.1243167).
2. Stranks S. D., Eperon G. E., Grancini G., Menelaou C., Alcocer M. J. P., Leijtens T., Herz L. M., Petrozza A., Snaith H. J. (2013), Electron-Hole Diffusion Lengths Exceeding 1 Micrometer in an Organometal Trihalide Perovskite Absorber, Science, 342, 341–344 (DOI: 10.1126/science.1243982).
3. Ponseca C. S. Jr., Savenije T. J., Abdellah M., Zheng K., Yartsev A., Pascher T., Harlang T., Chabera P., Pullerits T., Stepanov A., Wolf J.-P., Sundström V. (2014), Organometal Halide Perovskite Solar Cell Materials Rationalized: Ultrafast Charge Generation, High and Microsecond-Long Balanced Mobilities, and Slow Recombination, J. Am. Chem. Soc., 136, 5189–5192 (DOI: 10.1021/ja412583t).
4. Wehrenfennig C., Eperon G. E., Johnston M. B., Snaith H. J., Herz L. M. (2014), High Charge Carrier Mobilities and Lifetimes in Organolead Trihalide Perovskites, Advanced Materials, 26, 1584–1589 (DOI: 10.1002/adma.201305172).
5. McMeekin D. P., Sadoughi G., Rehman W., Eperon G. E., Saliba M., Hörantner M. T., Haghighirad A., Sakai N., Korte L., Rech B., Johnston M. B., Herz L. M., Snaith H. J. (2016), A mixed-cation lead mixed-halide perovskite absorber for tandem solar cells, Science, 351, 151–155 (DOI: 10.1126/science.aad5845).
6. Jeon N. J., Noh J. H., Yang W. S., Kim Y. C., Ryu S., Seo J., Seok S. I. (2015), Compositional engineering of perovskite materials for high-performance solar cells, Nature, 517, 476–480 (DOI: 10.1038/nature14133).
7. De Wolf S., Holovsky J., Moon S.-J., Löper P., Niesen B., Ledinsky M., Haug F.-J., Yum J.-H., Ballif C. (2014), Organometallic Halide Perovskites: Sharp Optical Absorption Edge and Its Relation to

Photovoltaic Performance, J. Phys. Chem. Lett., 5, 1035–1039 (DOI: 10.1021/jz500279b).

8. Best Research-Cell Efficiency Chart. Available at: https://www.nrel.gov/pv/cell-efficiency.html. Accessed on 25 September 2023.
9. Konstantakou M., Stergiopoulos T. (2017), A critical review on tin halide perovskite solar cells, J. Mater. Chem. A, 5, 11518–11549 (DOI: 10.1039/C7TA00929A).
10. Kopacic I., Friesenbichler B., Hoefler S. F., Kunert B., Plank H., Rath T., Trimmel G. (2018), Enhanced Performance of Germanium Halide Perovskite Solar Cells through Compositional Engineering, ACS Appl. Energy Mater., 1, 343–347 (DOI: 10.1021/acsaem.8b00007).
11. Song T.-B., Yokoyama T., Stoumpos C. C., Logsdon J., Cao D. H., Wasielewski M. R., Aramaki S., Kanatzidis M. G. (2017), Importance of Reducing Vapor Atmosphere in the Fabrication of Tin-Based Perovskite Solar Cells, J. Am. Chem. Soc., 139, 836–842 (DOI: 10.1021/jacs.6b10734).
12. Ke W., Stoumpos C. C., Zhu M., Mao L., Spanopoulos I., Liu J., Kontsevoi O. Y., Chen M., Sarma D., Zhang Y., Wasielewski M. R., Kanatzidis M. G. (2017), Enhanced photovoltaic performance and stability with a new type of hollow 3D perovskite {en}$FASnI_3$, Science Advances, 3, e1701293 (DOI: 10.1126/sciadv.1701293).
13. Krishnamoorthy T., Ding H., Yan C., Leong W. L., Baikie T., Zhang Z., Sherburne M., Li S., Asta M., Mathews N., Mhaisalkar S. G. (2015), Lead-free germanium iodide perovskite materials for photovoltaic applications, J. Mater. Chem. A, 3, 23829–23832 (DOI: 10.1039/C5TA05741H).
14. Cortecchia D., Dewi H. A., Yin J., Bruno A., Chen S., Baikie T., Boix P. P., Grätzel M., Mhaisalkar S., Soci C., Mathews N. (2016), Lead-Free $MA_2CuCl_xBr_{4-x}$ Hybrid Perovskites, Inorg. Chem., 55, 1044–1052 (DOI: 10.1021/acs.inorgchem.5b01896).
15. Ahmad K., Mobin S. M. (2020), Organic–Inorganic Copper (II)-Based Perovskites: A Benign Approach toward Low-Toxicity and

Water-Stable Light Absorbers for Photovoltaic Applications, Energy Technology, 8, 1901185 (DOI: 10.1002/ente.201901185).

16. Li X., Zhong X., Hu Y., Li B., Sheng Y., Zhang Y., Weng C., Feng M., Han H., Wang J. (2017), Organic–Inorganic Copper(II)-Based Material: A Low-Toxic, Highly Stable Light Absorber for Photovoltaic Application, J. Phys. Chem. Lett., 8, 1804–1809 (DOI: 10.1021/acs.jpclett.7b00086).
17. Li X.-L., Li Z., Zhang G., Yang G.-J. (2020), Lead-free perovskite $[H_3NC_6H_4NH_3]CuBr_4$ with both a bandgap of 1.43 eV and excellent stability, J. Mater. Chem. A, 8, 5484–5488 (DOI: 10.1039/C9TA12872G).
18. Li X., Li B., Chang J., Ding B., Zheng S., Wu Y., Yang J., Yang G., Zhong X., Wang J. (2018), $(C_6H_5CH_2NH_3)_2CuBr_4$: A Lead-Free, Highly Stable Two-Dimensional Perovskite for Solar Cell Applications, ACS Appl. Energy Mater., 1, 2709–2716 (DOI: 10.1021/acsaem.8b00372).
19. Vargas B., Ramos E., Pérez-Gutiérrez E., Alonso J. C., Solis-Ibarra D. (2017), A Direct Bandgap Copper–Antimony Halide Perovskite, J. Am. Chem. Soc., 139, 9116–9119 (DOI: 10.1021/jacs.7b04119).
20. Ahmad K., Kumar P., Mobin S. M. (2020), Inorganic Pb-Free Perovskite Light Absorbers for Efficient Perovskite Solar Cells with Enhanced Performance, Chemistry – An Asian Journal, 15, 2859–2863 (DOI: 10.1002/asia.202000680).
21. Hebig J.-C., Kühn I., Flohre J., Kirchartz T. (2016), Optoelectronic Properties of $(CH_3NH_3)_3Sb_2I_9$ Thin Films for Photovoltaic Applications, ACS Energy Lett., 1, 309–314 (DOI: 10.1021/acsenergylett.6b00170).
22. Ahmad K., Kumar P., Mobin S. M. (2020), A Two-Step Modified Sequential Deposition Method-based Pb-Free $(CH_3NH_3)_3Sb_2I_9$ Perovskite with Improved Open Circuit Voltage and Performance, ChemElectroChem, 7, 946–950 (DOI: 10.1002/celc.201902107).
23. Kumar P., Ahmad K., Dagar J., Unger E., Mobin S. M. (2021), Two-Step Deposition Approach for Lead Free $(NH_4)_3Sb_2I_9$ Perovskite

Solar Cells with Enhanced Open Circuit Voltage and Performance, ChemElectroChem, 8, 3150–3154 (DOI: 10.1002/celc.202100957).

24. Zuo C., Ding L. (2017), Lead-free Perovskite Materials $(NH_4)_3Sb_2I_xBr_{9-x}$, Angewandte Chemie International Edition, 56, 6528–6532 (DOI: 10.1002/anie.201702265).
25. Okano T., Suzuki Y. (2017), Gas-assisted coating of Bi-based $(CH_3NH_3)_3Bi_2I_9$ active layer in perovskite solar cells, Materials Letters, 191, 77–79 (DOI: 10.1016/j.matlet.2017.01.047).
26. Ahmad K., Ansari S. N., Natarajan K., Mobin S. M. (2019), A $(CH_3NH_3)_3Bi_2I_9$ Perovskite Based on a Two-Step Deposition Method: Lead-Free, Highly Stable, and with Enhanced Photovoltaic Performance, ChemElectroChem, 6, 1192–1198 (DOI: 10.1002/celc.201801322).
27. Kulkarni A., Singh T., Ikegami M., Miyasaka T. (2017), Photovoltaic enhancement of bismuth halide hybrid perovskite by N-methyl pyrrolidone-assisted morphology conversion, RSC Adv., 7, 9456–9460 (DOI: 10.1039/C6RA28190G).
28. Huang J., Gu Z., Zhang X., Wu G., Chen H. (2018), Lead-free $(CH_3NH_3)_3Bi_2I_9$ perovskite solar cells with fluorinated PDI films as organic electron transport layer, Journal of Alloys and Compounds, 767, 870–876 (DOI: 10.1016/j.jallcom.2018.07.185).
29. Sun S., Tominaka S., Lee J.-H., Xie F., Bristowe P. D., Cheetham A. K. (2016), Synthesis, crystal structure, and properties of a perovskite-related bismuth phase, $(NH_4)_3Bi_2I_9$, APL Materials, 4, 031101 (DOI: 10.1063/1.4943680).
30. Zhuang R., Wang X., Ma W., Wu Y., Chen X., Tang L., Zhu H., Liu J., Wu L., Zhou W., Liu X., Yang Y. (Michael) (2019), Highly sensitive X-ray detector made of layered perovskite-like $(NH_4)_3Bi_2I_9$ single crystal with anisotropic response, Nat. Photonics, 13, 602–608 (DOI: 10.1038/s41566-019-0466-7).
31. Filip M. R., Hillman S., Haghighirad A. A., Snaith H. J., Giustino F. (2016), Band Gaps of the Lead-Free Halide Double Perovskites $Cs_2BiAgCl_6$ and $Cs_2BiAgBr_6$ from Theory and Experiment, J. Phys. Chem. Lett., 7, 2579–2585 (DOI: 10.1021/acs.jpclett.6b01041).

32. Kim Y., Yang Z., Jain A., Voznyy O., Kim G.-H., Liu M., Quan L. N., García de Arquer F. P., Comin R., Fan J. Z., Sargent E. H. (2016), Pure Cubic-Phase Hybrid Iodobismuthates $AgBi_2I_7$ for Thin-Film Photovoltaics, Angewandte Chemie International Edition, 55, 9586–9590 (DOI: 10.1002/anie.201603608).
33. Shao Z., Le Mercier T., Madec M. B., Pauporté Th. (2018), Exploring $AgBi_xI_{3x+1}$ semiconductor thin films for lead-free perovskite solar cells, Materials & Design, 141, 81–87 (DOI: 10.1016/j.matdes.2017.12.036).
34. Shao Z., Le Mercier T., Madec M. B., Pauporté, T. (2018), $AgBi_2I_7$ layers with controlled surface morphology for solar cells with improved charge collection, Materials Letters, 221, 135–138 (DOI: 10.1016/j.matlet.2018.03.085).
35. Zhu H., Pan M., Johansson M. B., Johansson E. M. J. (2017), High Photon-to-Current Conversion in Solar Cells Based on Light-Absorbing Silver Bismuth Iodide, ChemSusChem, 10, 2592–2596 (DOI: 10.1002/cssc.201700634).
36. Stoumpos C. C., Kanatzidis M. G. (2015), The Renaissance of Halide Perovskites and Their Evolution as Emerging Semiconductors, Acc. Chem. Res., 48, 2791–2802 (DOI: 10.1021/acs.accounts.5b00229).
37. Tang Z., Bessho T., Awai F., Kinoshita T., Maitani M. M., Jono R., Murakami T. N., Wang H., Kubo T., Uchida S., Segawa H. (2017), Hysteresis-free perovskite solar cells made of potassium-doped organometal halide perovskite, Sci Rep, 7, 12183 (DOI: 10.1038/s41598-017-12436-x).
38. Chen X., Myung Y., Thind A., Gao Z., Yin B., Shen M., Beom Cho S., Cheng P., Sadtler B., Mishra R., Banerjee P. (2017), Atmospheric pressure chemical vapor deposition of methylammonium bismuth iodide thin films, Journal of Materials Chemistry A, 5, 24728–24739 (DOI: 10.1039/C7TA06578G).
39. Qiu X., Jiang Y., Zhang H., Qiu Z., Yuan S., Wang P., Cao B. (2016), Lead-free mesoscopic Cs_2SnI_6 perovskite solar cells using different nanostructured ZnO nanorods as electron transport layers, physica

status solidi (RRL) – Rapid Research Letters, 10, 587–591 (DOI: 10.1002/pssr.201600166).

40. Chatterjee S., Pal A. J. (2018), Tin(IV) Substitution in $(CH_3NH_3)_3Sb_2I_9$: Toward Low-Band-Gap Defect-Ordered Hybrid Perovskite Solar Cells, ACS Appl. Mater. Interfaces, 10, 35194–35205 (DOI: 10.1021/acsami.8b12018).
41. Zhang C., Gao L., Teo S., Guo Z., Xu Z., Zhao S., Ma T. (2018), Design of a novel and highly stable lead-free Cs_2NaBiI_6 double perovskite for photovoltaic application, Sustainable Energy Fuels, 2, 2419–2428 (DOI: 10.1039/C8SE00154E).
42. Johansson M. B., Philippe B., Banerjee A., Phuyal D., Mukherjee S., Chakraborty S., Cameau, M., Zhu H., Ahuja R., Boschloo G., Rensmo H., Johansson E. M. J. (2019), Cesium Bismuth Iodide Solar Cells from Systematic Molar Ratio Variation of CsI and BiI3, Inorg. Chem., 58, 12040–12052 (DOI: 10.1021/acs.inorgchem.9b01233).
43. Zuo C., Ding L. (2017), Lead-free Perovskite Materials $(NH_4)_3Sb_2I_xBr_{9-x}$, Angewandte Chemie, 129, 6628–6632 (DOI: 10.1002/ange.201702265).
44. Yokoyama T., Song T.-B., Cao D. H., Stoumpos C. C., Aramaki S., Kanatzidis M. G. (2017), The Origin of Lower Hole Carrier Concentration in Methylammonium Tin Halide Films Grown by a Vapor-Assisted Solution Process, ACS Energy Lett., 2, 22–28 (DOI: 10.1021/acsenergylett.6b00513).
45. Ahmad K., Kumar P., Shrivastava P., Mobin S. M. (2022), Sn(IV) Inserted Lead-Free Perovskite Materials $(MA_3(Bi_{1-x}Sn_x)_2I_9)$ as Light Absorbers: Bandgap Engineering and Enhanced Photovoltaic Performance, Energy Technology, 10, 2100717 (DOI: 10.1002/ente.202100717).
46. Burgelman M., Nollet P., Degrave S. (2000), Modelling polycrystalline semiconductor solar cells, Thin Solid Films, 361–362, 527–532 (DOI: 10.1016/S0040-6090(99)00825-1).

CHAPTER 5

Development of Moisture Stable Lead-Free Halide Double Perovskite (Cu_2AgBiI_6) with Improved Photovoltaic Performance

5.1. Introduction

Over the ensuing more than ten years, lead-halide perovskites have experienced remarkable and outstanding development, especially in the field of innovative solar cell materials [1]. The significant enhancement of power conversion efficiencies (PCEs) for single-junction cells to over 25 % and perovskite-silicon tandems to beyond 29 % show the potential for perovskites to be utilized for photovoltaic applications [2,3]. However, there are still concerns about the toxicity of the leading perovskite solar cell components, the most of which contain lead [4], as well as ongoing problems with maintaining their long-term stability [5]. The safest alternative would be to employ light-harvesting materials that remove lead from their composition while retaining the excellent optoelectronic features of lead-halide perovskites, also including high optical absorption [1], tunable band gaps [6], high charge-carrier mobilities, and long charge-carrier lifetimes [7,8]. Such elements would alleviate concerns regarding toxicity as well as provide stable high-efficiency solar cells [4, 9]. Replace lead with isoelectronic elements is a difficulty for alternative approaches, but it is the only way to ensure stability and get rid of lead toxicity, which motivates the scientific community. Homo-valent metal ions like Sn^{2+} and Ge^{2+} have already been used in this context, and they have been shown to have greater PCE, although being less stable than Pb-based perovskites [10,11].

The maximum PCE that the Sn-based perovskite materials could attain was 14% [12], however due to the rapid oxidation of Sn, which invariably causes flaws, their performance degraded quickly in the ambient environment [13]. Perovskite materials have shown high stability towards the replacement of lead by hetero-valent metal ions, although their optoelectronic characteristics were unfavorable for solar

applications [14]. Hetero-valent ions, such as the perovskite made of bismuth (III) and antimony (III), which has the general formula $A_3M_2X_9$ (A^+ = Cs^+, $(NH_4)^+$, $(CH_3NH_3)^+$, M= Bi^{+3}, Sb^{+3}, X^- = Cl^-, Br^-, I^-). $A_3Bi_2X_9$ structural dimensionality was reduced due to their wider band gap (>2.0 eV), and greater excitonic binding energies may be too responsible for their worse photovoltaic performance [15, 16]. Due to their outstanding properties and potential applications halide double perovskites are an interesting and versatile family of materials that have garnered a lot of attention recently. Halide double perovskites having a general formula, $A_2BB`X_6$, B and B` are two distinct cations [17]. The variable electronic, optical properties of halide double perovskites, which can be tailored by altering their combination of cations and halides, are one of its most fascinating characteristics. Halide double perovskites have also demonstrated outstanding stability and durability, even in ambient conditions, which increases their potential for use in real-world applications [18].

Bismuth has attracted interest due to its excellent thermal stability and environmental friendliness. Worldwide reports of hetero-valent ion-based light absorbers that utilize various cations have been presented. In order to attain excellent PCE, Zuo *et al.* [19] and Kumar *et al.* [20] investigated the optoelectronic characteristics of an ammonium antimony-based PSC. On the other hand, Sun *et al.* [21] and Zhuang *et al.* [22] investigated the $(NH_4)_3Bi_2I_9$ perovskite used in PSCs, as well as X-rays and their crystalline characteristics were explored. Kumar *et al.* recently reported $AgBi_2I_7$ light absorber attained 0.96% PCE via solvent engineering technique [23]. Halide double perovskite materials like $Cs_2AgBiBr_6$ have also shown promise in photoelectric devices like light emitting diodes [24] and photo-detectors [25]. Due to its decreased band gap [26], the halide double perovskite (Cs_2AgBiI_6) containing iodide as an anion indicated could potentially use as a light absorber. The first report on Cu_2AgBiI_6 as a light absorber has been proven by Sansom *et al.* in order to further study the Bi based light absorber materials for photovoltaic use. The mere fact that the PCE measured only 0.43 % better might be explained through lower solubility in

commonly used solvents [27]. Similar to the lead halide-based perovskite, bismuth halides have poor crystallization and coverage, which leads to defects and poorer PCE. In this regard, investigation of appropriate solvents and suppression of defect are crucial for film processing.

5.2. Experimental section

5.2.1. Materials

BiI_3, AgI, CuI, Spiro-MeOTAD, 4-tert-butylpyridine, TiO_2 precursors, bis(trifluoromethylsulfonyl)imide lithium salt, solvents (chlorobenzene, m-Xylene, Toluene, EtOH, Methanol and DMF), FTO glass substrates, and other precursors have all been purchased from Merck, SRL, Dyesol, Loba, Sigma Aldrich, BAT-SOL, Alfa Aesar, and Solaronix. The compounds and precursors weren't further purified before being employed.

5.2.2. Characterization methods

The RINT 2500 V x-ray diffractometer (Rigaku, Japan), (Source=Cu K irradiation; = 1.5406), was used to conduct the Powder X-ray Diffraction (PXRD) experiments. The Supra 55 Zeiss Field Emission Scanning Electron microscope was used to obtain the morphological images. UV-vis absorption spectroscopy on a Varian UV-vis spectrophotometer was used to calculate the optical band gap (model: Carry 100). Under AM 1.5 G conditions (illumination of 100 mW/cm^2), the photocurrent-voltage (J-V) curves were measured. Using the Nova software, cyclic voltammetry (CV) measurements were performed on a Metrohm potentiostat/galvanostat.

5.2.3. Electrochemical investigations

A UV-vis and CV technique was employed to calculate the Cu_2AgBiI_6 highest occupied molecular orbital (HOMO) and lowest unoccupied molecular orbital (LUMO) energy values. Using a three-electrode assembly, the Cu_2AgBiI_6 CV curve was recorded. Glassy carbon electrodes (GCE), Ag/AgCl and Pt wire utilized as working electrode, the reference and counter electrodes respectively. The potential of the ferrocene/ferrocenium (Fc/Fc^+) in the three-electrode system has been

determined using the GCE. Cu_2AgBiI_6 was dissolved in 0.1M tetrabutylammonium hexafluorophosphate ($TBAPF_6$) in acetonitrile containing 0.001M ferrocene at a scan rate of 20mV/s to record the Cu_2AgBiI_6 CV curve.

5.2.4. Perovskite film preparations

CuI, AgI and BiI_3 was dissolved in 2 mL of N,N-dimethylformamide (DMF) using ultra-sonicator and further solution was stirred at 120°C for 30 minutes. The molar ratio of the CuI, AgI and BiI_3 was fixed to 2:1:1. The obtained reaction mixture was denoted as Cu_2AgBiI_6 and filtered through a 0.22 μm PTFE filter. The filtered Cu_2AgBiI_6 solution was spin-coated onto the FTO glass for 30 sec at rpm of 1500. The deposited films were annealed at 100°C for 15 min. Further, we have employed two-step deposition method by utilizing solvent engineering approach to prepare the Cu_2AgBiI_6 films.

5.2.5. Device fabrication

The fluorine-doped tin oxide (FTO) was patterned and cleaned using an ultrasonicator for 15 minutes while using detergent, water, acetone, and 2-propanol. 20 mM titanium diisopropoxide bis(acetylacetonate) solution was used to deposit the blocking layer of TiO_2 (bl-TiO_2), which was then annealed at 450°C for 30 minutes. Moreover, a mesoporous TiO_2 film (mp-TiO_2) was applied on the FTO/bl-TiO_2 and sintered for 45 minutes at 500°C. Moreover, as previously mentioned, the perovskite film (Cu_2AgBiI_6) was deposited on the FTO/bl-TiO_2/mp-TiO_2. Moreover, a layer of hole transport material (HTM) was added on the FTO/bl-TiO_2/mp-TiO_2/Cu_2AgBiI_6. the perovskite made of FTO, bl-TiO_2, and mp-TiO_2. The HTM was prepared by utilizing spiro-OMeTAD in chlorobenzene (90 mg/mL) with bis(trifluoromethylsulfonyl)imide lithium salt (Li-TFSI;99.95%), tris(2-(1H-pyrazol-1-yl)-4-tert-butylpyridine)-cobalt(III)tris-(bis(trifluoromethyl lsulfonyl)imide=FK209) and 4-tert-butylpyridine (4-tBP). Li-TFSI, FK209, and 4-tBP all a fixed molar ratio of 0.45, 0.035, and 3.1. Finally, using the thermal evaporation technique, the Au counter electrode was placed over the FTO/bl-TiO_2/mp-TiO_2/ Cu_2AgBiI_6/HTM.

5.3. Results and discussion

In this study, we attempted to limit the crystallization process of the Cu_2AgBiI_6 perovskite by employing various antisolvents, including ethanol (EtOH), chlorobenzene (CB), m-Xylene (mXylene), and toluene (tol). The main issue was the stability of perovskite materials, which limited their capacity to fabricate at a big scale. In regard of this, we experienced our perovskite material is water stable, with and without an antisolvent. To the best of our knowledge, this is the first report on the water stability performance on lead-free halide double perovskite light absorber. Prior to treating the water, the thin layer of these light absorbers was prepared. The thin film water treatment pictures shown in Figure. 5.1. These thin films were validated after they had been removed from water and dried, which shows nearly negligible effect after water treatment.

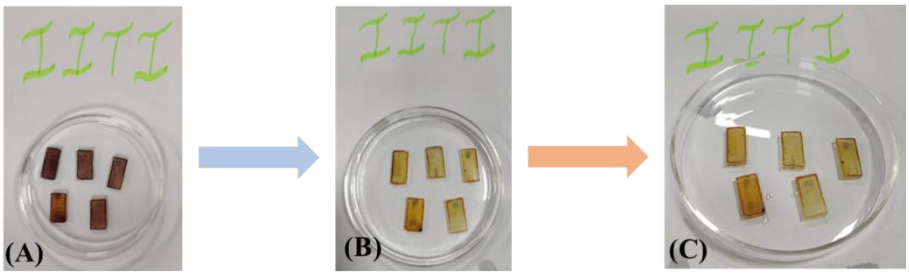

Figure 5.1. Digital picture of the Cu_2AgBiI_6 perovskite material films (A), thin films in water (B), thin films after water removal (C) immersed in water.

In Addition, the light absorber photovoltaic performance was examined, and it exhibits good open circuit voltage and short circuit current together with a strong power conversion efficiency. The fabrication process for a solar cell using a Cu_2AgBiI_6 perovskite light absorber is shown in Scheme 5.1. Under 1 sun condition and 30–40% humidity, results in the maximum PCE as achieved to only 0.98%.

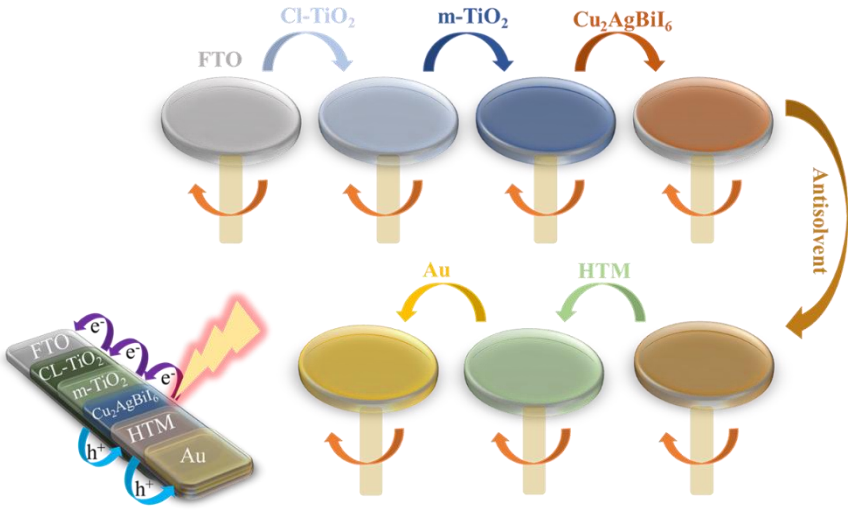

Scheme 5.1. Schematic Fabrication of Cu_2AgBiI_6 perovskite device architecture.

Thin films of Cu_2AgBiI_6 were investigated to powder X-ray diffraction (PXRD), to corroborate the composition and formation of the specific samples. The synthesis of perovskite material was confirmed by the PXRD pattern, which revealed its crystalline character (Figure 5.2).

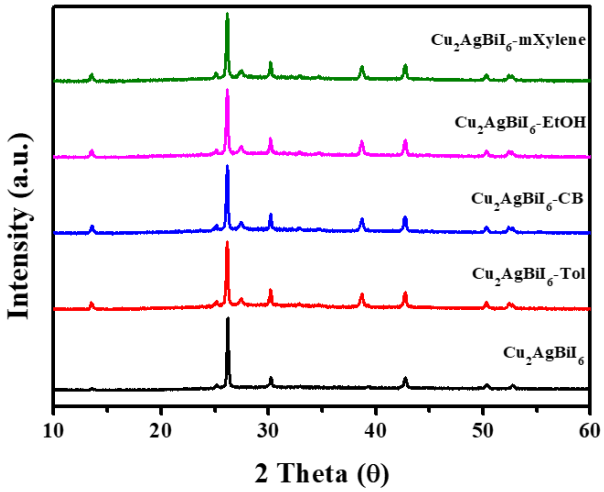

Figure 5.2. PXRD of Cu_2AgBiI_6 (black), Cu_2AgBiI_6+toluene (red), Cu_2AgBiI_6+chlorobenzene (blue), Cu_2AgBiI_6+Ethanol (pink), Cu_2AgBiI_6+m-Xylene (green) (Solvent DMF, thin film on FTO glass, Room Temperature).

The observed exceptionally intense peak was confirmed as belonging to the (012), (104) plane by the material and the peak at near 25° is mainly characteristic to the Cu_2AgBiI_6 material. Figure 5.2 shows the PXRD of

Cu_2AgBiI_6 in its pure form (black) and with several antisolvents, including ethanol (pink), toluene (red), chlorobenzene (blue) and m-Xylene (green). Surprisingly, the band gap and absorption coefficients of the absorption spectra of Cu_2AgBiI_6 and with antisolvents are quite comparable. Using the Tauc plot ((αhν)n against hν), where α, h, and ν are the absorption coefficient, Planck's constant, and excitation frequency correspondingly, the optical band gap was determined to be 2.06 eV (Figure 5.4). The fabricated perovskite has a high absorbance and the potential to be employed as a light absorber in solar cells, according to the computed optical band gap.

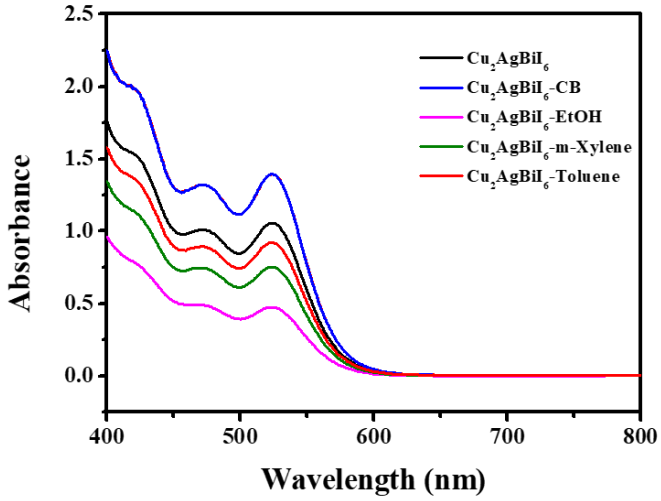

Figure 5.3. UV-vis Absorption spectra of Cu_2AgBiI_6 (black), Cu_2AgBiI_6+toluene (red), Cu_2AgBiI_6+chlorobenzene (blue), Cu_2AgBiI_6+Ethanol (pink), Cu_2AgBiI_6+m-Xylene (green) of Cu_2AgBiI_6 light absorber. (Solvent DMF, thin film on FTO glass, Room Temperature).

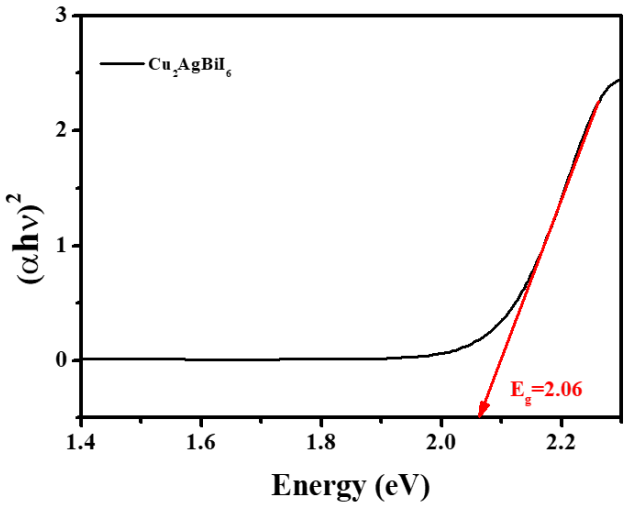

Figure 5.4. Tauc-Plot of Cu_2AgBiI_6 perovskite material (the linear fitting region of the Tauc plot is extrapolated to the energy axis (X-axis) to estimate the optical band gap Eg).

We concurrently employed the tauc plot and the cyclic voltammetry (CV) graph to determine the optical band gap and energy levels of Cu_2AgBiI_6 material. The onset reduction potential was computed using a CV graph (Figure 5.5 A), and the optical band gap was determined using a Tauc plot, equations A and B used for calculations.

$E_{CB}(E_{LUMO}) = -(E_{red} + 4.725)eV$…… (Equation 5.1)

$E_{VB}(E_{HOMO}) = -(E_{CB} - E_g)eV$ …….... (Equation 5.2)

Here, E_{red} is onset reduction potential, E_g is optical band gap, E_{VB} and E_{CB} are valance band and conduction band energy levels. Figure 5.5 B showed the HOMO and LUMO energy levels of Cu_2AgBiI_6 perovskite calculated by CV and UV/Vis spectra. According to the CV graph and Tauc plot, the valency band (VB) and conduction band (CB) energy levels of the perovskite material are predicted to be -3.80 eV and -5.86 eV, respectively. In comparison to lead-based perovskites, the energy level demonstrated good electron and hole transporting materials, which makes Cu_2AgBiI_6 perovskite ideal in terms of band alignment and displaying a wide range of options for their devices.

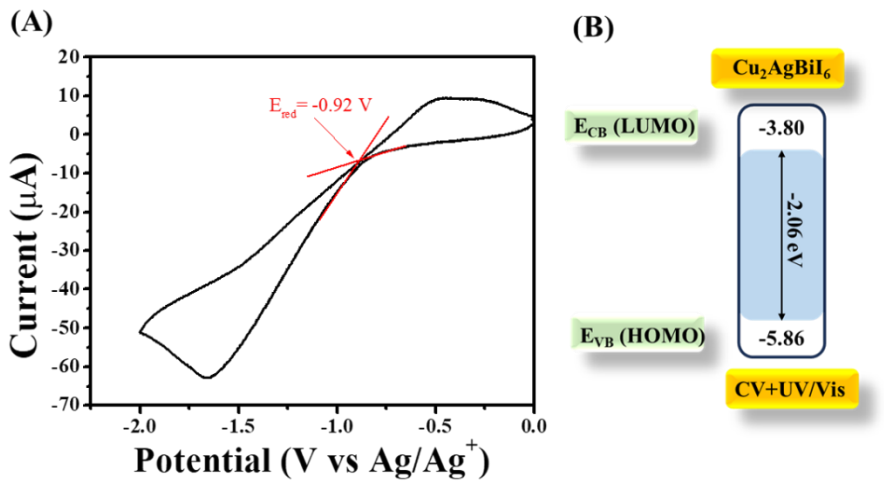

Figure 5.5. (A) Cyclic Voltammetry graph and (B) calculated HOMO, LUMO of Cu_2AgBiI_6 perovskite material. (Glassy carbon electrodes, Ag/AgCl and Pt wire utilized as working electrode, the reference and counter electrodes respectively. The potential of the ferrocene/ferrocenium (Fc/Fc^+) in the three-electrode system has been determined using the GCE. Cu_2AgBiI_6 was dissolved in 0.1M tetrabutylammonium hexafluorophosphate ($TBAPF_6$) in acetonitrile containing 0.001M ferrocene at a scan rate of 20 mV/s to record the Cu_2AgBiI_6 CV curve).

We observed a good eminence light absorbers film, after performing scanning electron microscopic (SEM). SEM images help to observe the effect of antisolvent content engagement with perovskite Cu_2AgBiI_6 material. The better shape and good surface coverage may be enhanced or reason for good photovoltaic performance of Cu_2AgBiI_6 material. With a homogeneous surface on the film, the Cu_2AgBiI_6 material twisted a morphology that looks as grains. We were able to successfully improve the shape of the perovskite material, as shown by the SEM results Figure 5.6. SEM images with different antisolvent were depicted from Figure 5.6 A-F.

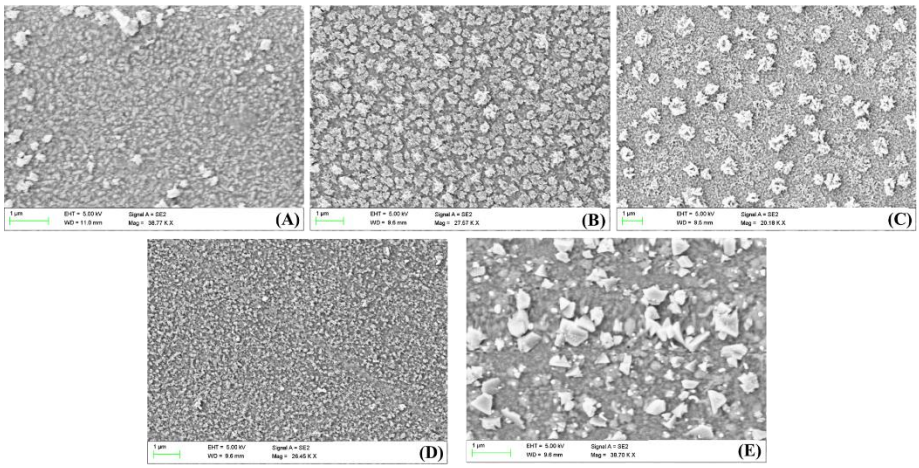

Figure 5.6. FE-SEM of Cu_2AgBiI_6 (A), Cu_2AgBiI_6+toluene (B), Cu_2AgBiI_6+chlorobenzene (C), Cu_2AgBiI_6+Ethanol (D), Cu_2AgBiI_6+m-Xylene (E) (Solvent DMF, thin film on FTO glass, Room Temperature).

The atomic and weight percentage were calculated by EDX spectra of the element showed in Figure 5.7.

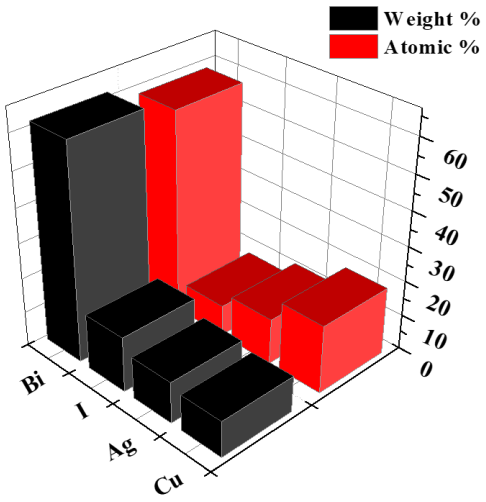

Figure 5.7. Atomic and weight percentage of elements in Cu_2AgBiI_6 perovskite material. (Solvent DMF, thin film on FTO glass, Room Temperature).

Furthermore, EDX spectrum and EDX mapping (Figure 5.8) were performed to checked the compositions of Cu_2AgBiI_6 perovskite materials and it showed a smooth coverage on the film**.** From the EDX

mapping the element dispersion observed throughout the surface, confirm the better combination in between the elements.

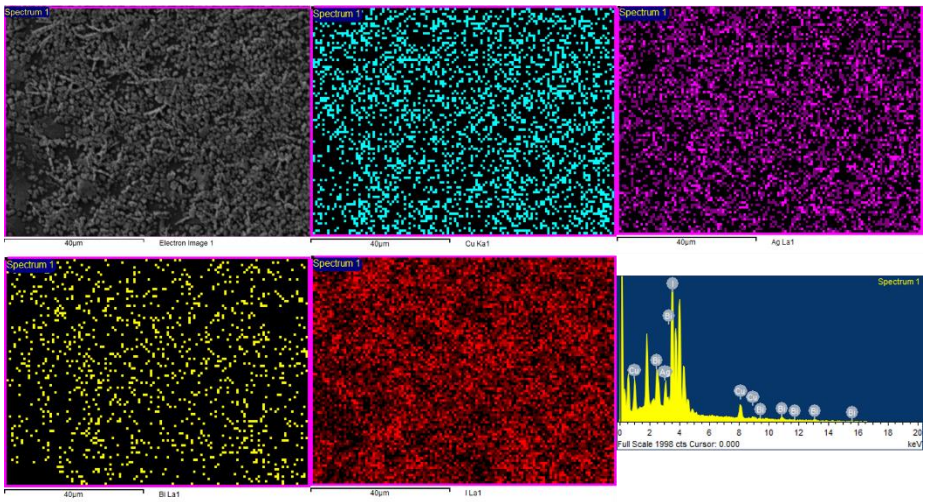

Figure 5.8. EDX mapping of Cu_2AgBiI_6 perovskite material (Solvent DMF, thin film on FTO glass, Room Temperature).

Furthermore, the solar cell device was fabricated using Cu_2AgBiI_6 perovskite material as light absorber and explore the photovoltaic performance under one sun conditions (1.5 AM; 100 mW cm^{-2}), using the FTO/bl-TiO_2/mp-TiO_2/Cu_2AgBiI_6/HTM device configuration (Scheme 5.2 A). The energy levels for back contact (Au), electron transport materials (ETM), and hole transport materials (HTM) were taken out from the reported literature. Our perovskite materials estimated energies were determined to be extremely suited for usage as charge-transporting materials with ETM and HTM (Scheme 5.2 B).

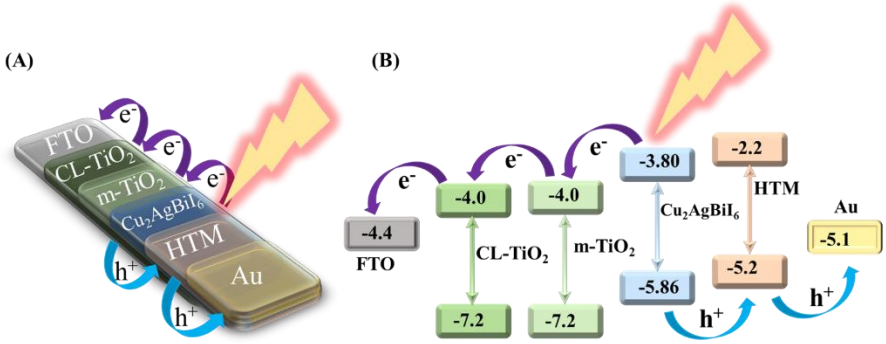

Scheme 5.2. (A) Schematic device structure, (B) Energy level diagram of ETL, Cu_2AgBiI_6, HTM, FTO, Au materials utilized in PSCs. Energy level values as per reported literature.

Figure 5.9 showed the J-V graph of the fabricated device based on the Cu_2AgBiI_6 light absorber with and without antisolvent. The higher PCE achieved with EtOH as antisolvent as compared to other, however the low PCE with the m-Xylene as antisolvent.

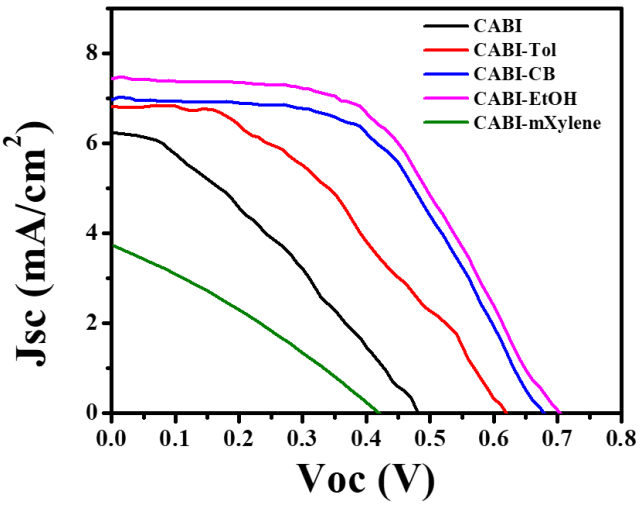

Figure 5.9. Photovoltaic performance of Cu_2AgBiI_6 and with various antisolvents under 1 sun conditions (Forward Bias, AM 1.5 G; 100 mW/cm^2, Active Area is 0.1 cm^2, Room temperature).

The maximum open circuit voltage (Voc) and short circuit current (Jsc) found to be 700 mV and 7.4 mA/cm^2 respectively. On compare of various published perovskite materials with their photovoltaic performances Cu_2AgBiI_6 showed good performance Table A5.

Herein, simulation investigation was also carried out to observed the potential of Cu_2AgBiI_6 perovskite materials in solar cell. The theoretical results pave a promising strategy towards the utilization of Cu_2AgBiI_6 perovskite in experiment. SCAPS_1D software [28] utilized for simulation and photovoltaic properties, the evaluation was taken under standard condition (AM 1.5 G; 100 mW/cm^2). The device architecture uses the TiO_2 as ETM, Cu_2AgBiI_6 as light absorber layer, and spiro-OMeTAD as HTM. 500 nm and 100 nm thickness of light absorber and ETM were used respectively, while varying in ETM thickness (100 nm to 500 nm) to investigate the variation in photovoltaic parameters. The obtained J-V response of simulated device was depicted in Figure 5.10 A. Other parameters such as Voc, Jsc, FF and PCE for Cu_2AgBiI_6 device

were depicted in Figure 5.10 B. Highest PCE was observed at 100 nm thickness of TiO_2 is 8.01% along with Voc of 1.88 V, and Jsc of 8.82 mA/cm^2. However, according to the reported literature, the thickness of ETM largely affect the photovoltaic performance of device, as it collects the electrons and block the holes generated from perovskite absorber layer. Thick layer of ETM might not be block holes efficiently that may enhance the recombination rate. As ETM thickness increases Jsc and PCE decrease which might be increase in recombination rate. Whereas, insignificant decrease observes for the FF and Voc.

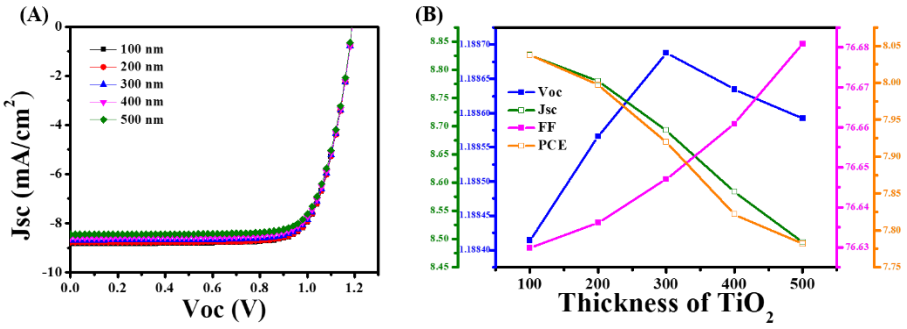

Figure 5.10. (A) J-V curves and (B) Photovoltaic parameters of the simulated Pb-free PSCs with device architecture of FTO(500 nm)/TiO_2(varying)/ Cu_2AgBiI_6 (500 nm)/spiro-MeOTAD(100 nm)/Au.

Variation in HTM thickness were also examined, as HTM is significantly affect the photovoltaic parameters. Therefore, variation of HTM thickness from 100 nm to 500 nm were observed while keeping the light absorber and ETM thickness constant as 500 nm and 100 nm respectively. The JV response of simulated device with variation in HTM were depicted in Figure 5.11 A. Whereas, other photovoltaic parameters results were showed in Figure 5.11 B. On increase in thickness Jsc, FF and PCE of the device decrease whereas, insignificant change observed in Voc. The higher PCE were 8.07 % with an Jsc of 8.87 mA/cm^2, FF of 76.6 % and Voc of 1.188 V at 100 nm of HTM.

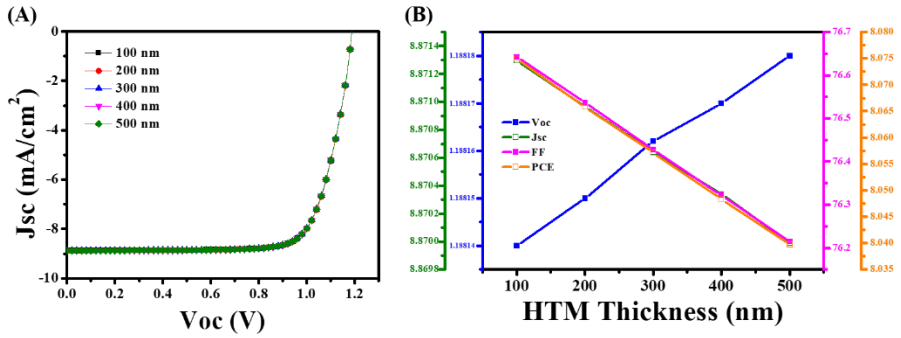

Figure 5.11. (A) J-V curves and (B) Photovoltaic parameters of the simulated Pb-free PSCs with device architecture of FTO(500 nm)/TiO_2(100 nm)/ Cu_2AgBiI_6 (500 nm)/spiro-MeOTAD(varying)/Au.

To achieve higher PCE, each layer is crucial with a significant thickness. The thickness of ETM and HTM were optimized and found that it should not be thicker, and with result 100 nm thickness of ETM and HTM finds suitable for higher PCE. The thickness variation of the perovskite light absorber on device are significantly affect the performance. In this regard, we have optimized the thickness of the perovskite and observed the relevance of variation in thickness between 100 nm and 500 nm with keeping the ETM and HTM thickness constant i.e 100 nm. At 100 nm thickness of Cu_2AgBiI_6, a very thin layer formed and it cause difficult for higher wavelength photons to be absorbed, however as the layer thickness increases, more photons may be absorbed [29]. Furthermore, highly thick perovskite materials layer promotes electrons and holes to travel farther to reach electrodes, potentially increasing the possibility of carrier recombination [30]. The effect on JV response with variation in thickness of Cu_2AgBiI_6 light absorber were depicted in Figure 5.12 A. Photovoltaic parameters such as Voc, Jsc, FF and PCE graph showed in Figure 5.12 B, the obtained results showed that with increase in thickness from 100 nm to 500 nm on light absorber enhancement in Jsc observed.

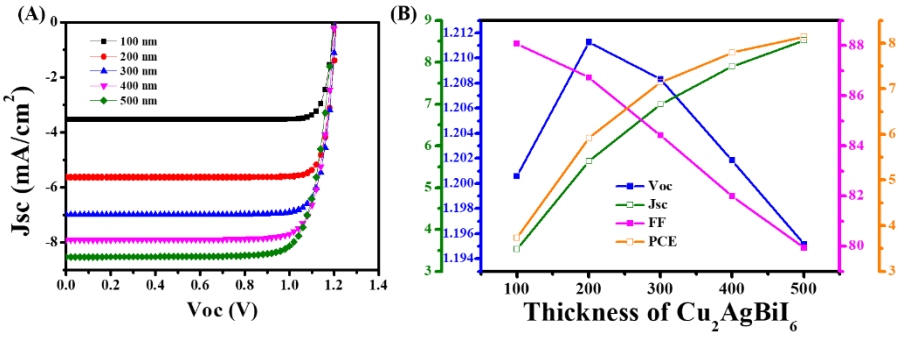

Figure 5.12. (A) J-V curves and (B) Photovoltaic parameters of the simulated Pb-free PSCs with device architecture of FTO (500 nm)/TiO_2(100 nm)/ Cu_2AgBiI_6 (varying)/spiro-MeOTAD(100 nm)/Au.

This may be attributes to the higher absorber area, which significantly absorbs photons and efficiently generates the electron and holes. With increase in Jsc, efficiency of the photovoltaic device increases, but FF decrease and little drop observed in Voc which once increases and then decrease.

To improve our knowledge and maximize the performance of perovskite materials for solar applications, theoretical and experimental research are complimentary and crucial. It is possible to predict the characteristics of novel perovskite compositions, detect potential issues, and develop materials with better performance because of theoretical studies. Comparison table of simulated results of different light absorber material had been presented in Table A6. Experimental investigation, on the other hand, supports theoretical predictions, offers insights into actual outcomes, and supports in the optimization of materials and device structures for utilization in photovoltaic applications. While experimental research offers validation, practical use, and optimization opportunities, theoretical investigations offer basic insights and estimation potential. It is important that these two methods be combined to advance the area of perovskite-based photovoltaics.

5.4. Summary

We have demonstrated the antisolvent technique to control the crystallization of Cu_2AgBiI_6 perovskite light absorber and utilization in solar cell. Incorporation of Copper in Ag and Bi based perovskite enhance its stability in moisture condition, with showed its stability as dipped thin film in water. The antisolvent method enhance the stability with improvements in photovoltaic performance of the device. Device with Cu_2AgBiI_6 perovskite light absorber showed higher power conversion efficiency to be 0.98% with good open circuit voltage and short circuit current. Furthermore, the performance of device is still low need to improve, which can be done with precisely fabrication of device it may be thickness, insertion or doping, or composition of the perovskite. Simulation investigation with the Cu_2AgBiI_6 perovskite light absorber was also performed which showed the potential of the following materials in photovoltaic devices.

5.5. References

1. Green M. A., Ho-Baillie A., Snaith H. J. (2014), The emergence of perovskite solar cells, Nature Photon, 8, 506–514 (DOI: 10.1038/nphoton.2014.134).
2. Best Research-Cell Efficiency Chart. Available at: https://www.nrel.gov/pv/cell-efficiency.html. Accessed on 25 September 2023.
3. Green M., Dunlop E., Hohl-Ebinger J., Yoshita M., Kopidakis N., Hao, X. (2021), Solar cell efficiency tables (version 57), Progress in Photovoltaics: Research and Applications, 29, 3–15 (DOI: 10.1002/pip.3371).
4. Giustino F., Snaith H. J. (2016), Toward Lead-Free Perovskite Solar Cells, ACS Energy Lett., 1, 1233–1240 (DOI: 10.1021/acsenergylett.6b00499).
5. Boyd C. C., Cheacharoen R., Leijtens T., McGehee M. D. (2019), Understanding Degradation Mechanisms and Improving Stability of Perovskite Photovoltaics, Chem. Rev., 119, 3418–3451 (DOI: 10.1021/acs.chemrev.8b00336).
6. Protesescu L., Yakunin S., Bodnarchuk M. I., Krieg F., Caputo R., Hendon C. H., Yang R. X., Walsh A., Kovalenko M. V. (2015), Nanocrystals of Cesium Lead Halide Perovskites ($CsPbX_3$, X = Cl, Br, and I): Novel Optoelectronic Materials Showing Bright Emission with Wide Color Gamut, Nano Lett., 15, 3692–3696 (DOI: 10.1021/nl5048779).
7. Stranks S. D., Eperon G. E., Grancini G., Menelaou C., Alcocer M. J. P., Leijtens T., Herz L. M., Petrozza A., Snaith H. J. (2013), Electron-Hole Diffusion Lengths Exceeding 1 Micrometer in an Organometal Trihalide Perovskite Absorber, Science, 342, 341–344 (DOI: 10.1126/science.1243982).
8. Wehrenfennig C., Eperon G. E., Johnston M. B., Snaith H. J., Herz L. M. (2014), High Charge Carrier Mobilities and Lifetimes in Organolead Trihalide Perovskites, Advanced Materials, 26, 1584–1589 (DOI: 10.1002/adma.201305172).

9. Flora G., Gupta D., Tiwari A. (2012), Toxicity of lead: A review with recent updates, Interdiscip Toxicol, 5, 47–58 (DOI: 10.2478/v10102-012-0009-2).
10. Igbari F., Wang Z.-K., Liao L.-S. (2019), Progress of Lead-Free Halide Double Perovskites, Advanced Energy Materials, 9, 1803150 (DOI: 10.1002/aenm.201803150).
11. Xiao Z., Song Z., Yan Y. (2019), From Lead Halide Perovskites to Lead-Free Metal Halide Perovskites and Perovskite Derivatives, Advanced Materials, 31, 1803792 (DOI: 10.1002/adma.201803792).
12. Yu B.-B., Chen Z., Zhu Y., Wang Y., Han B., Chen G., Zhang X., Du Z., He Z. (2021), Heterogeneous 2D/3D Tin-Halides Perovskite Solar Cells with Certified Conversion Efficiency Breaking 14%, Advanced Materials, 33, 2102055 (DOI: 10.1002/adma.202102055).
13. Cao J., Yan F. (2021), Recent progress in tin-based perovskite solar cells, Energy & Environmental Science, 14, 1286–1325 (DOI: 10.1039/D0EE04007J).
14. Volonakis G., Filip M. R., Haghighirad A. A., Sakai N., Wenger B., Snaith H. J., Giustino F. (2016), Lead-Free Halide Double Perovskites via Heterovalent Substitution of Noble Metals, J. Phys. Chem. Lett., 7, 1254–1259 (DOI: 10.1021/acs.jpclett.6b00376).
15. Wang M., Wang W., Ma B., Shen W., Liu L., Cao K., Chen S., Huang W. (2021), Lead-Free Perovskite Materials for Solar Cells, Nano-Micro Lett., 13, 62 (DOI: 10.1007/s40820-020-00578-z).
16. Zhang L., Wang K., Zou B. (2019), Bismuth Halide Perovskite-Like Materials: Current Opportunities and Challenges, ChemSusChem, 12, 1612–1630 (DOI: 10.1002/cssc.201802930).
17. Ghosh S., Shankar H., Kar P. (2022), Recent developments of lead-free halide double perovskites: a new superstar in the optoelectronic field, Mater. Adv., 3, 3742–3765 (DOI: 10.1039/D2MA00071G).
18. Ji F., Boschloo G., Wang F., Gao F. (2023), Challenges and Progress in Lead-Free Halide Double Perovskite Solar Cells, Solar RRL, 7, 2201112 (DOI: 10.1002/solr.202201112).

19. Zuo C., Ding L. (2017), Lead-free Perovskite Materials $(NH_4)_3Sb_2I_xBr_{9-x}$, Angewandte Chemie International Edition, 56, 6528–6532 (DOI: 10.1002/anie.201702265).
20. Kumar P., Ahmad K., Dagar J., Unger E., Mobin S. M. (2021), Two-Step Deposition Approach for Lead Free $(NH_4)_3Sb_2I_9$ Perovskite Solar Cells with Enhanced Open Circuit Voltage and Performance, ChemElectroChem, 8, 3150–3154 (DOI: 10.1002/celc.202100957).
21. Sun S., Tominaka S., Lee J.-H., Xie F., Bristowe P. D., Cheetham A. K. (2016), Synthesis, crystal structure, and properties of a perovskite-related bismuth phase, $(NH_4)_3Bi_2I_9$, APL Materials, 4, 031101 (DOI: 10.1063/1.4943680).
22. Zhuang R., Wang X., Ma W., Wu Y., Chen X., Tang L., Zhu H., Liu J., Wu L., Zhou W., Liu X., Yang Y. (Michael) (2019), Highly sensitive X-ray detector made of layered perovskite-like $(NH_4)_3Bi_2I_9$ single crystal with anisotropic response, Nat. Photonics, 13, 602–608 (DOI: 10.1038/s41566-019-0466-7).
23. Kumar P., Ahmad K., M. Mobin S. (2023), Improved photovoltaic performance of Pb-free $AgBi_2I_7$ based photovoltaics, Nanoscale Advances, 5, 1624–1630 (DOI: 10.1039/D3NA00029J).
24. Liu X.-K., Xu W., Bai S., Jin Y., Wang J., Friend R. H., Gao F. (2021), Metal halide perovskites for light-emitting diodes, Nat. Mater., 20, 10–21 (DOI: 10.1038/s41563-020-0784-7).
25. Wu C., Du B., Luo W., Liu Y., Li T., Wang D., Guo X., Ting H., Fang Z., Wang S., Chen Z., Chen Y., Xiao L. (2018), Highly Efficient and Stable Self-Powered Ultraviolet and Deep-Blue Photodetector Based on $Cs_2AgBiBr_6/SnO_2$ Heterojunction, Advanced Optical Materials, 6, 1800811 (DOI: 10.1002/adom.201800811).
26. Savory C. N., Walsh A., Scanlon D. O. (2016), Can Pb-Free Halide Double Perovskites Support High-Efficiency Solar Cells?, ACS Energy Lett., 1, 949–955 (DOI: 10.1021/acsenergylett.6b00471).
27. Sansom H. C., Longo G., Wright A. D., Buizza L. R. V., Mahesh S., Wenger B., Zanella M., Abdi-Jalebi M., Pitcher M. J., Dyer M. S., Manning T. D., Friend R. H., Herz L. M., Snaith H. J., Claridge J.

B., Rosseinsky M. J. (2021), Highly Absorbing Lead-Free Semiconductor Cu2AgBiI6 for Photovoltaic Applications from the Quaternary CuI–AgI–BiI_3 Phase Space, J. Am. Chem. Soc., 143, 3983–3992 (DOI: 10.1021/jacs.1c00495).

28. Burgelman M., Nollet P., Degrave S. (2000), Modelling polycrystalline semiconductor solar cells, Thin Solid Films, 361–362, 527–532 (DOI: 10.1016/S0040-6090(99)00825-1).
29. Liu D., K. Gangishetty M., L. Kelly T. (2014), Effect of $CH_3NH_3PbI_3$ thickness on device efficiency in planar heterojunction perovskite solar cells, J. Mater. Chem. A, 2, 19873–19881 (DOI: 10.1039/C4TA02637C).
30. Yang C., Kneiß M., Schein F.-L., Lorenz M., Grundmann M. (2016), Room-temperature Domain-epitaxy of Copper Iodide Thin Films for Transparent CuI/ZnO Heterojunctions with High Rectification Ratios Larger than 109, Sci Rep, 6, 21937 (DOI: 10.1038/srep21937).
31. Zhang C., Gao L., Teo S., Guo Z., Xu Z., Zhao S., Ma T. (2018), Design of a novel and highly stable lead-free Cs_2NaBiI_6 double perovskite for photovoltaic application, Sustainable Energy & Fuels, 2, 2419–2428 (DOI: 10.1039/C8SE00154E).
32. Johansson M. B., Philippe B., Banerjee A., Phuyal D., Mukherjee S., Chakraborty S., Cameau M., Zhu H., Ahuja R., Boschloo G., Rensmo H., Johansson E. M. J. (2019), Cesium Bismuth Iodide Solar Cells from Systematic Molar Ratio Variation of CsI and BiI_3, Inorg. Chem., 58, 12040–12052 (DOI: 10.1021/acs.inorgchem.9b01233).
33. Ran C., Wu Z., Xi J., Yuan F., Dong H., Lei T., He X., Hou X. (2017), Construction of Compact Methylammonium Bismuth Iodide Film Promoting Lead-Free Inverted Planar Heterojunction Organohalide Solar Cells with Open-Circuit Voltage over 0.8 V, J. Phys. Chem. Lett., 8, 394–400 (DOI: 10.1021/acs.jpclett.6b02578).
34. Hebig J.-C., Kühn I., Flohre J., Kirchartz T. (2016), Optoelectronic Properties of $(CH_3NH_3)_3Sb_2I_9$ Thin Films for Photovoltaic

Applications, ACS Energy Lett., 1, 309–314 (DOI: 10.1021/acsenergylett.6b00170).

35. Zhang F., Hu Z., Zhang B., Lin Z., Zhang J., Chang J., Hao Y. (2022), Low-Temperature Solution-Processed Cu_2AgBiI_6 Films for High Performance Photovoltaics and Photodetectors, ACS Appl. Mater. Interfaces, 14, 18498–18505 (DOI: 10.1021/acsami.2c01481).
36. Cortecchia D., Dewi H. A., Yin J., Bruno A., Chen S., Baikie T., Boix P. P., Grätzel M., Mhaisalkar S., Soci C., Mathews N. (2016), Lead-Free $MA_2CuCl_xBr_{4-x}$ Hybrid Perovskites, Inorg. Chem., 55, 1044–1052 (DOI: 10.1021/acs.inorgchem.5b01896).
37. Arivazhagan V., Gun F., Kumar Reddy R. K., Li T., Adelt M., Robertson N., Chen Y., Ivaturi A. (2022), Indoor light harvesting lead-free 2-aminothiazolium bismuth iodide solar cells, Sustainable Energy & Fuels, 6, 3179–3186 (DOI: 10.1039/D1SE02017J).
38. Ahmad K., Mobin S. M. (2020), Organic–Inorganic Copper (II)-Based Perovskites: A Benign Approach toward Low-Toxicity and Water-Stable Light Absorbers for Photovoltaic Applications, Energy Technology, 8, 1901185 (DOI: 10.1002/ente.201901185).
39. Mehra S., Pandey R., Madan J., Sharma R., Goswami L., Gupta G., Singh V.N., Srivastava A.K., Sharma S.N. (2024), Experimental and theoretical investigations of MAPbX3-Based perovskites (X= cl, br, I) for photovoltaic applications, ChemistryOpen, 13(2), 202300055 (DOI: 10.1002/open.202300055).
40. Rai S., Pandey B. K., Garg A., Dwivedi D.K., (2021), Hole transporting layer optimization for an efficient lead-free double perovskite solar cell by numerical simulation, Optical Materials, 121, 111645 (DOI: 10.1016/j.optmat.2021.111645).
41. Ahmad K., Khan M.Q., Khan R.A., Kim H., (2022), Numerical simulation and fabrication of Pb-free perovskite solar cells (FTO/TiO2/Cs3Bi2I9/spiro-MeOTAD/Au), Optical Materials, 128, 112458 (DOI: 1016/j.optmat.2022.112458).
42. Alam I., Mollick R., Ashraf M.A., (2021), Numerical simulation of $Cs_2AgBiBr_6$-based perovskite solar cell with ZnO nanorod and

P3HT as the charge transport layers, Physica B: Condensed Matter, 618, 413187 (DOI: 10.1016/j.physb.2021.413187).

43. Samanta M., Ahmed S.I., Chattopadhyay K.K., Bose C., (2020), Role of various transport layer and electrode materials in enhancing performance of stable environment-friendly Cs2TiBr6 solar cell, Optik, 217, 164805 (DOI: 10.1016/j.ijleo.2020.164805).

CHAPTER 6

Conclusion and Future Outlook

The present form of thesis aims to facilitate the transition from lead-based to lead-free perovskite materials, which is essential for the sustainable advancement of perovskite solar cells. The development of lead-free perovskite solar cells involves utilizing various light absorbers, with antimony and bismuth being key elements explored for this purpose. Solvent engineering, antisolvent approach and one step or two step technique were utilized. $(NH_4)_3Sb_2I_9$, $(NH_4)_3Bi_2I_9$, $AgBi_2I_7$, Cu_2AgBiI_6, light absorber was synthesized and employed in the development of lead-free perovskite solar cells. The developed lead-free perovskite solar cells have shown good performance in terms of open circuit voltage. The perovskite solar cells have different components like electron transport layer, light absorber, hole transport material and metal contact. The backbone of the perovskite solar cells is electron transport layer which also influence the performance of the perovskite solar cells. Theoretical simulation study was also carried out to investigate the effect of thickness on the PSCs. Simulation result showed the potential of lead-free perovskite materials in PSCs, however suitable thickness of ETL, HTL and active layer enhances the efficiency of devices. With the simulation results, implementing appropriate thickness in experimental work might improve the PCE in real world. Moreover, annealing temperature also plays crucial role in the fabrication of high-performance PSCs.

A comparative assessment of the photovoltaic potential of the compounds $(NH_4)_3Sb_2I_9$**,** $(NH_4)_3Bi_2I_9$**,** $AgBi_2I_7$**,** and Cu_2AgBiI_6 has been conducted with respect to their crystal structure, electronic band gap, optical absorption, charge transport properties, and environmental stability. The ammonium-based iodides $(NH_4)_3Sb_2I_9$ and $(NH_4)_3Bi_2I_9$ are categorized as low-dimensional (0D/2D) perovskite-derived structures, composed of isolated or layered $[M_2I_9]^{3-}$ ($M = Sb^{3+}$, Bi^{3+}) bioctahedra. These compounds exhibit relatively wide band gaps in the range of ~2.0–2.3 eV, resulting in limited optical absorption in the visible spectrum and

poor charge carrier mobility, which significantly constrain their photovoltaic performance. In contrast, $AgBi_2I_7$ displays a more interconnected and extended crystal framework, leading to enhanced orbital overlap. This compound possesses a moderate band gap (~1.8–2.0 eV), with improved light absorption and better charge transport properties relative to the ammonium-based analogues. Its performance, however, remains moderate due to partially indirect band character and structural limitations. Among the materials considered, Cu_2AgBiI_6 emerges as the most promising candidate. It adopts a three-dimensional double perovskite structure, which facilitates efficient charge transport pathways. The material exhibits a direct-like optical band gap (~1.9–2.0 eV) that aligns well with the solar spectrum, strong visible light absorption, and excellent thermal and environmental stability. Moreover, it is lead-free and non-toxic, addressing key environmental concerns associated with conventional Pb-based perovskites. These characteristics make it a highly suitable lead-free and eco-friendly material for next-generation solar cell applications.

Toxicity and stability concerns associated with lead, motivated researchers to utilize lead-free perovskite materials in the fabrication solar cell devices. It is possible to obtain single crystals and well-crystallized thin films from these lead-free materials by employing economical solution processing methods. Altering synthesis methods, might help in lowering the bandgap. To enhance film quality, more investigation is being done to better understand carrier dynamics and the crystallization mechanism. Understudied metal halide double perovskites, bismuth-based perovskite derivatives, and air-stable perovskites are some of the potential options for further research. However, achieving optimal performance in large-area modules remains challenging. Key areas for improvement include lowering the band gap, controlled and uniform morphology, modifying fabrication methods, optimizing films thickness, solvent engineering, employing different architectures or new electron transport layers, hole transport materials and strategic doping.

Employing suitable fabrication techniques is crucial for enhancing device performance. To further advance the efficiency of perovskite-based devices, it is essential to delve deeper into the carrier dynamics and crystallization mechanisms, reduce defect density, and identify suitable charge carrier materials for device fabrication. Finally, in tandem solar cells, wide bandgap perovskites are combined with silicon or other semiconductors to increase light absorption and enhance device performance. Additionally, research should focus on optimizing the performance of these lead-free perovskites and addressing the challenges related to their stability and scalability for commercial applications.

APPENDIX 1

Table A1–A7

Chapter 2

Table: A1 Photovoltaic parameter comparisons of recently observed Pb free PSCs.

S. No.	Light absorber	Voc(mV)	Jsc (mA/cm^2)	FF (%)	PCE (%)	References
1.	$(CH_3NH_3)_3Bi_2I_9$	810	2.95	69	1.64	47
2.	Cs_2NaBiI_6	470	1.99	44	0.42	48
3.	$(CH_3NH_3)_3Sb_2I_9$	740	1.40	47	0.54	22
4.	$(C_6H_5CH_2NH_3)_2CuBr_4$	680	0.73	41	0.2	49
5.	$Cs_3Bi_2I_9$	570	2.22	49	0.62	50
6.	$Cs_3Sb_2I_9$	620	2.34	-	0.67	51
7.	$(NH_4)_3Sb_2I_9$	1003	1.15	42.9	0.51	34
8.	**PSC-1**	**942**	**0.80**	**34**	**0.20**	**Present work**
9.	**PSC-2**	**945**	**1.16**	**42**	**0.42**	**Present work**

*References in Chapter 2.

Chapter 3

Table: A2 Photovoltaic parameters of the developed PSCs.

S. No.	Materials	Jsc (mA/cm^2)	FF	V_{oc} (mV)	PCE (%)
1.	ABI-1	0.19	0.37	316	0.02
2.	ABI-2	0.60	0.31	488	0.1
3.	ABI-3	2.62	0.48	376	0.6

Table: A3 Photovoltaic parameters of the developed PSCs.

S. No	Light absorbers	Voc (mV)	FF (%)	Jsc (mA/cm^2)	PCE (%)	References
1	$(FA)_3Bi_2I_9$	480	0.46	0.11	0.022	32
2	$(HDABiI_5)$	384	0.43	0.124	0.027	33
3	$(CH_3NH_3)_3Bi_2I_9$	580	0.41	1.04	0.25	34
4	$(CH_3NH_3)_3Bi_2I_9$	590	0.57	0.5	0.17	35
5	$(CH_3NH_3)_3Bi_2I_9$	400	0.36	0.11	0.016	36
6	$(CH_3NH_3)_3Bi_2I_9$	680	0.33	0.52	0.12	37
7	$(CH_3NH_3)_3Sb_2I_9$	740	0.52	1.48	0.57	38
8	$(CH_3NH_3)_3Sb_2I_9$	896	0.55	1.0	0.49	21
9	$(CH_3NH_3)_2CuCl_2Br_2$	290	0.52	0.216	0.017	39
10	$C_6H_4NH_2CuBr_2I$	200	0.46	6.2	0.46	15
11	$(CH_3NH_3)_3Sb_2I_9$	740	0.47	1.40	0.54	40
12	**ABI-3**	**376**	**0.48**	**2.62**	**0.6**	***This Work***

*References in Chapter 3.

Chapter 4

Table: A4 Showing the comparison of reported photovoltaic performance with SBI-D and SBI-DM.

S. No	**Light absorbers**	**Voc (mV)**	**FF (%)**	**Jsc (mA/cm^2)**	**PCE (%)**	**References**
1	$(CH_3NH_3)_3Sb_2I_9$	896	55	1.0	0.49	[21]
2	$C_6H_4NH_2CuBr_2I$	200	46	6.2	0.46	[16]
3	Cs_2SnI_6	520	52	3.2	0.86	[39]
4	$AgBi_2I_7$	690	43	2.76	0.83	[34]
5	$(CH_3NH_3)_3Sb_2I_9$	740	52	1.48	0.57	[40]
6	Cs_2NaBiI_6	470	44	1.99	0.42	[41]
7	$Cs_3Bi_2I_9$	570	222	49	0.62	[42]
8	$(NH_4)_3Sb_2I_9$	1003	115	42.9	0.51	[43]
9	$CH_3NH_3SnBr_3$	490	46	2.2	0.5	[44]
10	$(MA_3(Bi_{1-x}Sn_x)_2I_9)$	556	48	3.70	0.91	[45]
11	**SBI-D**	**540**	**46**	**2.81**	**0.69**	***This Work***
12	**SBI-DM**	**650**	**48**	**3.07**	**0.96**	

*References in Chapter 4.

Chapter 5

Table: A5 Comparison of various published perovskite materials with their photovoltaic performances

S. No	**Light absorbers**	**FF (%)**	**Voc (V)**	**Jsc (mA/cm^2)**	**PCE (%)**	**References**
1	Cs_2NaBiI_6	44	0.47	1.98	0.42	31
2	$Cs_3Bi_2I_9$	49	0.57	2.22	0.62	32
3	$MA_3Bi_2I_9$	37	0.83	1.39	0.39	33
4	$(CH_3NH_3)_3Sb_2I_9$	52	0.885	1.0	0.46	34
5	Cu_2AgBiI_6 (With PEAI)	49	0.55	2.26	0.61	35
6	Cu_2AgBiI_6 (Without PEAI)	47	0.64	3.34	1.00	
7	Cu_2AgBiI_6	59	0.47	1.54	0.43	27
8	$MA_2CuCl_2Br_2$	32	0.256	0.216	0.017	36
9	$(NH_4)_3Sb_2I_9$	42.9	1.03	1.15	0.51	19
10	$ATBiI_4$	43.4	0.82	1.49	0.53	37
11	$C_6H_4NH_2CuBr_2I$	36	0.370	5.70	0.63	38
12	**Cu_2AgBiI_6**	**19**	**0.700**	**7.4**	**0.98**	**This Work**

Table: A6 Comparison of various published perovskite materials with their photovoltaic performances

S. No.	**Absorber**	**Thickness (nm)**	**J_{SC} ($mA.cm^{-2}$)**	**V_{OC} (V)**	**FF (%)**	**PCE (%)**	**References**
1	$MAPbBr_3$	500	7.5	1.23	73.9	6.87	39
2	$MAPbCl_3$	500	4.8	1.35	76.1	4.98	39
3	$AgBi_2I_7$	500	14.36	1.20	76.5	13.2	23
4	$Cs_2AgBiBr_6$	400	14.51	0.99	68.88	9.98	40
5	$Cs_3Bi_2I_9$	650	1.22	77.73	12.19	11.54	41
6	$Cs_2AgBiBr_6$	600	11.10	0.9156	44.02	4.48	42
7	Cs_2TiBr_6	330	10.25	1.12	73.59	8.51	43
8	**Cu_2AgBiI_6**	**500**	**8.52**	**1.195**	**79.9**	**8.01**	**This Work**

*References in Chapter 5.

Table: A7 Permissions for re-producing the materials

Figure 1.1	Diagram showing the efficiency of renewable energy cells	Reproduced from Ref. [16], (https://www.nrel.gov/pv/cell-efficiency.html)
Figure 1.2	Structure of perovskites with ABX_3 formula	Reproduced from Ref. [35], with permission from the Royal Society of Chemistry
Figure 1.3	(a) Cubic crystal structure of perovskite (b) double perovskite crystal structure	Reproduced from Ref. [37], with permission from Springer Nature
Figure 1.5	PSCs working principle (a) Device designs, (b) mesoporous n–i–p, (c) planar n–i–p, and (d) inverted p–i–n structured PSCs	Reproduced from Ref. [43], with permission from the Royal Society of Chemistry
Figure 1.6	General scalable solution deposition techniques for fabrication of PSCs	Reproduced from Ref. [57], with permission from the Springer Nature
Figure 1.7	HOMO-LUMO level of few perovskites, ETL, HTL, and back contact metal electrode used in PV devices.	Reproduced from Ref. [65], with permission from the Royal Society of Chemistry
Figure 1.9	SEM and cross-section image of $(CH_3NH_3)_3Bi_2I_9$ perovskite layer deposited on compact layer TiO_2 (a, b), brookite mesoporous (c, d), anatase mesoporous (e, f).	Reproduced from Ref. [70], with permission from the American Chemical Society
Figure 1.12	(A) spinning-coating process (B) X-ray diffraction (C) AFM and SEM images on Si substrate of samples ($MABr : SnBr_2 = 4 : 1$).	Reproduced from Ref. [95], with permission from the American Chemical Society Reproduced from Ref. [96], with permission from the Royal Society of Chemistry
Figure 1.13	(A) Crystal structures of $A_3Sb_2I_9$ perovskite (B) representation of photovoltaic device (C, D) Absorbance spectra of $MA_3Sb_2I_9$ and $Cs_3Sb_2I_9$, (E, F)	Reproduced from Ref. [115], with permission from the Royal Society of Chemistry

	J–V characteristics of $MA_3Sb_2I_9$ and $Cs_3Sb_2I_9$.	
Figure 1.14	Schematic diagram of PSCs device and some owing properties perovskite materials based on Bi.	Reproduced from Ref. [65], with permission from the Royal Society of Chemistry
Figure 1.15	(A) Representation of the synthesis of $Cs_2AgBiBr_6$ films by vacuum-sublimation and solution-processing, (B) Device structure, (C) J–V curves, (D) EQE spectra, (E) stability.	Reproduced from Ref. [128], with permission from the American Chemical Society
Figure 1.16	SEM images of $Cs_3Bi_2I_9$, $CsBi_3I_{10}$, BiI_3 under high and low magnification	Reproduced from Ref. [50], with permission from the American Chemical Society
Figure 1.17	(A, B, C) optical images, absorbance spectra, X-RD patterns of $Cs_3Bi_2I_{9-x}Br_x$ films (D) Tauc plots, (E) J–V curves of $Cs_3Bi_2I_9$ and $Cs_3Bi_2I_6Br_3$	Reproduced from Ref. [75], with permission from the Royal Society of Chemistry